

METAMATERIAL MICROSTRIP TRANSMISSION LINE BASED
MICROWAVE CIRCUITS AND SENSORS

By

Nophadon Wiwatcharagoses

A DISSERTATION

Submitted to
Michigan State University
in partial fulfillment of the requirements
for the degree of

DOCTOR OF PHILOSOPHY

Electrical Engineering

2012

ABSTRACT

METAMATERIAL MICROSTRIP TRANSMISSION LINE BASED MICROWAVE CIRCUITS AND SENSORS

By

Nophadon Wiwatcharagoses

There is significant interest in metamaterials (MTMs) for the design of novel microwave circuits and sensors. Metamaterials with their unique properties allow for the design of circuits and sensors that are compact and provide new functionalities that are difficult to achieve using conventional design approaches. Split ring resonators (SRRs) and complimentary split ring resonators (CSRRs) have been studied in great detail over the last decade as metamaterial structures. However, so far these designs have largely been implemented at low-frequencies (1-3 GHz) and require complex fabrication. To design active microwave circuits, planar metamaterial unit cell structures that readily allow the integration of active devices as an integral part of the structure are necessary.

This thesis investigates the use of composite right/left handed microstrip metamaterial transmission lines in the design of microwave planar circuits and sensors. Microstrip based designs are compatible with wafer-level integration and lead to the integration of active device elements as an integral part of the metamaterial unit cell. Microfluidic channels can also be integrated with these planar structures to form sensors. Here, high frequency metamaterial transmission lines integrated with active devices to design microwave circuits are studied. Such metamaterial structures that are sensitive to their environments in the near-field are also investigated for sensor design applications.

Metamaterial structures can be designed to achieve high field strengths at local spots within the unit cell structure. Dielectric (or capacitive) loading at these local spots is investigated in detail. Actively changing the capacitance at these spots using varactor diodes leads to reconfigurable circuits and allows for the design of new functions that are difficult to achieve using conventional circuit designs. In contrast, observing a change in the performance of microwave circuits by loading with biological or chemical samples allows for the design of novel microwave sensors. The dispersion diagram of these structures shows composite right/left handed properties. These properties change upon loading with capacitive elements and are analyzed to demonstrate the working principle of the sensor circuits.

In order to accommodate active device elements as an integral part of the MTM structure, a new metamaterial unit cell is proposed in the X-band (7.5-12 GHz) frequency range that utilizes single-side metallization. Detailed analysis of the unit cell is carried out to incorporate varactor diodes at optimum locations for the design of reconfigurable or tunable microwave circuits. A novel reconfigurable power splitter with unequal power division function, a wide-band reconfigurable X-band phase shifter with high linearity of phase shift, and a miniaturized reconfigurable antenna are designed and demonstrated.

Apart from the design of high frequency microwave circuits, metamaterial structures have been exploited in the designs of novel microwave sensors. A metamaterial-inspired microfluidic sensor and a novel high-Q compact volatile molecular sensor are designed and demonstrated. Furthermore, a near-field RF probe array for material characterization and simultaneous sub-wavelength imaging of structures is demonstrated. Sensors built using metamaterials-based microstrip transmission show high sensitivity compared to conventional designs.

.

Copyright by
NOPHADON WIWATCHARAGOSES
2012

For loving memory of my dear grandparents

and

In memory of 26 years of our sincere friendship, Werachai Wongkiatthaworn.

ACKNOWLEDGEMENTS

There are many people who deserve acknowledgement throughout my years at Michigan State University. First and foremost, many special thanks to my advisor, Dr. Premjeet Chahal for everything that he has done for me. His magnificent ideas and suggestions inspired me to discover the new things while I was doing the research. In other words, this thesis is really the outcome of his encouragement, support and generosity over many years in my research under his guidance. I could not have asked for better guidance from anyone.

I would like to express my gratitude to my committee members, Dr. Tim Hogan, Dr. Alejandro R. Diaz and Dr. Fang Z. Peng for their invaluable comments and for inspirational ideas for my research since part B of the doctoral qualifying examination. I really appreciate their help and guidance and most importantly for serving as my PhD committee.

Also, I would like to thank my colleagues at the Terahertz Systems Laboratory, NDE laboratory and EM Research Group for their helpful discussions. Many thanks to Brian Wright for helpful discussions in microfabrication. Special thanks to Dr. J. A. Hejase, X. Yang, C. S. Meierbachthol, J. C. Myers, C. Acosta and my best labmate - Kyoung Youl Park for all their help, encouragement as well as sincere friendship in many years at Michigan State University. I sincerely hope our friendship never ends.

Especially, I would like to thank Gordon Jensen, Heidi Jensen and their cute daughter - Nori Jensen for their good friendships and entire dedication during these years in Michigan. They introduced me to learn many things about American culture and visit various places in Michigan. Moreover, they helped me a lot with assimilation in language. I had a great time with them and their hospitality will be missed.

Furthermore, I am thankful to the Royal Thai Government and the Department of Electrical and Computer Engineering at King Mongkut's University of Technology (North Bangkok) for funding my PhD study in the States. I express my greatest thanks to my friends in Thailand, especially Chaiyan Suwancheewasiri, Chavana Yoopakdee, Dr. Phoemphun Oothongsap and Dr. Pisit Liutanakul, for their steadfast friendships and strong support, despite the large distance between us.

Also, I would like to thank my Thai friends at Michigan State University, especially Tanatorn Tongsumrith and his family for their help and encouragement throughout my studies at MSU.

Finally, I deeply want to thank my parents, Opas Wiwatcharagoses, Orasa Wiwatcharagoses, Niwat Palapinyo, Tadsanee Palapinyo, and my parents in-law, Piboon Anuraksakul, Prapai Anuraksakul and all of my family members for their generous contributions and unconditional support, especially the last period of my study here. Also, I would like to express my sincere thanks to my wife's colleagues and neurosurgery team including critical care unit staff at Rajavithi Hospital who provided my beloved wife with the best medical treatment in time to save her life. It is really a miracle that I still have her in my life; I could not imagine my life without her. Lastly, the most important one to whom I am indebted is my beloved wife, Dr. Kittiyaporn Wiwatcharagoses. My deepest gratitude is reserved for her whom I love with all my heart. Everything in my life is possible because of her love, her support, her understanding, her trust, her belief and especially her sacrifice. Although she was in the most critical time of her life, she still insisted and convinced me to stay for completing my PhD study as well as promised to stay strong until I return.

TABLE OF CONTENTS

LIST OF TABLES	x
LIST OF FIGURES	xi
 CHAPTER 1	
INTRODUCTION	1
1.1 Background and Motivation	1
1.2 Dissertation Overview	3
1.3 Research Contribution	6
 CHAPTER 2	
FUNDAMENTAL THEORY OF METAMATERIALS.....	9
2.1 Definition of Metamaterials and Left-Handed Media	9
2.2 Experimental Left-Handed Metamaterials.....	11
2.3 Composite Right/Left-Handed (CRLH) Metamaterials.....	14
2.3.1 Pure Right-Handed Transmission Line.....	20
2.3.2 Pure Left-Handed Transmission Line.....	21
2.3.3 Composite Right/Left Handed Transmission Line (Unbalanced)	23
2.3.4 Composite Right/Left Handed Transmission Line (Balanced).....	24
2.4 LC Network Implemented on Metamaterials	26
2.5 Periodic Analysis Addressed LC Loaded Transmission Line Network	29
2.5.1 Periodic Lumped-Element Right-Handed Line	31
2.5.2 Periodic Lumped-Element Left-Handed Line	33
2.5.3 Periodic Lumped-Element CRLH Transmission Line.....	35
2.6 Selected Metamaterial Structures	46
2.7 Proposed Metamaterial Structures	48
2.8 Metamaterials Inspired Microwave Circuits and Sensors	51
 CHAPTER 3	
METAMATERIAL INSPIRED POWER DIVIDER	56
3.1 A Novel Metamaterial Structure Based Microstrip Technology	56
3.2 Compact Power Splitter Design and Reconfigurability.....	59
3.2.1 A Novel Metamaterial Structure Based Microstrip Technology	62
3.2.2 A Novel Metamaterial-Inspired Reconfigurable Power Divider	63
3.3 Fabrication and Experimental Results	67
3.3.1 Reconfigurability with Equal Power Division.....	68
3.3.2 Reconfigurability with Unequal Power Division.....	70
3.4 Conclusion	73

CHAPTER 4

METAMATERIAL-INSPIRED PHASE SHIFTER DESIGN	75
4.1 Network Parameter Analysis	76
4.2 Electrically Tunable Components.....	78
4.3 Simulated and Experimental Results	79
4.4 Discussion	88
4.5 Conclusion	88

CHAPTER 5

METAMATERIAL-INSPIRED MICROFLUIDIC SENSOR	90
5.1 Metamaterial Transmission Line Based Spiral Structure	90
5.1.1 Left-Handed Media Based Double Spiral Structure	91
5.1.2 Double Spiral Structure Based Microstrip TL.....	93
5.2 Microfluidic Based Sensors	97
5.3 Fabrication and Experimental Results	99
5.3.1 RF Measurements.	100
5.3.2 Interpretation of Results.....	104
5.4 Conclusion	113

CHAPTER 6

METAMATERIAL-INSPIRED COMPACT VOLATILE MOLECULAR SENSOR	114
6.1 Metamaterial-Inspired Resonator Probe	114
6.2 Design and Simulation.....	116
6.3 Experimental Results	120
6.4 Discussion	125

CHAPTER 7

METAMATERIAL-INSPIRED MICROWAVE PROBES	126
7.1 Microwave Sensing Probe Regions	126
7.1.1 Modified Split Ring Resonators.....	127
7.1.2 Reflective Split Ring Resonators	128
7.2 Design and Simulation.....	130
7.2.1 Modified Split Ring Resonators.....	130
7.2.2 Reflective Split Ring Resonators	132
7.3 Experimental Results	134
7.3.1 Experiments on Modified Split Ring Resonators	134
7.3.2 Experiments on Reflective Split Ring Resonators.....	140
7.4 Probing and Dielectric Imaging by Edge-Coupling Array	145
7.4.1 Reliaization of Edge Coupling Under Dielectric Loading.....	147
7.4.2 Reliaization on Non-Destructuve Evaluation	149
7.5 Conclusion	152

CHAPTER 8

METAMATERIAL-INSPIRED RECONFIGURABLE ANTENNA	154
8.1 Antenna Description	155
8.2 Validation of Reconfigurable Antenna Model.....	158
8.3 Experimental Results	162
8.4 Conclusion	166

CHAPTER 9

CONCLUSIONS AND FUTURE WORK	164
9.1 Conclusions	167
9.2 Future Work on MTM Microstrip T-line based Microwave Circuits and Sensors.....	169
9.2.1 Fully Hybrid Split Ring Resonator and Higher Bit Phase Shifter	170
9.2.2 Novel Chemical and Biological Sensors based MTM Resonator.....	173
9.2.3 Metamaterial Antennas Based Phased Arrays	175
9.2.4 Use of Metamaterial Structures for MMIC Designs.....	175

APPENDICES	176
Appendix A: Equivalent circuit for the 1-D CRLH Transmission Line	177
Appendix B: Microfabrication Process.....	183
Appendix C: Basic Calculation Based on the Ideal Gas Law	186

BIBLIOGRAPHY	188
---------------------------	------------

LIST OF TABLES

Table 2-1: Summary and comparison of MTM-inspired resonant structures based microstrip line	46
Table 3-1: Essential Scattering Parameters for Equal Dividing	69
Table 3-2: Essential Scattering Parameters for Unequal Dividing	71
Table 4-1: Characteristic performances of the reconfigurable X-band phase shifter.....	87
Table 6-1: Summary of the essential parameters in the experiment	123
Table 6-2: Q-factors and resonance frequency, f_c of the proposed sensor with different vaporized liquid loads.....	123
Table 7-1: Delta resonant frequency shift from dielectric loading in the probing regions.....	145
Table 8-1: Summary and comparison of MTM-inspired antenna structure for miniaturization	157
Table 8-2: The resonant frequency and radiation pattern of the reconfigurable antenna	161

LIST OF FIGURES

Figure 1-1. Schematic layout of (a) SRRs, (b) CSRRs, and (c) DS-CSRRs (Metal patterning is expressed as dark gray).....	2
Figure 2-1. Permittivity-permeability ($\epsilon - \mu$) and refractive index (n) diagram [5].....	11
Figure 2-2. First negative- ϵ /positive- μ and positive- ϵ /negative- μ MTM structures ($p \ll \lambda_g$), (a) Thin-wire (TW) structure exhibiting negative- ϵ /positive- μ if $\mathbf{E} \parallel z$ [2], (b) Split-ring resonator (SRR) structure exhibiting positive- ϵ /negative- μ if $\mathbf{H} \perp y$ [3].....	13
Figure 2-3. The effective magnetic permeability of MTM from artificially induced magnetic dipole moments.....	14
Figure 2-4. A representative of an ideal homogeneous transmission line and its equivalent circuit model for ideal CRLH approach.....	15
Figure 2-5. Dispersion diagram of a CRLH TL for energy propagation along the +z direction (unbalanced mode).....	19
Figure 2-6. Dispersion diagram of a CRLH TL for energy propagation along the +z direction (balanced mode).....	19
Figure 2-7. As energy propagation along the +z direction of PRH transmission line, (a) dispersion diagram and (b) its phase velocity and group velocity diagram.....	20
Figure 2-8. As energy propagation along the +z direction of PLH transmission line, (a) dispersion diagram and (b) its phase velocity and group velocity diagram.....	21
Figure 2-9. Incremental equivalent circuit of a PLH transmission line which can be model a uniform one-dimensional distributed transmission line.....	22

Figure 2-10. As energy propagation along the $+z$ direction of PLH transmission line, (a) dispersion diagram and (b) its phase velocity and group velocity diagram.....	22
Figure 2-11. As energy propagation along the $+z$ direction of CRLH (unbalanced) transmission line, (a) dispersion diagram and (b) phase velocity and group velocity diagram.....	24
Figure 2-12. As energy propagation along the $+z$ direction of CRLH (balanced) transmission line, (a) dispersion diagram and (b) phase velocity and group velocity diagram.....	25
Figure 2-13. Unit cell of LC network implemented on CRLH transmission line (a) a general circuit (b) a balanced circuit ($L_R C_L = L_L C_R$).....	26
Figure 2-14. Periodic ladder network implemented LC CRLH transmission line in a restricted frequency range, (a) an ideal transmission line representative, (b) a general LC CRLH transmission line, (c) a balanced LC CRLH transmission line.....	28
Figure 2-15. Equivalent circuit models of an ideal homogeneous transmission line, (a) general circuit, (b) T-circuit and (c) π -circuit.....	30
Figure 2-16. A representative of a two-port network as a model of the unit cell.....	30
Figure 2-17. Dispersion diagrams for representatives of transmission line, compared between the incremental circuit analysis (Telegrapher's equations) and the periodic lumped-element approach (Bloch and Floquet analysis) as energy propagation along the $+z$ direction, (a) PRH transmission line, (b) PLH transmission line.....	35
Figure 2-18. Simplified equivalent circuit (T -configuration) of 1-D ideal CRLH homogeneous transmission line having the physical length d	36
Figure 2-19. Generic unit cell (T -configuration) of a metamaterial line having the physical length d	37
Figure 2-20. Dispersion diagrams computed by equation 2-61 of CRLH transmission line at a forward propagation ($+z$ direction), (a) balanced mode, (b) unbalanced mode.....	40

Figure 2-21. Dispersion diagrams computed by equation 2-61 of CRLH transmission line at a forward propagation (+z direction) in the alternative illustrations, (a) general illustration, (b) preferable illustration.....	41
Figure 2-22. The transformation of T -unit cell into π -unit cell of a metamaterial line having the physical length d	44
Figure 2-23. The transformation of the proposed unit cell in this research work into the T -unit cell based the CRLH transmission line.....	49
Figure 2-24. Dispersion relation of the proposed mSRR unit cell design.....	49
Figure 2-25. Dispersion relation of the proposed OmSRR unit cell design.....	50
Figure 2-26. Potential locations on the unit cell for the integration of active elements.....	51
Figure 2-27 Dispersion diagrams of the OmSRR unit cell integrated with three different capacitances.....	52
Figure 2-28 The derivative of group velocity diagrams of the OmSRR unit cell integrated with three different capacitances.....	55
Figure 2-29 The normalized derivative of group velocity diagrams of the OmSRR unit cell integrated with three different capacitances.....	55
Figure 3-1. Topologies of the metamaterial structures and their equivalent circuit models (a) split ring resonator (SRR), (b) open split ring resonator (OSRR).....	57
Figure 3-2. Topology of the new MTM unit cell and its equivalent circuit model. This structure avoids the use of vias, and requires only single level fabrication (ground plane is solid.....	58
Figure 3-3. Simulated fields overlays on the proposed unit cell by Ansoft HFSS, (a) electric field (b) magnetic field.....	61

Figure 3-4. Basic topology for a power divider with 90° impedance inverter.....	62
Figure 3-5. The novel MTM unit cell inspired power divider with reconfigurability and unequal power dividing features.....	64
Figure 3-6. Simulated fields overlays on the proposed unit cell inspired power divider by Ansoft HFSS, (a) electric field (b) magnetic field, when $C1 = C2$	65
Figure 3-7. Simulated fields overlays on the proposed unit cell inspired power divider by Ansoft HFSS, (a) electric field (b) magnetic field, when $C1 > C2$	66
Figure 3-8. Photograph of the fabricated novel MTM unit cell inspired reconfigurable power divider. (inset-right) Zoom-in for the proposed unit cell, integrated with the varactor diodes clearly visible in the circuit. (inset-left) Actual dimension of the prototype before varactor diode integration.....	68
Figure 3-9. Measured return loss, S_{11} of the proposed unit cell inspired reconfigurable power splitter based equal mode.....	69
Figure 3-10. Measured insertion loss, S_{21} and S_{31} of the proposed unit cell inspired reconfigurable power splitter based equal mode.....	70
Figure 3-11. Measured scattering responses of the proposed unit cell inspired reconfigurable power splitter based unequal mode at $C1=2.2\text{pF}$, $C2=0.98\text{pF}$	71
Figure 3-12. Measured scattering responses of the proposed unit cell inspired reconfigurable power splitter based unequal mode at $C1=2.2\text{pF}$, $C2=0.38\text{pF}$	72
Figure 3-13. Measured scattering responses of the proposed unit cell inspired reconfigurable power splitter based unequal mode at $C1=2.2\text{pF}$, $C2=0.32\text{pF}$	72
Figure 3-14. Measured scattering responses of the proposed unit cell inspired reconfigurable power splitter based unequal mode at $C1=2.2\text{pF}$, $C2=0.30\text{pF}$	73

Figure 4-1. Physical layouts of the proposed MTM unit cell for phase shifter application, (a) modified split ring resonator (mSRR), (b) modified split ring resonator with open-gap (OmSRR).....	75
Figure 4-2. Dispersion relation of the mSRR unit cell (as shown in Figure 4.1(a)), (inset) the equivalent model of mSRR unit cell with <i>LC</i> -parameters.....	77
Figure 4-3. Dispersion relation of the OmSRR unit cell (as shown in Figure 4-1(b)), (inset) the equivalent model of OmSRR unit cell with <i>LC</i> -parameters	77
Figure 4-4. (a) The MTM unit cell with a varactor diode embedded in the structure, (b) its equivalent circuit model (assuming ideal varactor diode).....	79
Figure 4-5. Proposed reconfigurable X-band phase shifter simulated using Ansoft HFSS.....	80
Figure 4-6. Simulated E-fields overlays at 10 GHz on the proposed reconfigurable X-band phase shifter MTMs simulated using Ansoft HFSS.....	81
Figure 4-7. Simulated surface current density (<i>J</i> _{surf}) overlays at 10 GHz on the proposed reconfigurable X-band phase shifter MTMs simulated using Ansoft HFSS.....	81
Figure 4-8. Simulated insertion loss, <i>S</i> ₂₁ (dB) of the reconfigurable X-band phase shifter.....	82
Figure 4-9. Simulated return loss, <i>S</i> ₁₁ (dB) of the reconfigurable X-band phase shifter.....	82
Figure 4-10. Simulated insertion phase responses with various capacitance values the MTM-inspired reconfigurable X-band phase shifter.....	84
Figure 4-11. Photograph of a fabricated reconfigurable X-band phase shifter, (inset) a blow-out of the figure showing surface mount varactor diode.....	84
Figure 4-12. Measured insertion loss, <i>S</i> ₂₁ (dB) of the reconfigurable X-band phase shifter.....	85
Figure 4-13. Measured return loss, <i>S</i> ₁₁ (dB) of the reconfigurable X-band phase shifter.....	86

Figure 4-14. Measured insertion phase responses of the reconfigurable X-band phase shifter at different DC bias voltages.....	87
Figure 5-1. (a) Double spiral unit cell with its equivalent circuit, and (b) Dispersion relation for the spiral split-loop grounded periodic array by the periodic Bloch-Floquet analysis.....	92
Figure 5-2. Normalized values of E -field and H -field distributions in spiral split-loop element array.....	93
Figure 5-3. (a) A model of the artificially structured periodic media based double spiral by Ansoft HFSS, (b) a fabricated MTM microstrip TL based double spiral structure.....	94
Figure 5-4. Simulated and measured frequency responses of the MTM microstrip technology based spiral structure. The simulated structure model is depicted in the inset.....	95
Figure 5-5. Vector field distributions on the unit cells of double spiral array based microstrip line at resonance frequency, f_o : (a) E -field distribution, (b) H -field distribution.....	96
Figure 5-6. (a) Optical photograph of a PDMS microfluidic channel before laminated PI film, and (b) Fabrication process of a microfluidic chip in this work.....	98
Figure 5-7. Simulated and measured frequency responses of the fabricated metamaterial RF device attached with PDMS microfluidic channel on the top. The simulated structure model is depicted in the inset.....	99
Figure 5-8. (a) Fabricated MTM RF sensor device integrated with PDMS microfluidic channels, (b) Measurement setup diagram of the experiment.....	100
Figure 5-9. Measured return loss, S_{11} under test corresponding different concentrations of water-methanol mixtures.....	101
Figure 5-10. Measured insertion loss, S_{21} under test corresponding different concentrations of water-methanol mixtures.....	101

Figure 5-11. Measured return loss - phase under test corresponding different concentrations of water-methanol mixtures.....	102
Figure 5-12. Measured return loss, S_{11} under test corresponding different concentrations of water-IPA mixtures.....	102
Figure 5-13. Measured insertion loss, S_{21} under test corresponding different concentrations of water-IPA mixtures.....	103
Figure 5-14. Measured return loss – phase under test corresponding different concentrations of water-IPA mixtures.....	103
Figure 5-15. (a) Dielectric constant, ϵ' and (b) loss tangent, $\tan \delta$ of water-methanol mixtures at various frequencies based on [44].....	106
Figure 5-16. (a) Dielectric constant (ϵ') and loss tangent ($\tan \delta$) of water-IPA mixtures at various frequencies based on [44].....	107
Figure 5-17. Dielectric constant of the samples at 2.1 GHz by cubic curve fitting, (a) water-methanol and (b) water-2-propanol mixtures.....	108
Figure 5-18. Loss tangent of the samples at 2.1 GHz by cubic curve fitting, (a) water-methanol and (b) water-2-propanol mixtures.....	109
Figure 5-19. Correlation between dielectric constant and loss tangent of the samples at each concentration index (X).....	110
Figure 5-20. Change in the resonance frequency, $S_{11}(f_r)$, with approximate dielectric constant of water –methanol and water-2-propanol mixtures.....	110
Figure 5-21. Dependency of steepness of reflection on (a) water-methanol samples and (b) water-2-propanol.....	112
Figure 6-1. The representative of vapor-exposure on the volatile molecular sensor leading to a significant shift of resonant characteristics.....	116

Figure 6-2. Configuration of the OmSRR inspired the volatile molecular sensor base 1-port microstrip technology.....	117
Figure 6-3. The simulated return loss, $S_{11}(\text{dB})$ of the proposed volatile molecular sensor by Ansoft HFSS.....	117
Figure 6-4. Simulated E-field pattern along the volatile molecular sensor based on OmSRR structure by Ansoft HFSS.....	119
Figure 6-5. Simulated E-field pattern along an open-circuited half wavelength microstrip line by Ansoft HFSS.....	119
Figure 6-6. Photograph of the fabricated OmsRR-inspired compact volatile molecular sensor.	120
Figure 6-7. Measurement set-up of the compact volatile molecular sensing experiment. (inset-right) Zoom-in for the proposed unit cell inside the enclosed 250mL-bell jar.....	121
Figure 6-8. Different spectral resonant shift in measurement for different acetone droplets.....	122
Figure 6-9. Different spectral resonant shift in measurement for different methanol droplets.....	122
Figure 6-10. Correlation of shift – in resonant frequency and estimated volatile molecular concentrations of vaporized acetone and methanol.....	124
Figure 7-1. (a) Microstrip transmission line coupled mSRRs sensing probe, (b) Cross section of a microstrip transmission line with schematic E -field and H - field distributions.....	128
Figure 7-2. (a) Microstrip transmission line coupled rSRRs sensing probe, (b) Cross section of a microstrip transmission line with schematic E -field and H - field distributions.....	129
Figure 7-3. Simulated scattering parameters (S_{21} and S_{11}) of the mSRR-inspired microwave sensing probes.....	131

Figure 7-4. Simulated, using Ansoft HFSS®, fields overlays at resonance frequency of mSRRs <i>E</i> -field (left), surface current density distribution (right).....	131
Figure 7-5. Simulated scattering parameters (S_{21} and S_{11}) of the rSRR-inspired microwave sensing probes.....	133
Figure 7-6. Simulated, using Ansoft HFSS®, fields overlays at resonance frequency of rSRRs <i>E</i> -field (left), surface current density distribution (right).....	133
Figure 7-7. Photograph of a fabricated microwave sensing probe based mSRRs (inset) a blow-out of the figure showing the mSRR structure.....	135
Figure 7-8. Measured and simulated insertion loss (S_{21} , dB) of mSRRs based sensing probe..	135
Figure 7-9. (a) The measured insertion loss (S_{21} , dB) and (b) the measured insertion phase (degree) of the mSRRs sensing probe loaded with different dielectric constant samples.....	137
Figure 7-10. (a) The measured insertion loss (S_{21} , dB) and (b) the measured insertion phase (degree) of the mSRRs sensing probe loaded with different dielectric constant samples (one-side is loaded by reference dielectric material).....	138
Figure 7-11. Shift in resonance frequency as a function of dielectric loading relative to two different reference samples.....	139
Figure 7-12. Photograph of a fabricated microwave sensing probe based rSRRs, (inset) a blow-out of the figure showing the array of rSRR structure.....	141
Figure 7-13. Measured and simulated insertion loss (S_{21} , dB) of an array of microwave sensing probe utilizing rSRRs, (inset) the structure model of the sensing probe.....	141
Figure 7-14. Measured insertion loss (S_{21} , dB) of an array of rSRRs microwave sensing probe loaded with different dielectric samples; MUT is in half side of probing region array with only on single side of the unit cell.....	142

Figure 7-15. Measured insertion loss (S_{21} , dB) of an array of rSRRs microwave sensing probe loaded with different dielectric samples; MUT is in all of probing region array with only on single side of the unit cell.....	143
Figure 7-16. The correlation between the measured frequency and dielectric constant of MUT in probing regions, (a) resonance frequency, (b) difference in each resonance frequency of the array of microwave sensing probe.....	144
Figure 7-17. A proposed approach to image the surface of a plane structure using a linear array of band stop resonator structure for imaging applications, (a) using a material sample as reference, (b) using air as reference.....	146
Figure 7-18. Layout of the edge-coupling probe design (resonance frequencies for each resonator, f_{c1} 7 GHz and f_{c2} 9 GHz).....	147
Figure 7-19. Measured S_{21} of the edge-coupling dual ring design loaded transmission line with different dielectric materials. Inset is the fabricated circuit in the experiment.....	148
Figure 7-20. Measured insertion phase, S_{21} (degree) of the edge-coupling dual ring design loaded transmission line with different dielectric materials.....	149
Figure 7-21. Realization on a defect dielectric material, (a) resolution measurement setup, (b) measured resolution characteristics.....	151
Figure 7-22. Scanned smart card using the proposed probe. Shown on the top are optical photographs and THz image in the transmission mode. Measured relative insertion phase changes correlate well with THz image	152
Figure 8-1. Configuration of the mSRR inspired compact antenna structure.....	155
Figure 8-2. Physical layout and simulated reflection coefficients of monopole antennas: (a) U-folded type, (b) R-folded type, (c) mSRR type.....	158
Figure 8-3. Equivalent circuit model of the proposed reconfigurable mSRR inspired microstrip antenna).....	159

Figure 8-4. The relationship between capacitance and bias voltage from a candidate varactor diode (SMV1408-079LF) [42].	160
Figure 8-5. Simulated reflection coefficients of the reconfigurable mSRR inspired microstrip antenna. Inset shows the structure of the mSRR integrated with a varactor diode. (with a ground plane at the back side).	160
Figure 8-6. Photograph of the fabricated novel reconfigurable antenna (integrated with a varactor diode and a solid ground plane at the back side).	162
Figure 8-7. Measurement setup for the experiment with zoom-in picture of the proposed antenna.	163
Figure 8-8. Measured return loss, S_{11} (dB) of the proposed reconfigurable antenna with various reverse bias voltage.	163
Figure 8-9. The correlation between reverse bias voltage versus capacitance and operating frequency of the proposed antenna.	164
Figure 8-10. The correlation between reverse bias voltage versus capacitance and operating frequency of the proposed antenna.	165
Figure 8-11. Measured 3-D radiation pattern of the proposed antenna by Satimo Passive Measurement 1.16.	165
Figure 9-1. A novel reconfigurable X-band phase shifter design using fully hybrid split ring resonators (FhSRRs).	171
Figure 9-2. Simulated insertion loss, S_{21} (dB) with various capacitances of the FhSRR-inspired reconfigurable X-band phase shifter circuit.	171
Figure 9-3. Simulated return loss, S_{11} (dB) with various capacitances of the FhSRR-inspired reconfigurable X-band phase shifter circuit.	172

Figure 9-4. Simulated insertion phase responses (degree) with various capacitances of the FhSRR-inspired reconfigurable X-band phase shifter circuit.....172

Figure 9-5. Proposed idea for the volatile molecular sensor integrated with CNTs in order to improve the sensor performance174

Figure B-1. An isotropic wet etch on a substrate creating round side walls.....185

Figure B-2. The example of an mask that its dimension is compensated to achieve the right dimension from the isotropic etch.....185

CHAPTER 1

INTRODUCTION

1.1 Background and Motivation

Recently, the use of metamaterials (MTMs) design has gained significant interest in the design of compact microwave circuits as they provide unique properties that are difficult to achieve otherwise. MTMs, first introduced by V. Veselago in 1967 [1], are defined as homogeneous electromagnetic structures which exhibit unique electromagnetic properties especially negative permeability and permittivity [1-5]. These properties open new degrees of freedom in the design of microwave circuits. Generally, MTMs implemented with split ring resonators (SRRs), complementary split ring resonators (CSRRs), double slit ring split ring resonators (DS-SRRs) and double slit ring complementary split ring resonators (DS-CSRRs) are the most intensively studied structures, Figure 1-1 [6-8]. These metamaterial structures are subwavelength in size at resonance. They are excited by time-varying electromagnetic fields with high-Q resonance frequency.

The promise of SRRs and CRRs is exploited in the design of miniaturized microwave circuits in microstrip design configuration. For example, a bandpass filter with controllable bandwidth has been proposed by using CSRRs, capacitive gaps, and shorted inductive lines [9-15]. Also, a band-reject filter using CSRR is presented by J.Martel, R.Marques *et al.* [9]. In reference [15], SRRs integrated with a varactor diode is implemented for band-stop tunable filter design. These example microwave circuit designs have demonstrated that microwave circuits can be miniaturized by incorporating metamaterial structures in circuit design. Furthermore, reconfigurable circuits can be designed by incorporating electronically tunable elements like

varactor diodes, micro-electromechanical (MEM) devices and PIN diodes. However, so far, these designs have largely been implemented at low-frequencies (1 - 3 GHz). Moreover, these existing metamaterial unit cells require double side metallization leading to perforated ground planes in a microstrip design which is difficult to implement in multi-level circuit designs and require double side metal processing.

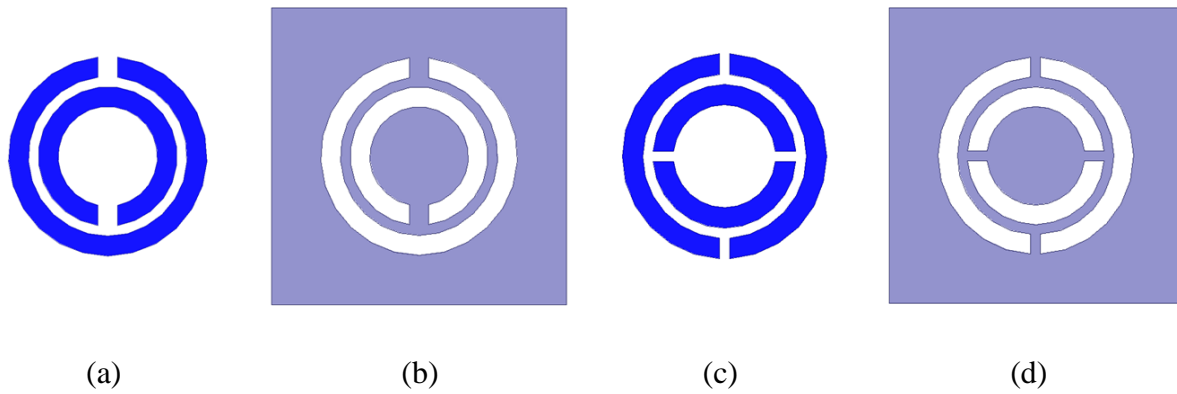


Figure 1-1. Schematic layout of (a) SRRs, (b) CSRRs, (c) DS-SRRs and (d) DS-CSRRs (Metal patterning is depicted in light blue for complimentary types). For interpretation of the references to color in this and all other figures, the reader is referred to the electronic version of this dissertation.

Now, the major challenge in metamaterials is to incorporate active elements to achieve electronic tunability/reconfigurability. Furthermore, there is a need to integrate metamaterial circuits in the design of high density integrated circuits (single and multi-level integration). This requires that the circuits be single side patterned and the ground plane allow isolation between multi-level circuits. In addition, there is a need to design microstrip metamaterial circuits that operate at high frequencies, especially in the X-band frequency range. Most commercial systems are expected to operate in this frequency range in the near future. The use of high frequencies for carrier waves in communications has the potential for higher data density or information density than lower frequency. In addition, the higher frequency permits a higher rate of information

transfer than could be achieved with lower frequencies. In this study, X-band is selected for microwave circuit design. In radar engineering, the frequency range in X-band is specified by the IEEE from 8.0 GHz to 12.0 GHz. Generally, X-band is used for satellite and space communications, radar for weather monitoring and air traffic control, including military or secure communications.

Apart from high frequency microwave circuits (esp. reconfigurable circuits), metamaterial structures have not been exploited for applications in microwave sensing applications. Generally, the metamaterial unit cells are sub-wavelength in size. The field confinement can be enhanced at local spots, which in turn can be used in the interrogation of small volumes of samples. Low-cost sensors are needed in applications such as biochemical, strain/stress, flow rate, pH and others. Among these structures that provide near-field sensing over a small lattice space are studied here using different metamaterial cell designs.

The purpose of this research work is two fold: First is to develop and analyze a novel unit cell for microwave circuits and applications in the X-band. The unit cell should be designed that can be easily fabricated on a single metal layer while allowing for the ease of integration of tuning elements at the same level. The second intent of this research is to design and demonstrate highly sensitive metamaterial based sensors for chemical and biological sensing applications. Here the samples to be interrogated are introduced in the near field region of a metamaterial structure. Different microstrip metamaterial structures are analyzed for sensor applications.

1.2 Dissertation Overview

This research focuses on design and analysis of novel metamaterial unit cell that provides the desired properties: 1) high frequency operation at X-band (7.5 – 12 GHz range), 2) ease of

integration and fabrication, 3) allows integration of active tuning element and 4) allows design of low-cost sensors with high sensitivity. Basic theory of composite right/left handed transmission line (CRLH TL) and principle expressions of dispersion relation are described and derived in order to realize the characteristics of the unit cell. Microwave circuits and sensors are demonstrated in order to express the high potential of the proposed unit cell. Novel reconfigurable power splitter with unequal power function, wide-band reconfigurable X-band phase shifter with high linearity, and miniaturized reconfigurable antenna are proposed, designed, fabricated, and characterized for microwave circuits and applications. A bio-sensor for microfluidic systems and a high-Q compact volatile molecular sensor are described to demonstrate the capability of RF near-field sensing of a unit cell. This dissertation is organized as follows:

In chapter 1, Background and motivation for the research work are presented.

Chapter 2 describes the fundamental concepts of MTMs, left-handed media (LHM), MTMs based transmission line approach, composite right/left-handed (CRLH) and periodic network parameter analysis which are behind of the unit cell in various microwave circuits and sensors.

Chapter 3 demonstrates a novel reconfigurable power splitter with unequal power division capability. The novel metamaterial unit cell is proposed and used in the construction of metamaterial media. Besides miniaturization, the new resonant structure provides new functionality that could not be achieved before using conventional design approaches.

In Chapter 4, a novel wide-band reconfigurable phase shifter design utilizing CRLH transmission line is demonstrated for X-band applications. The proposed MTM unit cells are designed that allows seamless integration of active devices (varactor diodes) in order to achieve

reconfigurability. Design equations and properties with arbitrary phase, band-pass characteristics, and dispersion diagram are presented.

Metamaterial microstrip transmission line based microwave sensors are studied and realized in Chapter 5, 6 and 7. In Chapter 5, spiral structured MTM design is first introduced and co-integrated with a microfluidic channel in order to demonstrate a novel RF near-field sensor. Chapter 5 also discusses the concepts of metamaterial-based and metamaterial-inspired microwave sensors.

Chapter 6 introduces a novel high-Q metamaterial resonator volatile molecular sensor. The design of the sensor is based on a planar metamaterial-inspired modified split ring resonator with open gap (OmSRR). The different molecular densities of vaporized liquids can be characterized by examining the resonant shift and Q-factor of the circuit.

Chapter 7 presents metamaterial-inspired miniaturized microwave sensing probes. Two metamaterial based microstrip transmission line structures are designed and implemented in near field sensing of dielectric materials in the X-band frequency region. One structure is designed for band-stop and the other is designed for band-pass performance.

Chapter 8 demonstrates a MTM-inspired antenna design with reconfigurability. By integrating a varactor diode as an integral part of the antenna, the resonance characteristics of the antenna can be electronically tuned. Details of design, simulations and experiments are presented.

The dissertation is concluded in Chapter 9 along with the summarized points of improvement and potential future applications and research topics.

1.3 Research Contributions

In this research, the novel microstrip metamaterial based layouts for microwave circuits and sensors are introduced. The proposed metamaterial unit cells allow miniaturization of the circuits and lead to new functionalities that are difficult to achieve using conventional designs. To this end, the following work has been completed:

- A novel compact *X*-band power divider with reconfigurability and an unequal power dividing feature is design to validate the practical use of the proposed unit cell. By incorporating varactor diodes, the electrical characteristics of the unit cell can be electronically reconfigured through dc voltage tuning. This impedes signal propagation in the proximity of the resonant frequency. Since the unit cell has a mirror image between each side, wave propagation can be independently controlled from dc biasing of each varactor diode. As a result, the output power at 2 ports can be manipulated to be equal or unequal associated with electrically tuning of such active devices (varactor diodes).
- A new type of the reconfigurable *X*-band phase shifter using cascaded 2 MTM unit cells with a varactor diode has been proposed and demonstrated. The reconfigurable phase shifter exhibits nearly linear phase responses over the designed frequency range. The proposed design offers significant advantages over conventional delay lines and uniform LH lines. It is compact in size, simple to design and fabricate, and allows direct integration of active devices within the unit cells.
- A novel microstrip-based metamaterial transmission line coupled with microfluidic channel is demonstrated for sensing of microliter sample volumes. Different liquids were mixed to attain varying complex permittivity as a function of frequency and utilized in

the characterization of these sensors. The dielectric properties of different samples are found by examining changes in both scattering coefficient, S_{21} and S_{11} of the samples in various concentration levels. Experimentally, the device has high sensitivity. Compared to previous studies using similar analysis techniques, the dielectric relaxation is easier to evaluate especially when samples become diluted. Also, the proposed RF-sensor is low-cost and easy to integrate for lab-on-chip applications.

- A compact volatile molecular sensor has been proposed and validated. The sensor can readily recognize different molecular densities of vaporized liquids with sensitivity and selectivity. The design of the volatile molecular sensor is based a high-Q planar metamaterial resonator (OmSRR) incorporated into microstrip transmission line as 1-port network. Since the introduction of vaporized sample liquids, the resonant frequency shifts relative to the reference resonant frequency. For the proposed sensor, it can be a highly selective sensor by exploiting the Q-factor. The higher the loss tangent of volatile molecules, the lower the Q-factor of the spectral resonance characteristic. In addition to very high sensitivity and selectivity, the proposed volatile molecular sensor is compact in size and is low cost.
- Two sensing probe designs that utilize metamaterial unit cells coupled to microstrip lines are presented. One design utilizes the band-stop properties and the other uses the band-pass characteristics. Both sides of the transmission lines are loaded with resonators. One side allows probing of samples and the other side provides a reference resonant frequency. These structures were tested for sensing applications by loading the unit cells with dielectric samples having different dielectric properties. It is shown that high sensitivity probes can be designed for chemical and biological sensing, and in non-

destruction evaluation of samples through surface imaging using an array of metamaterial probes. Upon introduction of a sample, the resonance frequency shifts relative to the reference resonance frequency. This approach provides high sensitivity detection with built in reference providing high signal to noise ratio. In addition, this allows a simple approach to compare two samples using only a single probe and does not require calibration.

- A novel unit cell loaded compact antenna has been proposed and demonstrated. By incorporating a ground plane, to achieve negative permeability, a significant reduction in the operating frequency is achieved. The novel unit cell-inspired reconfigurable antenna exhibits resonance characteristics independent of the radiator length and is electrically small. The structure is simple to fabricate as it requires only single side metal patterning, and is compatible with MMIC integration. The proposed antenna design allows tuning of center frequency using a single varactor diode element while providing similar radiation pattern over the frequency tuning range.

CHAPTER 2

FUNDAMENTAL THEORY OF METAMATERIALS

The theoretical speculation of electromagnetic metamaterials (MTMs) was first presented by Viktor Veselago in 1967 [1]. He proposed the existence of “substances with simultaneously negative permittivity ϵ and permeability μ ” which is at the origin of all research on MTMs or Left-Handed Media (LHM). In LH substances the electric field, magnetic field, and phase constant propagation vectors follow an left-handed coordinate system, while conventional material exhibit right-handed coordination of these electromagnetic propagation vectors. However, MTMs were not attractive over 30 years in the scientific community since the non-existence in nature and lack of experimental verification. After the first demonstration of MTMs by Pendry et al. in 1996 [2-3], MTMs have attracted a lot of attention in both theoretical exploration and experimental study because of the unique electromagnetic properties which are not available in nature.

2.1 Definition of Metamaterials and Left-Handed Media

Electromagnetic MTMs are defined as artificially effectively homogeneous electromagnetic structures with unusual properties not readily available in nature [4]. For an effective homogeneous structure, the MTMs are required to have the cellular size or structural average cell size p that is much smaller than the guided wavelength λ_g . It should be at least less than a quarter wavelength ($p < \lambda_g/4$) in size. As a rule of thumb, effective condition, the limit $p = \lambda_g/4$ is usually used to distinguish each essence of components where p is the size of the component

which is considered. For example, the components are classified as lumped components ($p < \lambda_g/4$), quasi-lumped components ($\lambda_g/4 < p < \lambda_g/2$) and distributed components ($p > \lambda_g/2$) [4].

Therefore, the effective-homogeneity limit is referred as the condition $p \leq \lambda_g/4$ in order to assure that refractive phenomena will dominate over scattering/diffraction phenomena, when a wave propagates inside the MTM medium. If the effective homogeneous condition is satisfied, the structure can be treated to behave like a real material in the sense that electromagnetic waves are essentially myopic to the lattice and only probe the average, or effective, macroscopic and well-defined constitutive parameters, which depend on the nature of the unit cell [5]. The constitutive parameters of such a medium are ϵ and μ , which are imparted to the refractive index n by

$$n = \pm \sqrt{\epsilon_r \cdot \mu_r} \quad (2-1)$$

where ϵ_r and μ_r are the relative permittivity and permeability related to the free space.

Generally, the free space permittivity and permeability are defined by $\epsilon_0 = \epsilon/\epsilon_r = 8.854 \times 10^{-12}$ F/m and $\mu_0 = \mu/\mu_r = 4\pi \times 10^{-7}$ H/m, respectively.

The four possibilities of sign combinations in pair (ϵ and μ) are shown in Figure 2-1. The first three combinations, $(+, +)$, $(+, -)$ and $(-, +)$, are well-known as conventional materials. The last combination, $(-, -)$, corresponds to a new class of materials known as LHM. This class is characterized with having double simultaneously negative signs of ϵ and μ . LH materials express various unique properties such as antiparallel phase and group velocities, or negative refractive index (NRI), etc. According to the definition given above, it is clear that LH structures are a subset of MTMs since they are artificial, effectively homogeneous ($p < \lambda_g/4$) and exhibit unusual constitutive parameters such as NRI.

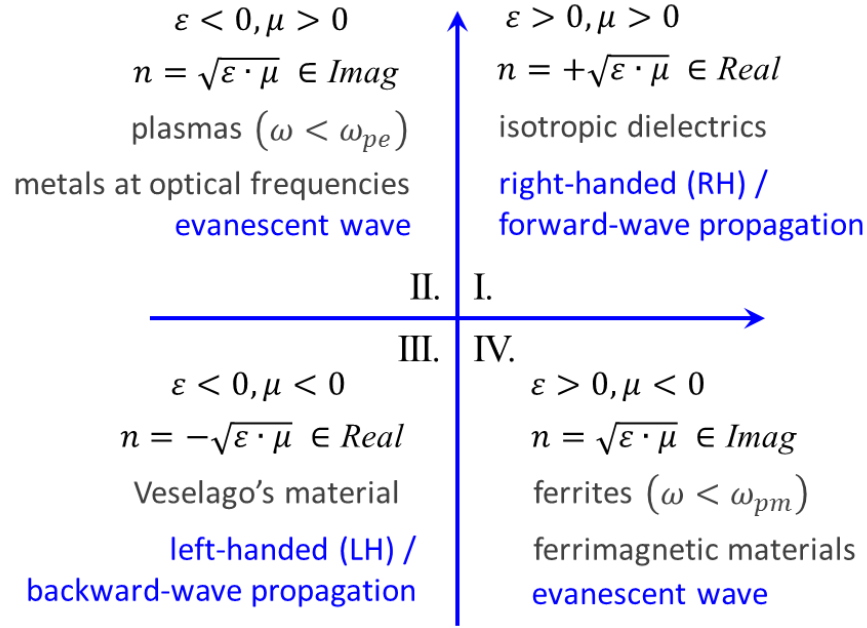


Figure 2-1. Permittivity-permeability ($\varepsilon - \mu$) and refractive index (n) diagram [5]

2.2 Experimental Left-Handed Metamaterials

To give a brief background on metamaterials, here several papers are reviewed, [2-3], [5-6] and are summarized in a systematic way for convenience. The negative- ε /positive- μ and positive- ε /negative- μ structures were first introduced by Smith et al [6]. Actually, their promising work was inspired by the pioneering work of Pendry et al [2-3]. The structures are effectively homogeneous structures or MTMs since their average cell size p is much smaller than the guided wavelength λ_g ($p \ll \lambda_g$). The metal thin-wire (TW) structure is the negative- ε /positive- μ MTM as shown in Figure 2-2(a). The excitation electric field \mathbf{E} in parallel to the axis of the wires ($\mathbf{E} \parallel z$) leads to induced current along them and generate equivalent electric dipole moments. This MTM exhibits the effective permittivity function of the wire medium as [2]:

$$\varepsilon_r = 1 - \frac{\omega_{pe}^2}{\omega^2 + j\omega\zeta} = 1 - \frac{\omega_{pe}^2}{\omega^2 + \zeta^2} + j \frac{\zeta \omega_{pe}^2}{\omega(\omega^2 + \zeta^2)} \quad (2-2)$$

where, electric plasma frequency, $\omega_{pe} = \sqrt{2\pi c^2 [p^2 \ln (p/a)]}$:rad/s (in GHz range)

speed of light, $c = 3 \times 10^8$:m/s

radius of wires, a :m

damping factor due to metal losses, $\zeta = \epsilon_0 (p\omega_{pe}/a)^2 / (\pi\sigma)$

conductivity of the metal, σ :S/m

It is clear from this formula that $Re(\epsilon_r) < 0$ for $\omega^2 < \omega_{pe}^2 - \zeta^2$ which could be further reduced in the loss-less case. If $\zeta = 0$, the permittivity $\epsilon_r < 0$ for $\omega < \omega_{pe}$. In case the excitation electric field \mathbf{E} is exactly perpendicular to the axis of wires ($\mathbf{E} \perp z$), a situation of cross polarization occurs, where no effect is produced. On the other hand, no magnetic dipole moment is generated since no magnetic material is present ($\mu = \mu_0$).

The metal split-ring resonator (SRR) structure that exhibits the positive- ϵ /negative- μ structures is shown in Fig. 2-2(b). Similarly, the structures are effectively homogeneous structures or MTMs since their average cell size p is much smaller than the guided wavelength ($p \ll \lambda_g$). The excitation magnetic field \mathbf{H} is perpendicular to the plan of the rings ($\mathbf{H} \perp y$) leads to induce resonating currents in the loop and generate equivalent magnetic dipole moments. Consequently, the MTM exhibits the effective permeability function as follows [3]:

$$\mu_r = 1 - \frac{F\omega^2}{\omega^2 - \omega_{om}^2 + j\omega\zeta} = 1 - \frac{F\omega^2(\omega^2 - \omega_{om}^2)}{(\omega^2 - \omega_{om}^2)^2 + (\omega\zeta)^2} + j \frac{F\omega^2\zeta}{(\omega^2 - \omega_{om}^2)^2 + (\omega\zeta)^2} \quad (2-3)$$

where, magnetic resonance frequency, $\omega_{om} = c \sqrt{3p / [\pi a^3 \ln (2w/\delta)]}$:rad/s (in GHz range)

speed of light, $c = 3 \times 10^8$:m/s
inner radius of the smaller ring, a	:m
width of rings, w	:m
radial spacing between the rings δ	:m
damping factor due to metal losses, $\zeta = 2pR'/(a\mu_0)$	

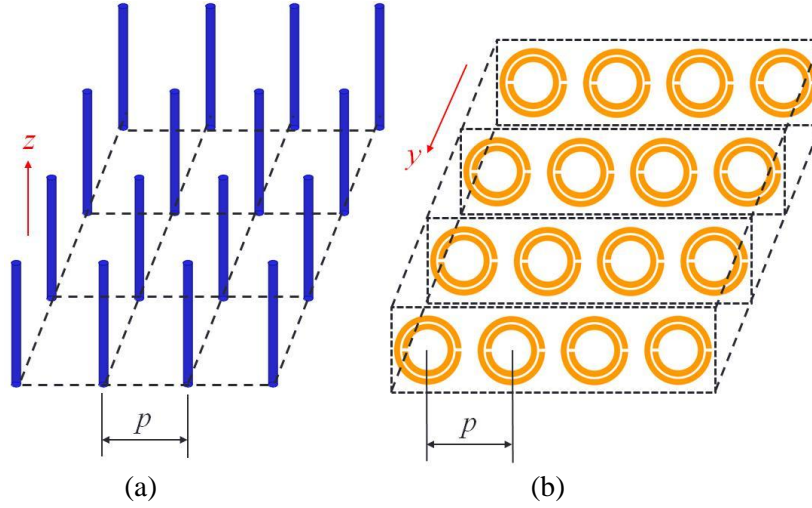


Figure 2-2. First negative- ϵ /positive- μ and positive- ϵ /negative- μ MTM structures ($p \ll \lambda_g$), (a) Thin-wire (TW) structure exhibiting negative- ϵ /positive- μ if $\mathbf{E} \parallel z$ [2], (b) Split-ring resonator (SRR) structure exhibiting positive- ϵ /negative- μ if $\mathbf{H} \perp y$ [3].

It should be noticed that the SRR structure could have an un-natural magnetic response that occurs due to the presence of artificially induced magnetic dipole moments caused by the ring resonators. For the loss-less case $\zeta = 0$, the negative permeability $\mu_r < 0$ exists for the range of frequency as

$$\omega_{om} < \omega < \omega_{om}/\sqrt{1 - F} = \omega_{pm} \quad (2-4)$$

In Equation (2-4), ω_{pm} is the magnetic plasma frequency. Therefore, it is important to note the difference between the plasmonic expressions of ϵ and μ . The latter is of resonant nature since μ_r diverges when $\omega = \omega_{om}$. On the contrary, the former is a non-resonant expression. The sketch of the effective magnetic permeability is shown in Figure 2-3.

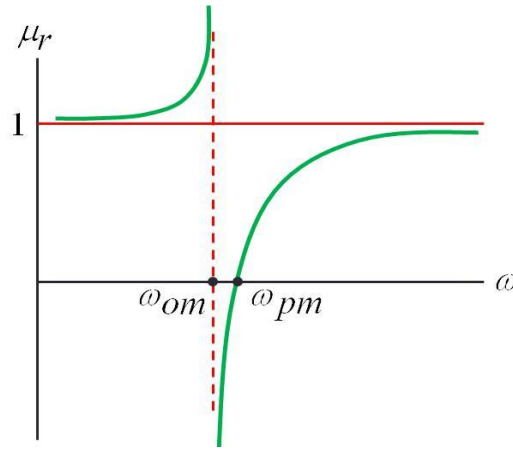


Figure 2-3. The effective magnetic permeability of MTM from artificially induced magnetic dipole moments.

According to Smith et al [6], the TW and SRR structures are combined together and designed with overlapping frequency ranges of negative permittivity and permeability. Due to electromagnetic wave $e^{-j\beta r}$ propagating through the structure, it concludes from the fact that a passband experimentally appears in the frequency range of interest with simultaneously negative permeability and permittivity. It is confirmed on the basis of the fact that $\beta = nk_0 = \pm\sqrt{\epsilon_r\mu_r}$ has to be real in the bandpass region.

2.3 Composite Right/Left-Handed (CRLH) Metamaterials

MTMs are operating in their fundamental mode (effectively homogeneous), where $p \ll \lambda_g$, so that effective macroscopic ϵ and μ could be rigorously defined. Due to their effective

homogeneity, MTMs can be modeled as one-dimensional (1-D) transmission lines (TLs), whose propagation direction represents any direction in the material. A representation of an ideal homogeneous TL in the form of its incremental model is shown in Figure 2-4(a). The ideal homogeneous TL means that it is perfectly uniform and it can transmit signals at all frequencies ($\omega = 0 \rightarrow \infty$). As the basis of conventional TL, a perfectly homogeneous TL has an incremental length $\Delta z \rightarrow 0$. However, an effectively homogeneous TL has only to consider the restriction of incremental length $\Delta z \ll \lambda_g$ or at least $\Delta z < \lambda_g/4$ where λ_g is the guided wavelength and Δz is typically equal the average unit cell size p . The average unit cell size can be represented as the lattice constant for crystals as in solid state physics.

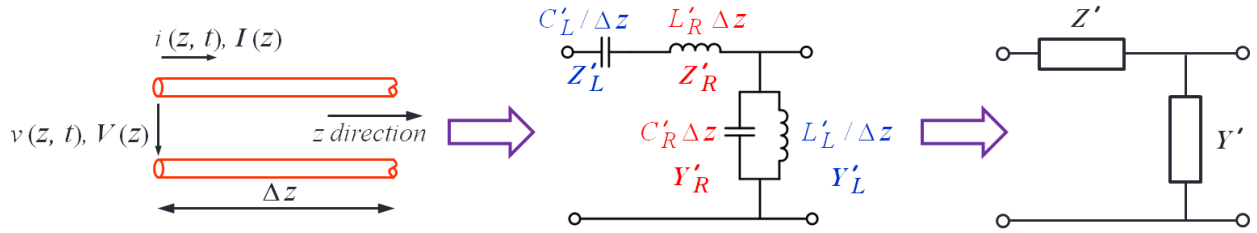


Figure 2-4. A representative of an ideal homogeneous transmission line and its equivalent circuit model for ideal CRLH approach.

Analysis of a uniform LH transmission line, also known as a backward-wave transmission line [7-8], shows an applicable circuit model for a combined right/left hand (CRLH) system consists of the superposition of the conventional RH series-L/shunt-C circuit model with a LH series-C/shunt-L model as shown in Figure 2-4. This model yields a per-unit length impedance term Z' (Ω/m) and a per-unit-length admittance term Y' (S/m). The Z' term is constituted by a RH per-unit-length inductance L'_R (H/m) in series with a LH times-unit-length capacitance C'_L (F·m). For the Y' term, it is composed of a RH per-unit-length capacitance C'_R (F/m) in parallel

with a LH times-unit-length inductance L'_L (H·m). In order to carry out the analysis of the CRLH TL, the wave equations at steady state are:

$$\frac{d^2 V}{dz^2} - \gamma^2 V = 0 \quad (2-5)$$

$$\frac{d^2 I}{dz^2} - \gamma^2 I = 0 \quad (2-6)$$

In (2-5) and (2-6), the complex propagation constant γ is expressed in terms of the per-unit-length immittances Z' and Y' as follows:

$$\gamma = \alpha + j\beta = \sqrt{Z' \cdot Y'} \quad (2-7)$$

$$Z' = j(\omega L'_R - \frac{1}{\omega C'_L}) \quad (2-8)$$

$$Y' = j(\omega C'_R - \frac{1}{\omega L'_L}) \quad (2-9)$$

For convenience, four resonance and one constant terms of the circuit are initially introduced as follows:

$$\omega'_R = 1/\sqrt{L'_R C'_R} \quad (2-10)$$

$$\omega'_L = 1/\sqrt{L'_L C'_L} \quad (2-11)$$

$$\omega_{se} = 1/\sqrt{L'_R C'_L} \quad (2-12)$$

$$\omega_{sh} = 1/\sqrt{L'_L C'_R} \quad (2-13)$$

$$\kappa = L'_R C'_L + L'_L C'_R \quad (2-14)$$

where ω'_R and ω'_L are right-handed and left-handed resonance frequencies in terms of rad/(m·s), respectively. ω_{se} and ω_{sh} are series and shunt resonance frequencies in terms of rad/s, respectively. κ is resonance factor in terms of (s/rad)². Therefore, the complex propagation constant can be expressed as

$$\gamma = \alpha + j\beta = js(\omega) \sqrt{\left(\frac{\omega}{\omega'_R}\right)^2 + \left(\frac{\omega'_L}{\omega}\right)^2 - \kappa\omega'^2_L} \quad (2-15)$$

where $s(\omega)$ is the sign function as follows: -1 if $\omega < \min(\omega_{se}, \omega_{sh})$ or LH range, and $+1$ if $\omega > \max(\omega_{se}, \omega_{sh})$ or RH range. It is important to note that the propagation constant γ is not necessarily purely imaginary $\gamma = j\beta$ (pass band). It can be purely real $\gamma = \alpha$ (stop band) in some ranges of frequency although the transmission line is loss-less.

The sign function is easily explained by considering phase velocity ($v_p = \omega/\beta$) and group velocity ($v_g = d\omega/d\beta$). If $\omega < \min(\omega_{se}, \omega_{sh})$, phase velocity and group velocity have opposite signs meaning that they are antiparallel, $v_p \nparallel v_g$. Therefore, β is negative for LH transmission line. On the other hand, when $\omega > \max(\omega_{se}, \omega_{sh})$ or RH range, the phase and group velocities are parallel or have the same sign ($v_p \parallel v_g$) meaning that β is positive. Thus, the real dispersion diagram for energy (v_g) in the $+z$ direction is shown in Figure 2-5. The frequency of maximum attenuation ω_0 can be found by the derivative of the complex propagation constant, $d\gamma/d\omega = 0$ which yields Equation (2-16). For only in the passband, the guided wavelength (λ_g), phase velocity (v_p), and group velocity (v_g), of the CRLH transmission line, are also expressed as Equation (2-17), (2-18) and (2-19), respectively.

$$\omega_0 = \sqrt{\omega'_R \omega'_L} = \sqrt{\omega_{se} \omega_{sh}} \quad (2-16)$$

$$\lambda_g = \frac{2\pi}{|\beta|} = \frac{2\pi}{\sqrt{\left(\frac{\omega}{\omega'_R}\right)^2 + \left(\frac{\omega'_L}{\omega}\right)^2 - \kappa \omega'^2_L}} \quad (2-17)$$

$$v_p = \frac{\omega}{\beta} = s(\omega) \frac{\omega}{\sqrt{\left(\frac{\omega}{\omega'_R}\right)^2 + \left(\frac{\omega'_L}{\omega}\right)^2 - \kappa \omega'^2_L}} \quad (2-18)$$

$$v_g = \left(\frac{d\beta}{d\omega}\right)^{-1} = \frac{\sqrt{\left(\frac{\omega}{\omega'_R}\right)^2 + \left(\frac{\omega'_L}{\omega}\right)^2 - \kappa \omega'^2_L}}{\left| \left(\omega/\omega'^2_R\right) - \left(\omega'^2_L/\omega^3\right) \right|} \quad (2-19)$$

These two cut-off frequencies (ω_{se} , ω_{sh}) can be closed and the band becomes continuous when the matching condition is satisfied. Continuous band or the balanced mode of CRLH transmission line can be verified by Equation (2-20) and (2-21). Therefore, the dispersion relation of the balanced CRLH transmission line for energy (v_g) in the +z direction is shown in Figure 2-6.

$$L'_R C'_L = L'_L C'_R = L C \quad (2-20)$$

$$\omega_0 = \sqrt{\omega'_R \cdot \omega'_L} = \sqrt[4]{L'_R C'_L L'_L C'_R} = \sqrt{L C} \quad (2-21)$$

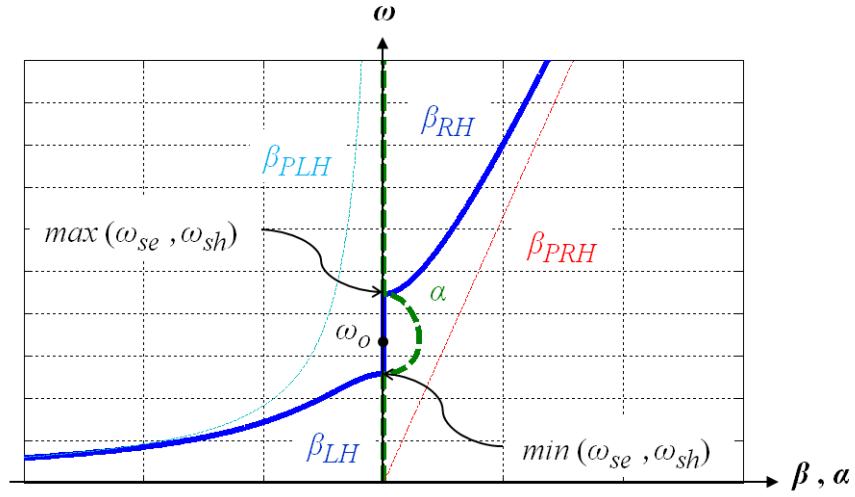


Figure 2-5. Dispersion diagram of a CRLH transmission line for energy propagation along the +z direction (unbalanced mode).

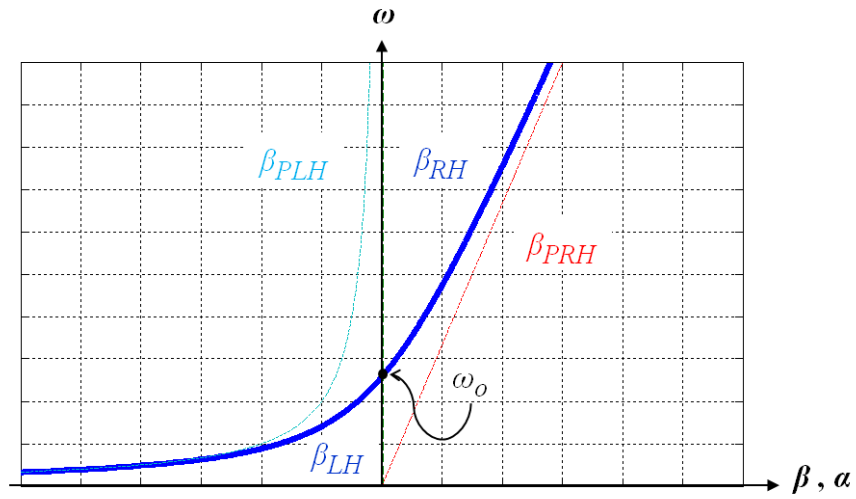


Figure 2-6. Dispersion diagram of a CRLH transmission line for energy propagation along the +z direction (balanced mode).

2.3.1 Pure Right-Handed Transmission Line

The transmission line becomes pure right-handed (PRH) or conventional, when C'_L is short and L'_L is open (LH parameters are infinite). Figure 2-7 shows the incremental equivalent circuit of a one-dimensional continuous transmission line. It is important to remind that the RH lumped-elements in the circuit are per-unit-length inductor (L'_R) and a per-unit-length capacitor (C'_R). The propagation constant can be easily simplified from Equation (2-15) to (2-22). Consequently, the phase and group velocities in the pure right-handed (PRH) transmission line are equal as shown in Equation (2-23). It can be stated that the Poyting vector $\vec{S} = \vec{E} \times \vec{H}$, and the wave vector \vec{k} are co-directional. That means the direction of power flow is the same as the direction of propagation (+z direction). The diagrams relative with the RH characteristic equations are shown in Figure 2-8.

$$\beta_{PRH} = \frac{\omega}{\omega'_R} \quad (2-22)$$

$$v_p^{PRH} = v_g^{PRH} = \omega'_R \quad (2-23)$$

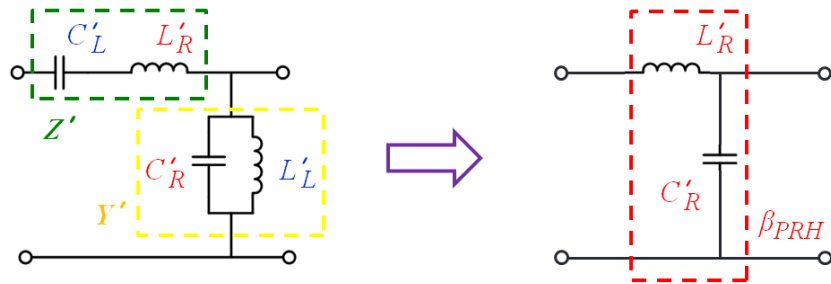


Figure 2-7. Incremental equivalent circuit of a PRH transmission line which can be model a uniform one-dimensional distributed transmission line.

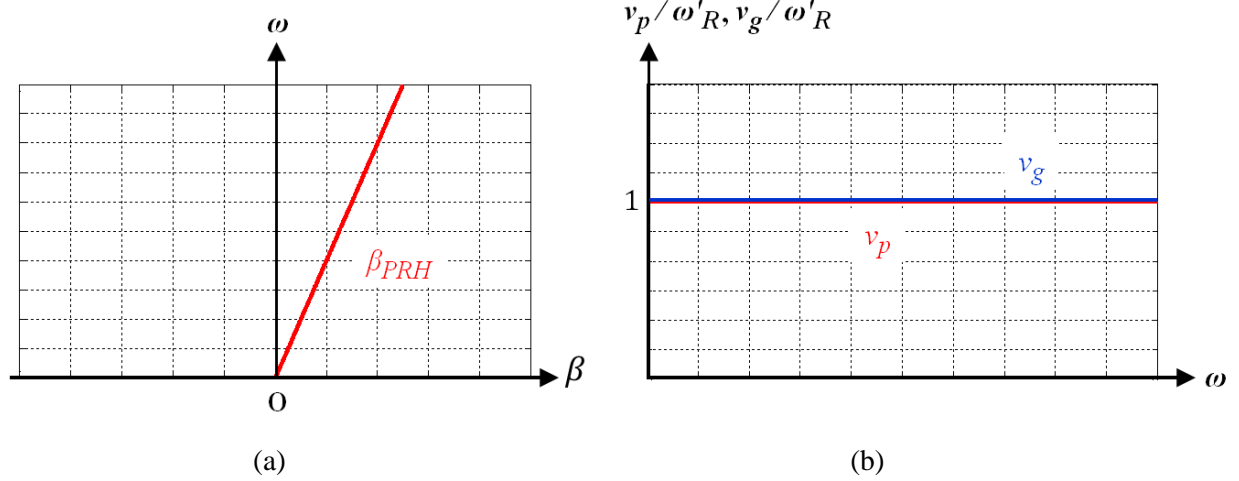


Figure 2-8. As energy propagation along the $+z$ direction of PRH transmission line, (a) dispersion diagram and (b) phase velocity and group velocity diagram.

2.3.2 Pure Left-Handed Transmission Line

In case of the pure left-handed (PLH) transmission line, the RH contributions become zero (L'_R is short and C'_R is open). Figure 2-9 shows the incremental equivalent circuit of a one-dimensional continuous transmission line. As mentioned above, the LH-lumped equivalent circuit are in terms of times-unit length ($L'_L \rightarrow \text{H}\cdot\text{m}$, $C'_L \rightarrow \text{F}\cdot\text{m}$). Therefore, the PLH propagation constant can be reduced to Equation (2-24). The PLH phase and group velocities are derived from Equation (2-18) and (2-19) with $L'_R = C'_R = 0$ resulting with Equation (2-25) and (2-26). As expected, the phase and group velocities in the PLH transmission line are antiparallel since the phase velocity is negative but the group velocity is positive. This means the Poyting vector \vec{S} , and the wave vector \vec{k} are oppositely directed. As a result, the power flow is still in the forward direction ($+z$ direction) while the propagation is in the opposite direction ($-z$ direction). Since this phenomenon, sometimes the PLH transmission line is named as the backward-wave line [16]. The diagrams relative with the LH dispersive relations are shown in Figure 2-10.

$$\beta_{PLH} = -\frac{\omega' L}{\omega} \quad (2-24)$$

$$v_p^{PLH} = \frac{-\omega^2}{\omega' L} = \frac{-\omega^2}{\omega_o^2} \omega' R \quad (2-25)$$

$$v_g^{PLH} = \frac{\omega^2}{\omega' L} = \frac{\omega^2}{\omega_o^2} \omega' R \quad (2-26)$$

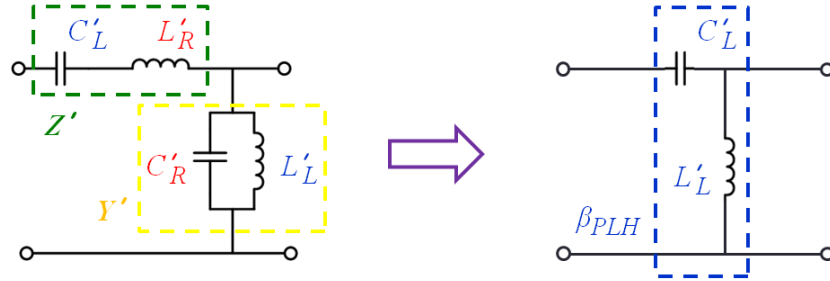


Figure 2-9. Incremental equivalent circuit of a PLH transmission line which can be model a uniform one-dimensional distributed transmission line.

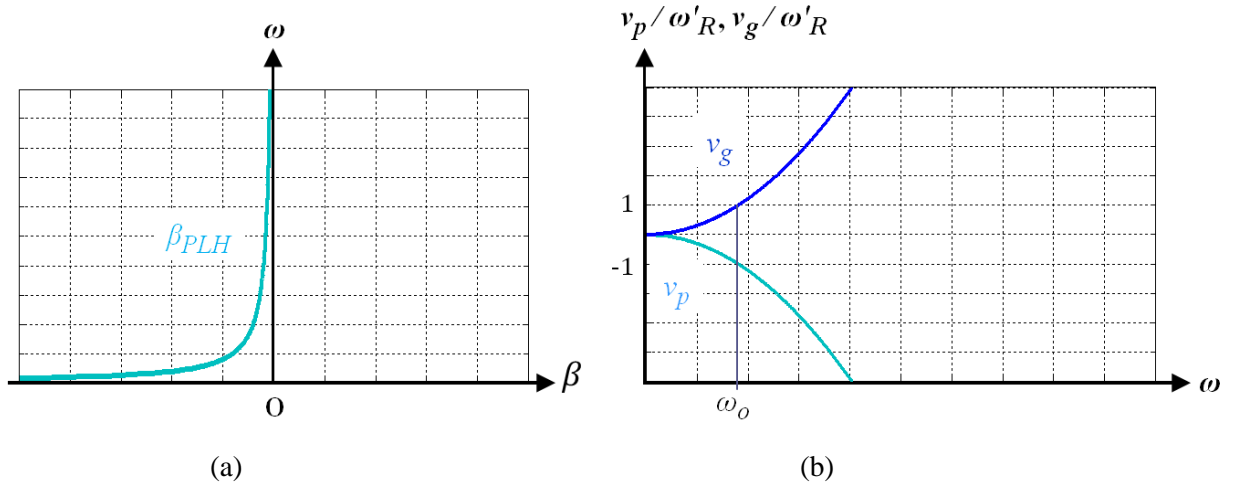


Figure 2-10. As energy propagation along the $+z$ direction of PLH transmission line, (a) dispersion diagram and (b) phase velocity and group velocity diagram.

Although, these PLH velocities seem unbounded at high frequencies, $v_p(\omega \rightarrow \infty) \rightarrow -\infty, v_g(\omega \rightarrow \infty) \rightarrow \infty$, the velocities are automatically suppressed by the parasitic RH contributions normally existing in a physical LH medium. In other words, it can be recognized that any realistic LH medium is effectively a CRLH medium such that the velocities are bounded at high frequencies to the velocities of the RH contributions.

2.3.3 Composite Right/Left-Handed Transmission Line (Unbalanced)

For CRLH (unbalanced) medium, the incremental equivalent circuit of such a transmission line is shown as Figure 2-4. Note that each of the RH contributions and the LH contributions represent the per-unit length lumped elements (L'_R, C'_R) and times-per-unit length lumped element (L'_L, C'_L), respectively. The criterion of CRLH (unbalanced) medium is that the series and shunt resonance frequencies are not equal $\omega_{se} \neq \omega_{sh}$. Therefore, the dispersion equation is fully expressed as Equation 2-15. The phase and group velocities relative with RH resonance frequency can be simplified from Equation (2-18) and (2-19) to Equation (2-27) and (2-28). Figure 2-11(a) shows the dispersion diagram related with Equation 2-15. The phase and group velocities diagrams relative with RH contributions are also shown in Figure 2-11(b).

$$v_p = s(\omega) \frac{\omega'_R}{\sqrt{1 + \left(\frac{\omega_o}{\omega}\right)^4 - \kappa \frac{\omega_o^4}{\omega^2}}} \quad (2-27)$$

$$v_g = \frac{\omega'_R \sqrt{1 + \left(\frac{\omega_o}{\omega}\right)^4 - \kappa \frac{\omega_o^4}{\omega^2}}}{\left|1 - \frac{\omega_o^4}{\omega^2}\right|} \quad (2-28)$$

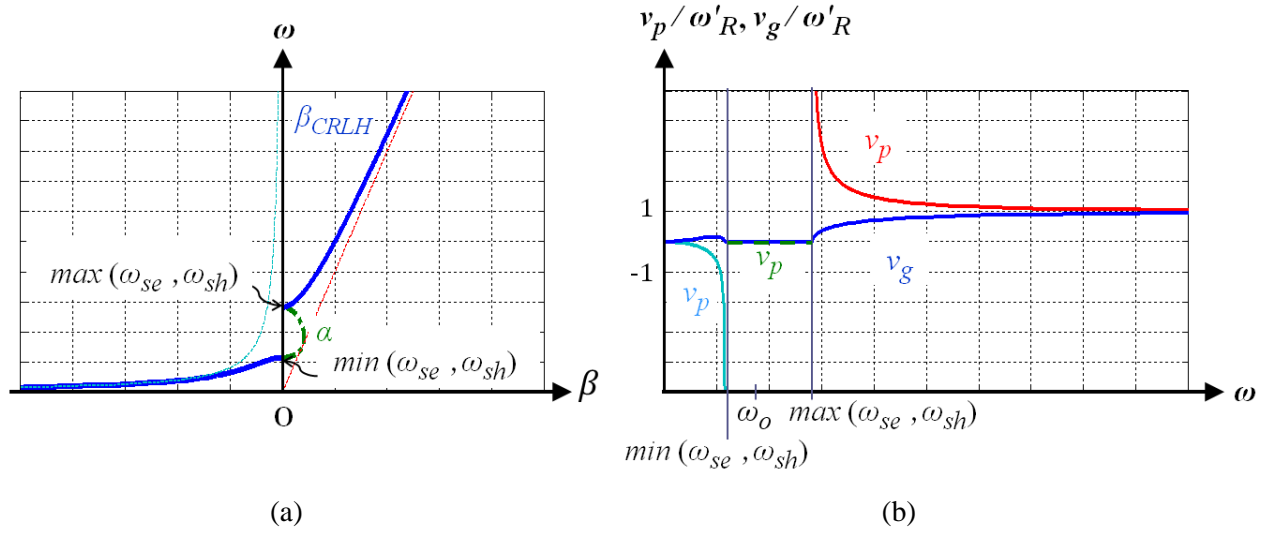


Figure 2-11. As energy propagation along the $+z$ direction of CRLH (unbalanced) transmission line, (a) dispersion diagram and (b) phase velocity and group velocity diagram.

It is clear from the results that the transmission line in the unbalanced mode exhibits LH-phenomenon at $\omega < \min(\omega_{se}, \omega_{sh})$ since the phase and group velocities are antiparallel. Furthermore, RH-phenomenon happens at $\omega > \max(\omega_{se}, \omega_{sh})$ since the phase velocity and group velocity are positive. In the CRLH gap or stop-band, $\min(\omega_{se}, \omega_{sh}) < \omega < \max(\omega_{se}, \omega_{sh})$, zero phase and group velocities are present since the propagation constant is purely real ($\gamma \neq 0, \beta = 0$). Considering the group velocity, it is always positive meaning that the power flow is always still in the forward direction ($+z$ direction). As mentioned before, the phase and group velocities are bounded to the velocities of the RH contributions at high frequency as clearly seen in Figure 2-8(b).

2.3.4 Composite Right/Left-Handed Transmission Line (Balanced)

For CRLH (balanced) medium, the phase and group velocities can be easily expressed as Equation (2-29) and (2-30). In general, the CRLH gap closes up under balanced condition since the series and shunt resonance frequencies are equal, $\omega_{se} = \omega_{sh}$. When it occurs, the CRLH

dispersion curve continues at the transition frequency, ω_o with nonzero phase and group velocities as illustrated in Figure 2-12(a) and (b). As expected, the CRLH phase and group velocities in balanced mode are also bounded to the velocities of the RH contributions at high frequencies. These circumstances are the same as in CRLH (unbalanced) medium. Finally, it is important to mention that the group velocity of CRLH (balanced) medium continues at the transition frequency, ω_o and the group velocity comes to be half of its RH contributions at this transition.

$$v_p = \frac{\omega^2 \omega'_R}{\omega^2 - \omega_o^2} \quad (2-29)$$

$$v_g = \frac{\omega^2 \omega'_R}{\omega^2 + \omega_o^2} \quad (2-30)$$

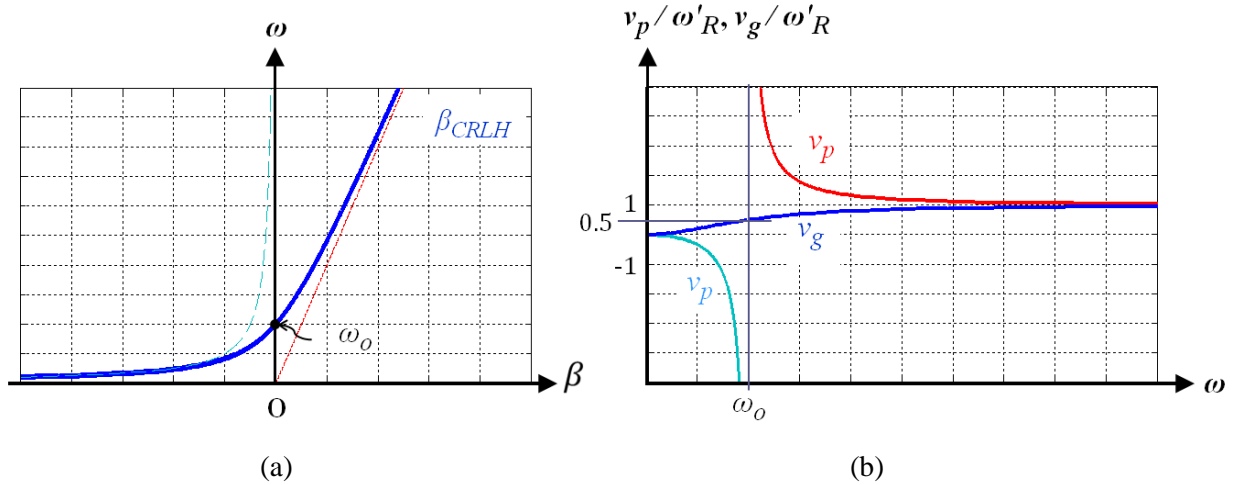


Figure 2-12. As energy propagation along the $+z$ direction of CRLH (balanced) transmission line, (a) dispersion diagram and (b) phase velocity and group velocities diagram.

2.4 LC Network Implemented on Metamaterials

Since the effective homogeneous CRLH transmission line operates only in a restricted frequency range, it can be realized by cascading the LC unit cell shown in Figure 2-13(a) so as to obtain the ladder network shown in Figure 2-13(b). The unit cell consists of an impedance Z (Ω) and admittance Y (S). The impedance Z is constituted by a RH inductance L_R (H) in series with a LH-capacitance C_L (F). The admittance Y (S) is constituted by a RH-capacitance C_R (F) in parallel with a LH-inductance L_L (H). Both of them can be expressed as

$$Z = j \left(\omega L_R - \frac{1}{\omega C_L} \right) = j \frac{(\omega/\omega_{se})^2 - 1}{\omega C_L} \quad (2-31)$$

$$Y = j \left(\omega C_R - \frac{1}{\omega L_L} \right) = j \frac{(\omega/\omega_{sh})^2 - 1}{\omega L_L} \quad (2-32)$$

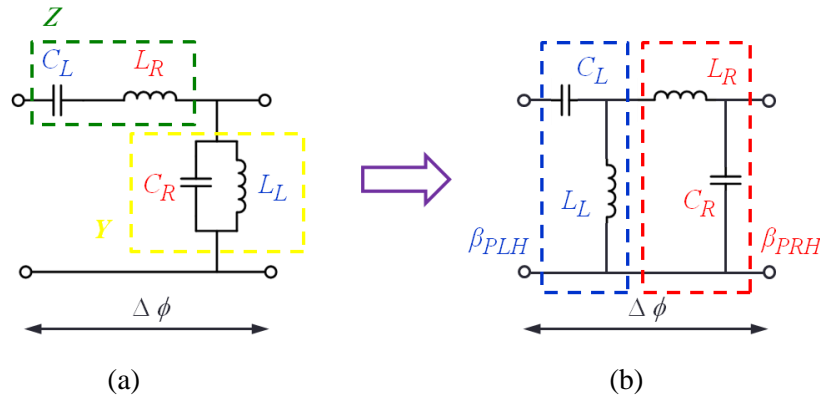


Figure 2-13. Unit cell of LC network implemented on CRLH transmission line (a) a general circuit, (b) a balanced circuit ($L_R C_L = L_L C_R$).

The phase shift $\Delta\phi$ induced by the unit cell is noted as $\Delta\phi$. It should be understood that the circuit models of Figure 2-13 are dimensionless. The circuit size can be described in terms of electrical length $\theta = |\Delta\phi|$ in radian unit. However, in practical circuitry, the inductors and

capacitors will occupy a physical length depending on the technology. In microstrip technology, for example, C_L can be implemented as interdigital capacitors, and L_L can be implemented as stub inductors. When the footprint of the unit cell is p in length, then the immittances along the length Δz can be written as

$$\frac{Z}{p} = j \left(\omega \left(\frac{L_R}{p} \right) - \frac{1}{\omega(C_L \cdot p)} \right) = j \frac{(\omega/\omega_{se})^2 - 1}{\omega(C_L \cdot p)} \quad (2-33)$$

$$\frac{Y}{p} = j \left(\omega \left(\frac{C_R}{p} \right) - \frac{1}{\omega(L_L \cdot p)} \right) = j \frac{(\omega/\omega_{sh})^2 - 1}{\omega(L_L \cdot p)} \quad (2-34)$$

By comparing Equation (2-8) to (2-33), and (2-9) to (2-34), when $p = \Delta z \rightarrow 0$ the immittances for the length p become $Z/p \rightarrow Z'$, and $Y/p \rightarrow Y'$. This means the LC implementation of Figure 2-13 is equivalent to the incremental model of Figure 2-4. The model of Figure 2-4 represents only a small length (Δz) of transmission line. However, a real total length line l is naturally obtained by repeating such a small piece with a suitable number of times N , such that $l = N \cdot \Delta z$. Such an equation, when $\Delta z \rightarrow 0$ and l is finite resulting in $N \rightarrow \infty$. Thus, cascading N -cells of LC unit cell as in the ladder network shown in Figure 2-14(b) leads to a TL equivalent to an ideal CRLH transmission line of the length l under the condition $p \rightarrow 0$, as the homogeneity condition ($\Delta z < \lambda_g/4$ and $\lambda_g \neq 0$). Thus, such an artificial line can be realized with a finite number of unit cells in a desired frequency range. Figure 2-14 shows the equivalent circuit models of a periodic ladder network (general and balanced) obtained from an ideal distributed CRLH transmission line with a physical length l , the propagation constant γ and characteristic impedance Z_c .

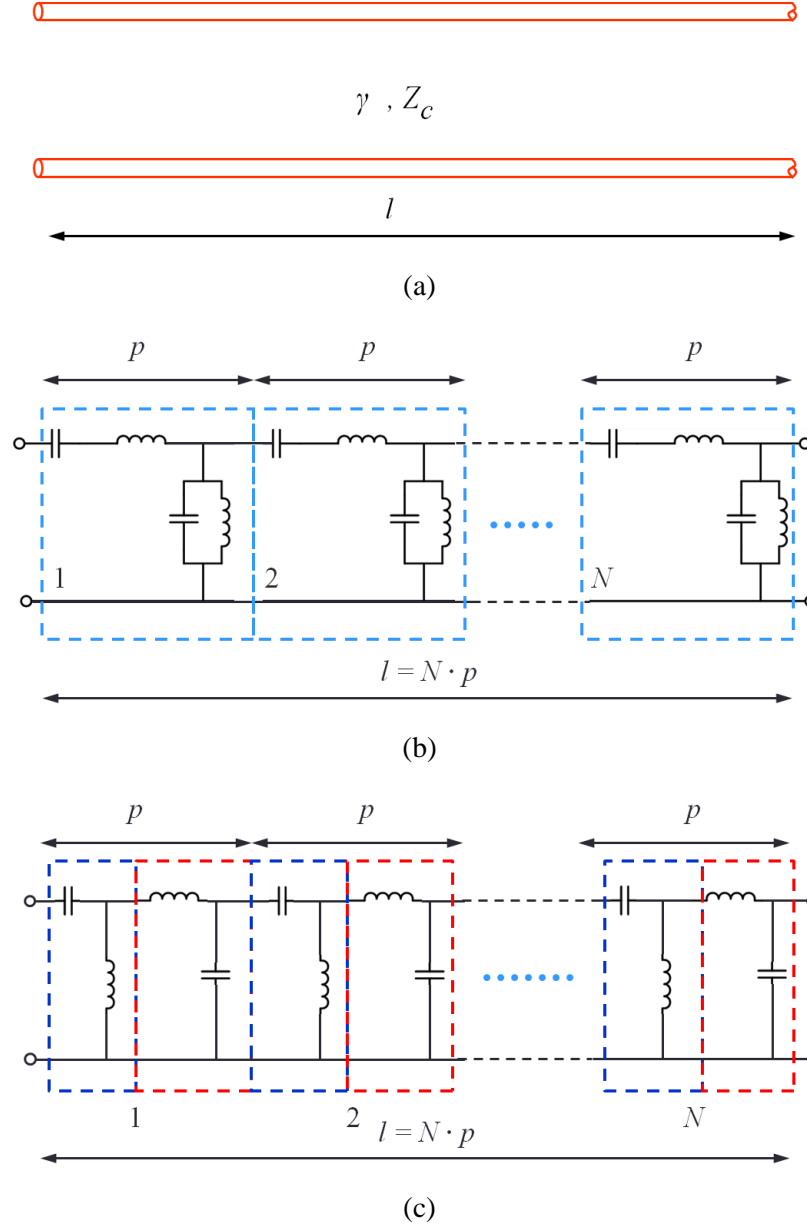


Figure 2-14. Periodic ladder network implemented LC CRLH transmission line in a restricted frequency range, (a) an ideal transmission line representative, (b) a general LC CRLH transmission line, (c) a balanced LC CRLH transmission line.

As shown in Figure 2-14, cascading N -cells of the unit cell in a network can serve as a real transmission line equivalent circuit and also represent as an ideal CRLH transmission line of the length (l) under the homogeneity condition with $p \rightarrow 0$. For practical purposes, this condition can be interpreted as a rule-of-thumb. The effective-homogeneity condition $p < \lambda_g/4$ is sufficient to

ensure the absence of Bragg-like interferences along the discontinuities of the line [5]. Consequently, the LC components are electrically very small and can be considered as lumped components. If the dimensionless LC ladder network constitutes an ideal inductor and capacitor, the homogeneity condition becomes $|\Delta\phi| \rightarrow 0$ or $|\Delta\phi| < \pi/2$, since $|\Delta\phi| = \beta \cdot p = 2\pi \cdot p/\lambda_g$. Generally speaking, if $p \neq 0$ and $p < \lambda_g/4$, the network still represents a good approximation of the ideal CRLH transmission line in a restricted frequency range. However, the ladder network model is valid for small unit cell electrical length $|\Delta\phi|$ due to the limit case of their homogeneous counterparts.

2.5 Periodic Analysis of LC Loaded Transmission Line Network

Previously, the one-dimensional (1-D) transmission line modeled as a distributed electromagnetic structure was rigorously mapped to the circuit expressions obtained from Kirchhoff's laws in order to reveal its general characteristics. As the circuit theory, it requires the physical dimensions of the LC network to be much smaller than the wavelength, such that each section can be treated as a lumped-element equivalent circuit. Moreover, such a transmission line can be modeled as the periodic ladder network or a series of the incremental lumped-elements having an infinitesimal size. However, when the circuit model with finite-dimension is periodically cascaded, a band structure is considerably developed on the corresponding dispersion relation [16]. Conducting periodic Bloch-Floquet analysis, the standard procedure for 1-D periodic of microwave networks [17], [18] is carried out and summarized below.

Alternatively, the ideal homogeneous CRLH transmission line can be modeled as a general T - or π -circuit as shown in Figure 2-15. It is worthy to distinguish that each of the series impedances and the shunt admittance (Z and Y) represent individual lumped elements which are

the total impedance and admittance over the length d . Furthermore, the physical length Δz or p is henceforth renamed as d (m) for convenience.

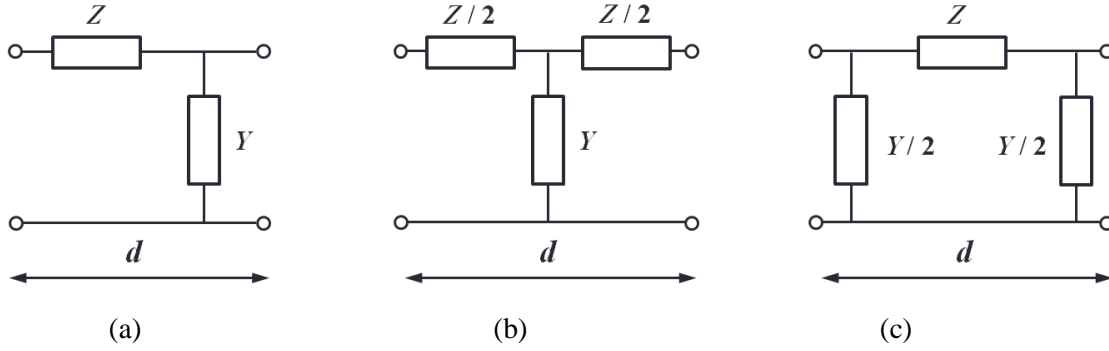


Figure 2-15. Equivalent circuit models of an ideal homogeneous transmission line, (a) general circuit, (b) T-circuit and (c) π -circuit.

According to the periodic Bloch-Floquet analysis with a forward propagation, the voltage and current at the terminal n th unit cell are related to the voltage and current at the terminal $(n+1)$ th unit cell by the propagation factor $e^{-j\beta_{BL}d}$, where β_{BL} is the Bloch propagation constant. For example, the symmetric T -network having a periodicity of d is proposed as a two port network. A two-port network can be represented as an equivalent $[ABCD]$, Figure 2-16. The matrix relates the input voltage and current to the output voltage and current as follows [40]:

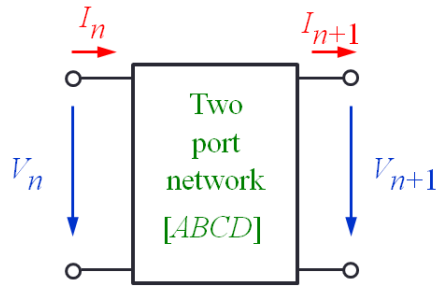


Figure 2-16. A representative of a two-port network as a model of the unit cell.

$$\begin{bmatrix} V_n \\ I_n \end{bmatrix} = \begin{bmatrix} A & B \\ C & D \end{bmatrix} \begin{bmatrix} V_{n+1} \\ I_{n+1} \end{bmatrix} \quad (2-35)$$

$$\begin{bmatrix} A & B \\ C & D \end{bmatrix} = \begin{bmatrix} 1 & \frac{Z}{2} \\ 0 & 1 \end{bmatrix} \begin{bmatrix} 1 & 0 \\ Y & 1 \end{bmatrix} \begin{bmatrix} 1 & \frac{Z}{2} \\ 0 & 1 \end{bmatrix} = \begin{bmatrix} 1 + \left(\frac{Z \cdot Y}{2}\right) & Z + \left(\frac{Z^2 \cdot Y}{4}\right) \\ Y & 1 + \left(\frac{Z \cdot Y}{2}\right) \end{bmatrix} \quad (2-36)$$

where it can be seen that after conversion from transmission parameters, $[ABCD]$ matrix to scattering parameters, S -parameter this 2-port network is symmetric since $A = D$ or $S_{11} = S_{22}$. The network is also reciprocal since $AD - BC = 1$ or $S_{21} = S_{12}$. In the case of a lossless network ($\alpha = 0, \beta \neq 0$), the solution of the dispersive relation can be analyzed as follows:

$$\cosh(\gamma d) \approx \cos(\beta_{BL} \cdot d) = 1 + \left(\frac{Z \cdot Y}{2}\right) \quad (2-37)$$

$$\text{or} \quad \sin^2\left(\frac{\beta_{BL} \cdot d}{2}\right) = -\frac{1}{4} Z \cdot Y \quad (2-38)$$

2.5.1 Periodic Lumped-Element Right-Handed Line

For a periodic lumped-element RH line or PRH TL, the total series impedance and shunt admittance over the specific length d are given by

$$Z = Z' \cdot d = j\omega(L'_R \cdot d) = j\omega L_R \quad (2-39)$$

$$Y = Y' \cdot d = j\omega(C'_R \cdot d) = j\omega C_R \quad (2-40)$$

It is important to emphasize that L'_R is a RH per-unit-length inductance (H/m), C'_R is a RH per-unit-length capacitance (F/m). However, L_R represents the total RH inductance (H) and C_R represents the total RH capacitance (F) that are parameters over the length d (m). In this condition, it can be concluded that $\beta_{BL} = \beta_{PRH}$ and the dispersion relation in the forward direction (+z direction) can be expressed as

$$\sin\left(\frac{\beta_{PRH} \cdot d}{2}\right) = \frac{1}{2} \omega \sqrt{L_R \cdot C_R} \quad (2-41)$$

Accordingly, if the phase shift per unit cell $|\Delta\phi|$ is small, the propagation constant from periodic approach as Equation (2-41) becomes close to the solution of the incremental circuit analysis (Telegrapher's equations). This can be confirmed using Equation (2-43).

$$\sin\left(\frac{\beta_{PRH} \cdot d}{2}\right) \approx \frac{\beta_{PRH} \cdot d}{2} = \frac{1}{2} \omega \sqrt{L_R \cdot C_R} \quad (2-42)$$

Therefore,
$$\beta_{PRH} = \omega \sqrt{\frac{L_R}{d} \cdot \frac{C_R}{d}} = \omega \sqrt{L'_R \cdot C'_R} \quad (2-43)$$

The dispersion diagrams for both the incremental circuit analysis and the periodic lumped-element approach are shown in Figure 2-17(a). The parameters in the simulation consists of $L_R = 695$ pH, $C_R = 278$ fF, which are related with a transmission line with parameters $Z_0 = 50 \Omega$, $d = 1.45$ mm and electrical length $\theta = 50^\circ$ at 10 GHz. It is clear from the results that the incremental transmission line model approached by the circuit analysis exhibits a continuous dispersive implying that no cut-off frequency. However, when the lumped-element periodic structure is

analyzed using the periodic Bloch-Floquet analysis, the dispersive expresses a high frequency cut-off condition at $\beta_{PRH} \cdot d = \pi$ as the forward direction of power flow (+z direction). It is interpreted that the lumped-element periodic model actually performs as a low-pass filter with a cut-off frequency f_c^{LP} . Above this frequency, no propagation occurs. It can also be observed that for a small phase shift per unit cell, the dispersive relations obtained using the periodic approach and Telegrapher's equations match very closely.

2.5.2 Periodic Lumped-Element Left-Handed Line

In a periodic lumped-element LH line or PLH TL, the total series impedance and shunt admittance over the specific length d are expressed by

$$Z = Z' \cdot d = \frac{1}{j\omega(C'_L/d)} = \frac{1}{j\omega C_L} \quad (2-44)$$

$$Y = Y' \cdot d = \frac{1}{j\omega(L'_L/d)} = \frac{1}{j\omega L_L} \quad (2-45)$$

It is important to remind that L'_L is a LH times-unit-length inductance (H·m), C'_L is a LH times-unit-length capacitance (F·m). However, L_L represents the total LH inductance (H) and C_L represents the total LF capacitance (F). These parameters are qualities over the length d (m). Generally, PLH structures do not exist in nature, and therefore they must be synthesized artificially. Consequently, the dispersive equation in forward direction of power flow (+z direction) with $\beta_{BL} = -\beta_{PLH}$ can be expressed as

$$\sin\left(\frac{\beta_{PLH} \cdot d}{2}\right) = \frac{-1}{2\omega\sqrt{L_L \cdot C_L}} \quad (2-46)$$

When the phase shift per unit cell $|\Delta\phi|$ is small, the propagation constant from periodic approach as Equation (2-46) gets close to the solution of the incremental circuit analysis (Telegrapher's equations). The above mention can be confirmed by Equation (2-48).

$$\sin\left(\frac{\beta_{PLH} \cdot d}{2}\right) \approx \frac{\beta_{PLH} \cdot d}{2} = \frac{-1}{2\omega\sqrt{L_L \cdot C_L}} \quad (2-47)$$

$$\text{Therefore, } \beta_{PLH} = \frac{-1}{\omega\sqrt{(L_L \cdot d) \cdot (C_L \cdot d)}} = \frac{-1}{\omega\sqrt{L'_L \cdot C'_L}} \quad (2-48)$$

The dispersion diagrams of LH transmission line for both the incremental circuit analysis and the periodic lumped-element approach are also shown in Figure 2-17(b). The parameters in the simulation, for an example are $L_L = 465$ pH, $C_L = 186$ fF. In the same manner, the incremental transmission line model approached by the Telegrapher's equations exhibits a continuous dispersion implying that there is no cut-off frequency. However, the lumped-element periodic structure approached by the periodic Bloch-Floquet analysis exhibits a low frequency cut-off condition f_c^{HP} at $\beta_{PLH} \cdot d = -\pi$ following a forward direction of power flow (+z direction).

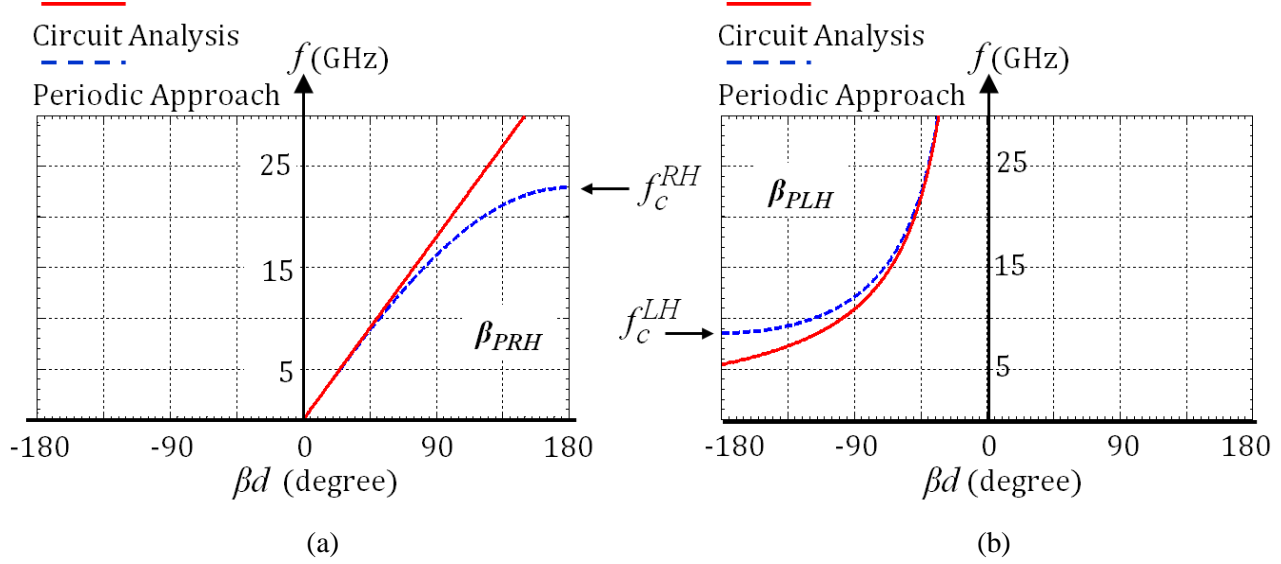


Figure 2-17. Dispersion diagrams for representatives of transmission line, compared between the incremental circuit analysis (Telegrapher's equations) and the periodic lumped-element approach (Bloch and Floquet analysis) as energy propagation along the +z direction, (a) PRH transmission line, (b) PLH transmission line.

2.5.3 Periodic Lumped-Element CRLH Transmission Line

In the CRLH transmission line, the LH line causes the phase leading in the direction of the group velocity [5]. It simply means that there is a positive phase shift propagating away from the source. On the other hand, the conventional transmission line or RH line obtains a lag in phase with the direction of positive group velocity. Thus, a negative phase shift of the RH line propagates away from the source. Under this phenomenon, the insertion phase of the CRLH transmission line is compensated at a given frequency by cascading a section of RH medium with a section of LH medium to form a MTM unit cell structure to achieve desired phase shift. Therefore, the total phase shift across the CRLH transmission line can be written as

$$\phi_{eff} = \phi_{LH} + \phi_{RH} \quad (2-49)$$

Nonetheless, it follows that the MTM unit cell consists of a host TL medium (RH line) with distributed lumped elements L, C integrated with discrete lumped element components L_o, C_o of LH-structure. Such a CRLH transmission line can be simplified to equivalent circuit model to determine the propagation characteristics of the MTM unit cell as illustrated in Figure 2-18. The simplified equivalent circuit is formed as T -configuration. The host TL medium or RH line is expressed with the characteristic impedance Z_o with physical length d . It is worthy to note that the physical length Δz (m) or p (m) is henceforth renamed as d (m). Moreover, the RH parameters, L_R, C_R are recalled as L, C respectively. In case of LH parameters, L_L and C_L are renamed as L_o and C_o , respectively. All of the parameters are renamed for convenience to write down the characteristic equations of CRLH transmission line by conducting a periodic Bloch-Floquet analysis.

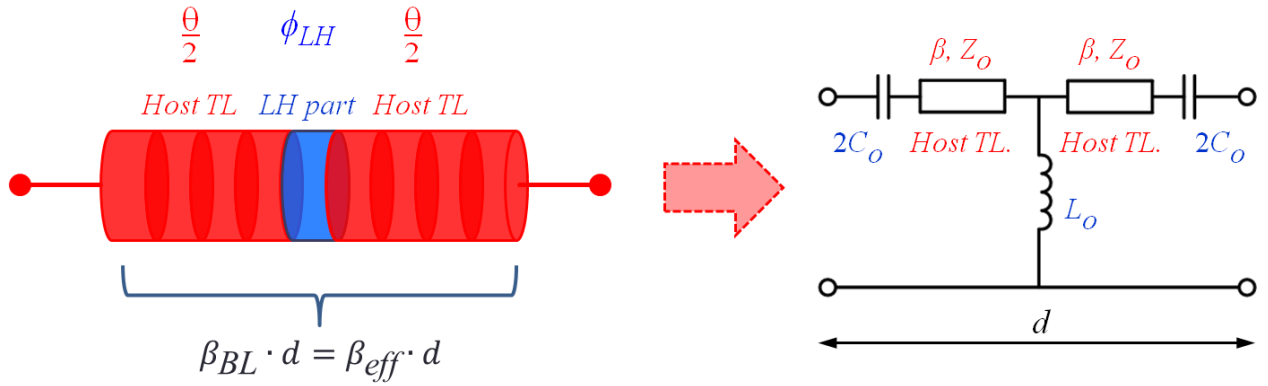


Figure 2-18. Simplified equivalent circuit (T -configuration) of 1-D ideal CRLH homogeneous transmission line having the physical length d .

As mentioned above, the propagation characteristics of a CRLH transmission line or metamaterial line can be determined by conducting the periodic Bloch-Floquet analysis with repeated symmetric unit cells. The configuration of T -unit cell of Figure 2-18 is transformed to

the generic unit cell of Figure 2-19 for the subsequent analysis. In the analysis, the lumped-elements are replaced with the following conventional expressions for simplification. It is important to emphasize that the host transmission line of the generic unit cell is characterized in terms of the characteristic impedance Z_o and electrical length θ .

$$Z = \frac{1}{j\omega C_o} \quad (2-50)$$

$$Y = \frac{1}{j\omega L_o} \quad (2-51)$$

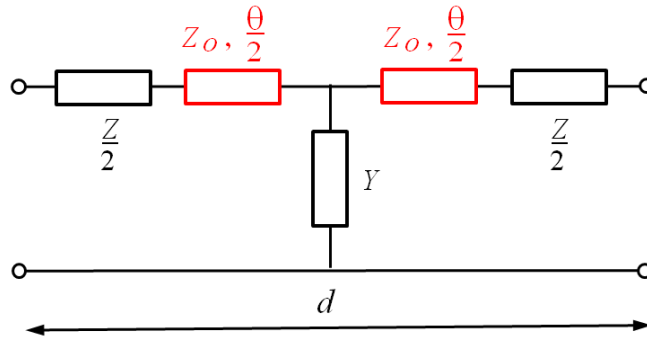


Figure 2-19. Generic unit cell (*T*-configuration) of a metamaterial line having the physical length d .

As the generic unit cell in Figure 2-19, the symmetric *T*-network having a periodicity of d is proposed as the two port network (Figure 2-16). Therefore, the $[ABCD]$ matrix can represent the input voltage and current at the terminals n th unit cell related with the output voltage and current at the terminal $(n+1)$ th unit cell through the transfer function yielding the expression of Equation 2-35. Generally, the $[ABCD]$ matrix of Figure 2-19 can be expressed in terms of the product of

the $[ABCD]$ matrix of the individual elements constituting the unit cell as mentioned above. It provides the following the relationship as

$$\begin{bmatrix} V_n \\ I_n \end{bmatrix} = \begin{bmatrix} A & B \\ C & D \end{bmatrix} \begin{bmatrix} V_{n+1} \\ I_{n+1} \end{bmatrix} \quad (2-35)$$

$$\begin{bmatrix} A & B \\ C & D \end{bmatrix} = \begin{bmatrix} 1 & \frac{Z}{2} \\ 0 & 1 \end{bmatrix} \begin{bmatrix} \cos\left(\frac{\theta}{2}\right) & jZ_o \sin(\theta/2) \\ jY_o \sin(\theta/2) & \cos\left(\frac{\theta}{2}\right) \end{bmatrix} \begin{bmatrix} 1 & 0 \\ Y & 1 \end{bmatrix} \quad (2-52)$$

$$\begin{bmatrix} \cos\left(\frac{\theta}{2}\right) & jZ_o \sin(\theta/2) \\ jY_o \sin(\theta/2) & \cos\left(\frac{\theta}{2}\right) \end{bmatrix} \begin{bmatrix} 1 & \frac{Z}{2} \\ 0 & 1 \end{bmatrix}$$

After expanding the above expression, the $[ABCD]$ matrix can be found as

$$A = \left(1 + \frac{ZY}{4}\right) \cos\theta + \frac{j}{2} (ZY_o + YZ_o) \sin\theta + \frac{ZY}{4} \quad (2-53)$$

$$B = \left(Z + \frac{Z^2 Y}{8} + \frac{Y Z_o^2}{2}\right) \cos\theta + \frac{j}{2} \left(\frac{Z^2 Y_o}{2} + Y Z Z_o + 2 Z_o\right) \sin\theta + \frac{Z^2 Y}{8} - \frac{Y Z_o^2}{2} \quad (2-54)$$

$$C = \frac{Y}{2} \cos\theta + j Y_o \sin\theta + \frac{Y}{2} \quad (2-55)$$

$$D = \left(1 + \frac{ZY}{4}\right) \cos\theta + \frac{j}{2} (ZY_o + YZ_o) \sin\theta + \frac{ZY}{4} \quad (2-56)$$

Likewise, it is clearly seen that the lossless 2-port network is symmetric ($A = D$ or $S_{11} = S_{22}$) and also reciprocal ($AD - BC = 1$ or $S_{21} = S_{12}$). For a forward travel wave, $+z$ direction, the dispersion relation therefore becomes

$$\cos(\beta_{BL} \cdot d) = \left(1 + \frac{ZY}{4}\right) \cos\theta + \frac{j}{2}(ZY_o + YZ_o) \sin\theta + \frac{ZY}{4} \quad (2-57)$$

Substituting the values of the impedance and admittance from Equation (2-50) and (2-51), the dispersion relation of the periodic structure as an infinite number of T -unit cell metamaterial line can be expressed as

$$\cos(\beta_{BL} \cdot d) = \left(1 - \frac{1}{4\omega^2 L_o C_o}\right) \cos\theta + \left(\frac{1}{2\omega C_o Z_o} + \frac{Z_o}{2\omega L_o}\right) \sin\theta - \frac{1}{4\omega^2 L_o C_o} \quad (2-58)$$

If θ is small, the sine and cosine function can be approximated to Equation (2-59) and (2-60). Since the characteristic impedance of the host line is $Z_o = \sqrt{L/C}$, this expression can be simplified to be Equation (2-61) [19].

$$\cos\theta \approx 1 - \frac{\theta^2}{2} \quad (2-59)$$

$$\sin\theta \approx \theta = \omega\sqrt{LC} \quad (2-60)$$

$$\cos(\beta_{eff} \cdot d) = 1 - \frac{1}{2} \left[\omega^2 LC + \frac{1}{\omega^2 L_o C_o} - \left(\frac{C}{C_o} + \frac{L}{L_o} \right) \right] \quad (2-61)$$

For example, the dispersion diagrams referred from Equation (2-61) are performed in both balanced and unbalanced modes. Assuming that the RH and LH contributions of balanced condition are $L = 1\text{nH}$, $C = 1\text{pF}$ and $L_o = 1\text{nH}$, $C_o = 1\text{pF}$, respectively. In case of unbalanced mode, only the LH parameters are changed to be $L_o = 0.5\text{nH}$, $C_o = 2\text{pF}$. Figure 2-20 shows the dispersion relations computed for examples of balanced and unbalanced CRLH transmission line.

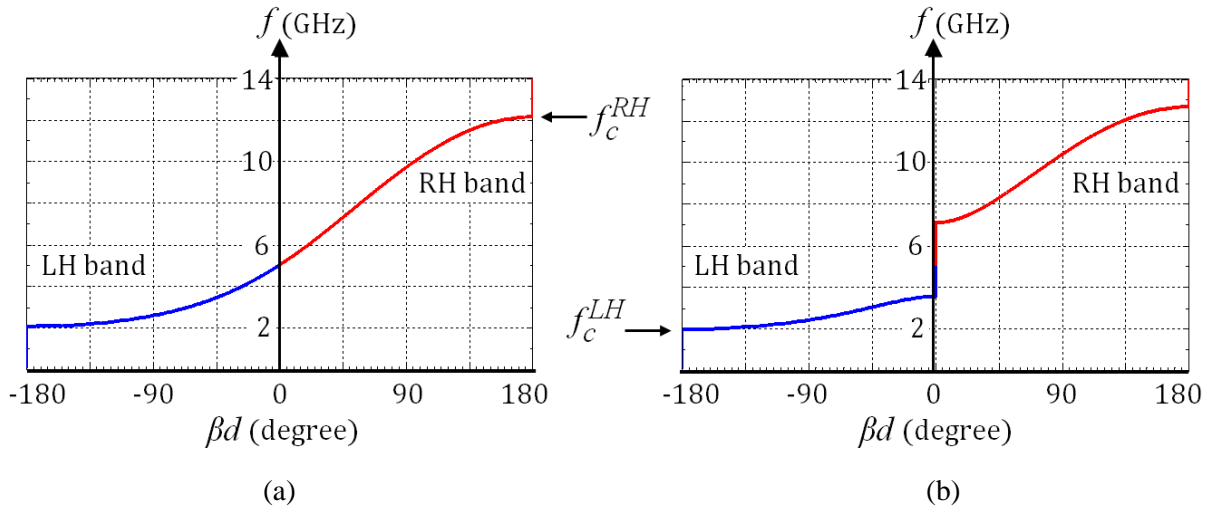


Figure 2-20. Dispersion diagrams computed by equation 2-61 of CRLH transmission line at a forward propagation (+z direction), (a) balanced mode, (b) unbalanced mode.

Typically, the dispersion plays a key role for exhibiting the characteristics of CRLH or metamaterial transmission line. As expected, continuous transition between LH and RH bands with non-zero group velocity can be accomplished in the balanced case. Discontinuous transition with zero group velocity occurs in the unbalanced mode related to series and shunt resonance frequencies. The dispersion relations found using periodic analysis help to express the cut-off frequency at the RH band and LH band, unlike using the Telegrapher's equations approach on the metamaterial line. It is an important consideration that the dispersive can be expressed in the different points of view as shown in Figure 2-21. The dispersion relations of balanced and

unbalanced modes compared each other at the same diagram is illustrated in Figure 2-21(a). Alternatively, these dispersion diagrams can be expressed as in Figure 2-21(b) with the knowledge that the phase shift at LH band is negative and RH band is positive. This is a preferred approach to presenting the dispersion diagram and is commonly used in literature.

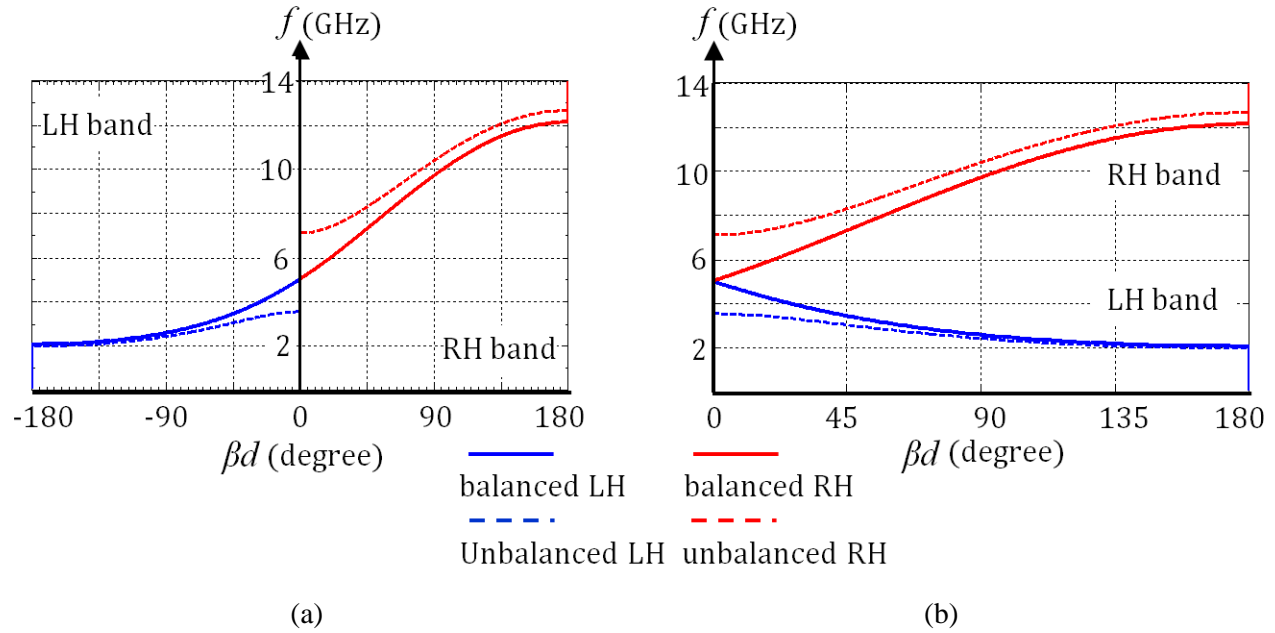


Figure 2-21. Dispersion diagrams computed using equation (2-61) of CRLH transmission line at a forward propagation (+z direction) in the alternative illustrations, (a) general illustration, (b) preferable illustration.

Therefore, the dispersion relation determined by the periodic analysis is sufficient to characterize the propagation characteristics of the periodic CRLH transmission line model. As mentioned above, the structure consists of a host TL medium (RH line) periodically loaded with LH contributions as the discrete lumped components, L_o and C_o . Such a model is sufficient to use for the periodic analysis and it can be considered an effective medium. It is important to emphasize that considering such a series of cascaded unit cells as an effective periodic medium, the physical length of the unit cell must be much smaller than a wavelength [20]. Beginning from

the dispersion relation from Equation (2-58) and referring to the simplified equivalent circuit (T -configuration) of a unit cell from Figure (2-18), an effective propagation constant β_{eff} can be defined for the medium. The details of the analysis are shown in Appendix A.

$$\sin^2\left(\frac{\beta_{BL} \cdot d}{2}\right) = \left(\sin\frac{\theta}{2} - \frac{\cos\frac{\theta}{2}}{2\omega C_o Z_o}\right) \left(\sin\frac{\theta}{2} - \frac{Z_o \cos\frac{\theta}{2}}{2\omega L_o}\right) \quad (2-62)$$

where θ and Z_o are electrical length, characteristic impedance of the host TL (RH contributions), respectively. LH contributions consist of the total shunt inductance L_o and series capacitance C_o over the physical length d . For convenience to reflect the effective nature of the periodic CRLH medium, β_{BL} is renamed as β_{eff} henceforth. Under the aforementioned assumption that a small phase shift per unit cell is required. The effective propagation constant can be determined as

$$(\beta_{eff} \cdot d)^2 = \left(\beta_{TL} \cdot d - \frac{1}{\omega C_o Z_o}\right) \left(\beta_{TL} \cdot d - \frac{Z_o}{\omega L_o}\right) \quad (2-63)$$

$$\beta_{eff}^2 = \omega^2 L_{eff} \cdot C_{eff} = \left(\omega L - \frac{1}{\omega C_o d}\right) \left(\omega C - \frac{1}{\omega L_o d}\right) \quad (2-64)$$

where, $\beta_{TL} = \theta/d = \omega\sqrt{LC}$ (2-65)

$$Z_o = \sqrt{L/C} \quad (2-66)$$

The expression of Equation (2-64) demonstrates that the effective propagation constant is similar to the propagation constant of a conventional transmission line (PRH line) with effective

terms of inductance, L_{eff} , and capacitance, C_{eff} . Moreover, it can be easily observed that the propagation of the medium can be positive, negative or zero as dictated by the loading LH parameters L_o and C_o . It can be confirmed from the equation that a forward wave is introduced when the effect of loading reactance (LH terms) is negligible. On the contrary, when the loading reactance is dominant and greater than the host transmission line parameters, L and C (RH terms), the effective terms L_{eff} and C_{eff} become double negative and therefore a backward wave is present along the structure. Finally, the effective propagation constant is zero when the host transmission line terms L and C are equal to the loading LH terms L_o and C_o . It means there is no propagation along the medium.

As mentioned above, the cascaded unit cell must meet impedance matching conditions, Equation (2-67), to provide a balanced mode in CRLH transmission line. Consequently, the effective propagation constant of the CRLH transmission line can be simply expressed from Equation (2-68) to (2-69).

$$Z_o = \sqrt{L/C} = \sqrt{L_o/C_o} \quad (2-67)$$

$$\beta_{eff} = \pm \omega \sqrt{L_{eff} \cdot C_{eff}} = \pm \omega \sqrt{\left(L - \frac{1}{\omega^2 C_o d}\right) \left(C - \frac{1}{\omega^2 L_o d}\right)} \quad (2-68)$$

$$\beta_{eff} = \omega \sqrt{LC} + \frac{-1}{\omega \sqrt{L_o C_o} \cdot d} \quad (2-69)$$

From Equation (2-69), derived under matching condition, an expression of the propagation constant can be interpreted as a sum of the propagation constants of the host RH medium

(forward wave) and a uniform LH medium (backward wave). Such a medium with periodicity d and phase shift of the host RH line, $\theta = \phi_{TL} = \beta_{TL} \cdot d = \omega\sqrt{LC} \cdot d$, the total phase shift per unit cell, $|\phi_o|$ under the matching condition can be simplified as

$$|\phi_o| = \beta_{eff} \cdot d = \phi_{TL} + \frac{-1}{\omega\sqrt{L_o C_o}} \quad (2-70)$$

A similar procedure can be carried out for the periodic analysis of the generic unit cell as π -configuration in Figure 2-22. The $[ABCD]$ matrix of Figure 2-22 can be expressed in terms of the product of the $[ABCD]$ matrix of the individual elements constituting the unit cell. Therefore, the $[ABCD]$ matrix of such a unit cell can be written as follows:

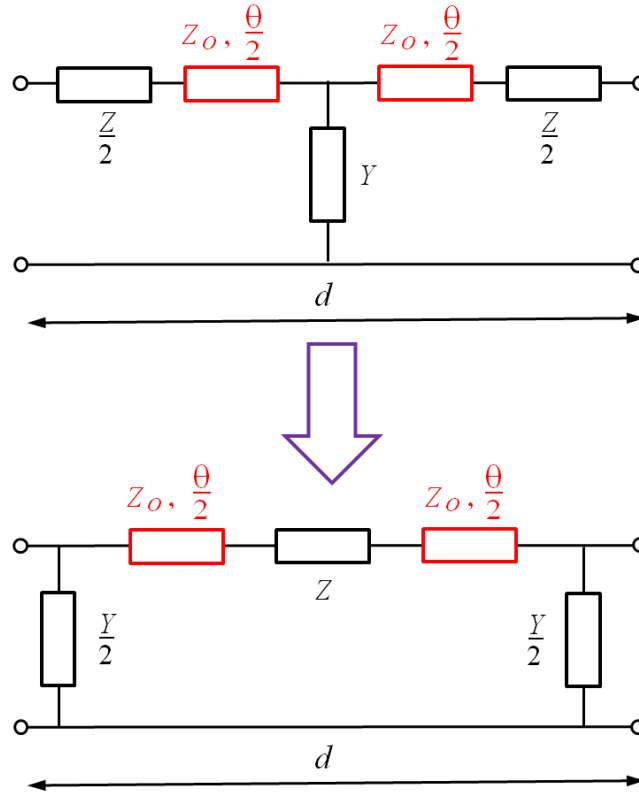


Figure 2-22. The transformation of T -unit cell into π -unit cell of a metamaterial line having the physical length d .

$$\begin{aligned}
\begin{bmatrix} A & B \\ C & D \end{bmatrix} &= \begin{bmatrix} 1 & 0 \\ Y/2 & 1 \end{bmatrix} \begin{bmatrix} \cos\left(\frac{\theta}{2}\right) & jZ_o \sin(\theta/2) \\ jY_o \sin(\theta/2) & \cos\left(\frac{\theta}{2}\right) \end{bmatrix} \begin{bmatrix} 1 & Z \\ 0 & 1 \end{bmatrix} \\
&\quad \begin{bmatrix} \cos\left(\frac{\theta}{2}\right) & jZ_o \sin(\theta/2) \\ jY_o \sin(\theta/2) & \cos\left(\frac{\theta}{2}\right) \end{bmatrix} \begin{bmatrix} 1 & 0 \\ Y/2 & 1 \end{bmatrix}
\end{aligned} \tag{2-71}$$

After expanding the above expression, the terms in the $[ABCD]$ matrix can be written as

$$A = \left(1 + \frac{ZY}{4}\right) \cos\theta + \frac{j}{2} (ZY_o + YZ_o) \sin\theta + \frac{ZY}{4} \tag{2-72}$$

$$B = \frac{Z}{2} \cos\theta + jZ_o \sin\theta + \frac{Z}{2} \tag{2-73}$$

$$\begin{aligned}
C &= \left(Y + \frac{ZY^2}{8} + \frac{ZY_o^2}{4}\right) \cos\theta + \frac{j}{2} \left(\frac{Y^2 Z_o}{2} + YZY_o + 2Y_o\right) \sin\theta + \frac{ZY^2}{8} \\
&\quad - \frac{ZY_o^2}{2}
\end{aligned} \tag{2-74}$$

$$D = \left(1 + \frac{ZY}{4}\right) \cos\theta + \frac{j}{2} (ZY_o + YZ_o) \sin\theta + \frac{ZY}{4} \tag{2-75}$$

As expected, it is clear from the results that the terms A and D of π -configuration are equal to the terms A and D of the symmetric T -configuration. Thus, the dispersion characteristics of the π -configuration are interchangeable with those of the T -configuration as Equation (2-57).

2.6 Selected Metamaterial Structures

There are a number of resonator types that exploit the unique properties of MTM in microwave circuit designs. Based on microstrip technology, a conventional transmission line is loaded with inductive and capacitive structures in order to obtain a propagation medium with controllable characteristics. Though each microwave filter application is very exciting and worth examining, only the use of metamaterial based 1-D uniplanar microstrip line is discussed and summarized as Table 2-1.

Table 2-1. Summary and comparison of MTM-inspired resonant structures based microstrip line

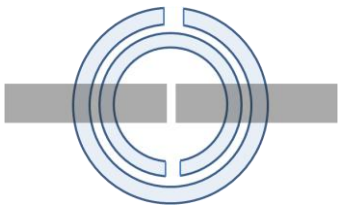

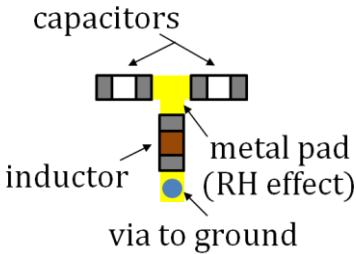
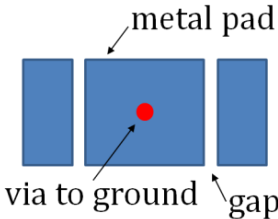

MTM-inspired resonant structures	Comments	References
<p>(a) CSRR structure.</p> 	<ol style="list-style-type: none"> 1. Double-side metal patterning. 2. No vias. 3. Resonant Frequency (f_c) at 1, 1.5, 2 and 2.5 GHz. 	<p>[9-15], [21-24]</p>
<p>(b) Interdigital capacitors and short stub inductors.</p> 	<ol style="list-style-type: none"> 1. One-side metal patterning. 2. Via to ground is needed. 3. Resonant Frequency (f_c) at 1.5, 1.9, 2.2 and 3.5 GHz. 	<p>[25], [26], [27], [28]</p>

Table 2-1 (cont'd) Summary and comparison of MTM-inspired resonant structures based microstrip line

MTM-inspired resonant structures	Comments	References
<p>(c) Lump element loading.</p> 	<ol style="list-style-type: none"> 1. One-side metal patterning. 2. Via to ground is needed. 3. Resonant Frequency (f_c) at 0.9 and 1.8 GHz. 	[20], [29]
<p>(d) Mushroom structure.</p> 	<ol style="list-style-type: none"> 1. One-side metal patterning. 2. Via to ground is needed. 3. Resonant Frequency (f_c) at 10 GHz. 	[30]
<p>(e) Double spiral structure</p> 	<ol style="list-style-type: none"> 1. One-side metal patterning. 2. No vias. 3. Resonant Frequency (f_c) at 3 GHz. 	[31], [32], [33]

2.7 Proposed Metamaterial Structures

As summarized in Table 2-1, there are many weak points about the existing MTM resonators that are loaded on a microstrip line. Most of these are limited to low frequency operation, approximately 1-3 GHz, and are difficult to scale for higher frequency applications. Moreover, some of resonator structure require double side metal patterning and/or via holes. These lead to complex fabrication process and therefore high fabrication costs. So, these issues are challenging and worth tackling. The novel resonator unit cells should be determined in order to design a unit cell that is simple to fabricate, scalable to different frequency ranges, and that avoids the use of vias. Here, the unit cells are designed for microwave applications in the X-band (7.5 – 12 GHz) frequency range.

For the research work, the layouts of novel MTM unit cells are proposed and their configurations are demonstrated in Figure 2-23. The proposed unit cells are designed based on microstrip technology and named as modified split ring resonator (mSRR) and modified split ring resonator with open gap (OmSRR). Details of these structure and their properties will be discussed later in Chapters 3 and 4. Dispersion diagrams of these unit cells are derived using the above theory. As illustrated, the balanced mode of CRLH TL and the impedance matching conditions are satisfied. The stopband is closed or in other words, RH passband and LH passband are continuous. It is important to note that at the transition frequency f_o the mSRR and OmSRR unit cells are approximately 10 GHz and 14 GHz, respectively. At the transition frequency (or resonance frequency), 0-degree phase shift is achieved for such MTM unit cells.

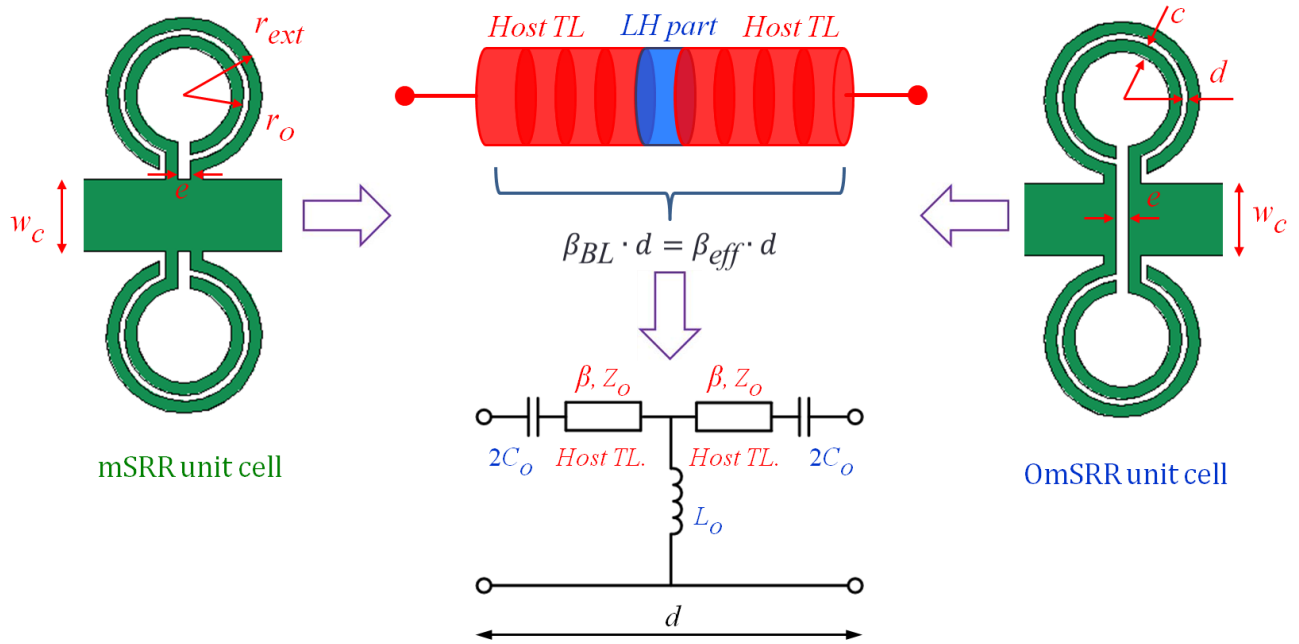


Figure 2-23. The transformation of the proposed unit cells in this research work into the *T*-unit cell based the CRLH transmission line.

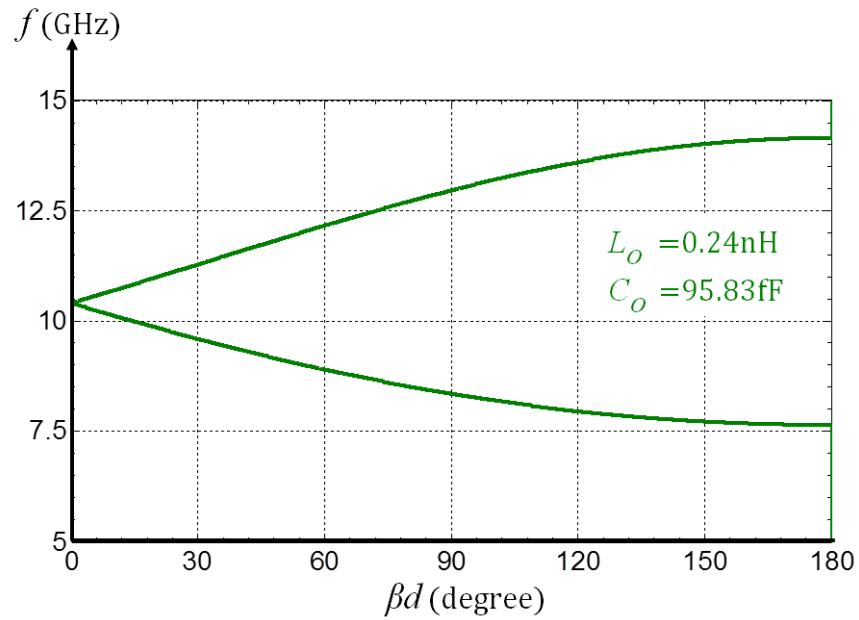


Figure 2-24. Dispersion relation of the proposed **mSRR** unit cell design.

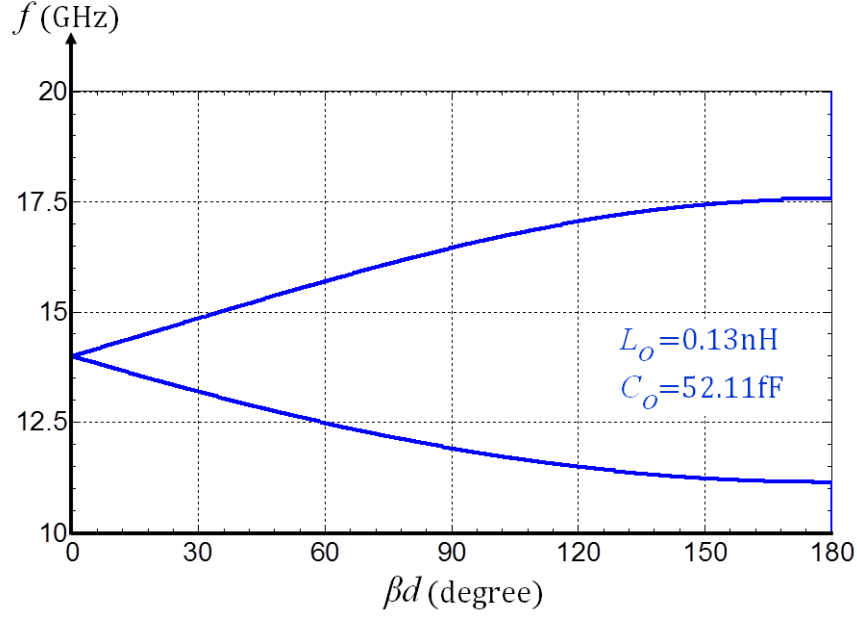


Figure 2-25. Dispersion relation of the proposed **OmSRR** unit cell design.

The possibility of manipulating the electrical characteristics such as image impedance (Z_B) and electrical length (βd) is the key point to using these kinds of unit cell in order to design reconfigurable RF/microwave circuits. For a specific operating frequency, such unit cells allow the control of important parameters through the physical layout of the unit cell. By incorporating tunable elements within the unit cell, it can be used in the design of tuning circuits in which the dispersion diagram is manipulated at the cell level. Figure 2-26 illustrates the unit cell with potential locations where active elements such as varactor diodes or MEM capacitive switches can be integrated. The tuning elements can be integrated at multiple locations within the unit cells in order to achieve the desired tuning properties with respect to phase, amplitude and group delay. Finally, it is worth noting that the configuration of unit cells avoids the use of vias and thus simpler to fabricate and integrate with other parts of microwave circuits. Also, biasing circuits required for the tunable elements is simpler to implement in this configuration.

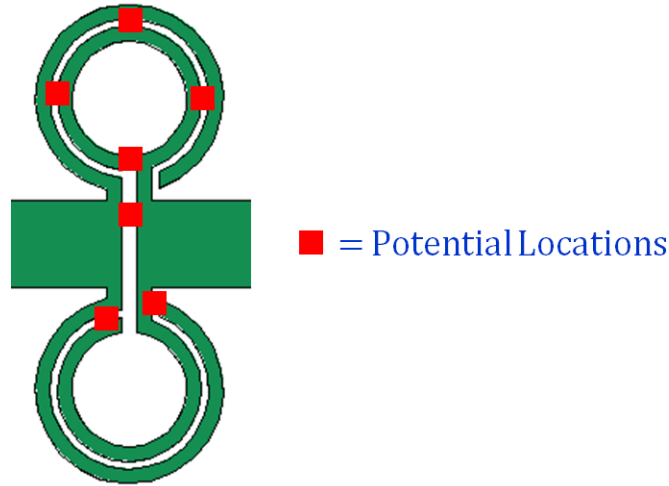


Figure 2-26. Potential locations on the unit cell for the integration of active elements (e.g., varactor diodes).

2.8 Metamaterials Inspired Microwave Circuits and Sensors

To express the promising unique properties of metamaterials, the OmSRR integrated with a capacitor is proposed and its characteristics with different capacitor values are analyzed using Ansoft HFSS® (3D finite element modeling). In these simulations, the capacitor is assumed as an ideal element. Three different values, 0.35 pF, 0.60 pF and 1.25 pF, were used in the simulations. Since the essential parameters of the unit cell (L_o , C_o and *host TL*) are altered by the capacitor and this in turn alters the dispersion diagram. The resonance frequency is shifted from its original value to 9.875 GHz, 10.10 GHz and 10.25 GHz for capacitance values of 0.35 pF, 0.60 pF and 1.25 pF, respectively. From simulated scattering responses, the equivalent circuit models of the unit cell integrated with each capacitance are extracted and their dispersion relations are analyzed. The dispersion diagrams are shown in Figure 2-27. As designed, the CRLH TL can be maintained in balanced mode within specific frequency range and the dispersion relation is altered related with the desired capacitance values. Such changes of

dispersive relations play a key to design new functionalities of microwave circuits and in the design of design of novel sensors.

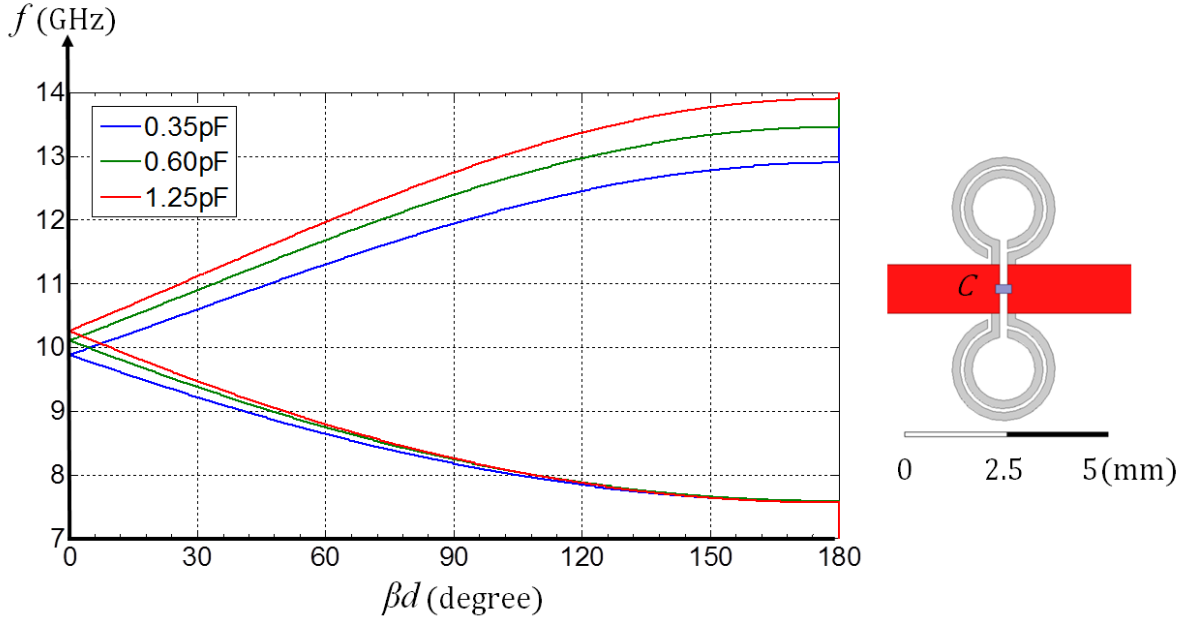


Figure 2-27. Dispersion diagrams of the OmSRR unit cell integrated loaded with three different capacitance values.

Changes in capacitance value integrated with the unit cell leads to reconfigurability and dispersive alteration especially in the LH-region. This phenomenon can be exploited in the design of new functionalities for microwave circuit applications. Changes in capacitance value of the unit cell can be manipulated by using a varactor diode or by loading with a dielectric material. The varactor diode is used to design reconfigurable microwave circuits. The changes of capacitance by dielectric material loading are exploited in the design of highly sensitive microwave sensors. A dielectric material loading the cells can be characterized by analyzing changes in scattering responses and dispersion relation.

To demonstrate such promising phenomenon of the MTM unit cell, the group velocity is further analyzed. As mentioned above, the group velocity of CRLH (balanced) medium

continues at the resonance (transition) frequency and the group velocity is half of its RH-contributions at the transition. The first derivative of the group velocity is first introduced here to clearly identify from the LH-contributions. Referred to Eq. 2-30, the first derivative of the group velocity can be expressed as

$$\frac{dv_g}{d\omega} = \frac{2\omega \cdot \omega_o^2 \cdot \omega'_R}{(\omega^2 + \omega_o^2)^2} \quad (2-76)$$

For each capacitance value, the first derivative of group velocities of the OmSRR unit cell integrated with the capacitor is determined. For each capacitance, the derivative of group velocity diagrams can be expressed as shown in Figure 2-28. It is clear from the result that the more capacitance leads to higher derivatives (slope) of group velocity. This result is attributed to larger RH contributions (ω'_R) caused by the higher capacitances. It is worth noting that the first derivative of group velocity is maximized in the LH-side which lies below resonance frequency. It can be interpreted that wave propagation of LH-range is more sensitive than that of RH-side. Moreover, the first derivative of each group velocity becomes zero as $\omega \rightarrow \infty$ since the group velocities are bounded to those of the RH-contributions at high frequency.

Importantly, the normalized derivative of group velocity is also presented to demonstrate the phenomenon of wave propagation along the MTM line when the parameters of the unit cell are altered using a varactor diode or through dielectric loading. The correlations of normalized derivative of group velocities for each capacitance as a function of frequency are shown in Figure 2-29. Undoubtedly, the unique electromagnetic properties of MTMs lead to promising new functionality and various applications in microwave circuits as clearly seen in the diagrams. For example, small changes of the capacitance lead to significant change in normalized

derivative of group velocities at LH-side more than those of RH-side. This leads to the design of MTM-inspired microwave sensors that provide higher sensitivity compared to conventional RH-based designs. Moreover, the normalized derivative of group velocity is almost linear around the resonance frequency. It can maintain linearity with different slopes related with the change in the loading capacitance values. This condition can be exploited in the design of MTM-inspired reconfigurable microwave circuits such as phase shifters and power dividers. This is because the rate of change in group velocity (frequency domain) can be linear change when the microwave circuit is designed with electrically tunable resonance. For the MTM-inspired microwave sensors, both of the wave propagation of LH-range and the change of resonance frequency can be exploited to characterize the properties of dielectric samples under test.

In summary, ongoing research in MTMs has led to promising new electromagnetic components and devices for various applications. Due to the unique unusual electromagnetic properties of MTMs, significant research effort has been focused on the development of microwave and millimeter-wave circuits such as couplers, resonators, electrically small antennas, leaky-wave antennas, invisibility cloaks, and perfect MTM absorbers, to name a few. Key advantages of MTM inspired RF/microwave devices and applications are as follows: 1) Circuit miniaturization, 2) Novel circuit designs especially reconfigurability, 3) New functions unattainable before such as invisibility, backward waves, 4) Lower cost due to circuit miniaturization, 5) Higher functional circuit density, 6) Simpler and efficient designs, 7) Combined with active devices, new reconfigurable RF circuits difficult to realize before, 8) Highly sensitive near-field sensing probes with high signal to noise ratio and 9) High throughput sensing of multiple samples using an array of sensors, etc.

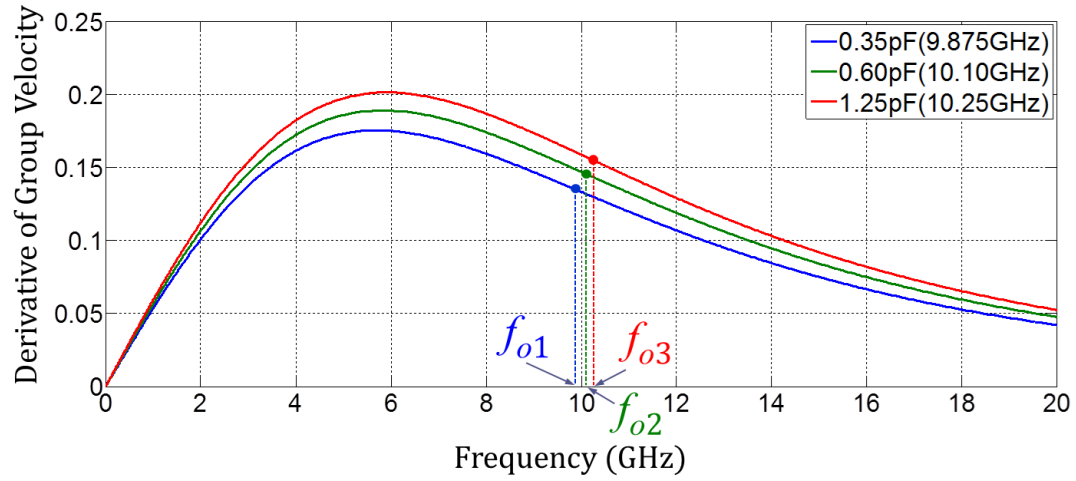


Figure 2-28. The derivative of group velocity diagrams of the OmSRR unit cell integrated with three different capacitances.

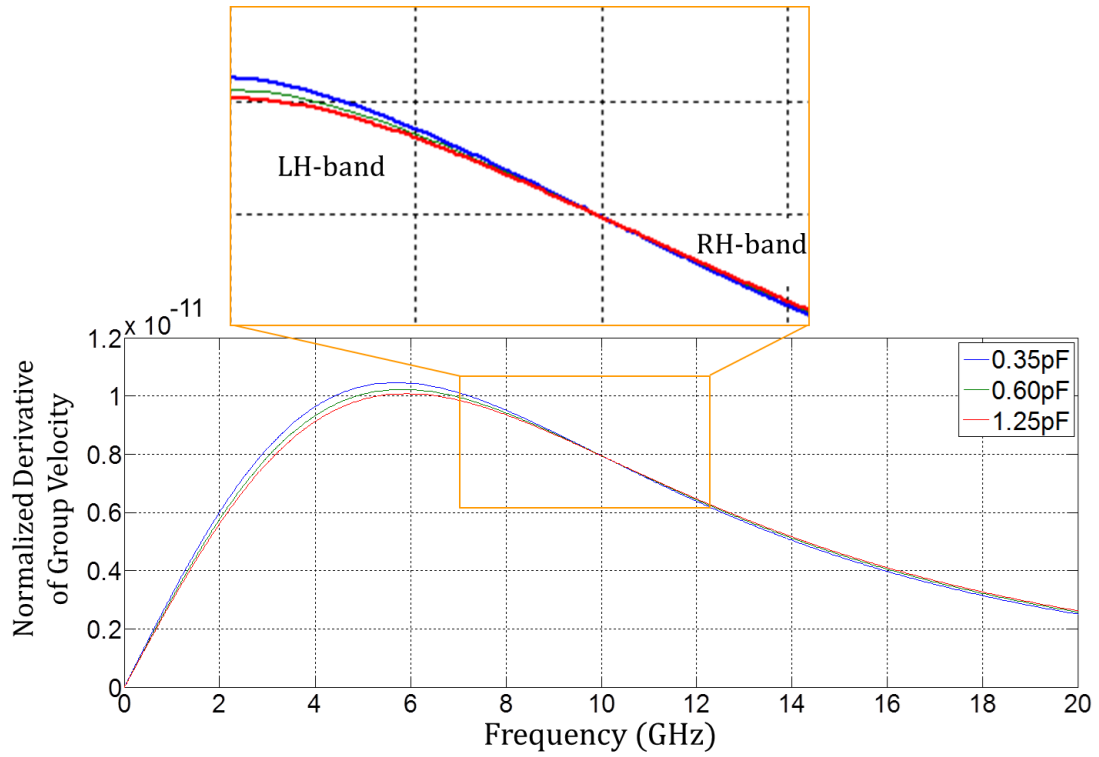


Figure 2-29. The normalized derivative of group velocity diagrams of the OmSRR unit cell integrated with three different capacitances.

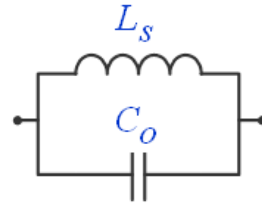
CHAPTER 3

METAMATERIAL INSPIRED POWER DIVIDER

A new metamaterial (MTM) unit cell based microstrip technology has been proposed, and implemented [34], [35]. The proposed MTM unit cell allows ease of integration of active devices (varactor diodes) and leads to design of novel microwave circuits. Moreover, the unit cell requires only single level metal patterning and avoids the use of vias. By incorporating varactor diodes, the electrical characteristics of the unit cell can be electronically reconfigured through dc voltage tuning. This impedes signal propagation in the proximity of the resonant frequency. A novel compact X-band power divider with reconfigurability and unequal power dividing feature is designed to validate practical uses of the new unit cell.

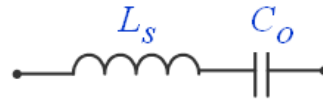
3.1 A Novel Metamaterial Structure Based Microstrip Technology

A novel metamaterial (MTM) unit cell, based on split ring resonators (SRRs, Figure. 3-1(a)) and open split ring resonators (OSRRs, Figure. 3.1(b)), is presented. The new MTM unit cell is implemented in a microstrip transmission line configuration with tuning elements. Unlike SRR- or OSRR- configurations (Figure. 3-1) conventionally used in microstrip circuitry [9-11], [21-24], a novel structure fabricated only on a single layer at the edge of the microstrip directly connected to the conductor strip (Figure. 3-2) is proposed here. Reconfigurability, miniaturization, and simple fabrication are key novel aspects of these structures.



(a)

Ground plan window



(b)

Figure 3-1. Topologies of the metamaterial structures and their equivalent circuit models (a) split ring resonator (SRR), (b) open split ring resonator (OSRR).

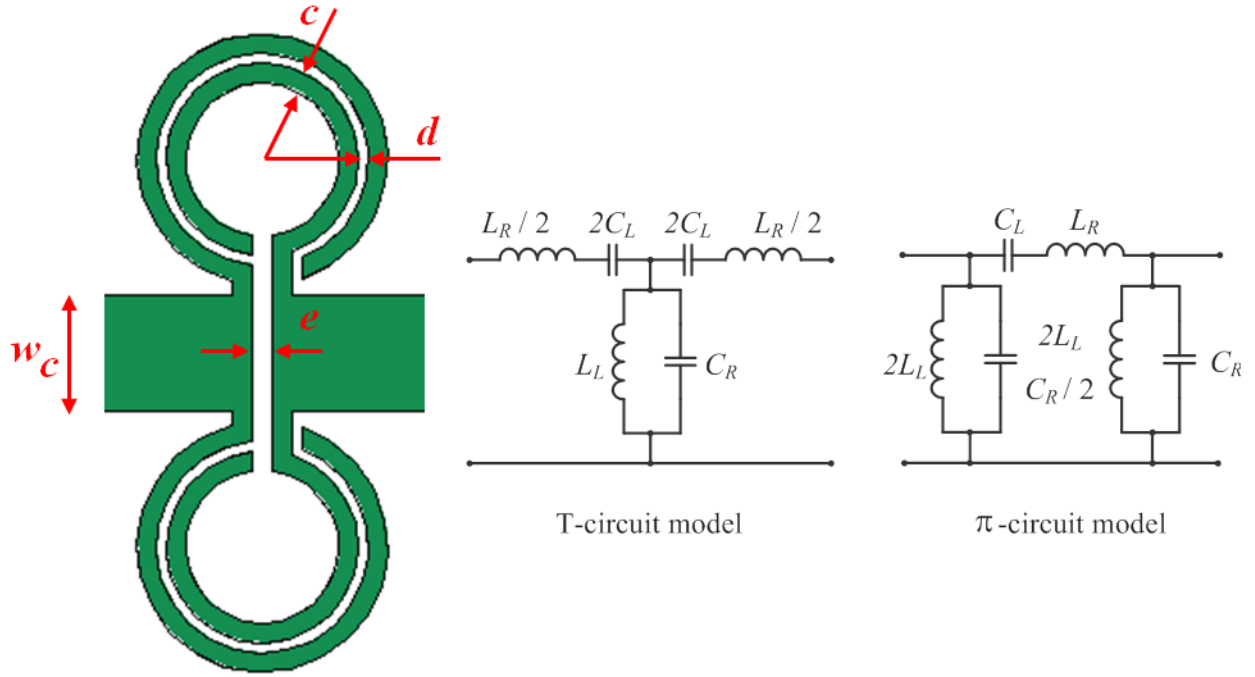


Figure 3-2. Topology of the new MTM unit cell and its equivalent circuit model. This structure avoids the use of vias, and requires only single level fabrication (ground plane is solid).

There are two essential characteristics of MTM transmission lines desirable for the design of the next generation of RF and microwave devices. The first one is compact in size, which opens the possibility of miniaturization of highly integrated microwave circuits. The second one is reconfigurability of electrical characteristics such as the characteristic impedance, Z_B and the electrical length, βl . Reconfigurability is dictated by the physical layout and the use of tunable elements. Conceptually, the implementation of the new MTM unit cell is resonant and its structure is highly dispersive. The physical layout and its equivalent model are shown in Figure 3-2. For the T-circuit model, the image impedance (characteristic impedance, Z_B) and the dispersion relation are respectively given by [11], [30].

$$Z_B(\omega) = \sqrt{Z_s(\omega)[Z_s(\omega) + 2Z_p(\omega)]} \quad (3-1)$$

$$\cos\beta l = 1 + \frac{Z_s(\omega)}{Z_p(\omega)} \quad (3-2)$$

where βl is the electrical length of the structure. $Z_s(\omega)$ and $Z_p(\omega)$ are the series and shunt impedances of the T -circuit model, respectively. Whereas for the π -circuit, the characteristic impedance is given as follows:

$$Z_B = \sqrt{\frac{Z_s(\omega)Z_p(\omega)/2}{1 + \frac{Z_s(\omega)}{2 \cdot Z_p(\omega)}}} \quad (3-3)$$

The possibilities of controlling the electrical characteristics (βl and Z_B) of the unit cell play a key role in the design of RF/microwave devices. For a specific operating frequency, the unit cell can be designed to provide desired values of phase and impedance [11-12]. As long as the dispersion relation and image impedance are controllable, such lines could be labeled as MTM transmission lines regardless of the number of unit cells.

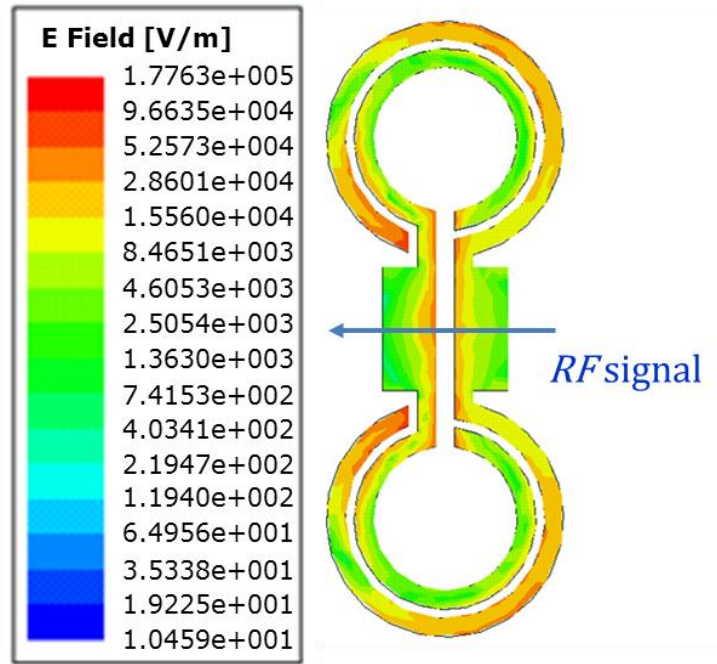
3.2 Compact Power Splitter Design and Reconfigurability

A novel MTM unit cell inspired microstrip transmission line is depicted in Figure 3-2. The series gap is added with the conductor strip in order to increase left handed wave propagation in the transmission band. To incorporate reconfigurability, the unit cell can be loaded with a varactor diode allowing design of novel microwave circuits as discussed later. Since the unit cell is based on OSRRs, the lumped element equivalent circuit model is a series resonant tank as

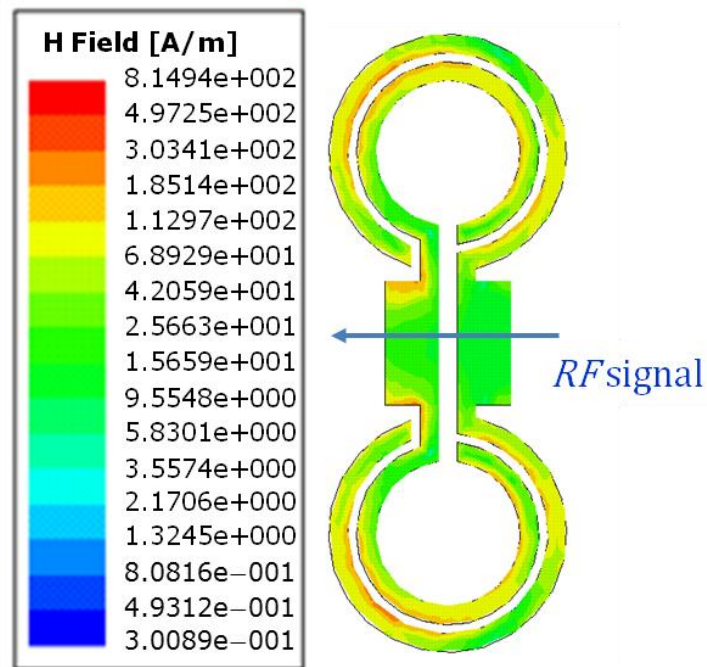
described in [9]. The equivalent capacitance can be further obtained from the edge capacitance of a disk of radius, d , surrounded by a conductor strip at a distance r_o from its edge [9], [13]. In practice, a varactor diode can be placed at the microstrip gap, on the top of the unit cell while conveniently eliminating the need for extra pads. As a result, the proposed unit cell can be implemented easily in the miniaturization and reconfigurability of various RF and microwave circuits.

To validate the proposed design, Finite Element Modeling (FEM analysis by Ansoft HFSS) was utilized. Rogers RO3010 substrate ($\epsilon_r = 10.2$ and thickness $h = 1.27$ mm) was used in the simulation. Relevant dimensions for the proposed unit cell are: ring width $c = 0.2$ mm, distance between the rings $d = 0.1$ mm, internal radius $r_o = 0.98$ mm, central strip width $W_c = 1.325$ mm, and width of the slot e or the series gap = 0.2 mm. Figure 3-4 shows simulated field overlays on the proposed MTM structure along with the microstrip connections.

As expected, loading the line with series gap leads to high pass frequency response. Moreover, the stop band is related to the presence of a transmission zero that nulls the shunt reactance and results in maximum rejection. The stop band can also be interpreted as owing to the high effective permittivity of the structure in the vicinity of the transmission zero. This is positive to the left side of the transmission zero and it is negative between the frequency at the transmission zero and the resonant frequency of the unit cell [13-15], [36-39]. For a homogeneous structure increased series capacitance, the stop band behavior can be switched to a pass band with left-handed wave propagation in the transmission band. For this phenomenon, it is essential that the resonance of the series branch should be higher than the resonance frequency of the shunt tank [13-15]. The results of this design were first presented in ref. [16].



(a)



(b)

Figure 3-3. Simulated fields overlays on the proposed unit cell by Ansoft HFSS ®,(a) electric field (b) magnetic field.

3.2.1 A Novel Metamaterial Structure Based Microstrip Technology

A power divider is a simple three-port network that can be used for power division, power combination, and other applications. In this work, the power divider is implemented by means of a 90° impedance inverter. The basic topology of the power divider is illustrated in Figure 3-4. In conventional design approaches, a simple transmission line is used to make the impedance inverter, requiring $\beta l = 90^\circ$. The goal here is to design this section using the proposed unit cell. The desired characteristic impedance of this branch is given by the following [12, 40].

$$Z_B = Z_o / \sqrt{2}, \quad \text{for (a)} \quad (3-4)$$

$$Z_B = \sqrt{2} \cdot Z_o \quad \text{for (b)}$$

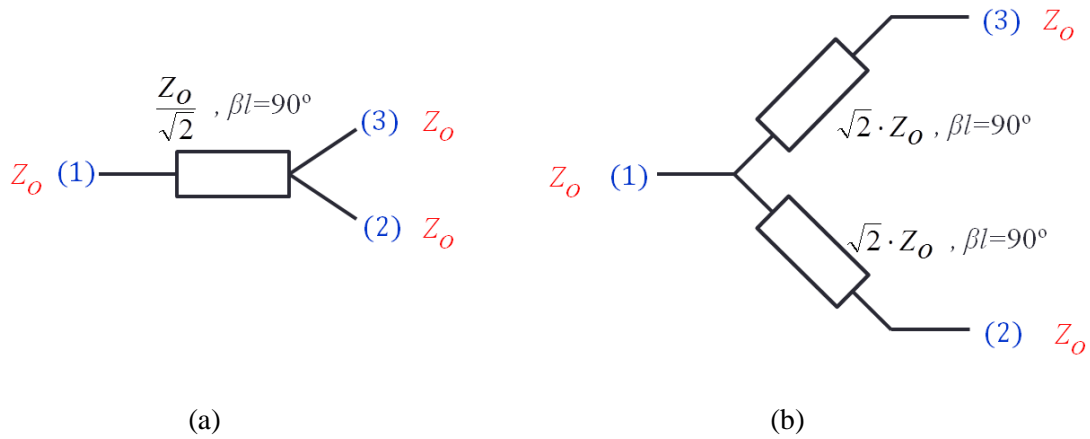


Figure 3-4. Basic topology for a power divider with 90° impedance inverter.

According to Equation (3-1) through (3-3), the characteristic impedance of the 90° impedance inverter is set to certain values over a certain frequency band. For the T -branch, the series and shunt impedances must satisfy the following [17]:

$$Z_S = Z_B \sqrt{(\cos\beta l - 1)/(\cos\beta l + 1)} \quad (3-5)$$

$$Z_P = Z_B / \sqrt{(\cos^2\beta l - 1)} \quad (3-6)$$

and for the π -circuit [17],

$$Z_S = Z_B / \sqrt{(\cos^2\beta l - 1)} \quad (3-7)$$

$$Z_P = Z_B \sqrt{(\cos\beta l + 1)/(\cos\beta l - 1)} \quad (3-8)$$

3.2.2 A Novel Metamaterial-Inspired Reconfigurable Power Divider

Based on this analysis, a power divider was designed using the proposed unit cells. It was designed to achieve 50- Ω input and output impedances. The overall goal is to reduce the quarter wavelength of the impedance inverter while maintaining its electrical characteristics. After optimization, the power divider based approach is depicted in Figure 3.5. This device is compatible with active device integration such as varactor diodes and in turn leads to reconfigurable circuits. Furthermore, a slit (100 μm) is added on the impedance inverter for controlling capacitance independently in each varactor diode. Difference capacitance values in each varactor diode come from asymmetric biasing feature in the circuit. Consequently, reconfigurability with unequal power dividing can be achieved also for this device.

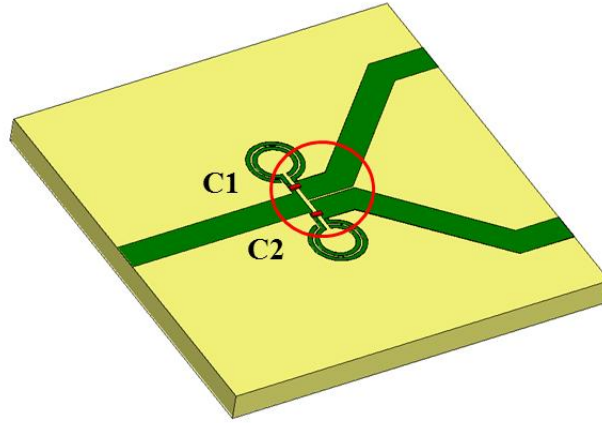
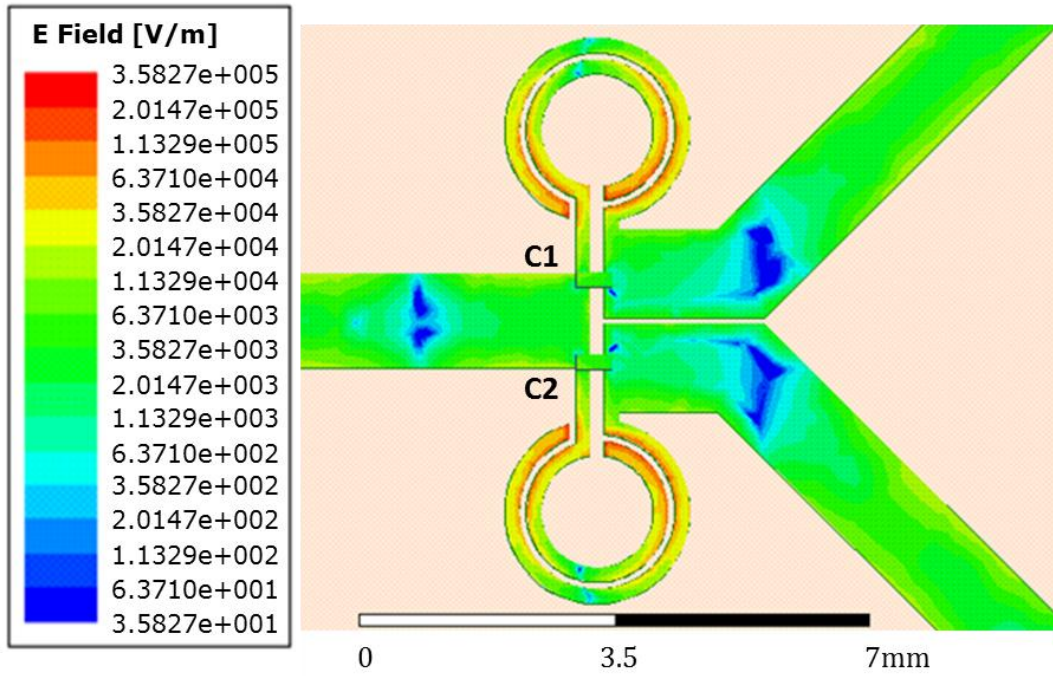
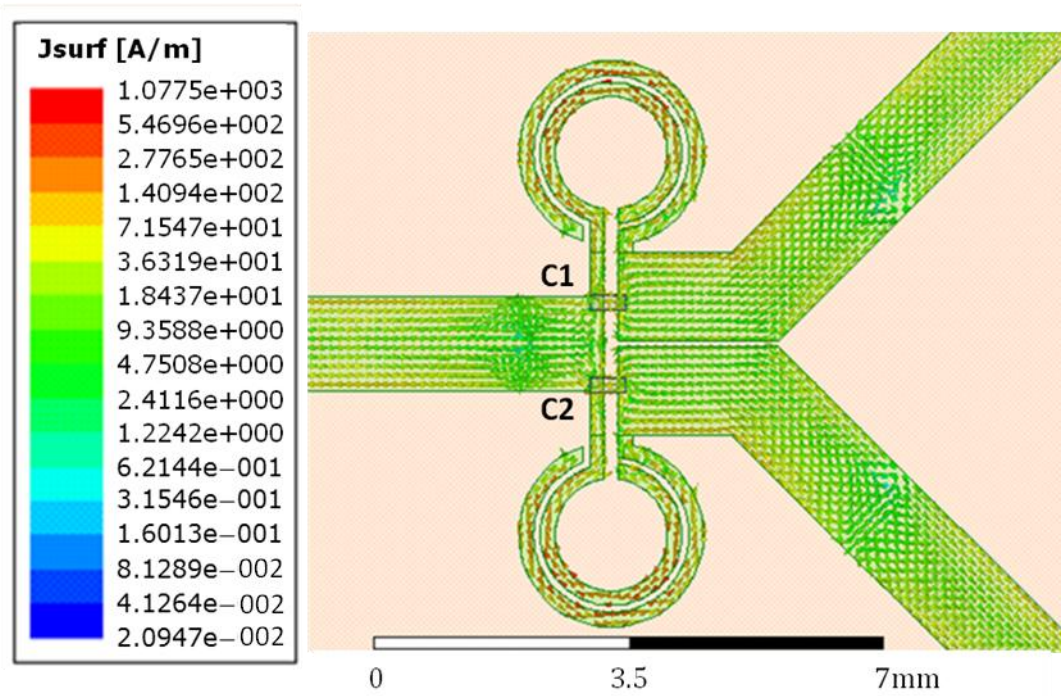


Figure 3-5. The novel MTM unit cell inspired power divider with reconfigurability and unequal power dividing features.

The novel reconfigurable power divider was analyzed using Ansoft HFSS® (3D finite element modeling). Because of the MTM transformer, the length of the quarter-wave impedance inverter can be reduced while maintaining its main properties. It means circuit miniaturization can be achieved when compared to the conventional design. For the feasibility of circuit reconfigurability, simulation overlays on the proposed unit cell inspired power divider by HFSS® are expressed in Figure 3-6. Figure 3-6 (a) and (b) show the simulated electric field and current surface density on the proposed power divider when the capacitance $C1$ is equal to $C2$. The simulated results show the equality mode of the circuit. On the other hand, when the capacitance $C1$ is unequal to $C2$ (such as $C1 > C2$), the unequal power dividing mode may be expressed from the circuit. This phenomenon can be confirmed by the simulated electric field and current surface density on the circuit as shown in Figure 3-7 (a) and (b). If the capacitance $C1$ is more than $C2$, the power will transfer to the lower output port more than the upper one.

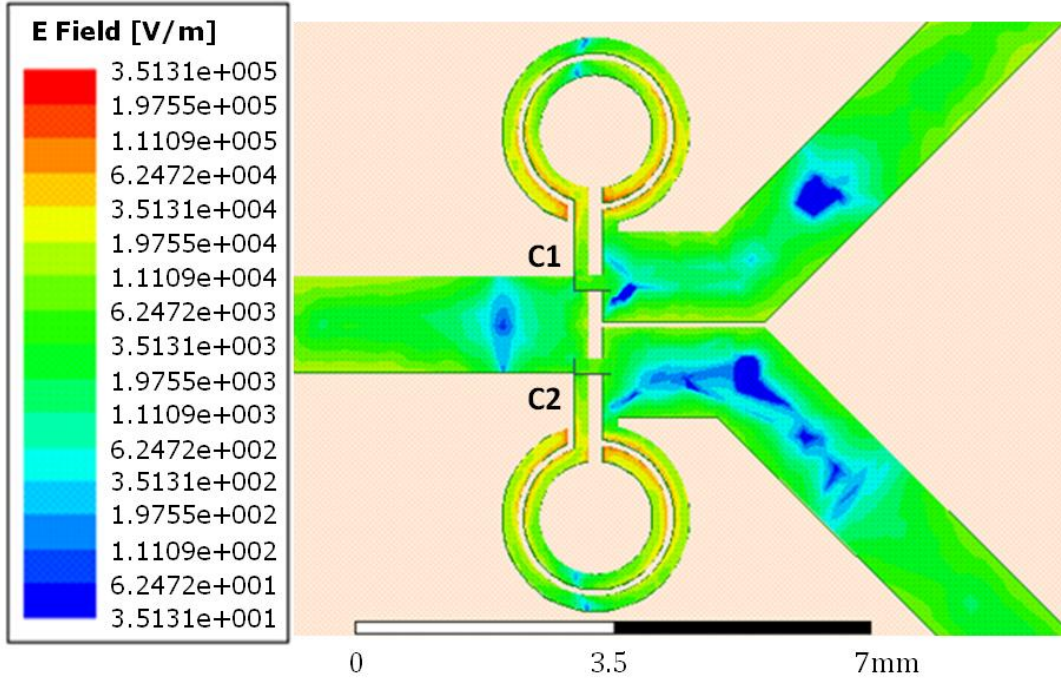


(a)

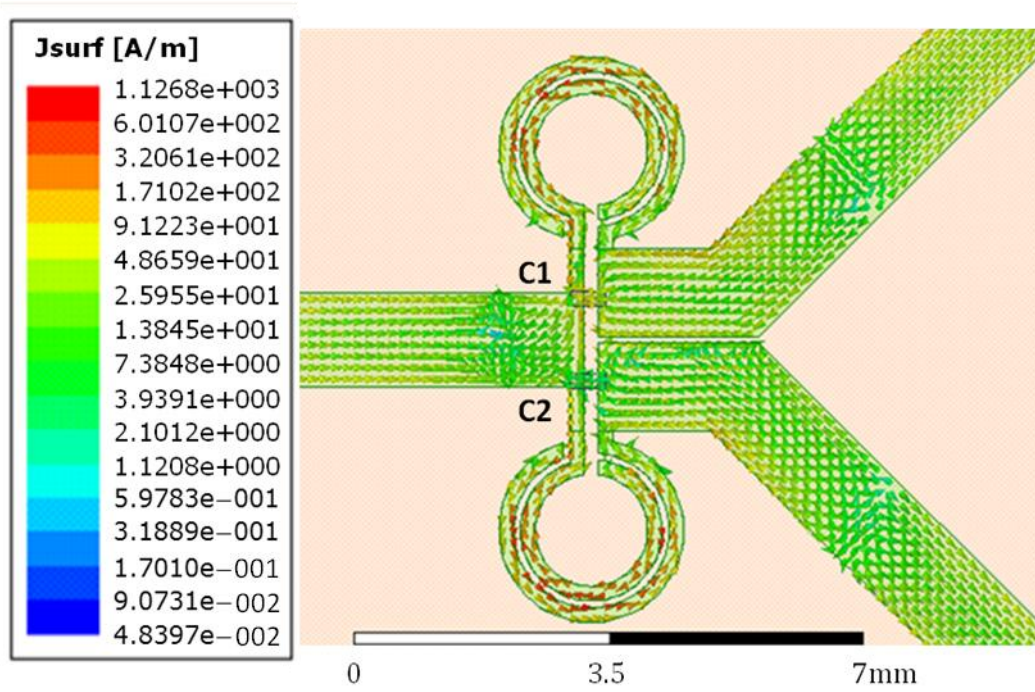


(b)

Figure 3-6. Simulated fields overlays on the proposed unit cell inspired power divider by Ansoft HFSS, (a) electric field (b) magnetic field, when $C1 = C2$.



(a)



(b)

Figure 3-7. Simulated fields overlays on the proposed unit cell inspired power divider by Ansoft HFSS,(a) electric field (b) magnetic field, when $C1 > C2$.

3.3 Fabrication and Experimental Results

Detailed experimental measurements were carried out to validate the proposed circuit. Photolithographic techniques have been used to fabricate a prototype circuit based microstrip technology. Figure 3-8 shows the prototype of the novel unit cell inspired reconfigurable power splitter. To implement reconfigurability, the power divider is integrated with two varactor diodes as shown in Figure 3-8. Hyper-abrupt junction tuning varactors, SMV2019-079LF from Skywork [41] were used for resonance tuning. The varactor diodes are used in voltage-controlled oscillators requiring tight capacitance tolerances. Low series resistance of the varactor is also appropriate for high-Q resonators in the unit cell circuit. Furthermore, the devices exhibit a high capacitance ratio with result in a wide tuning range. The SMV2019-079LF capacitance value decreases from 2.2 pF to 0.30 pF when reverse biasing from 0-20 V. A diagram showing how the dc bias voltage of the circuit provided is also shown in Figure 3-8. The plus-polarity of each voltage source, V1 and V2, is clearly separated by the 100 μm -slit between port 2 and port 3. However, the voltage sources have still the same common ground. As a result, the capacitance C1 and C2 could be equal or unequal by independent dc bias control. The experiments of the novel reconfigurable power divider are set up into equal and unequal power dividing features as described in the next two sections.

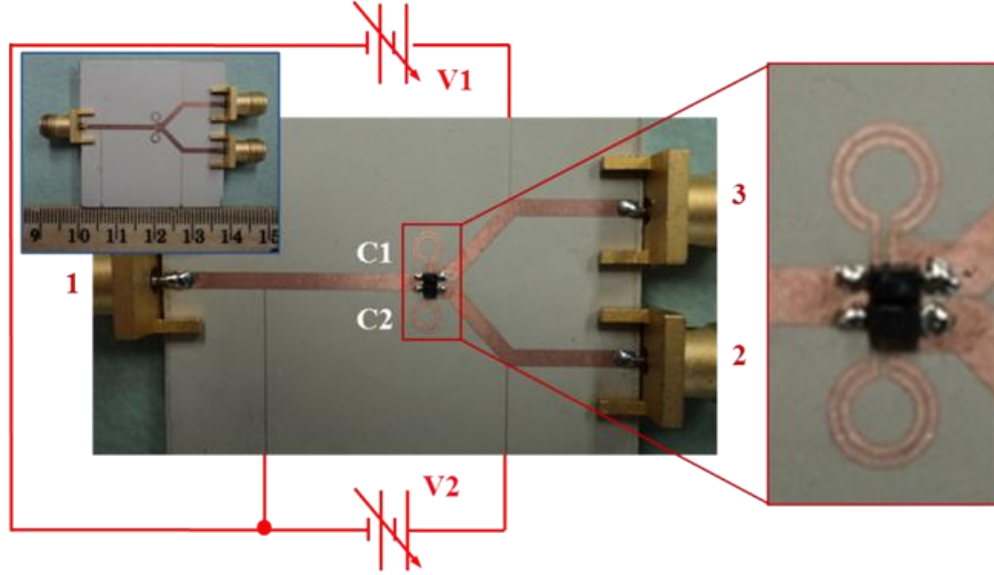


Figure 3-8. Photograph of the fabricated novel MTM unit cell inspired reconfigurable power divider. (inset-right) Zoom-in for the proposed unit cell, integrated with the varactor diodes clearly visible in the circuit. (inset-left) Actual dimension of the prototype before varactor diode integration.

3.3.1 Reconfigurability with Equal Power Division

For validate the reconfigurability of the proposed circuit, the varactors are supplied by the different reverse dc biases. The resonance frequency expresses a strong dependence on the bias voltage. To keep the equal power dividing, the voltage sources V1 and V2 must be equal. As the reverse bias increases from 0 to 20 V, the capacitance of the varactors decreases and the resonance frequency experiences a shift from 8.92 to 8.78 GHz. The bandwidth at -15 dB return loss is 0.5 GHz at 0 V reverse bias, and decreases to 0.41 GHz at 20 V reverse bias. The power at the output of each port shifts approximately -5.5 to -3.5 dB. The slightly higher loss value at the low reverse dc bias is attributed to improper capacitances of the varactors in the circuit. Moreover, the loss accounts for inaccuracies in fabrication, substrate properties, and connectors. Table I shows the essential scattering parameters from the experiment. The measured scattering

characteristics (return and insertion losses) for the proposed power divider at different dc biases are illustrated in Figure 3-9 and 3-10.

Table 3-1 Essential Scattering Parameters for Equal Dividing

Reverse bias (V)	0	1	5	7	10	15	20
Capacitance (pF)	2.22	1.51	0.66	0.48	0.38	0.32	0.30
S11 (dB)	-30	-33	-36	-27	-23	-22	-21
S21, S31 (dB)	-5.5	-5.5	-4.5	-4.1	-4	-3.5	-3.5
f_c (GHz)	8.92	8.91	8.89	8.87	8.85	8.80	8.78
B.W. @-15dB. (GHz)	0.50	0.50	0.47	0.46	0.45	0.41	0.41

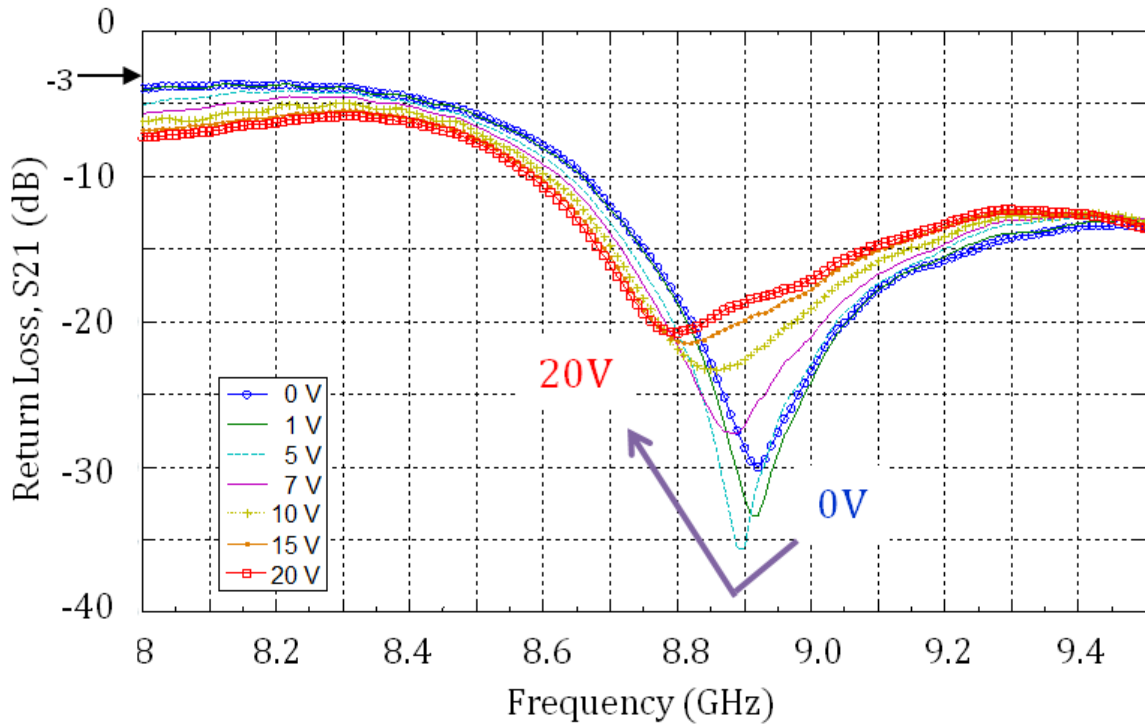


Figure 3-9. Measured return loss, S11 of the proposed unit cell inspired reconfigurable power splitter based equal mode.

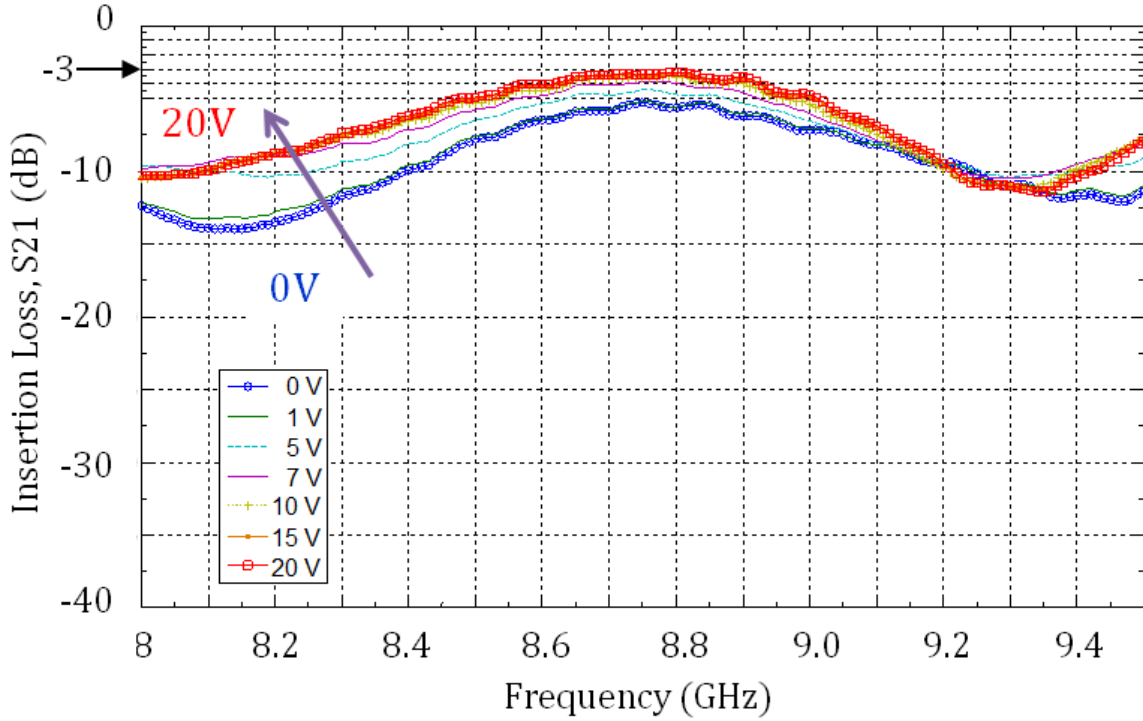


Figure 3-10. Measured insertion loss, S21 and S31 of the proposed unit cell inspired reconfigurable power splitter based equal mode.

3.3.2 Reconfigurability with Unequal Power Division

For unequal power division in the proposed circuit, the dc voltage source V1 and V2 are set to different values. For the experiments, the dc bias sources, V1 is set to a constant value, 0 V and V2 varies from 0 to 20 V. This causes the capacitance of the varactor C1 to be constant at 2.22 pF, as the capacitance of the varactor C2 varies from 2.22 to 0.30 pF. As the capacitance C2 decreases, the resonance frequency shifts from 8.92 to 8.83 GHz. Because of the different capacitances of the varactors, power transferred to the lower capacitance side of an output port is more than the power transferred to the higher capacitance. A maximum power transfer difference of 4.5 dB between the output ports can be achieved from the experiment. Table 3-2 shows the essential scattering parameters for unequal dividing experiment. The measured scattering characteristics (return and insertion losses) for the proposed reconfigurable power divider with

unequal power division are illustrated in Figure 3-10, 3-11, 3-12, and 3-13 related with the capacitance of the varactor C2 is 0.98, 0.38, 0.32, and 0.30 pF, respectively.

Table 3-2. Essential Scattering Parameters for Unequal Dividing

Reverse bias (V)	0	3	10	15	20
Capacitance (pF)	2.22	0.98	0.38	0.32	0.30
S11 (dB)	-30	-36	-34	-35	-41
S21 (dB)	-5.5	-5	-2.5	-2.5	-2.5
S31 (dB)	-5.5	-6	-7	-6.5	-6.5
f_c (GHz)	8.92	8.91	8.87	8.80	8.78
B.W. @-15dB. (GHz)	0.50	0.45	0.43	0.44	0.43

*C1 is constant at 2.22 pF @ 0V reverse bias

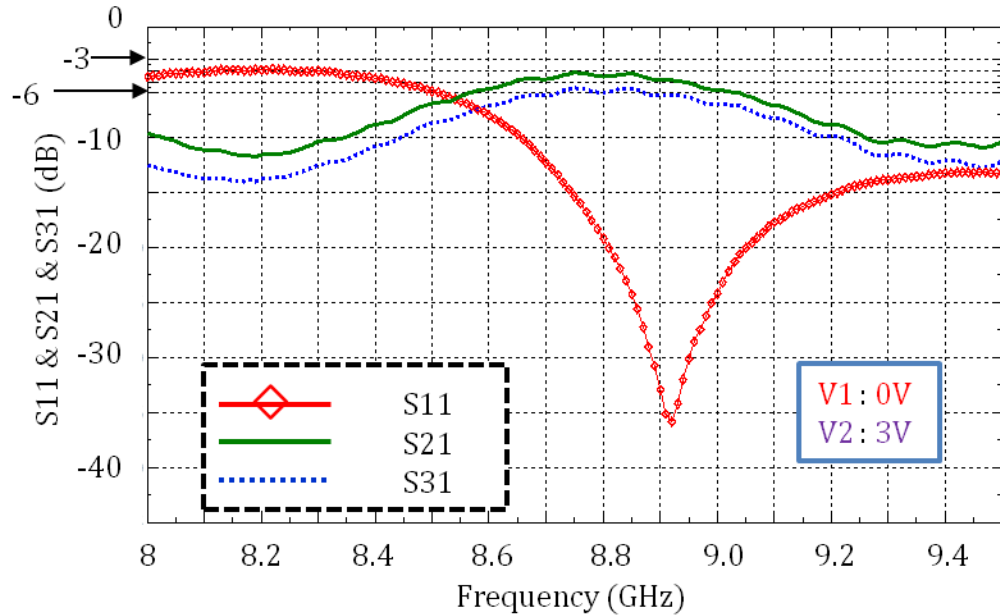


Figure 3-11. Measured scattering responses of the proposed unit cell inspired reconfigurable power splitter based unequal mode at C1 = 2.2 pF, C2 = 0.98 pF.

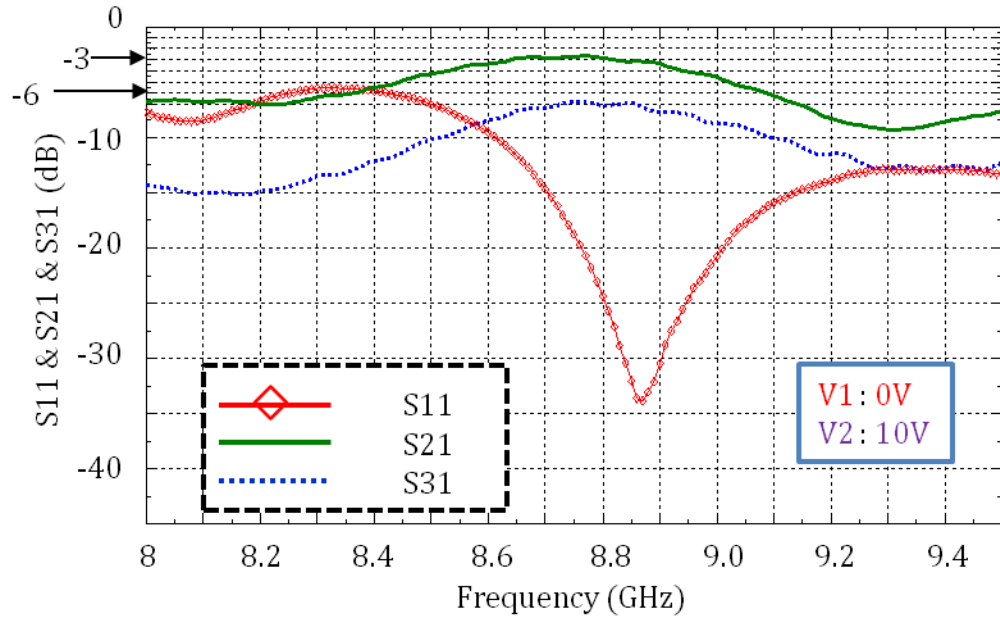


Figure 3-12. Measured scattering responses of the proposed unit cell inspired reconfigurable power splitter based unequal mode at $C1 = 2.2$ pF, $C2 = 0.38$ pF.

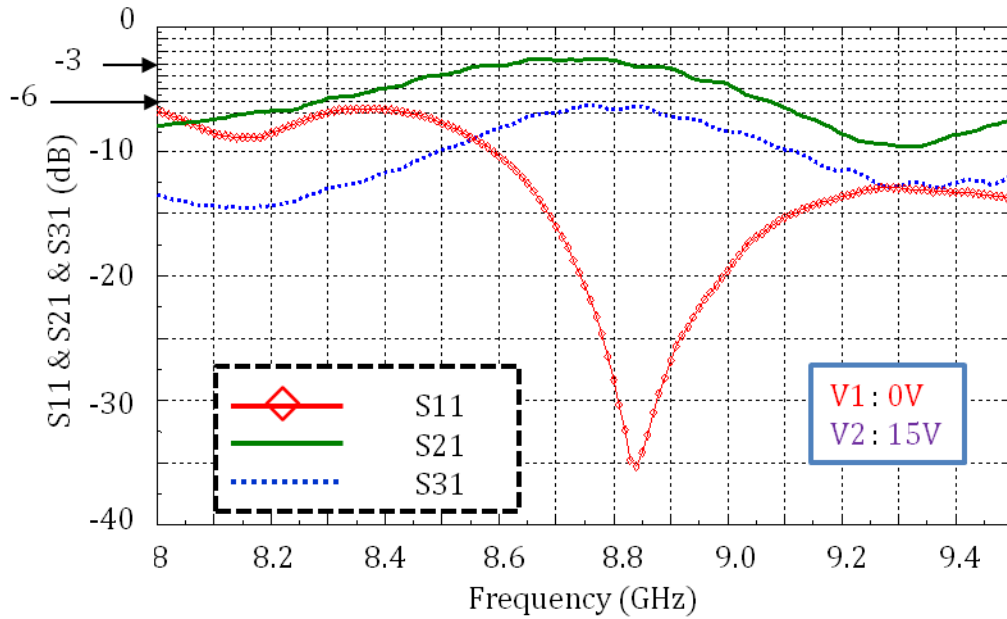


Figure 3-13. Measured scattering responses of the proposed unit cell inspired reconfigurable power splitter based unequal mode at $C1 = 2.2$ pF, $C2 = 0.32$ pF.

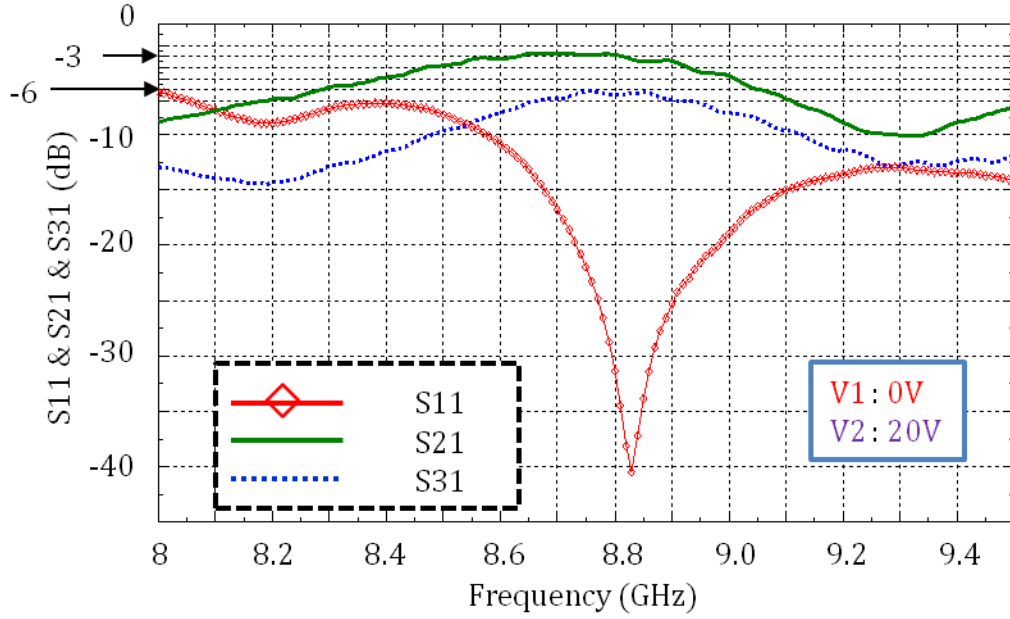


Figure 3-14. Measured scattering responses of the proposed unit cell inspired reconfigurable power splitter based unequal mode at $C1 = 2.2$ pF, $C2 = 0.30$ pF.

3.4 Conclusion

A novel reconfigurable metamaterial unit cell inspired unequal power divider design is proposed and implemented. Based on microstrip technology, the proposed unit cell requires only simple photolithographic techniques and single level metal patterning. The unit cell is compatible with integration of active devices, especially surface mount technology that allows design of novel microwave circuits. A compact X-band reconfigurable power divider is designed to validate the practical use of the new unit cell. The reconfigurable power divider has demonstrated a center frequency tuning capability of 140 MHz for equal power transferred condition. A maximum power transfer difference of 4.5 dB between the output ports can be achieved, when the capacitance of varactors $C1$ and $C2$ are 2.22 pF and 0.38 pF respectively. The performance of the circuit is limited by inaccuracies in fabrication, substrate properties,

connectors, and varactor diode packaging. In future experiments, unpackaged varactors will be implemented to improve the performance and efficiency of the circuit. Overall, the proposed novel MTM unit cell can be implemented in the miniaturization and reconfigurability of various RF and microwave circuits.

CHAPTER 4

METAMATERIAL-INSPIRED PHASE SHIFTER DESIGN

A novel reconfigurable phase shifter utilizing CRLH TL inspired MTMs is designed and demonstrated for X-band (7-12.5 GHz) applications utilizing cells presented in refs. [34-35]. These unit cells are designed for LH properties of CRLH TL. Unlike split ring resonator (SRR)- or open split ring resonator (OSRR)- configurations [10-12], each unit cell structure is connected directly to the edge of the microstrip TL. Layouts of modified split ring resonator (mSRR), and modified split ring resonator with open-gap (OmSRR) are shown in Figure 4-1(a) and (b), respectively. Both of these layouts utilize microstrip design with a solid ground plane. This structure is attractive as it allows seamless integration of active devices within the unit cell design. Reconfigurability, miniaturization, and simple fabrication process as one-side metal patterning are the key attractive aspects of these structures.

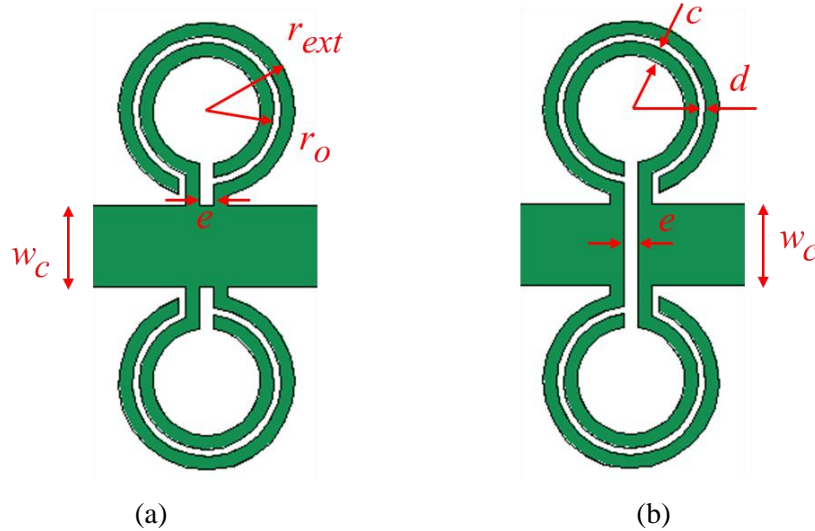


Figure 4-1. Physical layouts of the proposed MTM unit cell for phase shifter application, (a) modified split ring resonator (mSRR), (b) modified split ring resonator with open-gap (OmSRR).

4.1 Network Parameter Analysis

Based on microstrip technology, the proposed unit cells as shown in Figure 4-1 are designed at 10GHz using Finite Element Modeling (FEM)-analysis using commercial design tool, Ansoft HFSS®. Commercially available *Rogers* RO3010 substrate with dielectric constant $\epsilon_r = 10.2$ and thickness $h = 1.27$ mm is used for the circuit design. By tuning and optimizing physical dimensions of the structures, two 50 Ω CRLH TLs are designed and their relevant dimensions are as follows: ring width $c = 0.2$ mm, distance between the rings $d = 0.1$ mm, internal radius $r_o = 0.98$ mm, main microstrip line width $w_c = 1.2$ mm, and slot width $e = 0.2$ mm. The dispersion relations and equivalent circuits of the proposed unit cells, mSRR and OmSRR are shown in Figure 4-2 and 4-3, respectively. The balanced mode of CRLH transmission line and the impedance matching condition are satisfied. The stopband is closed. RH passband and LH passband are continuous. For the left-handed passband, the MTM unit cell without a gap or mSRR unit cell is obtained from 7.5 to 10 GHz and the MTM unit cell with open-gap (OmSRR) is useful from 11 to 14 GHz. It is also observed that at resonance frequency of each unit cell, the phase shift is 0 degree (approximately, mSRR unit cell at 10 GHz and OmSRR at 14 GHz). When the gap is designed to be part of the unit cell structure, the discrete lumped element components (L_o , C_o) of LH medium are decreases resulting in a higher resonance frequency. The possibility of electrically controlling the characteristic is the key point to using this type of unit cell leading to reconfigurable RF/microwave circuits. The gap plays a key role in the integration of the tuning element (varactor diode) within the unit cell to achieve desire properties with respect to phase, amplitude and group delay. As a practical realization of reconfigurability of RF circuits, a simple MTM phase shifter in X-band using the proposed unit cells was designed, simulated, fabricated and tested.

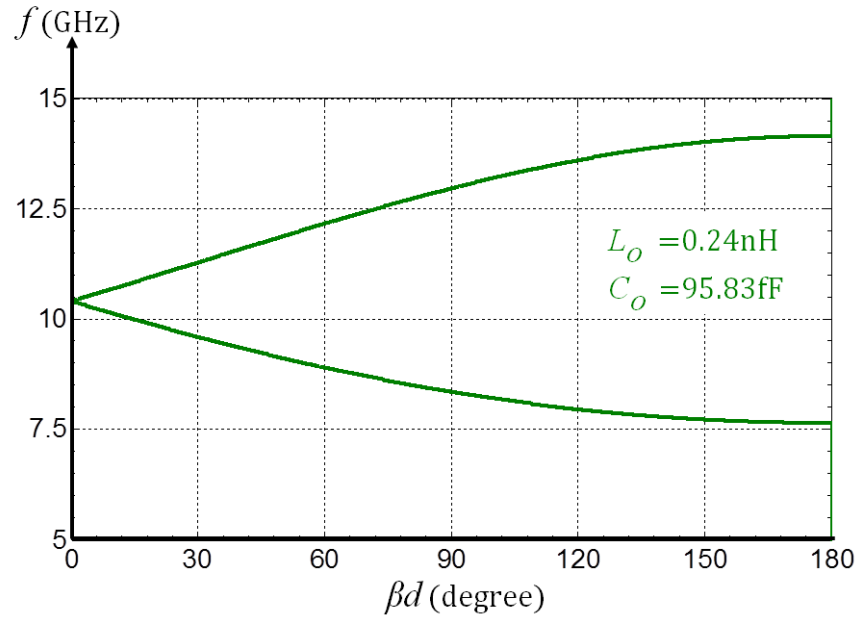


Figure 4-2. Dispersion relation of the mSRR unit cell (as shown in Figure 4.1(a)), (inset) the equivalent model of mSRR unit cell with LC -parameters.

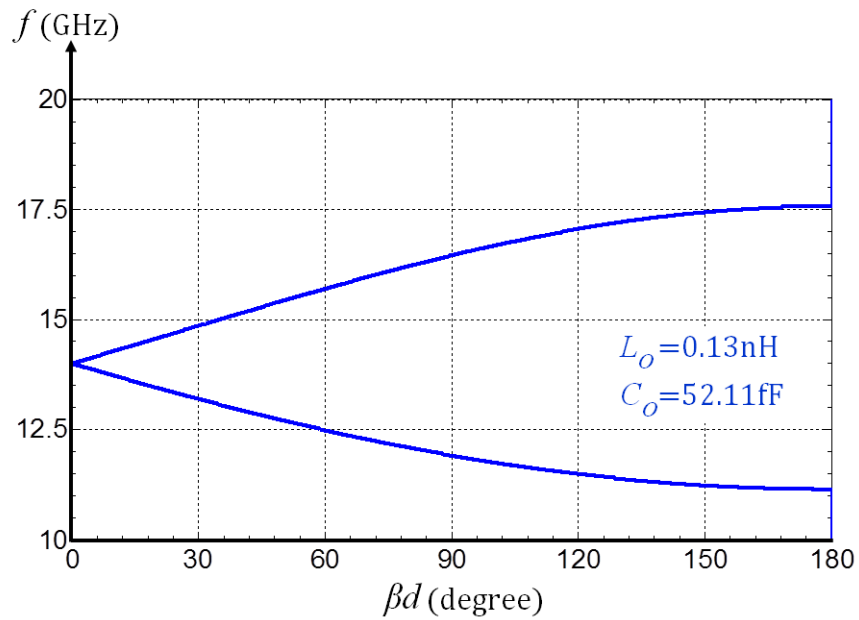


Figure 4-3. Dispersion relation of the OmSRR unit cell (as shown in Figure 4-1(b)), (inset) the equivalent model of OmSRR unit cell with LC -parameters.

4.2 Electrically Tunable Component

To achieve reconfigurability, a varactor diode is introduced in the unit cell as shown in Figure 4-4(a). A diagram of DC biasing is also shown. Voltage applied to a varactor translates into a change in capacitance of the diode. A change in capacitance of the varactor diode results in a variation on effective capacitance C'_o of LHM. Consequently, the dispersion relation of the MTM unit cell is reconfigurable. The equivalent circuit of the unit cell with integrated varactor diode is demonstrated in Figure 4-4(b). A Hyperabrupt junction tuning varactor type, SMV1430-079LF from Skywork, was used in the design for resonance tuning. Based on SMV1430-079LF data sheet [43], the device exhibits a high capacitance ratio which is necessary for wide range tuning. The capacitance can be changed from 1.24pF to 0.31pF when supplied reverse bias changes from 0V to 30V. Parasitic parameters of the varactor diode are as follows: a parasitic resistance value (R_s) is 3.15 Ω , a package capacitance value (C_p) is 0.13 pF, and a parasitic inductance (L_s) is 0.7nF. The package dimension of the varactor are 0.8mm x 1.6mm x 0.6 mm (width x length x height).

As shown in Figure 4-4(b), the effective capacitance C'_o of the LHM is varied by the varactor diode as it parallels with the discrete lumped elements (L_o , C_o) of the original OmSRR unit cell. The inherent capacitance C_o of the unit cell is much smaller than the capacitance of the varactor diode, the varactor diode capacitance thus dominates the effective capacitance of the circuit. According to Equation (2.11), the change of effective capacitance of the unit cell integrated with a varactor diode results in a shift in resonance towards lower side and it alters the dispersion relation. As long as the dispersion and characteristic impedance are controllable, such a CRLH transmission line could maintain continuity between RH pass band and LH pass band. The other type of unit cell (mSRR) is designed to be a cascade structure in the circuit since its

larger discrete lump elements at resonance frequency 10 GHz as shown in Figure 4-2. These parameters help the control dispersion relation over a wider frequency range. It also exhibits uniform performance or non-dispersive over such a wide band. Since the two unit cells have the same dimensional structure, periodic and symmetric circuit can be designed.

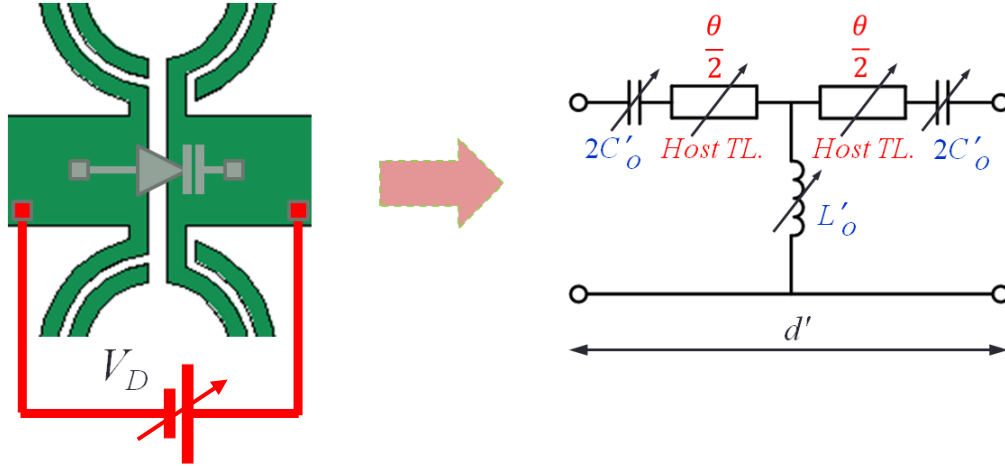


Figure 4-4. (a) The MTM unit cell with a varactor diode embedded in the structure, (b) its equivalent circuit model (assuming ideal varactor diode).

4.3 Simulated and Experimental Results

The reconfigurable X-band phase shifter, Figure 4-5, was designed and simulated using Ansoft HFSS®. A varactor diode is modeled and integrated within the OmSRR unit cell. Only the parasitic resistance ($R_S = 3.15 \, \Omega$) is included in this model. Through design optimization, two unit cells are placed at the distance $s = 4.05 \, \text{mm}$ from each other. This distance minimizes the interference between the unit cells, avoiding changes in their lumped element components (L_o , C_o). This simplifies the design and also leads to good matching over a wide frequency range. The distance is also optimized to achieve compact circuit layout. Figure 4-6 and 4-7 shows simulated electric field and vector surface current density overlays on the unit cells.

The simulated transmission and reflection coefficients of the reconfigurable X-band phase shifter are shown in Figure 4-8 and 4-9. The capacitance of the varactor diode model is changed in increment values to demonstrate the performances of the circuit. Using the zero bias capacitance of 1.24 pF as a reference (reverse bias voltage is zero). As expected, the simulated return loss (S_{11}) expresses two resonant peaks at 9.34 GHz and 10.5GHz at reference capacitance value. The higher resonance frequency is generated by mSRR unit cell and the lower resonance frequency results from OmSRR unit cell carrying a varactor diode. Forcing the discrete lump capacitance of the OmSRR unit cell to higher value leads to lowering of resonance frequency. Since the dispersion and characteristic impedance are controllable, RH-passband from the OmSRR unit cell continues with LH-passband from the mSRR unit cell exhibiting a wide bandpass range between two resonant frequencies. Figure 4-8 shows that a wide bandpass operation can be achieved from 8.85 to 11.9 GHz (at 10dB of $|S_{21}|_{dB}$).

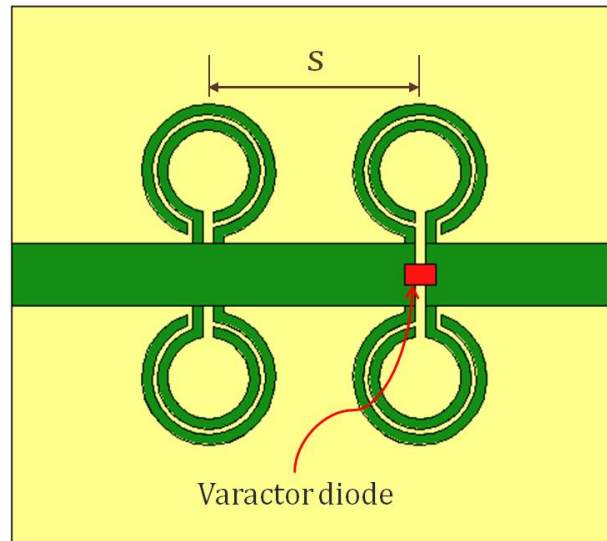


Figure 4-5. Proposed reconfigurable X-band phase shifter simulated using Ansoft HFSS.

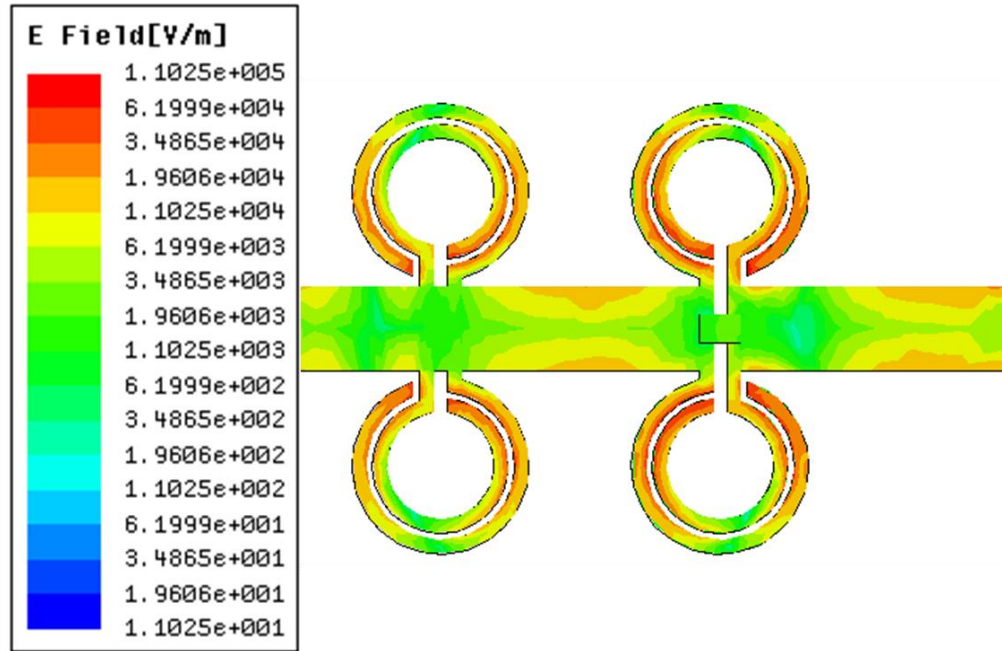


Figure 4-6. Simulated E-fields overlays at 10 GHz on the proposed reconfigurable X-band phase shifter MTMs simulated using Ansoft HFSS.

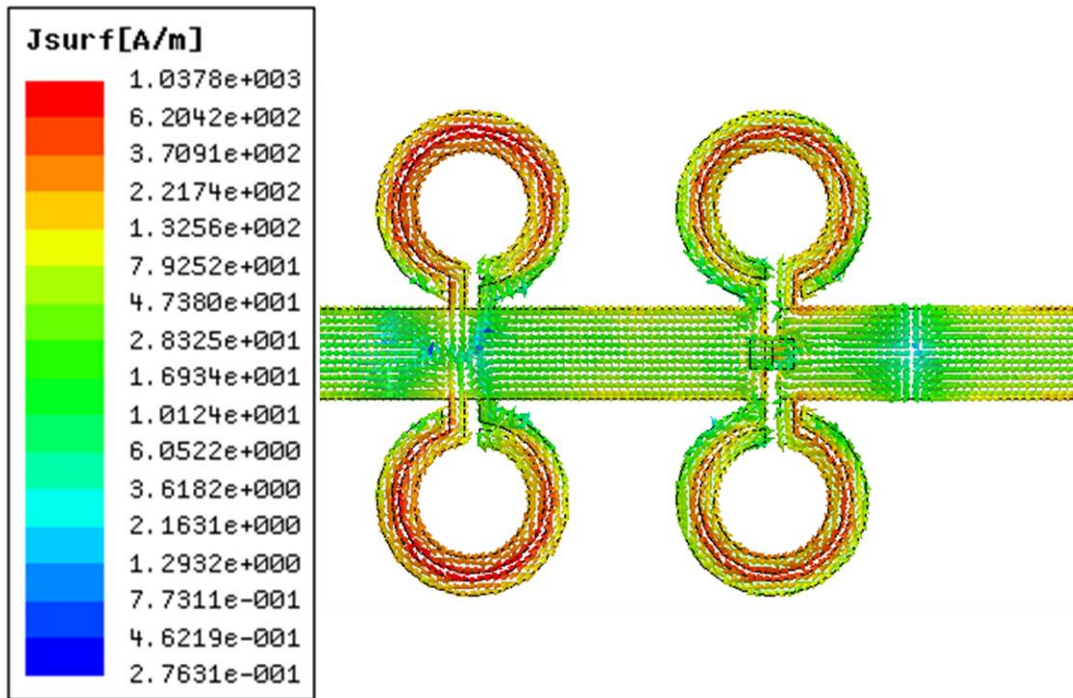


Figure 4-7. Simulated surface current density (Jsurf) overlays at 10 GHz on the proposed reconfigurable X-band phase shifter MTMs simulated using Ansoft HFSS.

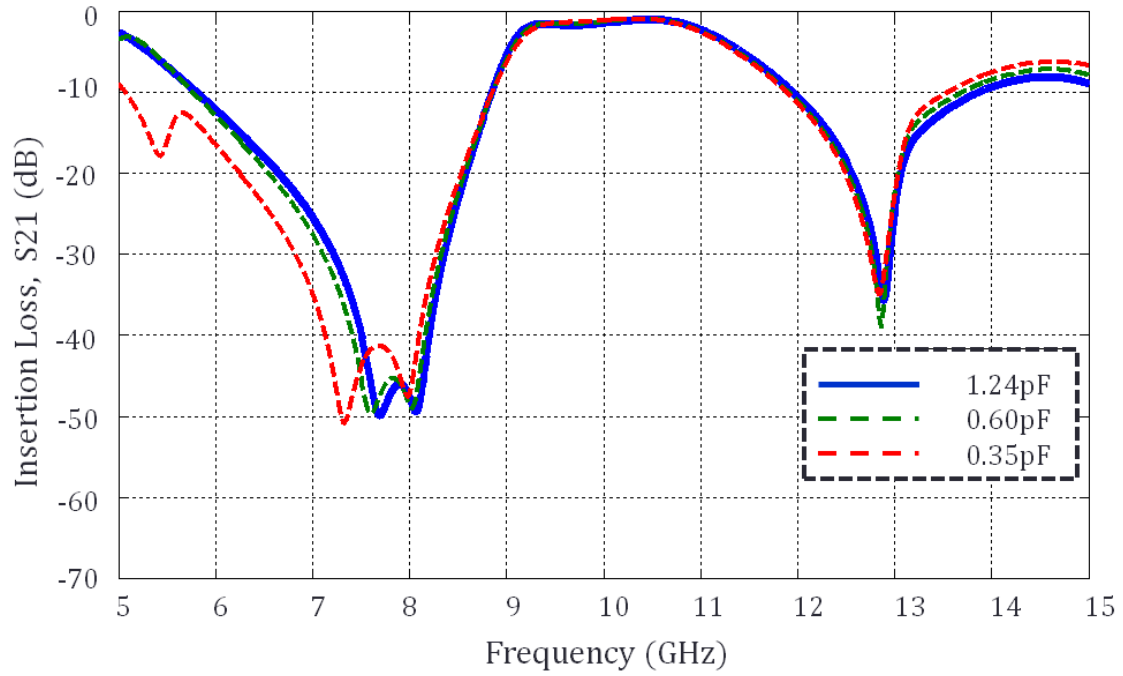


Figure 4-8. Simulated insertion loss, S_{21} (dB) of the reconfigurable X-band phase shifter.

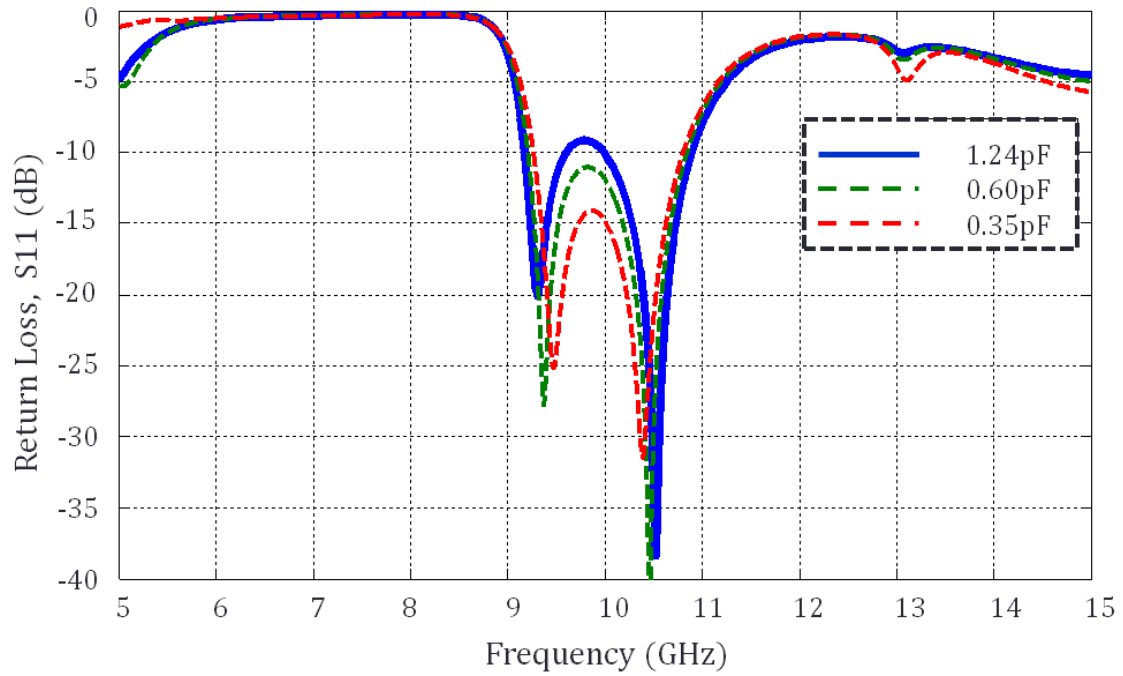


Figure 4-9. Simulated return loss, S_{11} (dB) of the reconfigurable X-band phase shifter.

Upon a decrease in capacitance the resonance frequency of the OmSRR unit cell increases as suggested by Equation. (2-11). Consequently, the lower resonant peak of the circuit is moved to the right side towards higher frequency. The characteristics of wide bandpass maintain good transmission characteristics. However, a change in resonance frequency leads to change in phase of the transmitted signal. This is a key attribute of the proposed X-band phase shifter that allows electronically phase tuning through dc biasing. It is important to note that the loss of transmission line from the simulation is approximately 1 dB. This is largely due to the parasitic resistance of the varactor diode and in part due the dielectric loss of the substrate.

The simulated insertion phase responses are shown in Figure 4-10. The operating frequency lies between 9.8 to 10.5 GHz it is designed to have a 0° insertion phase at 10GHz. It is clear that as the capacitance decreases the effective change in transmission phase is positive due to the LH-phenomenon. For each of capacitive values, the phase slope is close to linear and thus will have minimum dispersive effect on the transmitted signal.

The proposed X-band phase shifter structure was constructed using microstrip technology on a *Rogers* RO3010 substrate having $\epsilon_r = 10.2$ and dielectric height $h = 1.27\text{mm}$. Since it is one dimensional uniplanar structure, the circuit is simple to fabricate using conventional microfabrication. Measurements of S-parameter were carried out using a vector network analyzer. Figure 4-11 shows a fabricated reconfigurable X-band phase shifter. To achieve reconfigurability, a varactor diode is integrated within the unit cell as shown in blow-out of Figure 4-11.

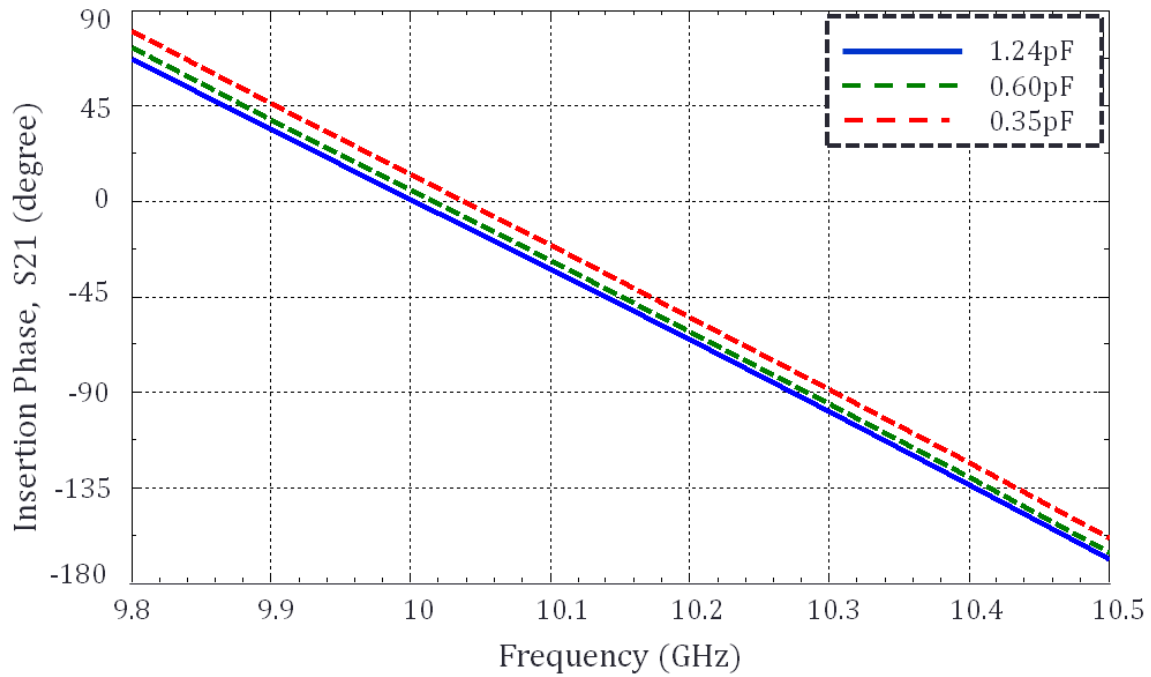


Figure 4-10. Simulated insertion phase responses with various capacitance values the MTM-inspired reconfigurable X-band phase shifter.

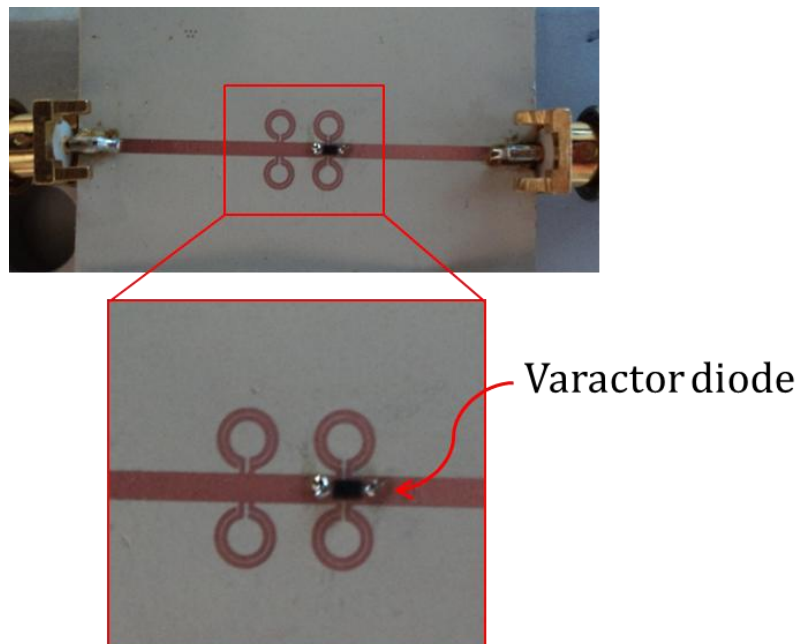


Figure 4-11. Photograph of a fabricated reconfigurable X-band phase shifter, (inset) a blow-out of the figure showing surface mount varactor diode.

The measured frequency responses of the reconfigurable X-band phase shifter are shown in Figure 4-12. By comparing the simulated and measured results (Figure 4-8 and 4.12), (Figure 4-9 and 4-13), it can be stated that the measured results match closely with the simulated results. At reference capacitance (zero bias), the two peak resonant frequencies are 8.95 GHz and 10.25 GHz. As discussed earlier, these frequencies originate from the resonant frequency of each MTM unit cell structure in the circuit and they closely match simulation results. Table 4-1 summarizes key performance parameters of the measured X-band phase shifter design.

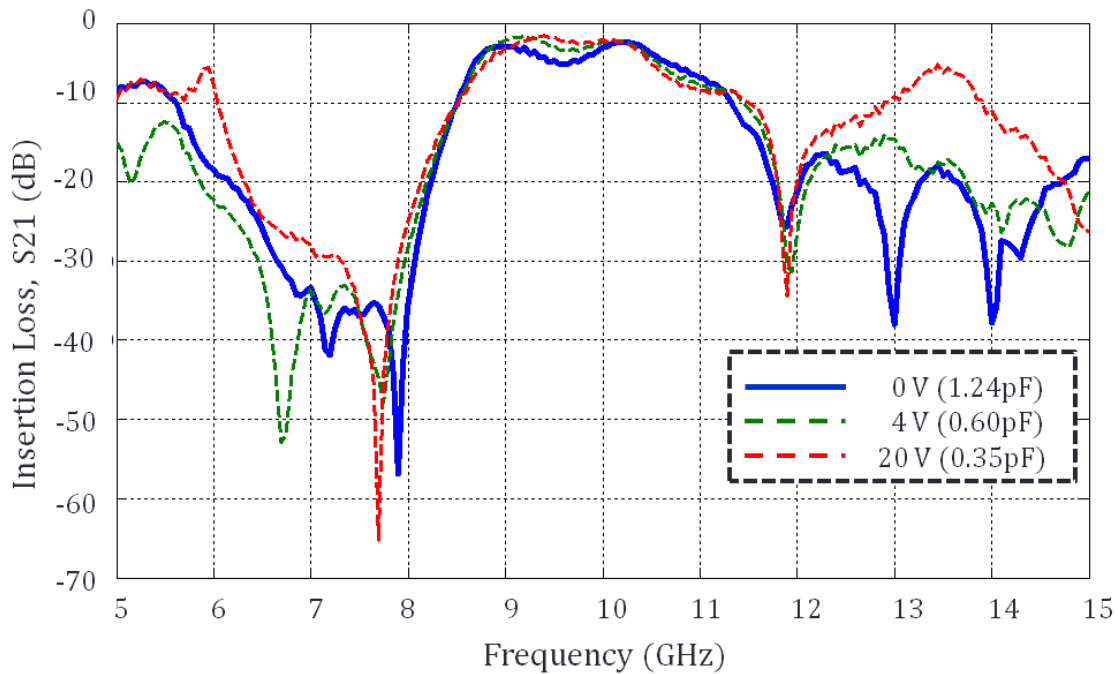


Figure 4-12. Measured insertion loss, S21 (dB) of the reconfigurable X-band phase shifter.

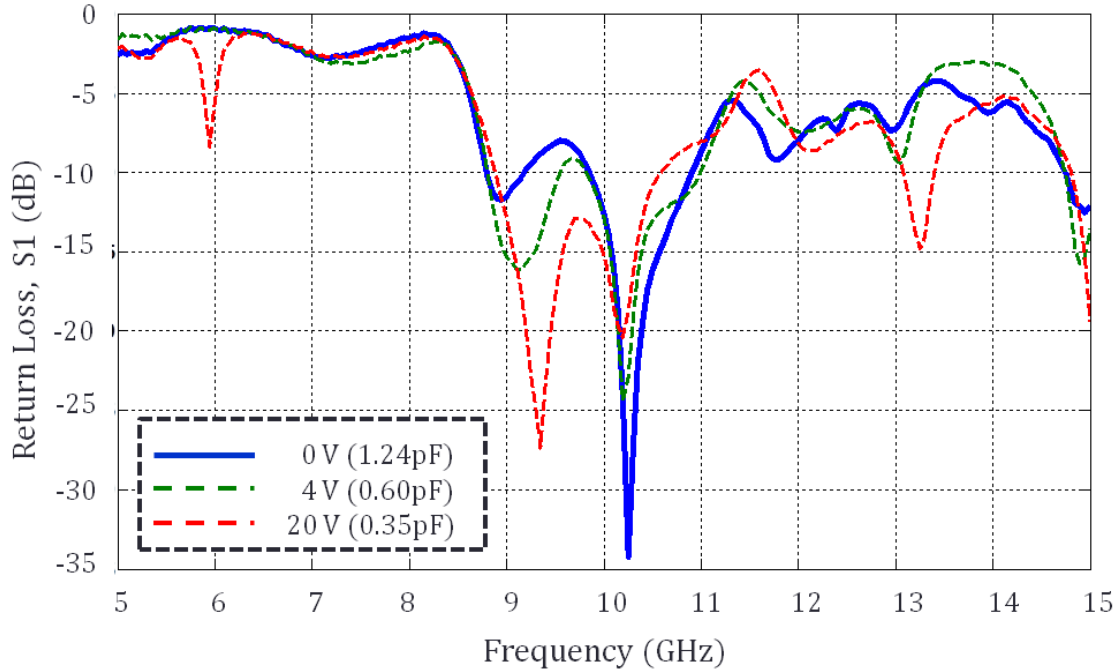


Figure 4-13. Measured return loss, S11(dB) of the reconfigurable X-band phase shifter.

As expected, the insertion phase can be reconfigurable by electronically varying the capacitance through dc biasing. Experiments are carried out for 3 different capacitance values through various dc biasing. According to data sheet for SMV1430-079LF [23], the varactor diode has a capacitance value at 1.25pF, 0.60 pF, and 0.35pF at DC bias values of 0 V, 4 V, and 20 V, respectively. Figure 4.14 shows the measured insertion phase of the proposed circuit. A phase tuning range of 18-degree for bias voltages between 0 V to 20 V (1.24pF to 0.35pF) is achieved over wide frequency range. This compares closely with simulated insertion phase response. The phase slope is close to linear and it closely maintains the same phase slope response at different varactor diode voltages.

Table 4-1 Characteristic performances of the reconfigurable X-band phase shifter

C (pF)	1.25 pF	0.60 pF	0.35 pF
f_{C1} (GHz)	8.95	9.15	9.35
$ S_{11} $ (dB)	11.72	16.13	27.35
$ S_{21} $ (dB)	2.8	1.6	1.5
f_{C2} (GHz)	10.25	10.20	10.20
$ S_{11} $ (dB)	34.25	24.39	20.38
$ S_{21} $ (dB)	2.3	2.1	1.9
-10dB Bandwidth	2.9 GHz	3.0 GHz	3.0 GHz

Notes: f_{C1} and f_{C2} are the center frequency of first and second resonance observed at reflection coefficient, respectively.

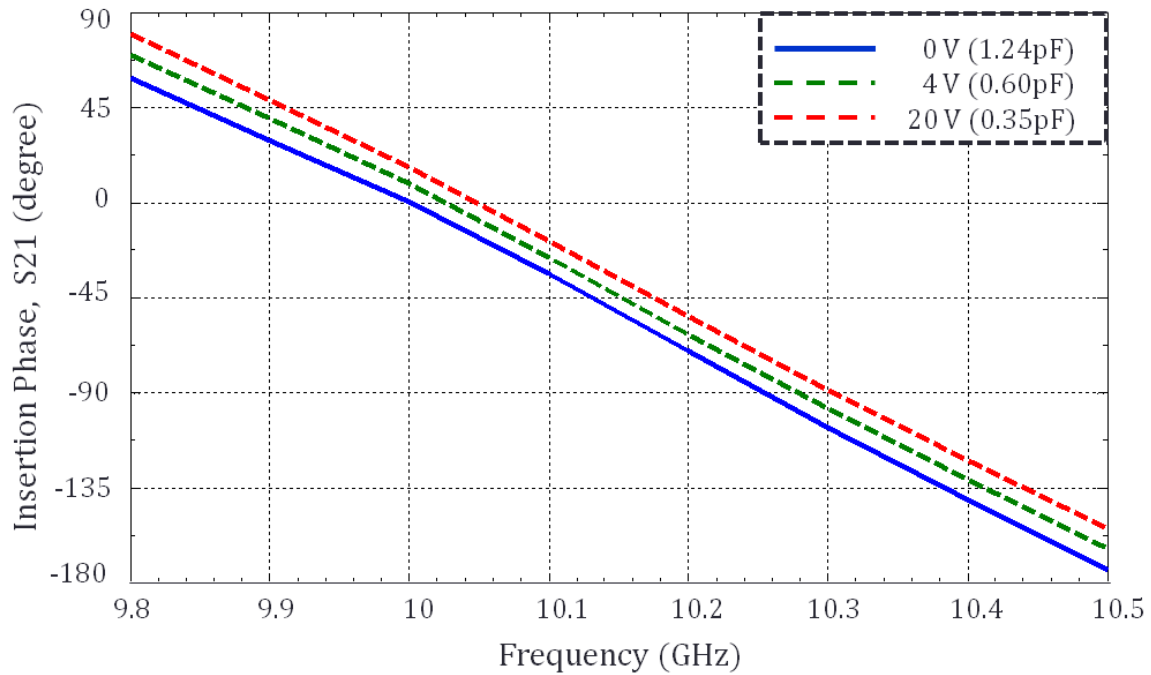


Figure 4-14. Measured insertion phase responses of the reconfigurable X-band phase shifter at different DC bias voltages.

4.4 Discussion

Generally stated, artificial structures or metamaterials exhibit narrow-band resonant frequency. However, as demonstrated in this paper, by cascading two MTM structures the MTM circuits can be designed to provide a wide band performance. The resonant frequency of the unit structure decreases when the discrete lump capacitance C_o is dominated by a varactor diode. Results show that the higher resonant frequency f_{C2} from the mSRR unit cell matches very closely between design and experiment. However, a slight difference in the lower resonant frequency f_{C1} can be attributed to parasitic parameters associated with the varactor diodes which were not incorporated in the simulations.

The reflection coefficient from experiment has wider bandwidth as compared to simulation results. This is largely due to high parasitic series resistance value of the varactor diode combined with series resistance from the connectors and soldering. This also leads to increase in transmission loss. Overall, the simulation and measured results match closely.

4.5 Conclusion

A new type of the reconfigurable X-band phase shifter using cascaded 2 MTM unit cells with a varactor diode has been proposed and demonstrated. Basic theory of CRLH transmission line and principle expressions of dispersion relation are described and derived in order to realize the characteristics of the unit cells. By integrating a varactor integrated within the unit cell an electronically tunable phase shifter was designed. The reconfigurable phase shifter exhibits linear phase responses over the designed frequency range. It also maintains the same slope while electronically varying the capacitance through dc biasing. The phase change slope is close to linear. The proposed design offers significant advantages over conventional delay lines and

uniform LH lines. It is compact in size, simple to design and fabricate, and allows direct integration of active devices.

CHAPTER 5

METAMATERIAL-INSPIRED MICROFLUIDIC SENSOR

Rapid characterization of chemical and biological samples is increasingly important in clinical, security, safety, drug discovery and industrial applications. Sensing approaches are needed that does not require tagging, (e.g., using fluorescent markers) in order to maintain the samples in their original form while under study. Along with rapid label-free characterization, interrogation of small sample volumes is critically needed in the areas of clinical diagnosis and drug discovery. In this Chapter, periodic media co-integrated with microfluidic leading to a novel RF near-field sensor is implemented to tackle these challenges. The proposed sensor is simple, cost effective, and can be used for label-free sensing.

5.1 Metamaterial Transmission Line Based Spiral Structure

Spiral structured artificial magnetic media (metamaterial) designs have been widely used in the design of compact coplanar waveguides (CPW) and microstrip-based circuit topologies. Recently, split-ring based metamaterial structures that are edge-coupled to a microstrip line have been used in the sensing of biomolecules [43]. In this structure, the interrogation signal (RF) edge couples from a microstrip transmission line to a ring resonator. The biomolecules are made to bind onto the ring resonator. A direct approach of interrogation will be desirable which is more compact and provides improved sensitivity and yet still simple to fabricate and implement. To meet this goal, in this paper, metamaterial structure that is integral part of the microstrip line is employed for sensing application. A spiral based metamaterial transmission was recently introduced, [31–32], and this design is implemented here for the first sensing application.

5.1.1 Left-Handed Media Based Double Spiral Structure

Generally, the LH nature is equipped with the shunt inductor and series capacitor, as opposed to the conventional right-handed transmission lines (PRH-TL) which is provided by the series inductor and shunt capacitor. Based on the double spiral structure as shown in Figure 5.1(a), a rectangular unit cell with an edge of ratio of 2:1 is proposed. A double split rectangular loop distributes the magnetic and electric fields in the unit cell taking into account the dual TL concept for LH media. The magnetic field is related to shunt inductance that would be created by an idea shunt inductor, i.e. the magnetic field in z -direction (H). Similarly, the electric field along the x -axis (E) would be produced by a capacitive loading of the gap in the unit cell assuming that voltage is applied along x -direction. The E -field is therefore represented the equivalent series capacitance in LH media.

The dispersion diagram is derived using the periodic Bloch-Floquet analysis as mentioned in Chapter 2. After the parameter extraction, the discrete lumped LH-parameters of the unit cell are $L_o = 540$ pH, $C_o = 216$ fF. For the host transmission line, the RH-parameters become $\beta_{TL}d = 0.25$ rad at 3.13 GHz. As the dispersion diagram, the balanced mode of 1-D CRLH transmission line and the impedance matching condition are satisfied. The stopband is closed. RH passband and LH passband are continuous. The MTM unit cell is performed with LH pass-band from 2.53 to 3.13 GHz. For right-handed pass band, the MTM unit cell is obtained from 3.13 to 3.86 GHz. It is also observed that the phase shift is 0 degree at $f_o = 3.13$ GHz.

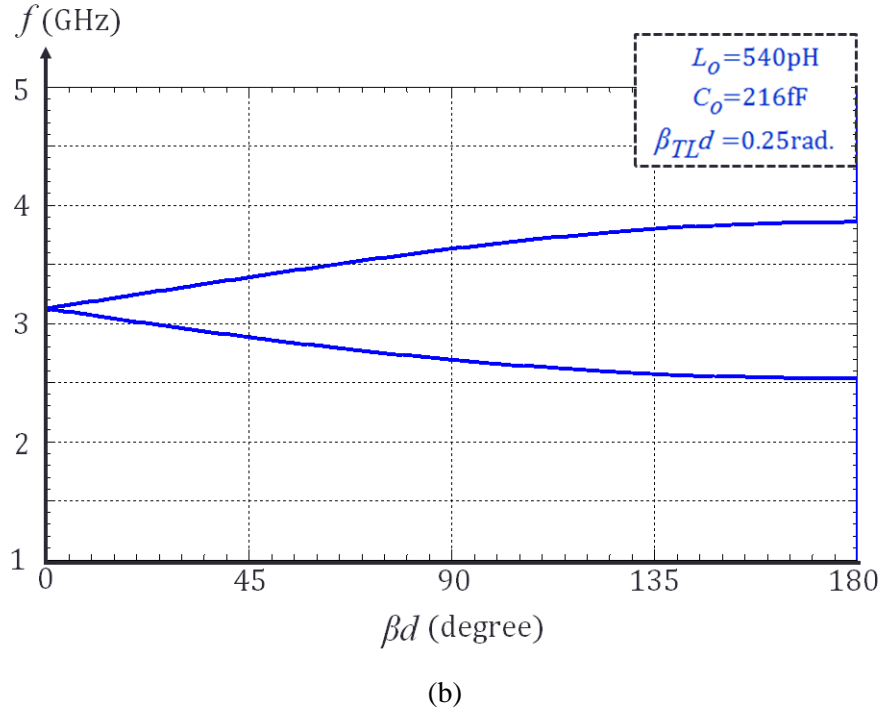
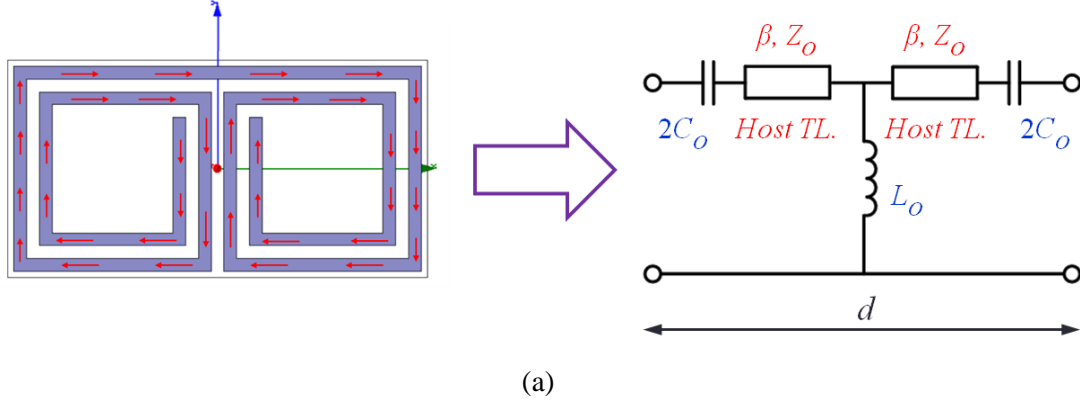


Figure 5-1. (a) Double spiral unit cell with its equivalent circuit, and (b) Dispersion relation for the spiral split-loop grounded periodic array by the periodic Bloch-Floquet analysis.

Figure 5-2 shows the E -field and H -Field distributions for the double spiral grounded periodic array. As mentioned earlier, strong capacitance emerges in the gap and between successive elements, where opposite charges gather on either side. Moreover, the current circulating along the spiral acts as a planar inductor. It results in excessive magnetic activity and therefore high inductance. These are indeed confirmed in Figure 5-2. According to [31-32], the

mutual inductance between two spirals is positive, increasing the equivalent shunt inductance in the LH media. Not only do powerful electric and magnetic field distributions support LH propagation but also can be advantageous in high sensitivity sensor applications.

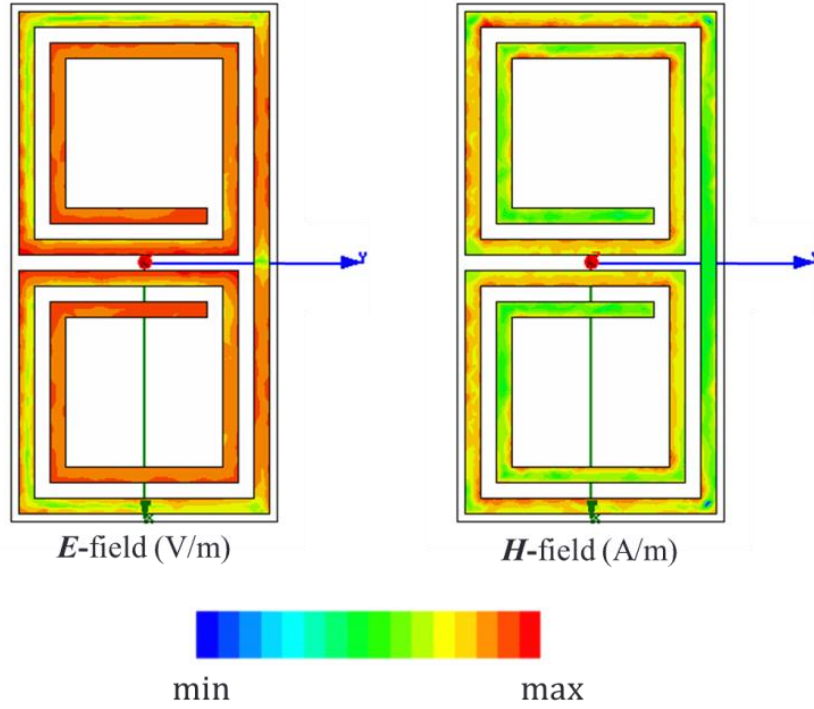


Figure 5-2. Normalized values of E -field and H -field distributions in spiral split-loop element array.

5.1.2 Double Spiral Structure Based Microstrip TL

The spiral split-loop periodic array or double spiral unit cell is proposed and designed for transmission line based microstrip technology. Figure 5-3(a) shows the layout of an artificially structured periodic media to be used for the design of a sensor. It is composed of three double spiral unit cells connected in series on the front side and a solid ground plane on the back side of the board. The asymmetry is carried out to restrain the capacitive coupling between them, in favor of the inductance coupling. This unit cell forms a double spiral resonator with dimensions

$dx = 6.4$ mm and $dy = 3.2$ mm. The periodic analysis of the double spiral unit cell shows that the structure supports backward waves as LH media at their fundamental mode [32].

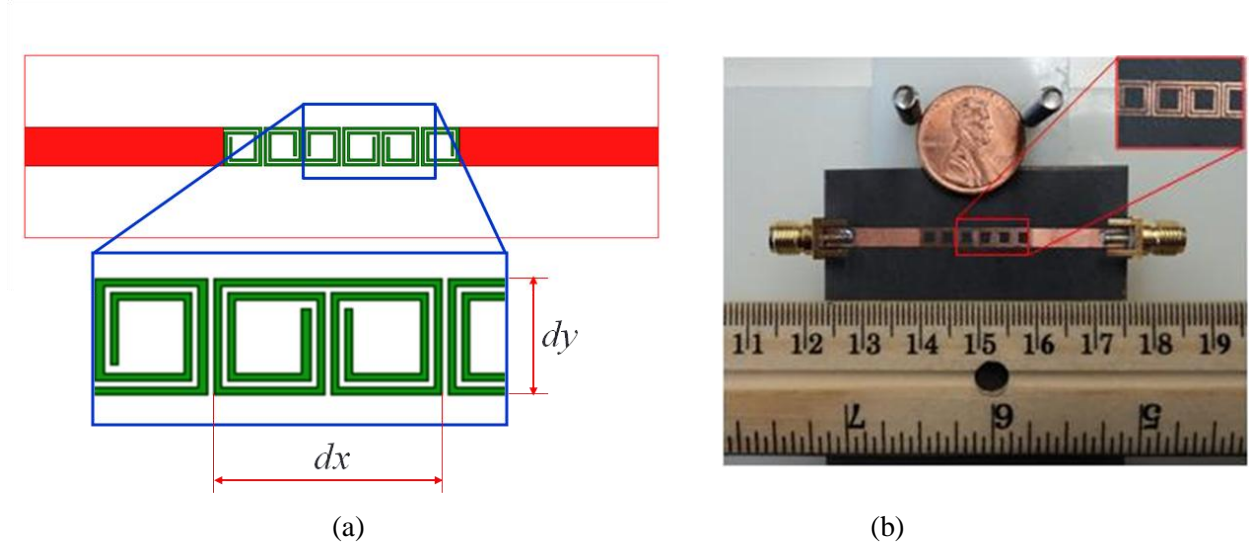


Figure 5-3. (a) A model of the artificially structured periodic media based double spiral designed using Ansoft HFSS, (b) a fabricated MTM microstrip TL based double spiral structure.

For this work, photolithographic techniques have been used to fabricate the spiral structure based microstrip technology. Figure 5-3(b) shows a fabricated metamaterial transmission line based on triple cells of double spiral components. It was fabricated on RT/Duroid® 5880 substrate having dielectric constant $\epsilon_r = 2.2$ and thickness of 1.575 mm using conventional microfabrication approaches. The measured and simulated, using the Ansoft HFSS®, frequency responses are shown in Figure 5-4. These results are before the integration of microfluidic layer. The simulated and measured responses match very closely and the measured insertion loss is approximately 1 dB for this structure. Upon fabrication of microfluidic layer on top of this structure, the resonance frequency shifts to lower frequency as discussed ahead.

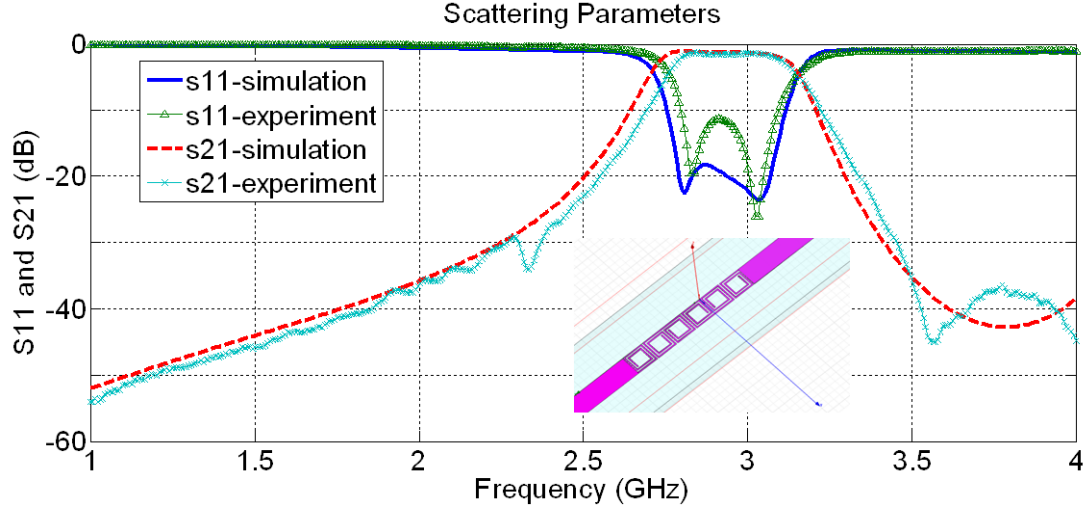
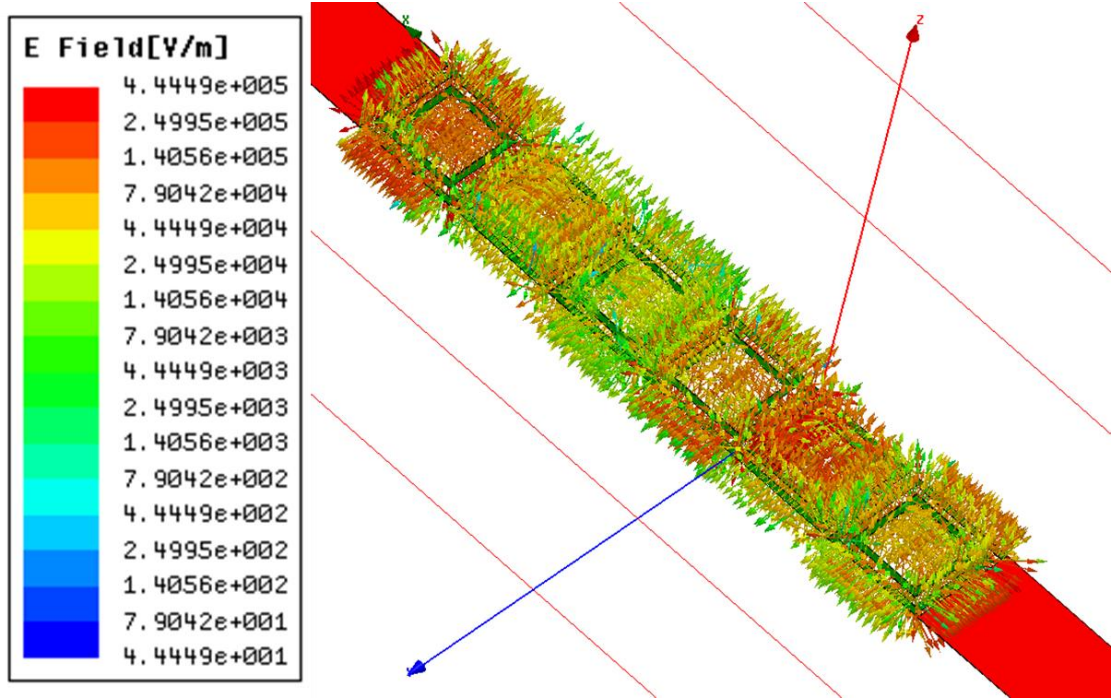
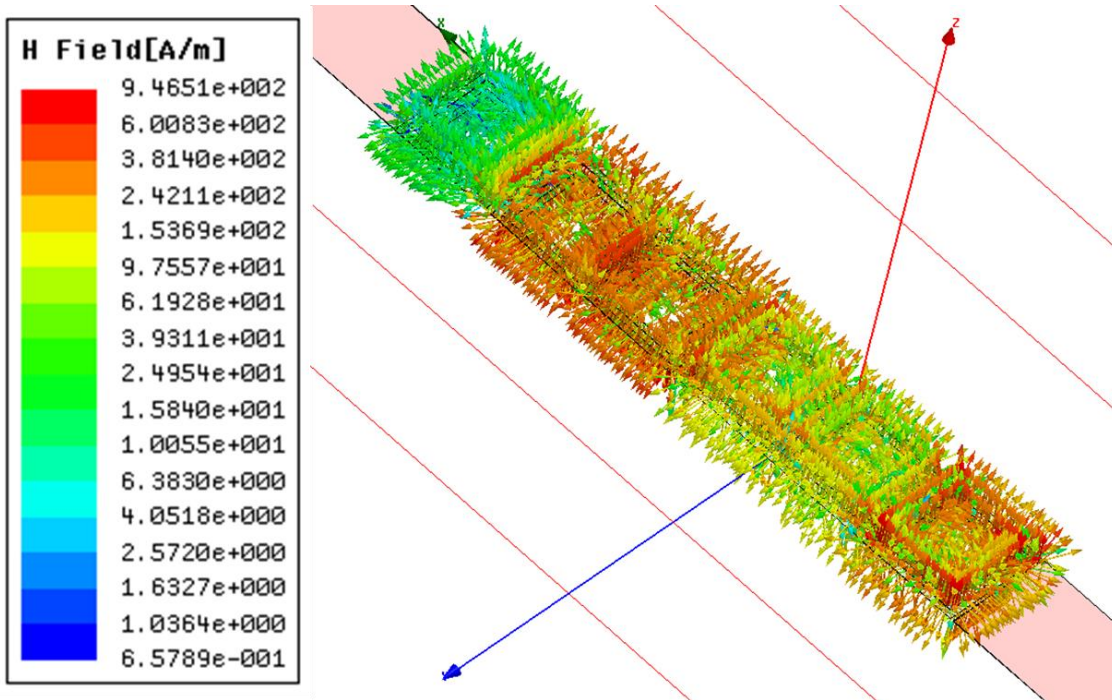


Figure 5-4. Simulated and measured frequency responses of the MTM microstrip technology based spiral structure. The simulated structure model is depicted in the inset.

Figure 5-5(a) and (b) show the simulated E -field and H -field distributions for the double spiral grounded periodic array based microstrip transmission line as designed for this work. It is clear that strong E -field appears in the structure gap corresponding to an increase of the series capacitance. This is the suitable position to place the sample in a spot to get the maximum interference effect with a high E -field strength. Furthermore, current also flows along the reentering load resulting in a further increase of H -field to support LH propagation. Overall, strong field distributions occurring from the circuit lead to very high sensitivity of the sensor device. The results clearly express that the proposed design supports LH propagation throughout Brillouin zone. It is more miniature and easy to integrate with microfluidic channel for high sensitivity sensing applications as expected.



(a)



(b)

Figure 5-5. Vector field distributions on the unit cells of double spiral array based microstrip line at resonance frequency, f_0 : (a) E -field distribution, (b) H -field distribution.

5.2 Microfluidic Channel for Sensing Application

A microfluidic channel was fabricated from elastomer polydimethylsiloxane (PDMS) using a SU8-2000 mold. A 100 μm thick layer of SU8-200 was spin coated on a thin Polytheretherketone (PEEK) film (250 μm). The PEEK film in turn was attached to a Si wafer during spin coating. SU-8-2000 has better adhesion with PEEK than bare Si-wafer. A prebake process, UV lithography, postbake process, development, and lift off are performed to fabricate the mold (master) of the microfluidic channels. To form the microfluidic channels, Polydimethylsiloxane (PDMS) elastomer is used that is a two-part resin system containing vinyl groups and hydrosiloxane groups. PDMS is a soft material and it can easily be separated from the SU-8 master, leaving the master intact for the fabrication of additional microfluidic channels. The PDMS microfluidic channel is designed in S-shape following the spiral line to couple with locations having stronger electric and magnetic fields on the spiral structures. The depth of the microfluidic channel is 100 μm .

Instead of directly attaching the mold to the circuit board, a thin film of PI (50 μm) was introduced between the PDMS channel and the copper traces. This film was attached to PDMS using a Siloxane adhesive. Polyimide acts as a chemical barrier between the copper traces and the liquid sample in the channels. Although this method may reduce the sensitivity, but it helps prevent any damage to the copper traces if harsh chemicals are to be interrogated. The overall of fabrication process of the SU-8 mold and PDMS microfluidic device in this study is demonstrated in Figure 5-6(b). An example fabricated microfluidic channel made from PDMS is also shown in Figure 5-6(a).

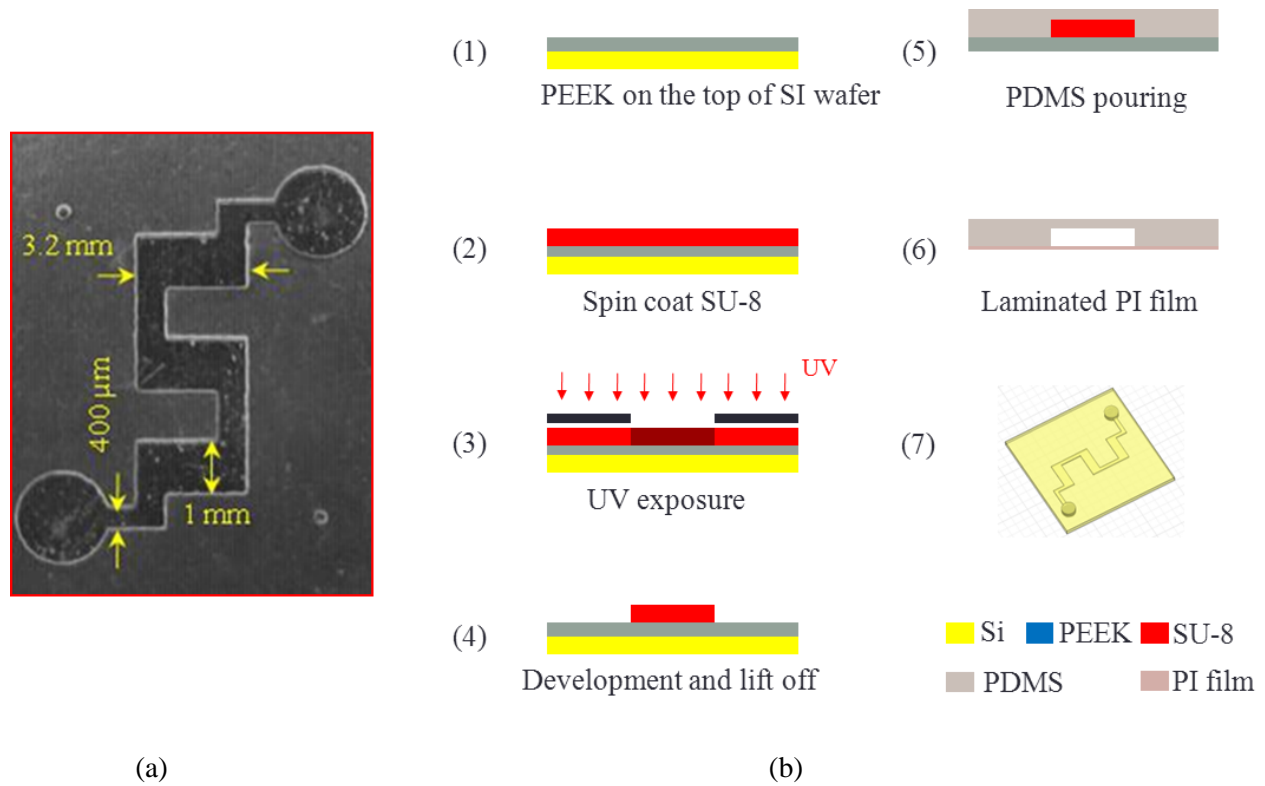


Figure 5-6. (a) Optical photograph of a PDMS microfluidic channel before laminated PI film, and (b) Fabrication process of a microfluidic chip in this work.

Integration of the PDMS onto the metamaterial microstrip structure loads the circuit and changes the S-parameters. Simulated and measured S-parameters of the loaded structure are shown in Figure 5-7. It is clear that they match very closely. Slight differences may be due to the dielectric properties of the PDMS used in the simulation of the structure.

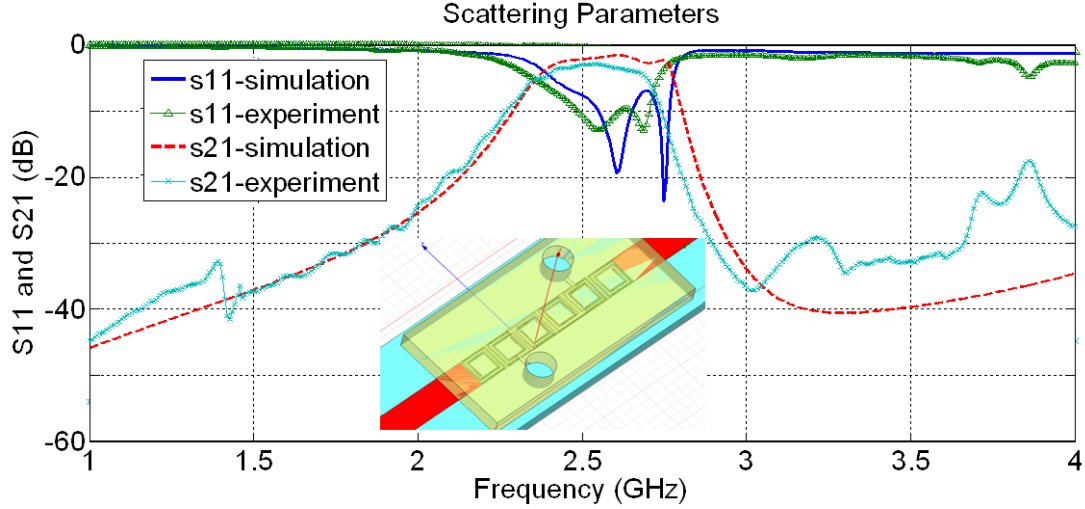
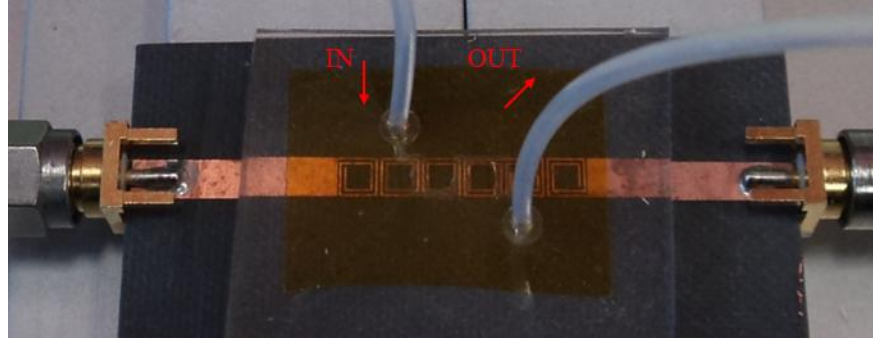


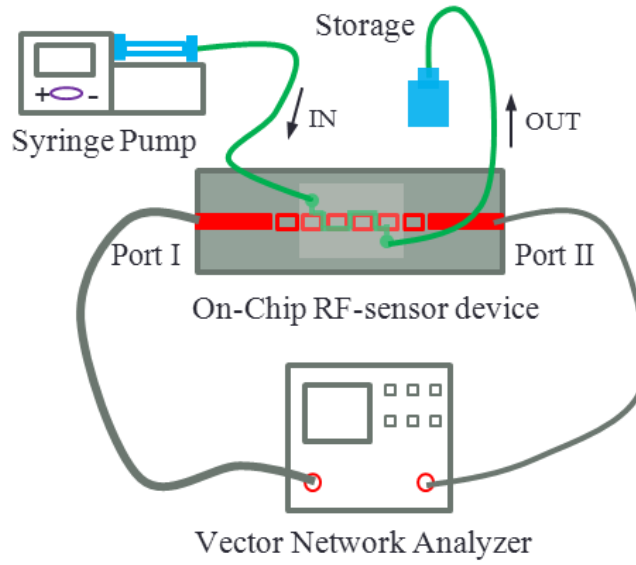
Figure 5-7. Simulated and measured frequency responses of the fabricated metamaterial RF device attached with PDMS microfluidic channel on top of the metamaterial transmission line structure. The simulated structure model is depicted in the inset.

5.3 Fabrication and Experimental Results

Preliminary experiments were carried out with the microfluidic channel filled with different concentrations of water-methanol and water-isopropanol (IPA or 2-propanol) sample mixtures. The solutions were prepared by molar fraction from Mallinckrodt Chemicals and de-ionized water at the concentration index, $X = 0, 0.2, 0.4, 0.6, 0.8$, and 1.0 at the room temperature. During the measurements, the sample was allowed to continuously flow using a syringe pump. Teflon tubing (inner and outer diameters are 0.8 mm and 1.6 mm respectively) was attached to the PDMS using epoxy. A syringe- 30 mL was used for sample handling. A Vector Network Analyzer was used to measure the scattering parameters of the loaded transmission line. Sufficient amount of liquid was allowed to flow through between samples to remove any residue in the microfluidic channel between the measurements. The transmission (S_{21}) and reflection (S_{11}) scattering parameters were measured for all the sample solutions. A close-up view and a diagram of the measurement setup are shown in Figure 5-8.



(a)



(b)

Figure 5-8. (a) Fabricated MTM RF sensor device integrated with PDMS microfluidic channels. (b) Measurement setup diagram of the experiment.

5.3.1 RF Measurements

Figure 5-9 to 5-14 express the measured scattering-parameters of different concentrations of water-methanol and water-2-propanol liquid solutions. The transmission properties and the resonant frequency, f_r , shifts depending upon the dielectric properties of the sample in the microfluidic channel. The shift in frequency indicates the effective dielectric constant and the change in amplitude indicates the loss-tangent of the liquid sample. Minimum value of the S11

parameter was used as the reference point of frequency measurement. This frequency can easily be measured from the phase plot of S_{11} .

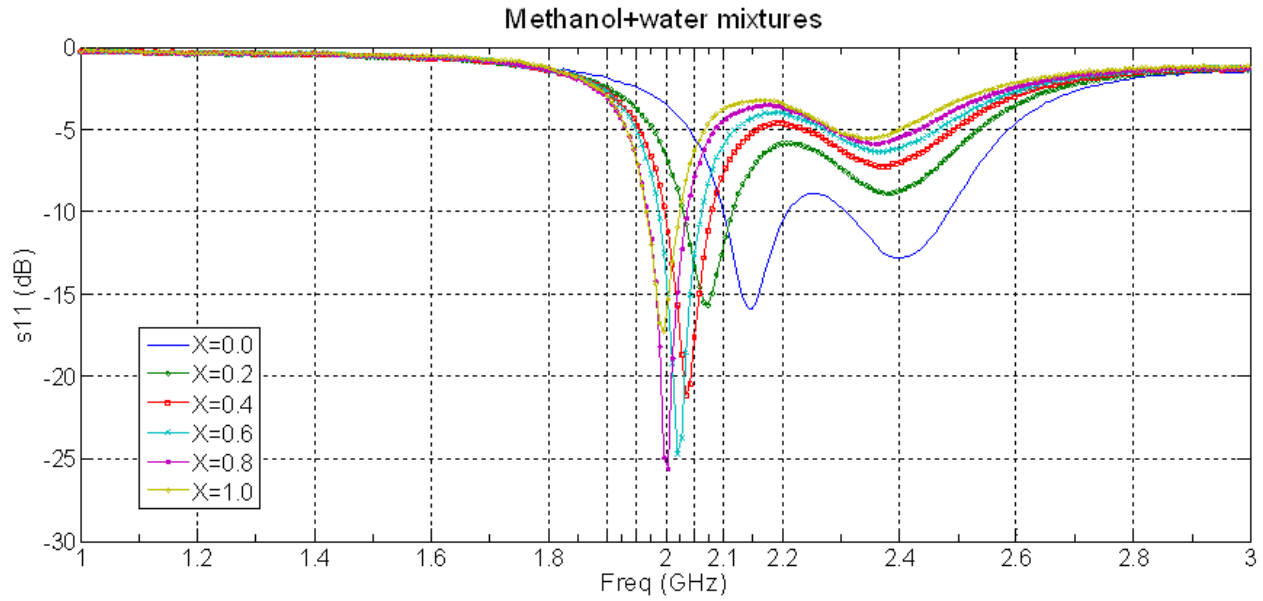


Figure 5-9. Measured return loss, S_{11} under test corresponding different concentrations of water-methanol mixtures.

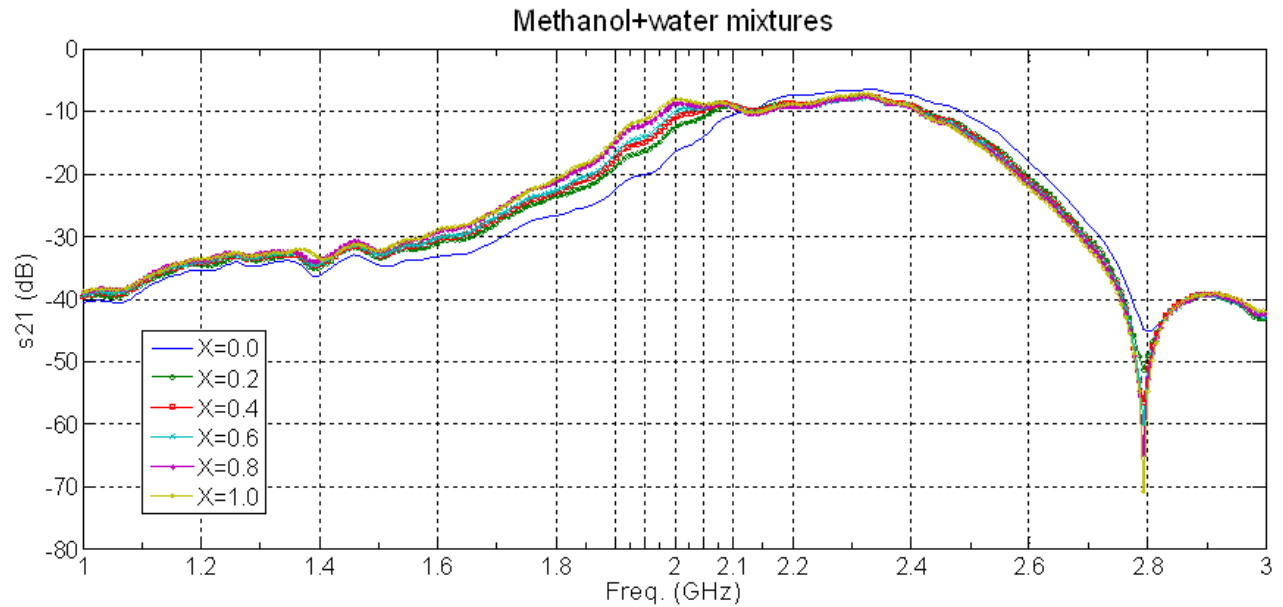


Figure 5-10. Measured insertion loss, S_{21} under test corresponding different concentrations of water-methanol mixtures.

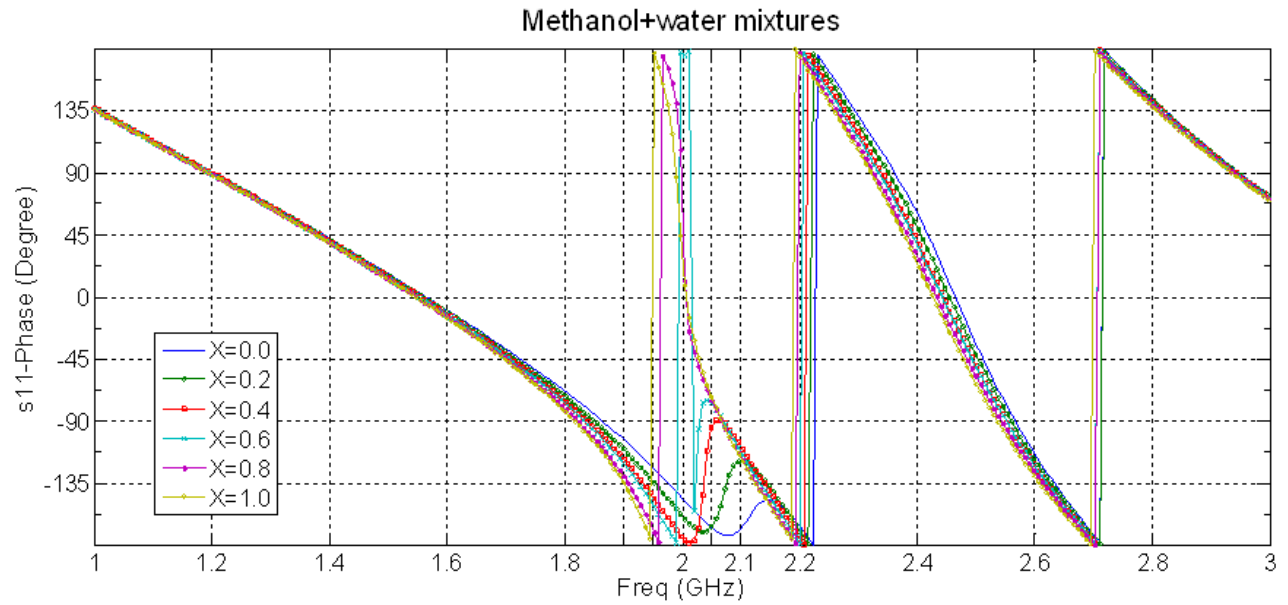


Figure 5-11. Measured return loss - phase under test corresponding different concentrations of water-methanol mixtures.

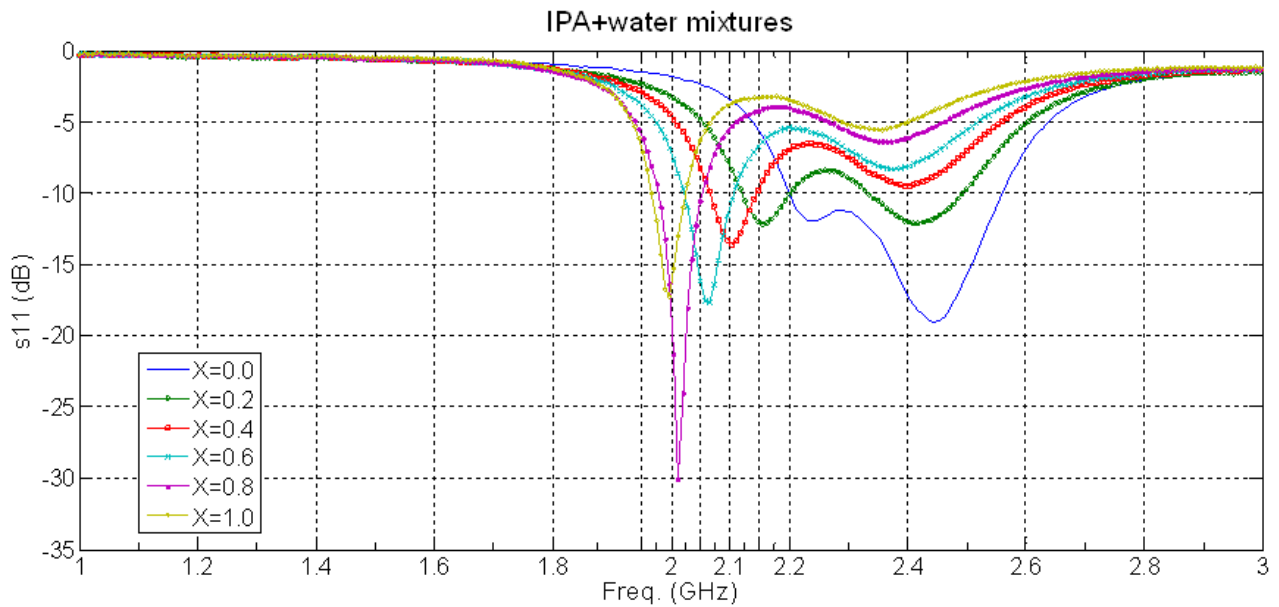


Figure 5-12. Measured return loss, S11 under test corresponding different concentrations of water-IPA mixtures.

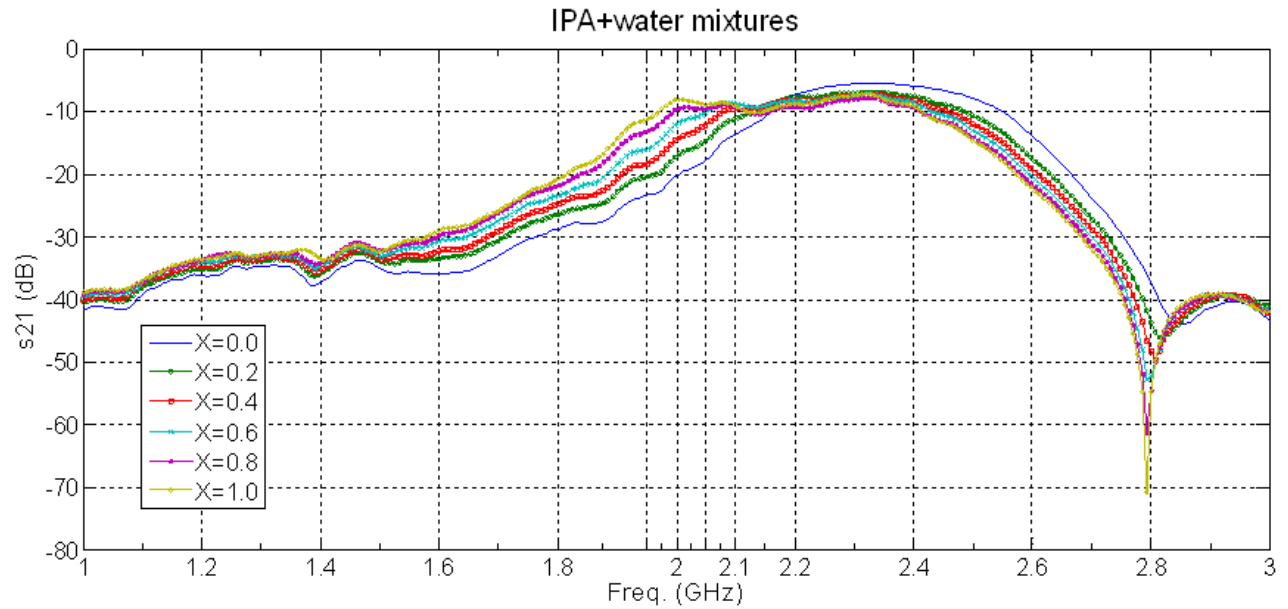


Figure 5-13. Measured insertion loss, S_{21} under test corresponding different concentrations of water-IPA mixtures.

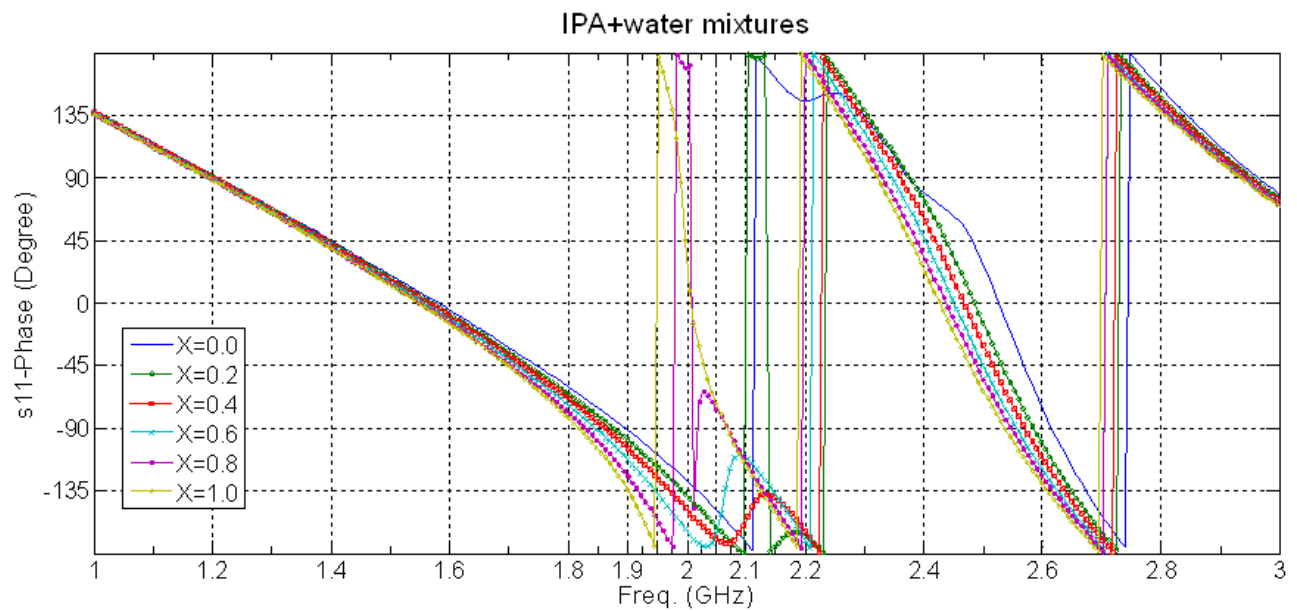


Figure 5-14. Measured return loss – phase under test corresponding different concentrations of water-IPA mixtures.

5.3.2 Interpretation of Results

The mixtures in various molar fractions can be translated approximately to the dielectric constant, ϵ' by the Davidson-Cole equation that is expressed by [44].

$$\epsilon^*(\omega) = \epsilon_{\infty} + \Delta\epsilon/(1 + i\omega\tau)^{\alpha} \quad (5-1)$$

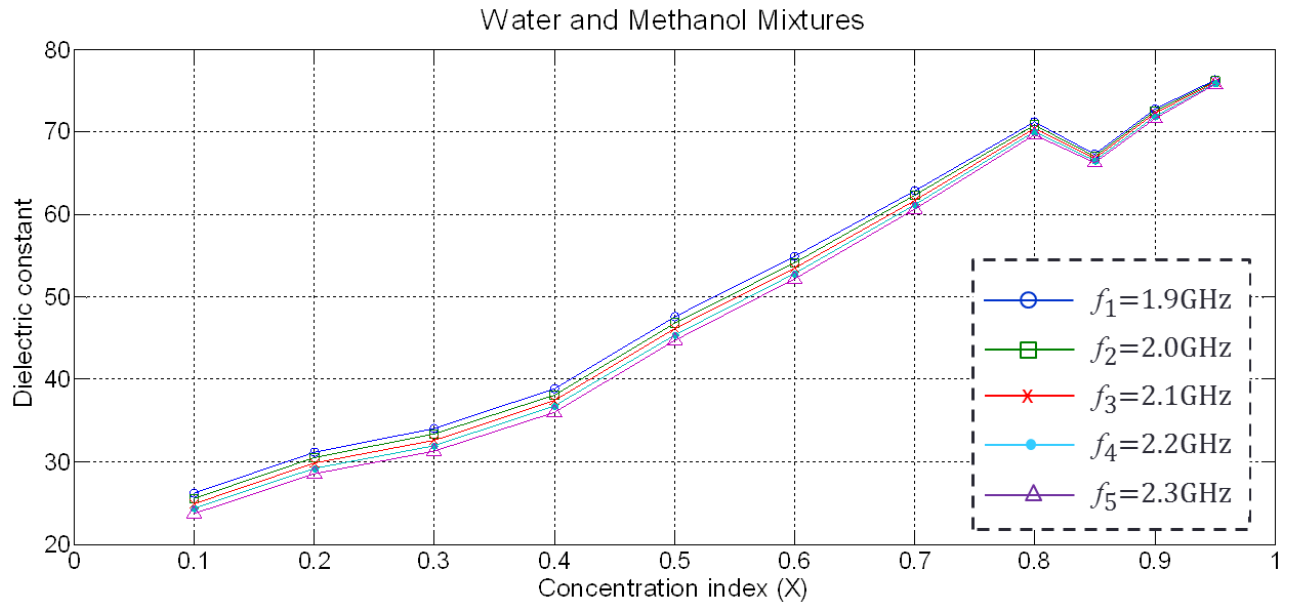
where ϵ^* is the complex permittivity at an angular frequency ω , ϵ_{∞} is the permittivity at $\omega \rightarrow \infty$, $\Delta\epsilon$ is the relaxation increment, and τ is the relaxation time. According to S. Mashimo and T. Umehara. [44], the dielectric constants of water-methanol mixtures in various frequencies can be investigated by Equation (5-1). Figure 5-15 shows the dielectric constant (ϵ') and loss tangent ($\tan\delta$) of water-methanol solutions for various concentrations based on the above equation. The results show that the dielectric constant and loss-tangent of methanol are approximately 27 and 0.6 at 2 GHz, respectively. Also for DI-water, these values are approximately 80 and 0.12, respectively. These values match very closely with those reported by J. Barthel *et al.* [45] and C. Oliver Kappe *et al.* [46]. Similarly, the dielectric constant (ϵ') and loss tangent ($\tan\delta$) of propanol mixtures for different concentration indexes are also expressed as Figure 5.16. All of them were used to convert from concentration levels to dielectric constant values.

Referring from the study by J. Barthel *et al.* [45], dielectric relaxation parameters of 1-propanol and 2-propanol are almost the same and readily available. To the first order, the dielectric relaxation parameters of water -1-propanol in [45] are used in Equation (5-1) for interpreting the dielectric relaxation parameters of water-2-propanol samples in this work. By cubic curve fitting at 2.1 GHz, the correlation between the complex permittivity of the solutions, water –methanol and –2-propanol, and concentration index can be plotted as Figure 5-17 and 5-18, respectively. On the other hand, the correlation between dielectric constant and loss tangent

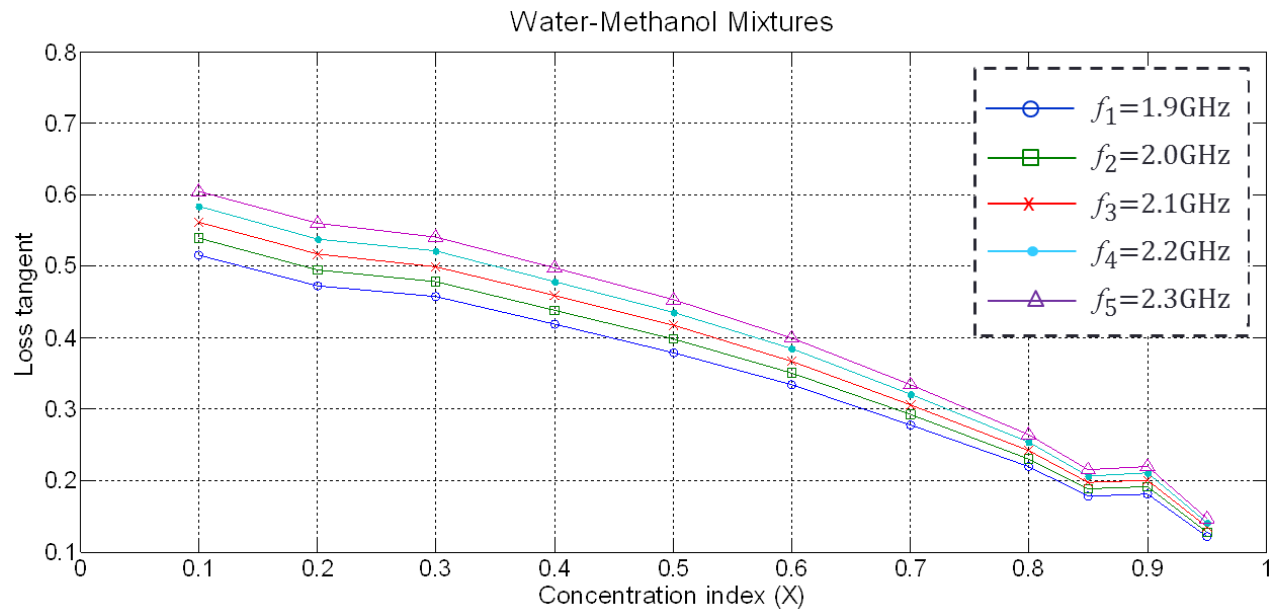
of the samples at each concentration index can be expressed as shown in Figure 5-19. These relationships are used to approximately predict the dielectric relaxation parameter of the samples in the experiments. After converting the unit from the concentration index to dielectric constant, the approximate dielectric constant (ϵ') of water-methanol and water-2-propanol mixtures can be predicted from the resonance shifting of the spectra in different concentration samples. If the resonance deviation is normalized by

$$\Delta f_{n,mut}(\%) = (f_{r,mut} - f_{r,water}) \times 100 / f_{r,water} \quad (5-2)$$

where $\Delta f_{n,mut}$ is the normalized resonance shifting of mixture under test, $f_{r,mut}$ is the resonant frequency of mixture under test, and $f_{r,water}$ is the resonant frequency of water. Figure 5-20 expresses the relationship between the normalized resonance shifting of water-methanol and water-2-propanol mixtures and approximate dielectric constant (ϵ') of the mixtures. Considering with the insertion loss S21 in Figure 5-10 and 5-13, it is clear that 2-propanal solution has higher dielectric absorption, more than methanol solutions.

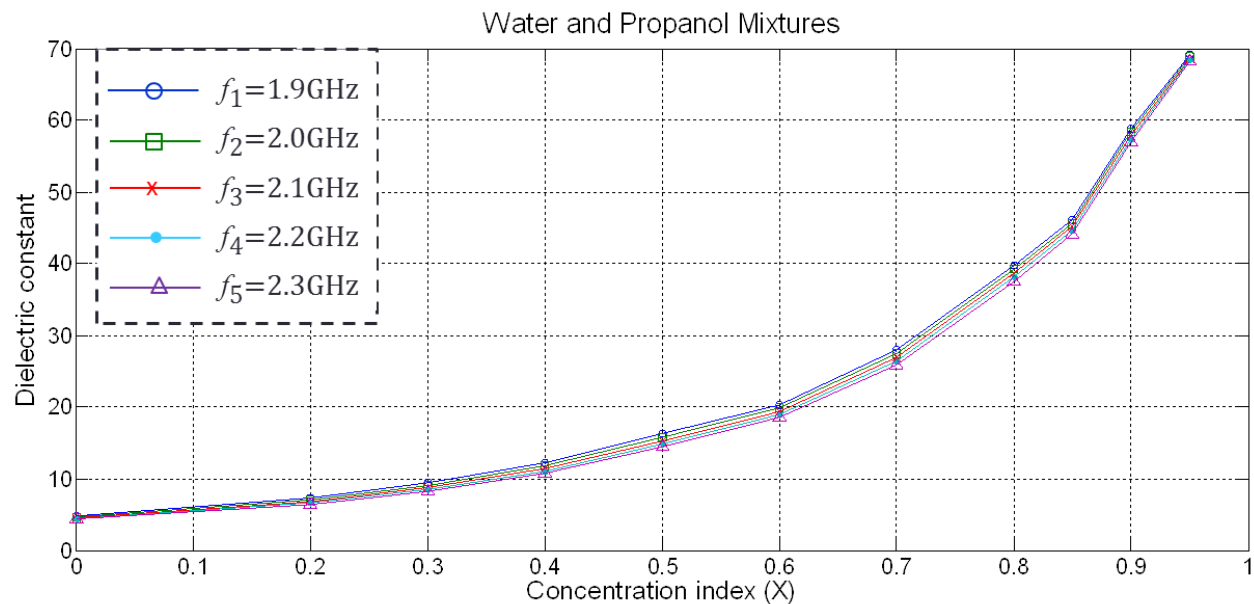


(a)

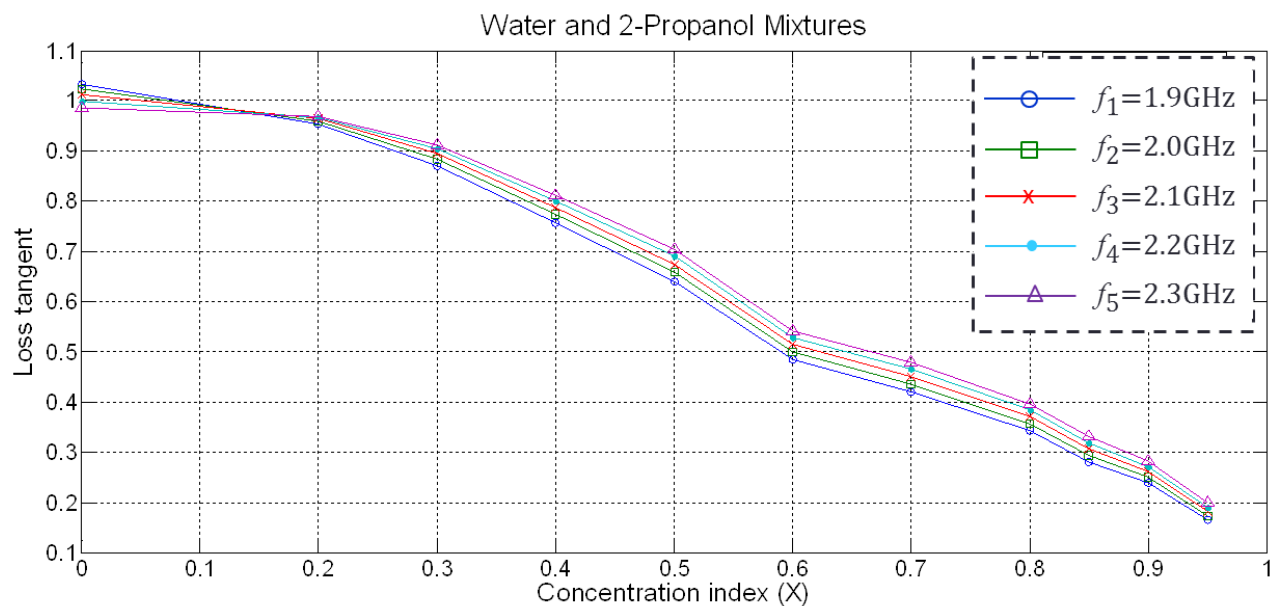


(b)

Figure 5-15. (a) Dielectric constant, ϵ' and (b) loss tangent, $\tan \delta$ of water-methanol mixtures at various frequencies based on [44].

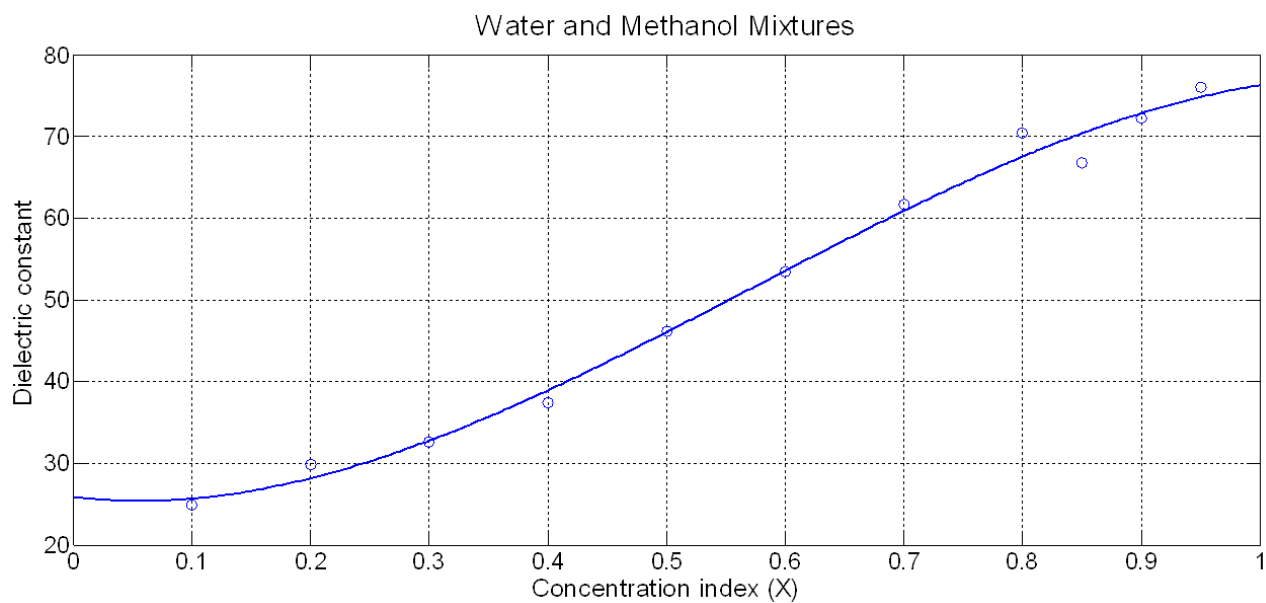


(a)

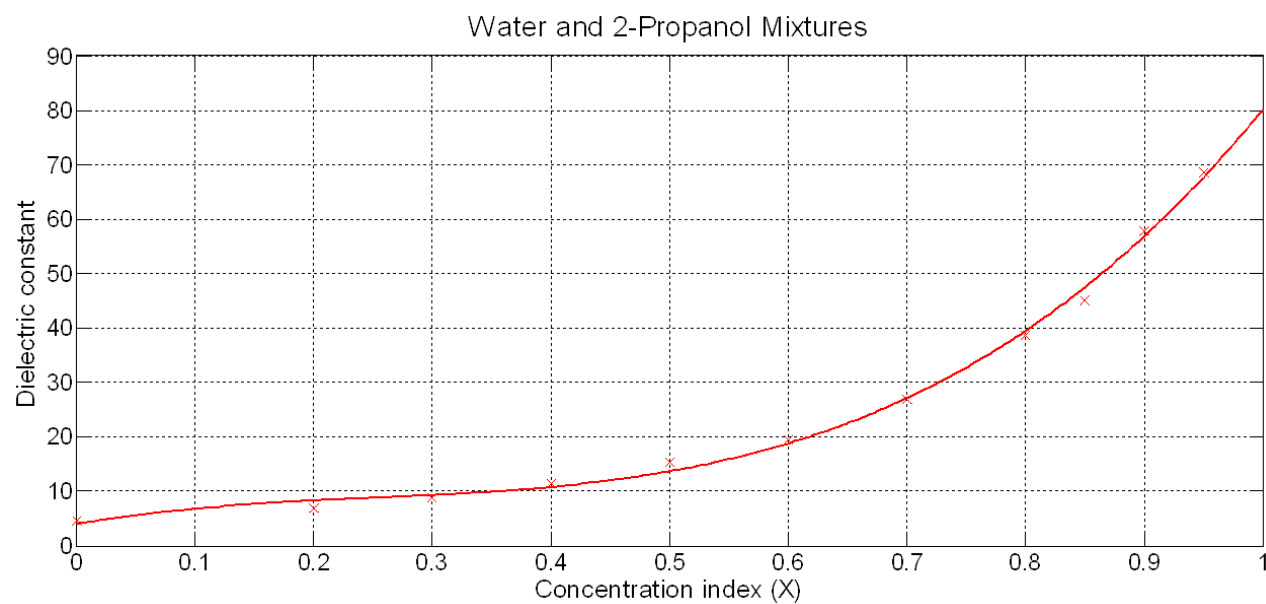


(b)

Figure 5-16. (a) Dielectric constant (ϵ') and loss tangent ($\tan \delta$) of water-IPA mixtures at various frequencies based on [44].

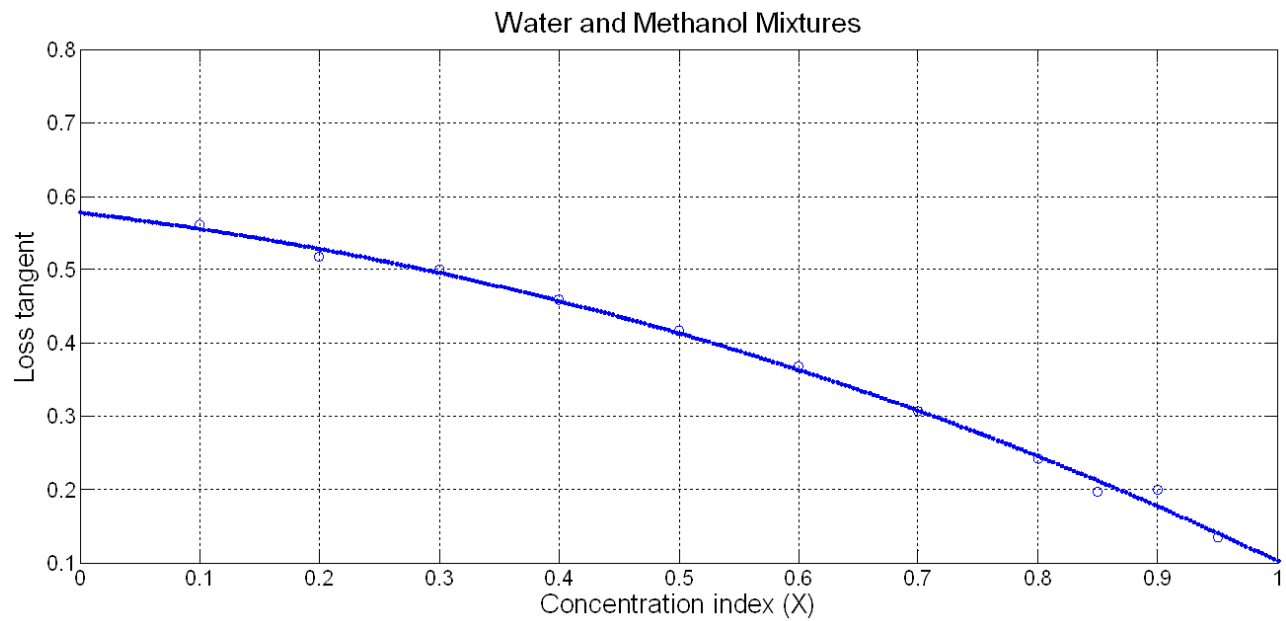


(a)

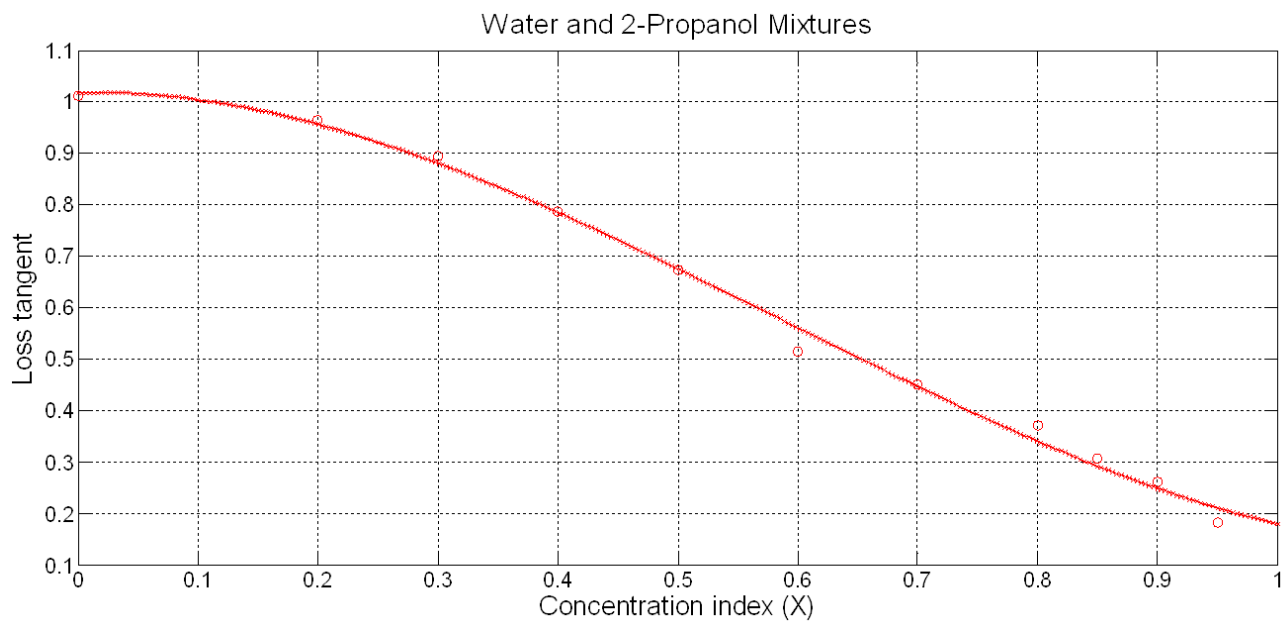


(b)

Figure 5-17. Dielectric constant of the samples at 2.1 GHz by cubic curve fitting, (a) water-methanol and (b) water-2-propanol mixtures.



(a)



(b)

Figure 5-18. Loss tangent of the samples at 2.1 GHz by cubic curve fitting, (a) water-methanol and (b) water-2-propanol mixtures.

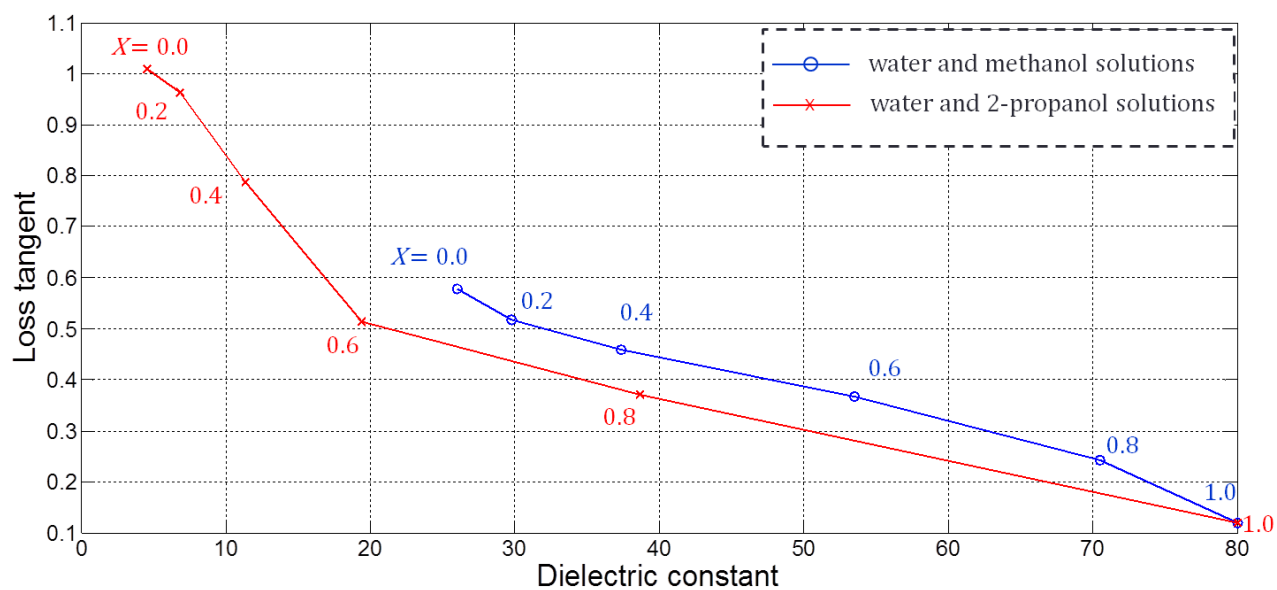


Figure 5-19. Correlation between dielectric constant and loss tangent of the samples at each concentration index (X).

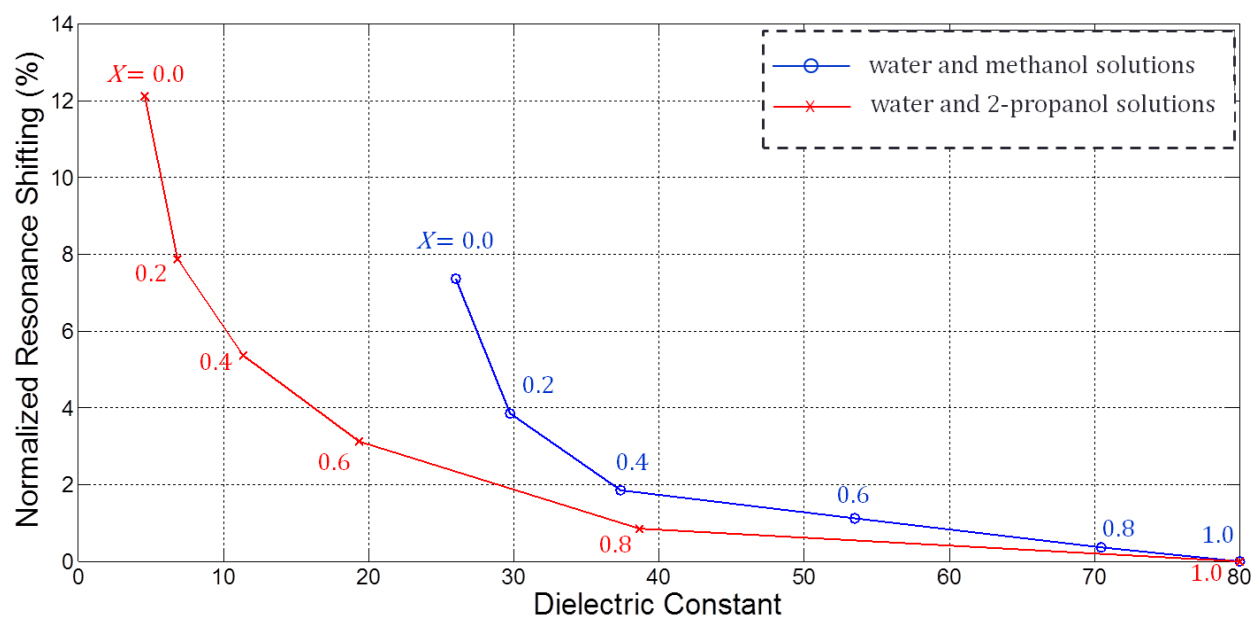


Figure 5-20. Change in the resonance frequency, $S_{11}(f_r)$, with approximate dielectric constant of water-methanol and water-2-propanol mixtures.

The main reason for using LH media in sensing applications is the interference effect associated with minute volumes of samples. A small change in properties of the dielectric medium loading the structure leads to a significant change in the resonant frequency (f_r) of the transmission line. From the experiments, the steepness of the insertion loss is further analyzed in order to express the sensitivity of the proposed sensor. It is analyzed by evaluating the frequency derivative of the spectra as shown in Figure 5-21. The results indicate that the high sensitivity of the sensor can be obtained.

In the view of maximizing the sensitivity, lower concentration sample is explored. The steepness of the spectra in methanol mixtures is higher than 2-propanol mixtures comparing at the same concentration index. It can be concluded that this sensor has higher sensitivity in methanol samples than 2-propanol samples. However, placing the sample in a spot with a high *E*-field strength or concentration maximizes the effect.

Finally, a promising concept for high sensitivity chemical and biochemical sensors based on metamaterial RF device is presented. Shift in resonant frequency can predict the complex permittivity of the samples. This shows a significant improvement in sensitivity as compared to data for similar liquid mixtures as presented in [47]. Furthermore, the circuit is simple to design, compact and easy to integrate with microfluidic channel.

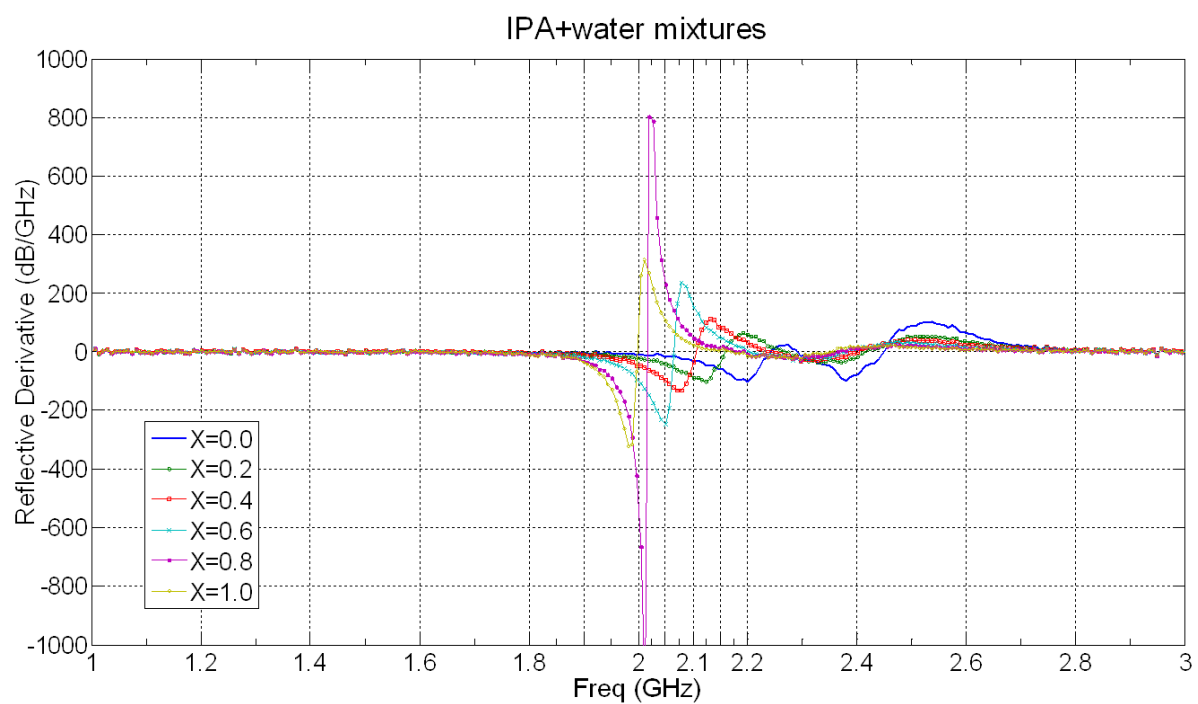
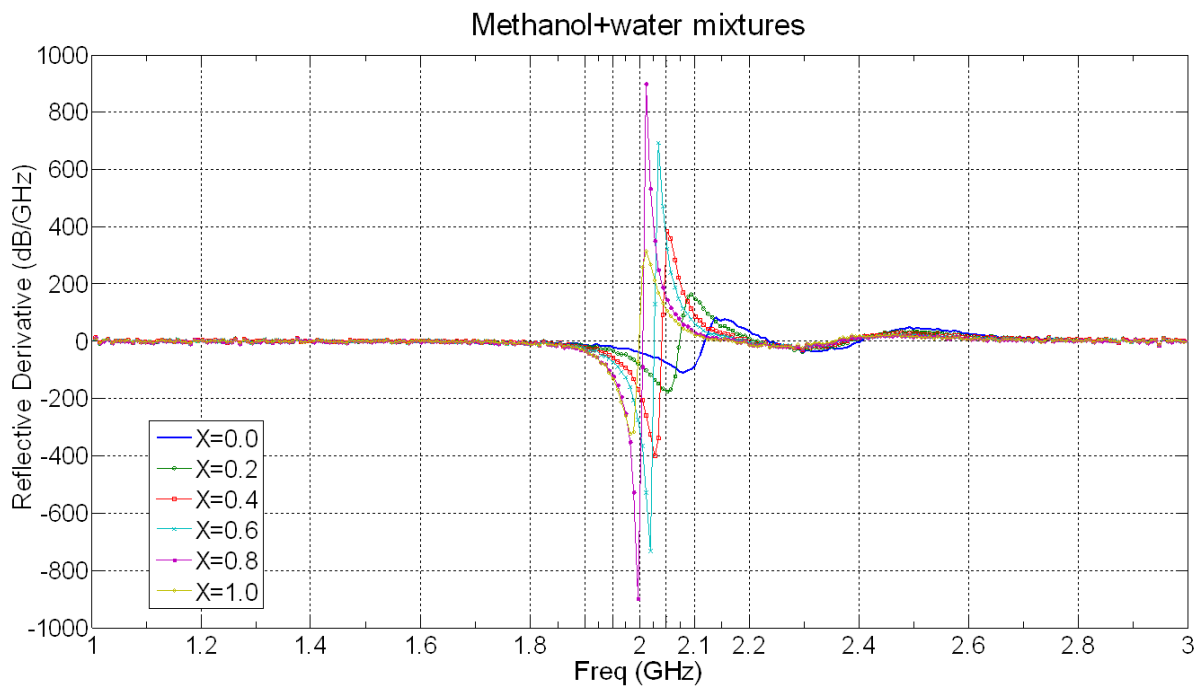


Figure 5-21. Dependency of steepness of reflection on (a) water-methanol samples and (b) water-2-propanol.

5.4 Conclusion

A novel microstrip-based metamaterial transmission line coupled with microfluidic channel is demonstrated for sensing of micro-liter volume of samples. Different liquids were mixed to attain varying complex permittivity as a function of frequency to be used to characterize the designed sensor. Micro-liter volume of liquid samples was injected in microfluidic channels that in turn load the MTM unit cell. The fluidic channels were routed directly above the locations on the spiral where the fields are strong in order to achieve high sensitivity. For water-methanol mixture, the resonance shifts by 7.6% when dielectric constant is varied from 26 to 80. For 2-propanol-water mixture, the resonant frequency shifts in 12.11% corresponding with the dielectric constant change from 4.6 to 80. Both dielectric constant and loss tangent affect the resonance value of the circuit structure. Higher dielectric constant leads to higher shift in resonance frequency. Moreover, higher loss tangent value in the sample causes a higher shift in resonance.

Results of this paper clearly show that CRLH-media can be used in making a promising sensor with very high sensitivity. Further improvements in sensitivity can be made by using a very thin chemical barrier PI layer between the copper traces and the microfluidic channels. It can lead to sensing of less sample volumes such as nano- to pico-liter volume ranges. The promising sensor can be used for sensing of various types of chemical and biological agents both in liquid and solid form. Furthermore, the frequency band of interrogation can be designed to sense specific samples in order to achieve high specificity along with high sensitivity.

CHAPTER 6

METAMATERIAL-INSPIRED COMPACT VOLATILE MOLECULAR SENSOR

Sensing in the microwave spectral region has gained significant attention for selective monitoring of biological and chemical compounds for rapid label-free characterization. Interrogation of minute amounts down to the molecular level without chemical label either by metal nanoparticles or light-emitting nanocrystals [48] is a critical requirement in order to maintain the samples in their original form during testing procedure. Therefore, microwave-inspired sensors that provide high sensitivity utilizing small volumes of samples and are low-cost are most desirable, and hold potential to meet this challenge. Here, a metamaterial based novel resonator structure is proposed and analyzed to comply with the above challenges. In particular, the proposed sensor that can easily be integrated on low-cost substrates for monitoring molecular level of vaporized samples.

6.1 Metamaterial-Inspired Resonator Probe

Metamaterials (MTMs) are artificial materials engineered to have unique electromagnetic properties that are difficult to achieve otherwise. Such electromagnetic properties rely heavily on the geometry of MTM-particles where sub-wavelength-engineered units are utilized as atoms and molecules as the determinants of electromagnetic properties [49-50]. This notion leads a new degree of freedom in the design of MTM-inspired microwave applications in particular of bio-sensing applications. These new types of sensors can significantly enhance sensitivity and selectivity while utilizing extremely small volumes of sample down to the molecular level.

Here, the novel MTM unit cell, named modified split ring resonator with open-gap (OmSRR) is proposed as a probe region of a new volatile molecular sensor. This unit cell was introduced and was validated for various compact microwave applications by our group [34-35, 49]. The unit cell structure is directly attached the edge of microstrip transmission line and the ring structures on each side of the transmission line forms a mirror image of each other. This configuration relaxes the ring structures from the coupling to each other. Since the resonator is connected to the microstrip line, the *E*-field directly excites the resonators rather than *H*-field. Within capacitive coupling, the microstrip line allows propagation of electromagnetic wave within a specific frequency. Normally, this structure can be easily considered as a simple *LC*-tank circuit that builds upon a half-wave open end microstrip resonator. Change in capacitance due to dielectric loading from biomolecules leads to a considerable shift in the resonance frequency of the circuit as

$$f_c = \frac{1}{2\pi\sqrt{LC}} \quad (6-1)$$

Figure 6-1 shows volatile molecules of vaporized liquid whirling around the OmSRR structure. As mentioned above, vapor acts as dielectric loading on the unit cell. Such volatile molecules cover the probe region and lead to change in effective capacitance. This phenomenon leads to a significant shift in resonance characteristics. Delta shift in resonance frequency can be interpreted to the unique properties of bio-molecular properties of samples.

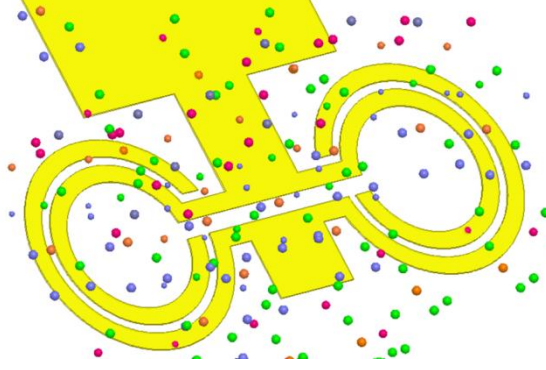


Figure 6-1. The representative of vapor-exposure on the volatile molecular sensor leading to a significant shift in resonant characteristics.

6.2 Design and Simulation

To validate the proposed design, Finite Element Modeling (FEM analysis by Ansoft HFSS) was utilized. The proposed sensor probe was designed and optimized for the desired center frequency, reflection loss (S11), bandwidth and high Q-factor by HFSS. Commercially available *Rogers RO3010* substrate having dielectric constant $\epsilon_r = 10.2$ and thickness $h = 1.27$ mm is used in the design and fabrication of the near-field probe. By tuning and optimizing physical dimensions of the structures, the proposed 1-port molecular volatile sensor based $50\ \Omega$ microstrip transmission line are designed with relevant dimensions are as follows: the outer (R_1) and inner (R_2) of radius rings = 1.25mm, 0.75mm, respectively, ring width = $200\ \mu\text{m}$, the gap between the rings = $100\ \mu\text{m}$, the open gap $G_1 = 200\ \mu\text{m}$, the length $L_1 = 3.75$ mm, $L_2 = 2.5$ mm, the width $W_1 = 1.2$ mm, $W_2 = 3.5$ mm as detailed in Figure 6-2. Simulated return loss of the designed resonator is clearly expressed in Figure 6-3 with high Q-factor of about 1140 at resonance frequency approximately 7.4 GHz.

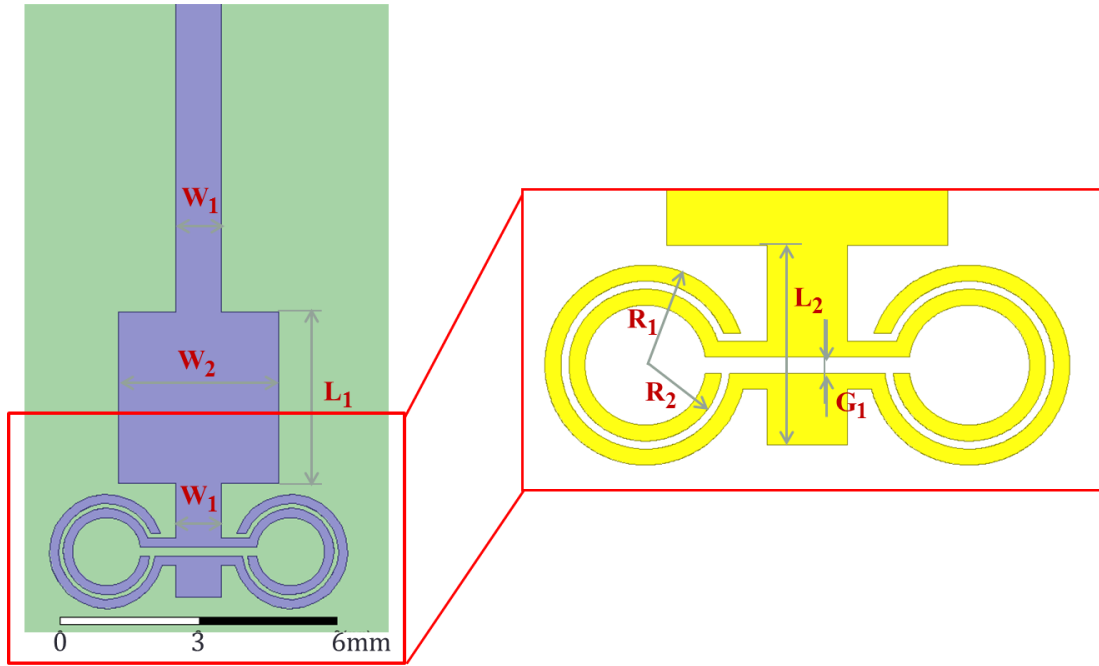


Figure 6-2. Configuration of the OmSRR inspired the volatile molecular sensor based 1-port microstrip technology.

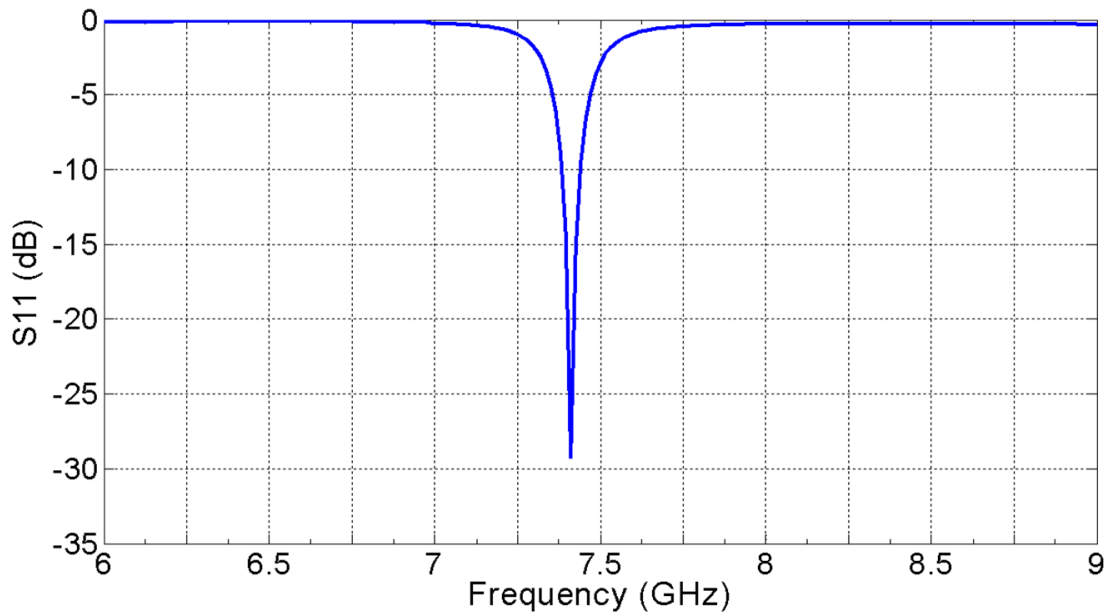


Figure 6-3. The simulated return loss, S11(dB) of the proposed volatile molecular sensor by Ansoft HFSS.

Normally, a microstrip resonator is able to contain at least one oscillating electromagnetic field and is exploited in the design of microwave circuits as open or short-circuited stubs. For the OmSRR, it can be represented as an open ended half wavelength transmission line that forms an effective LC resonant structure. Since the OmSRR is a MTM unit cell as described in Chapter 2, the circuit can be miniature and its LH phenomenon is exploited to achieve high sensitivity in sensor applications. Figure 6-4 shows the simulated E-field patterns at the resonance frequency in different sections of the circuit. As illustrated, the OmSRR unit cell region strongly confines the E-field and this region can be used in near-field sensing. To compare the field distribution, an open ended half-wave length transmission was also simulated having a similar resonant frequency. Figure 6-5 shows the simulated E-field pattern at the resonance frequency in different directions.

As expected, E-field of the conventional resonator is much less in strength than the OmSRR structure near the open end of the transmission line. The field also propagates slightly above the resonator structure. To analyze the structure as an antenna, the radiation efficiency of the structure was also calculated. From the simulation, the open-circuited half wavelength line and the OmSRR have the radiation efficiency of 0.0104 and 0.0023, respectively. It is well known that a half-wavelength microstrip resonator is a poor antenna. The radiation efficiency numbers confirm this point. It can be stated that the resonator built using OmSRR does not act as an antenna but a good resonator that stores energy in the LC component of the unit cell.

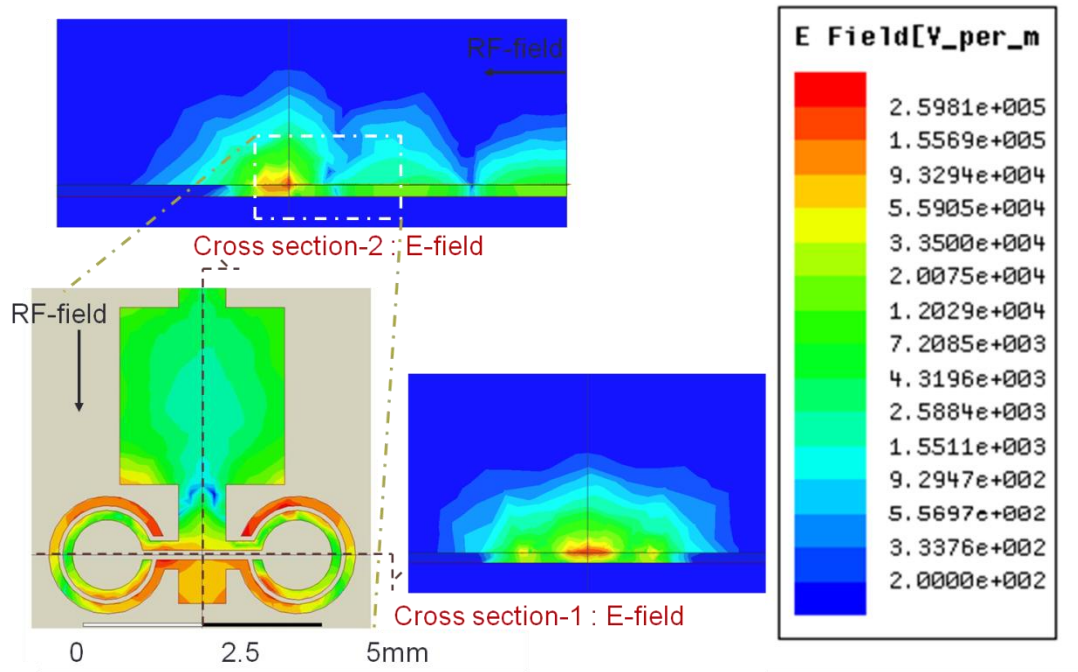


Figure 6-4. Simulated E-field pattern along the volatile molecular sensor based on OmSRR structure by Ansoft HFSS.

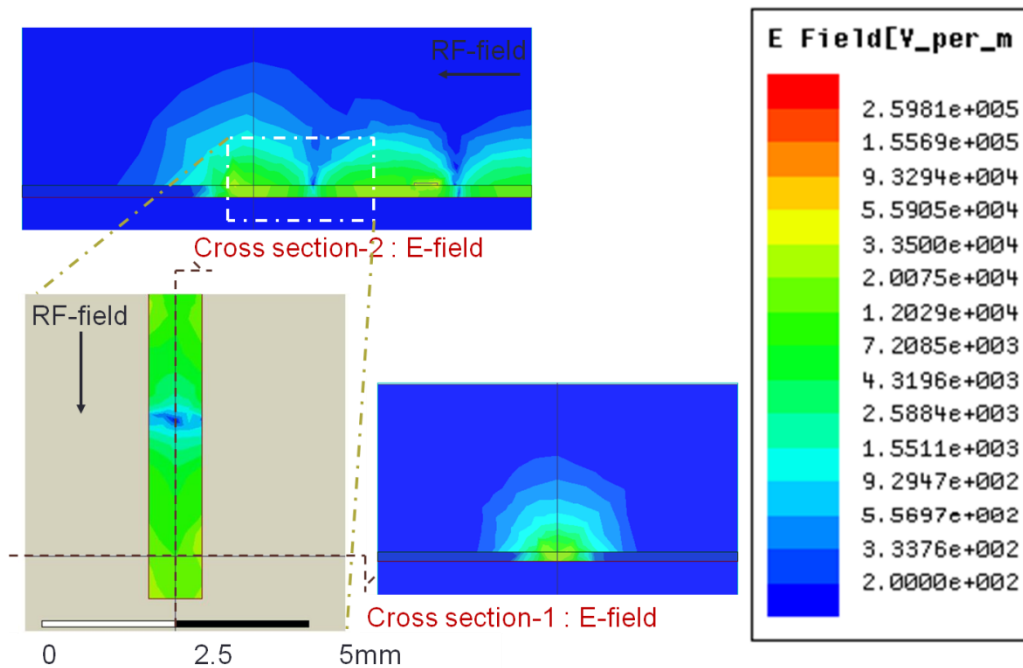


Figure 6-5. Simulated E-field pattern along an open-circuited half wavelength microstrip line by Ansoft HFSS.

6.3 Experimental Results

Since it is one dimensional uniplanar structure, the sensing probe is simple to fabricate using conventional microfabrication and is thus low-cost. The fabricated volatile molecular sensing probe is shown in Figure 6-6. In the volatile molecular sensing experiment, a 250 mL-bell jar is used to confine various vaporized liquid samples that easily evaporate into atmosphere within the bell jar as volatile molecules. The vaporized liquid samples were dropped and sealed inside the bell jar using a 1.0mL-syringe attached to Teflon tubing. The inner and outer diameters of the tubing are 0.8 and 1.6 mm, respectively. The sensor was installed and sealed inside the enclosed bell jar. The resonance frequency of the sensor is observed using a PNA network analyzer, N5227A. The experiment setup with a zoom-in picture is shown in Figure 6-7. When the vaporized liquid is dropped and sealed the molecules of the vaporize samples interact with the resonator structure leading to change in resonance frequency and Q-factor as shown in Figure 6-8.



Figure 6-6. Photograph of the fabricated OmSRR inspired compact volatile molecular sensor.

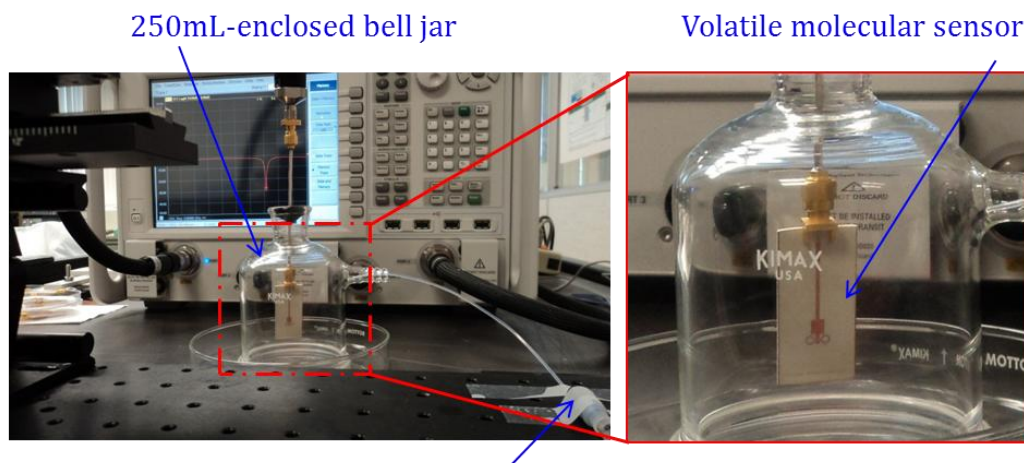


Figure 6-7. Measurement set-up of the compact volatile molecular sensing experiment. (inset-right) Zoom-in for the proposed unit cell inside the enclosed 250mL-bell jar.

In the experiment, two vaporized liquid samples, acetone and methanol are used to demonstrate and validate the proposed sensor. In general, different volatile liquids have their own unique saturated vapor pressure at normal atmospheric pressure and temperature. Consequently, they generate different quantities of volatile molecules inside the sealed jar. For qualitative analysis, the volatile molecules examined in this work are considered to be ideal gases and the volatile molecular concentration of each sample would be calculated based on ideal-gas law [52]. The temperature during the experiment is approximately 27°C and very dry

Figure 6-8 shows various shifts of resonance frequency of the sensor resulting from different droplets of the vaporized acetone sample. At beginning, the spectral resonance dip is positioned at 7.43 GHz. After dropping the acetone sample, the spectral resonance dip position is altered to 7.42 GHz, 7.41 GHz, 7.39 GHz, 7.37 GHz and 7.35GHz for the amount acetone volume at 0.05 mL, 0.10 mL, 0.15 mL, 0.20 mL, and 0.25 mL respectively. For vaporized methanol sample, the spectral resonance dip position is shifted to 7.42 GHz and 7.39 GHz for 0.05 mL and 0.10 mL of

methanol volume, respectively. The spectral resonance characteristics of different vaporized methanol molecules are shown in Figure 6-9.

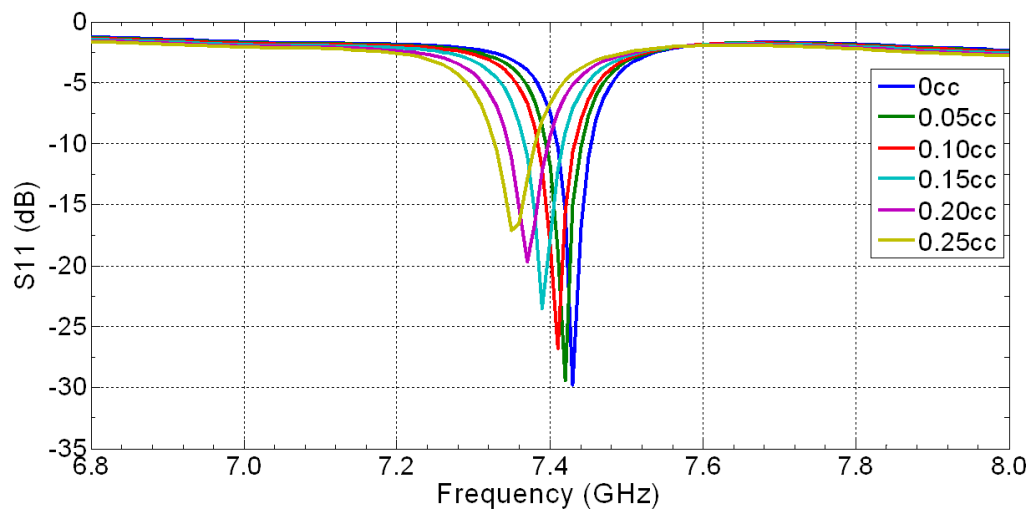


Figure 6-8. Measured resonant frequency as a function of different concentrations of acetone vapor in the bell jar.

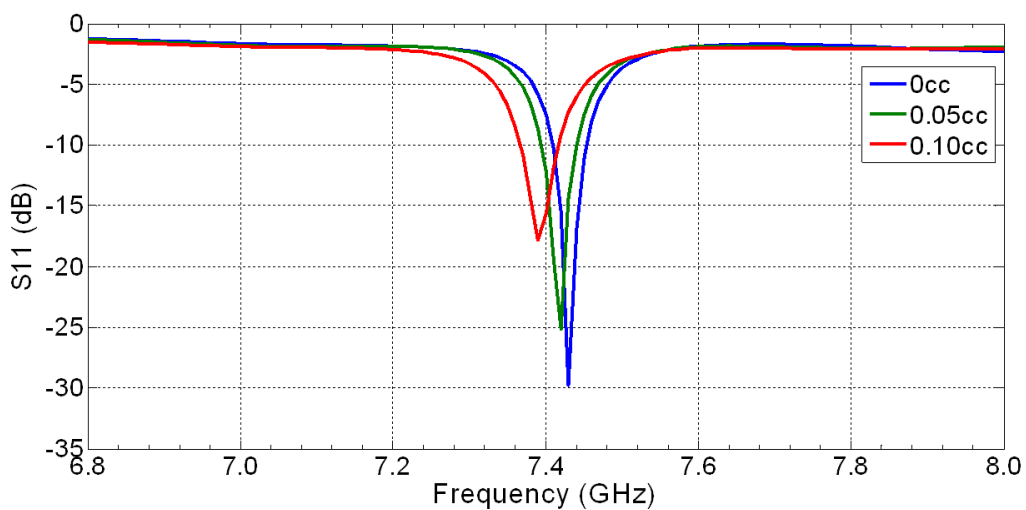


Figure 6-9. Measured resonant frequency as a function of different concentrations of methanol vapor in the bell jar.

It is important to note that the resonance frequency hardly changes when more than 0.25 mL, and 0.10 mL for acetone and methanol, respectively are dropped inside the jar. As expected, the number droplets of methanol liquid are less than of acetone liquid for meeting the saturation point of the volatile molecular density in the experiment. This is reasonable because the vapor pressures of acetone and methanol at 1 atmosphere and 30°C are approximately 285 mm-Hg and 157 mm-Hg, respectively [51-52]. The essential parameters from this experiment are summarized in Table 6-1.

Table 6-1. Summary of the essential parameters in the experiment.

	Acetone	Methanol
Vapor Pressure (torr) at 30°C	285	157
Density (g/mL)	0.791	0.7918
Molar mass (g/mol)	58.081	32.04
1-Droplet (cc, mol)	0.05	0.05
: mass (g)	39.55×10^{-3}	39.59×10^{-3}
: molecules (mol)	6.860946×10^{-4}	12.35643×10^{-4}
250mL-Enclosed Bell Jar		
: molecules (mol)	37.68647×10^{-4}	20.76062×10^{-4}
: #droplets (0.05cc / droplet)	5.534	1.680

According to specific vapor pressure and the ideal gas law [52], the maximum densities of vaporized molecules in the experiment which are present in the gas phase at equilibrium are approximately estimated at $13.62 \times 10^{-9} \text{ mol/mm}^3$ and $8.00 \times 10^{-9} \text{ mol/mm}^3$. The relation between molecular concentration (density) and spectral dip-shift relative to the original resonance frequency of 7.43 GHz is shown in Figure 6-10. The non-linear trend of vaporized

acetone is fitted as $y = -0.013743x^3 + 0.49736x^2 + 1.3616x + 0.47619$ with norm of residuals is 2.3726, where the spectrum deviation in the experiment is 10 MHz based on repeatable measurements of resonance frequency shift.

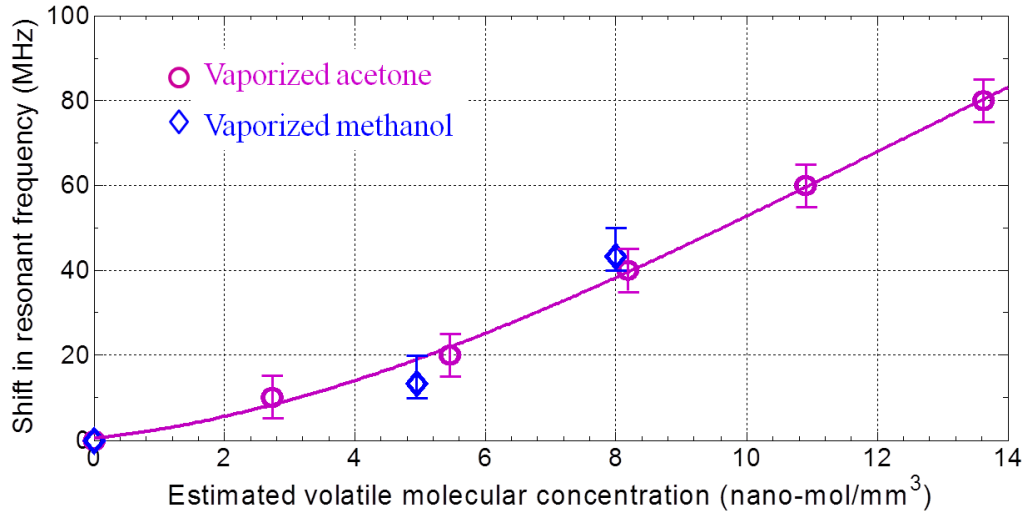


Figure 6-10. Correlation of shift-in resonant frequency and estimated volatile molecular concentrations of vaporized acetone and methanol.

Table 6-2 summarizes key measured characteristics of the resonator when exposed to different solvent vapors and their concentrations. As expected, a delta shift in resonance frequency is dictated by the number of volatile molecules in air and which is proportion to the effective dielectric constant. For higher concentration the frequency shifts to lower resonance frequency values and vise versa. Generally, each vaporized liquid has a unique dielectric constant and loss tangent values. The loss-tangent affects the Q-factor of the resonator. Thus, by measuring resonance frequency and Q-factor vapors could be uniquely identified. With the same number of molecular density, the resonator loaded acetone vapor has a Q-factor higher than methanol. It can be interpreted that the loss tangent of methanol is higher than acetone. For

example, at approximately 8 mol/mm^3 , the Q-factor of vaporized acetone is 827 as compared to a Q-factor of 353 for methanol. It can be interpreted that the loss tangent of methanol is higher than that of acetone. These results correlate with those reported in refs. [52-53]. According to these references, the loss tangent of methanol and acetone are approximately 1.0145 and 0.1430 at 7.50GHz, respectively.

Table 6-2. Q-factors and resonance frequency, f_c of the proposed sensor with different vaporized liquid loads

	No Load	Acetone (mL)					Methanol (mL)	
	0	0.05	0.10	0.15	0.20	0.25	0.05	0.10
f_c (GHz)	7.43	7.42	7.41	7.39	7.37	7.35	7.42	7.39
Q-factor	1675	1508	1183	827	450	291	931	353

6.4 Conclusion

In conclusion, a novel high-Q MTM resonator-inspired volatile molecular sensor has been proposed and successfully demonstrated. It is a promising sensor for the detection down to the molecular level with very high sensitivity and selectivity. The shift in resonance frequency can be used to recognize the molecular density. Moreover, the Q-factor can be exploited to classify types of volatile molecules surrounding the sensor. A larger loss tangent leads to the lower Q-factor of the spectral resonance. Such a MTM-inspired sensor could potentially be used in gas sensing applications or low density analyses such as toxic gas or bio-chemical detection. Also, it can be utilized in the design of wireless moisture sensors.

CHAPTER 7

METAMATERIAL-INSPIRED MICROWAVE PROBES

Metamaterials (MTMs) are defined as homogeneous electromagnetic structures which exhibit unique electromagnetic properties such as backward wave propagation and negative refraction [1-6], [53-55]. These properties rely heavily on the geometry of metamaterial particles where subwavelength-engineered units are utilized as atoms and molecules as the determinants of electromagnetic properties [5], [54-55]. Such a concept allows higher degree of freedom in the design of new types of sensors that significantly enhances sensitivity and specificity while utilizing small volumes of samples.

7.1 Microwave Sensing Probes

Among the many MTM unit cell designs, metal split ring resonators (SRRs) are studied the most. In these structures, the excitation of time-varying magnetic field component (H -field) in perpendicular to the plan of the rings. This leads to induced resonating current in the loop and generate an equivalent dipole moment which exhibit negative electromagnetic permeability [2], [5-6], [55-56]. Such a structure excited by a microstrip transmission line holds great potential for bio-sensing [33], [57]. This structure can be considered as a simple LC resonance circuit, the change in capacitance due to dielectric loading from biomolecules leads to a considerable shift in the resonance frequency f_c which is given by equation (7-1). Measurement of delta shift in resonance frequency allows direct sensing of biomolecules.

$$f_c = \frac{1}{2\pi\sqrt{LC}} \quad (7-1)$$

On a similar line in our previous study [33], a uniplanar double spiral metamaterial structure was utilized in the design of microfluidic sensors. In that design, shift in resonance frequency was observed due to dielectric loading by various chemical solutions. It was demonstrated that dielectric relaxation could be measured using metamaterial structures. The proposed structure builds upon these designs by incorporating a built in reference resonator to improve signal to noise ratio (S/N) while simplifying calibration of these sensors. Two metamaterial unit cell designs were studied and are presented here. Also, one of the designs is further enhanced to measure multiple samples simultaneously using single input/output ports. Details of these two designs are discussed below.

7.1.1 Modified Split Ring Resonators

This topology is based upon the novel MTM unit cell, termed here as modified split ring resonator (mSRR). This structure was presented in ref. [34] for compact microwave circuit design applications. In this structure, the unit cell is directly connected to the edge of the microstrip transmission line as shown in Figure 7-1(a). The resonators on each side of the transmission line forms a mirror image of each other. This relaxes the coupling between the two structures. Since the resonator is attached to the microstrip line, the E -field component directly excites the resonators rather than the H -field component. The microstrip line allows propagation of electromagnetic wave within a specific frequency band. Consequently, the mSRR unit cell exhibits band-pass transmission characteristics. Figure 7-1(b) depicts a cross section of a microstrip line with the incident electric and magnetic field components (E -field and H -field) in

a direction perpendicular to the surface of the mSRR unit cell. This mSRR structure can be used for sensing by introducing a sample in the gap between the rings which modifies the coupling capacitance. Since the coupling between the two sides is weak, one side of the unit cell can be used as a reference while the other side can be used as a sensing probe.

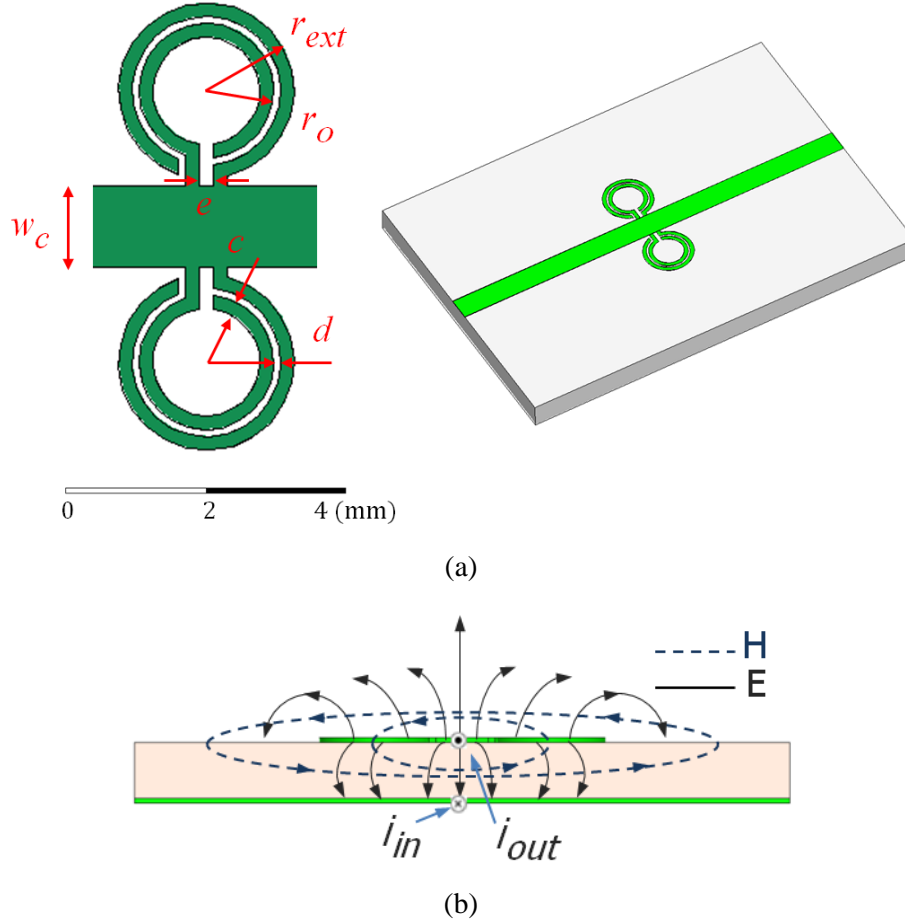


Figure 7-1. (a) Microstrip transmission line coupled mSRRs sensing probe, (b) Cross section of a microstrip transmission line with schematic E -field and H -field distributions.

7.1.2 Reflective Split Ring Resonators

This design of reflective split ring resonators (rSRRs) is based on conventional design in which the SRR are edge coupled to a microstrip as shown in Figure 7-2(a). Here these resonators are excited by time-varying H -field of the microstrip transmission line. Rather than being

directly attached, each resonator is located in close proximity to the microstrip line for edge coupling. Figure 7-2(b) shows a cross section of a microstrip line with the incident electric and magnetic field components (E -field and H -field) in a direction perpendicular to the surface of a pair of SRRs. The microstrip line performs independent of these resonant structures except at resonant frequency. Upon excitation, high- Q resonators lead to narrow band-suppression of transmitted coefficient. Similar to the above design, two resonators are edge loaded forming a mirror image to each other. One side can be used in probing the sample and the other side as a reference.

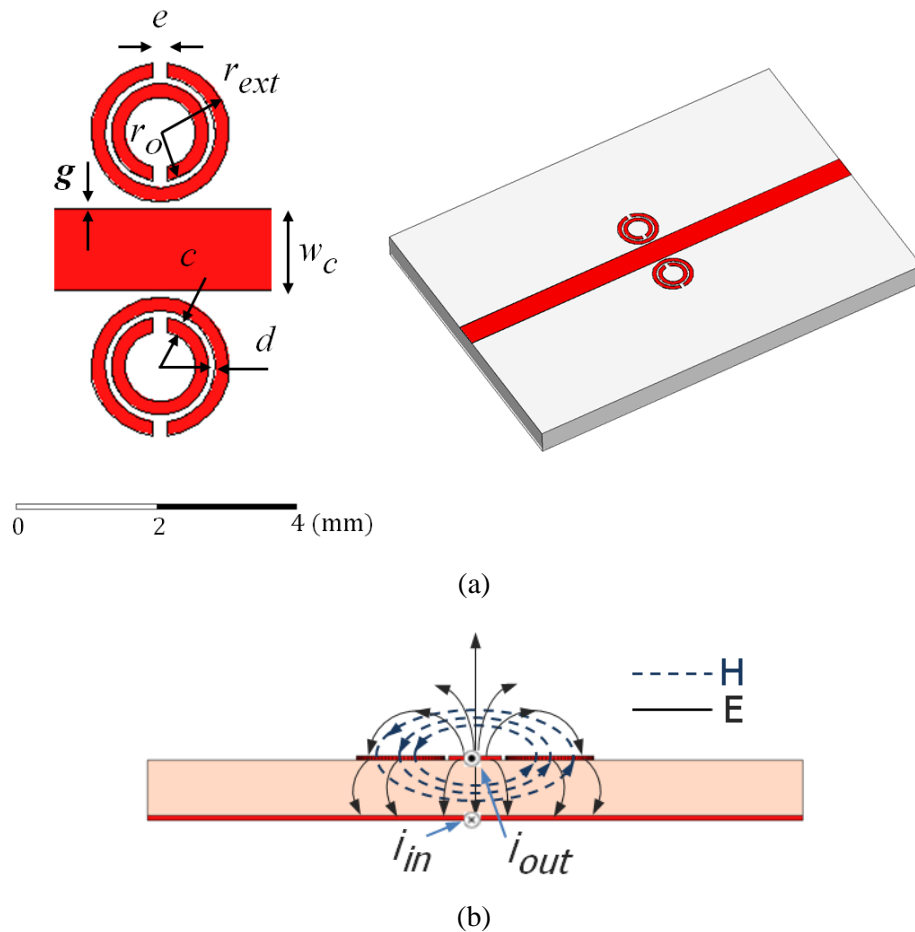


Figure 7-2. (a) Microstrip transmission line coupled rSRRs sensing probe, (b) Cross section of a microstrip transmission line with schematic E -field and H -field distributions.

7.2 Design and Simulation

Both of the proposed unit cells of Figure 7.1 and 7.2 were designed to operate near 10GHz using Finite Element Modeling (FEM)-analysis by Ansoft HFSS®. Commercially available Rogers RO3010 substrate having dielectric constant $\epsilon_r = 10.2$ and thickness $h = 1.27$ mm is used in the design and fabrication of these near field probes. The microstrip line integrated with MTM unit cell has a line width of 1.2 mm corresponding to the characteristic impedance of 50 Ω .

7.2.1 Modified Split Ring Resonators

The layout of the modified split ring resonators (mSRRs) unit cell was optimized for center frequency, bandwidth and transmission loss, and the following parameters were extracted: ring width $c = 0.2$ mm, distance between the rings $d = 0.1$ mm, average radius between rings $r_{av} = 1.03$ mm, and slot width $e = 0.2$ mm. Simulated scattering parameters are shown in Figure 7-3. The resonance frequency, return loss (S11), of unit cell is at 10 GHz with an insertion loss of less than 1 dB. It is important to note that the physical layout of mSRR-geometry is approximately $\lambda/12$ of free space wavelength. The simulated electric field (E -field) and induced surface current distribution at resonance frequency are illustrated in Figure 7-4. At resonant frequency, the electric field becomes intense over the ring structures resulting band-pass transmission characteristic. Also, the distribution of surface current density is concentrated on the edge between the strip line and unit cell due to passband characteristics of the circuit.

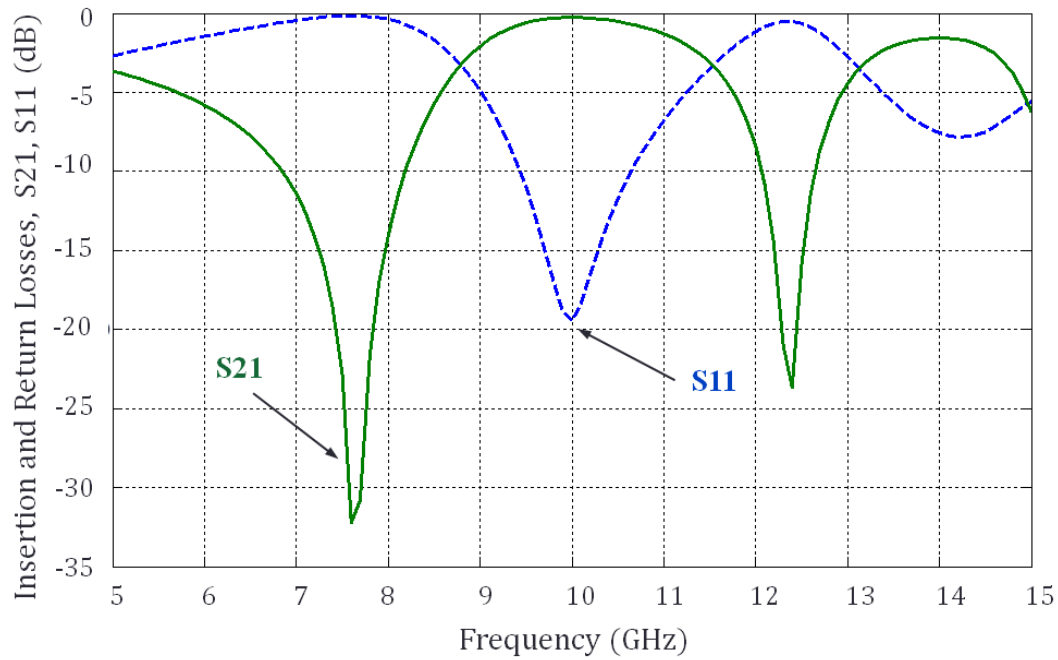


Figure 7-3. Simulated scattering parameters (S21 and S11) of the mSRR-inspired microwave sensing probes.

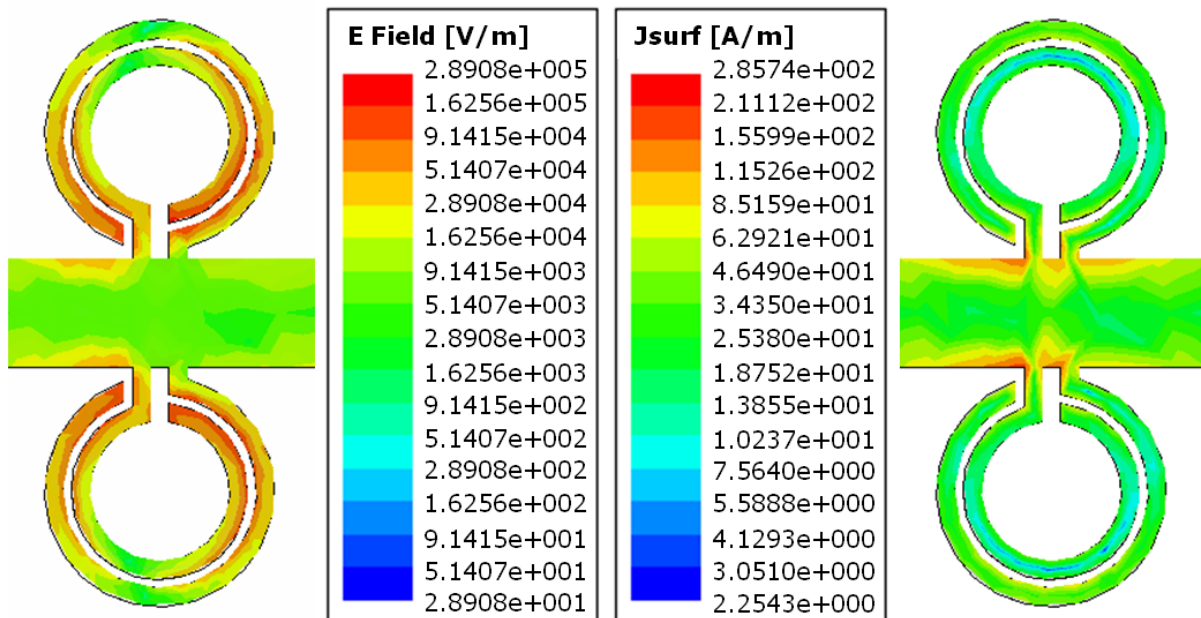


Figure 7-4. Simulated, using Ansoft HFSS®, fields overlays at resonance frequency of mSRRs *E*-field (left), surface current density distribution (right).

7.2.2 Reflective Split Ring Resonators

Optimized dimensions of the reflective split ring resonator (rSRRs) structure are as follows: ring width $c = 0.2$ mm, the gap between the rings $d = 0.1$ mm, average radius between rings $r_{av} = 0.76$ mm, the gap between each resonator and the microstrip line $g = 0.1$ mm, and split-gap of each ring $e = 0.2$ mm. Figure 7-4 shows the resonance of insertion loss (S21) having the magnitude of -20.5 dB at approximately 9 GHz. The effective dimension of the rSRR-geometry is approximately $\lambda/16$ in size in free space wavelength. At resonant frequency, surface current flowing on the medium is effectively induced by the time varying H -field component from the microstrip line in parallel to the axis of the resonators. Such surface current therefore generate magnetic field that is in a dipolar pattern. The resonator can thus exhibit resonance wavelength much larger than the diameter of the rings.

Simulated electric field (E -field) and induced surface current distribution at resonance frequency are expressed in Figure 7-5. At resonance, the electric field intensity is reduced thus showing band-stop transmission characteristic. In addition, there is concentration of surface current distributions on the edges of the inner and outer rings due to the proximity effect and well-known Maxwellian distribution [9].

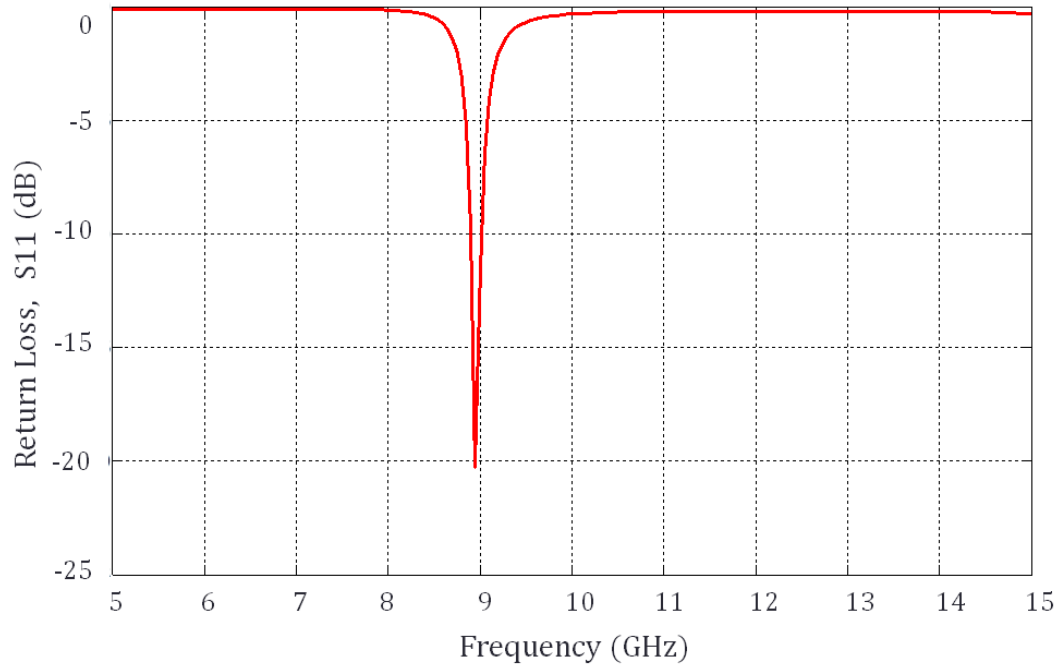


Figure 7-5. Simulated scattering parameters (S_{21} and S_{11}) of the rSRR-inspired microwave sensing probes.

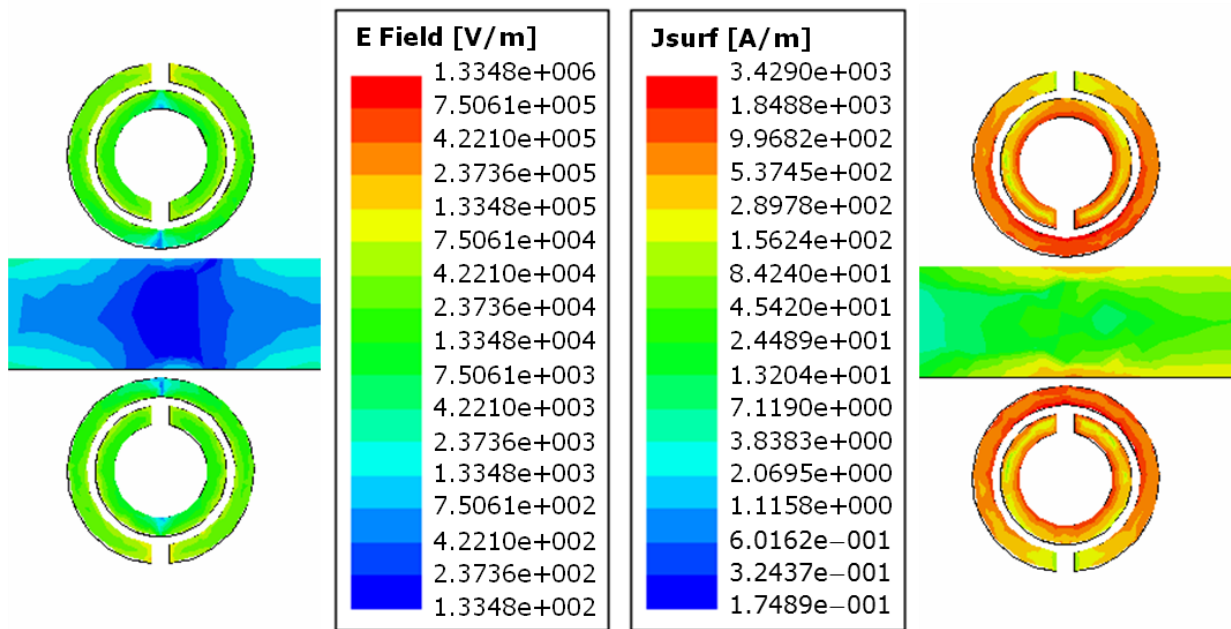


Figure 7-6. Simulated, using Ansoft HFSS®, fields overlays at resonance frequency of rSRRs E -field (left), surface current density distribution (right).

7.3 Experimental Results

In order to demonstrate the above design for sensing applications, the designs were fabricated using standard photolithography on *Roger* RO3010 substrates. The substrate has dielectric constant $\epsilon_r = 10.2$ and dielectric height $h = 1.27\text{mm}$. Only the top side was patterned and the ground plane was left intact. Connectors were mounted on both ends of the microstrip TL. Measurements of S-parameter were carried out using a PNA network analyzer.

7.3.1 Experiments on Modified Split Ring Resonators

Figure 7-7 shows a fabricated microwave sensing probe with a zoom-in picture of the mSRR unit cell. The measured insertion loss (S21) of the microwave sensing probe based mSRRs is shown in Figure 7-8 comparing with the simulated result. It is clear that they are matched very closely. The resonance frequency is approximately 7.6 GHz and it is used to be an effective microwave parameter of the sensing probe. The insertion loss is approximately 1 dB at 10 GHz. Since the mSRR can be considered to be a simple *LC*-circuit, the resonance frequency as Equation (7-1), can be altered depending on the changes of capacitor and/or inductor in the circuit. In this case, dielectric constant of air ($\epsilon_r = 1.0$) is used to be as a reference. If this microwave sensing probe is used to characterize dielectric constant of a material under test (MUT), the resonance frequency is shifted towards lower side. This is because the effective *LC* parameter of the circuit becomes greater from MUT. As a result, the more the dielectric constant of MUT is, the lower the resonance frequency will be.

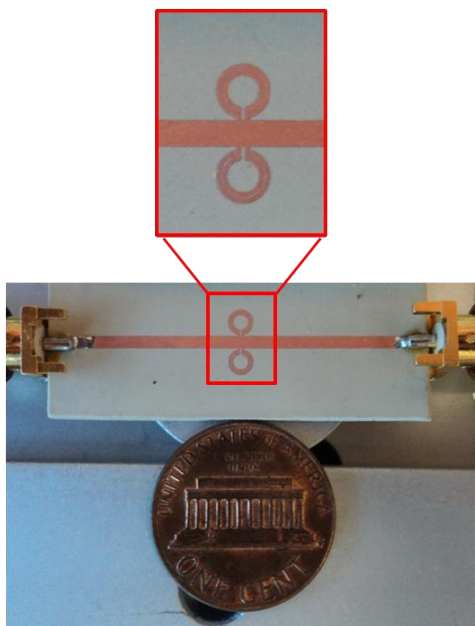


Figure 7-7. Photograph of a fabricated microwave sensing probe based mSRRs (inset) a blow-out of the figure showing the mSRR structure.

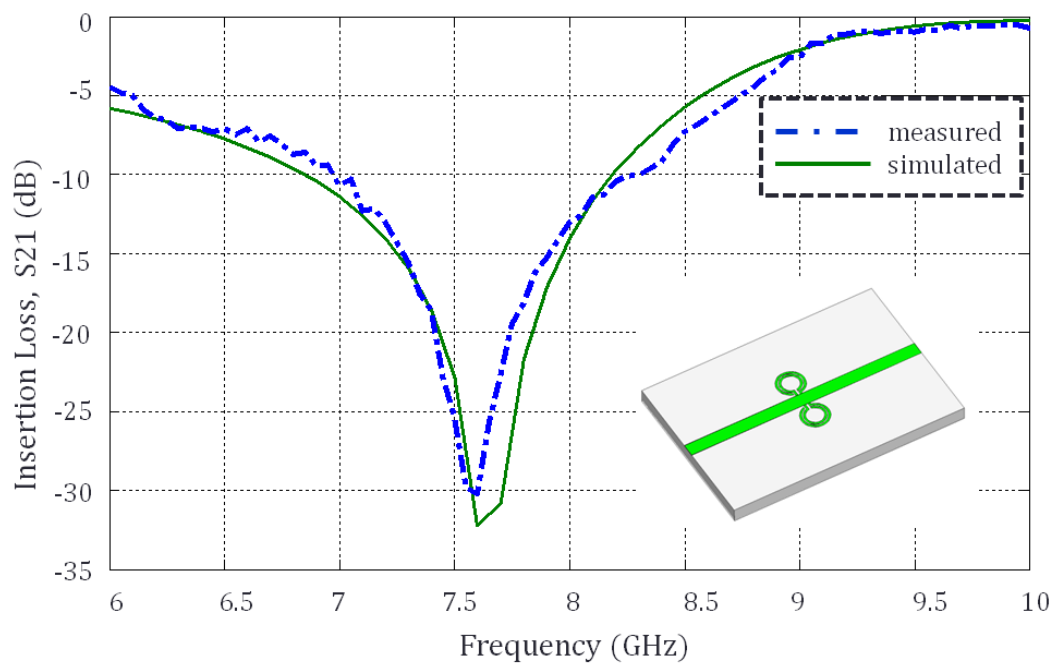
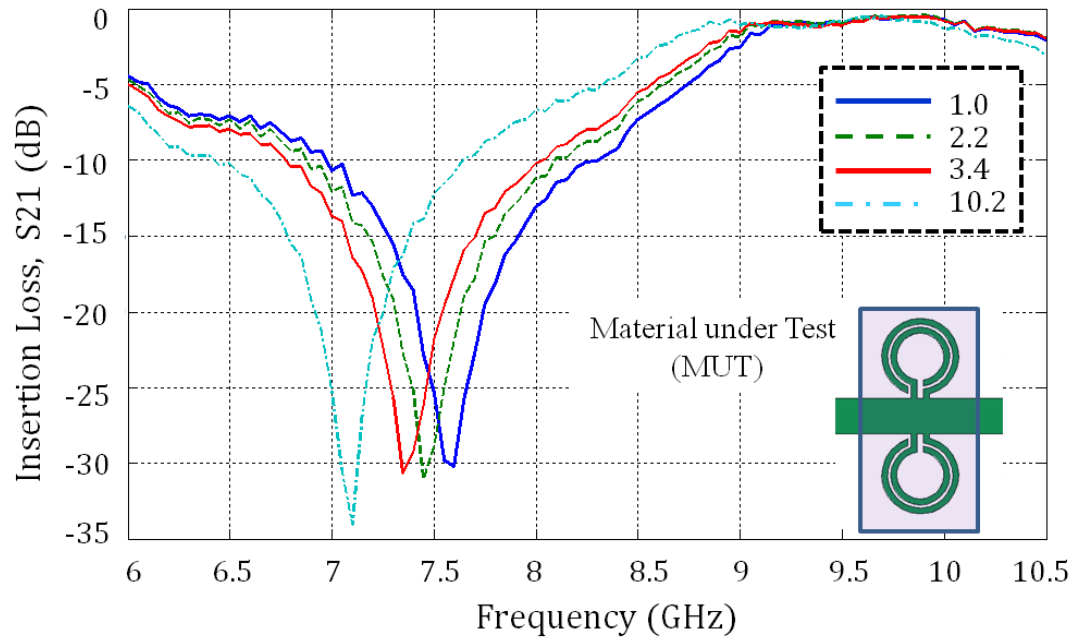


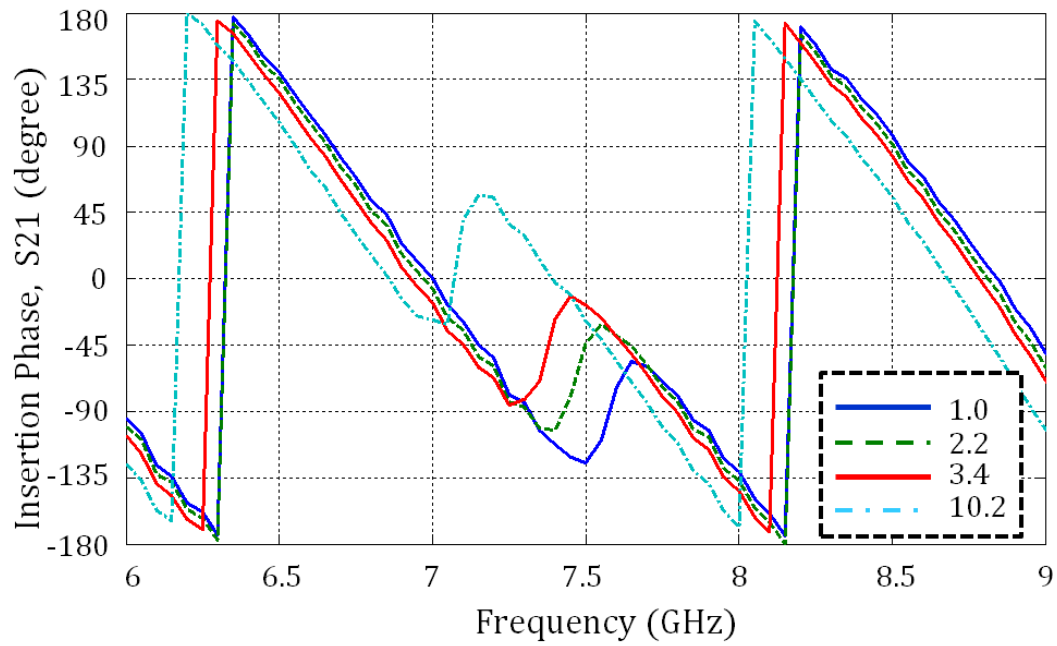
Figure 7-8. Measured and simulated insertion loss (S_{21} , dB) of mSRRs based sensing probe.

Figure 7-9(a) shows the measured results of insertion loss (S21, dB) and insertion phase (degree) before and after loading with a sample. Three dielectric materials having different dielectric properties from *Rogers*® were used to characterize the mSRRs probes. Dielectric materials, samples, used includes RT5880 ($\epsilon_r = 2.2$), RO4003 ($\epsilon_r = 3.4$), and RO3010 ($\epsilon_r = 10.2$). The natural resonance frequency, without the sample, is 7.60 GHz. Upon loading, the resonance frequency is shifts down with increasing dielectric constant of the sample. The resonance frequency shifts to 7.45 GHz, 7.35 GHz, and 7.10GHz upon loading with samples RT5880 ($\epsilon_r = 2.2$), RO4003 ($\epsilon_r = 3.4$), and RO3010 ($\epsilon_r = 10.2$), respectively. These measured results are also plotted in Figure 7-10. Alternatively, the insertion phase can be used in measuring shift in resonance frequency. Measured insertion phases are shown in Figure 7-9(b) for different sample loadings.

For the next study, RT5880 is used as a reference sample placed on one side of the mSRR structure while a sample is introduced on the opposite side, See inset of Figure. 7.10(a). The dielectric constant of the reference sample, RT5880 ($\epsilon_r = 2.2$), is more than dielectric constant of air ($\epsilon_r = 1.0$) and the resonance frequency shifts to a lower frequency (7.5 GHz). Upon introducing samples on the opposite side, the resonance frequency shifts to 7.45 GHz, 7.40 GHz, and 7.21GHz for RT5880, RO4003, and RO3010, respectively. This shows that the resonant frequency shift can be tailored for a desired reference dielectric sample.

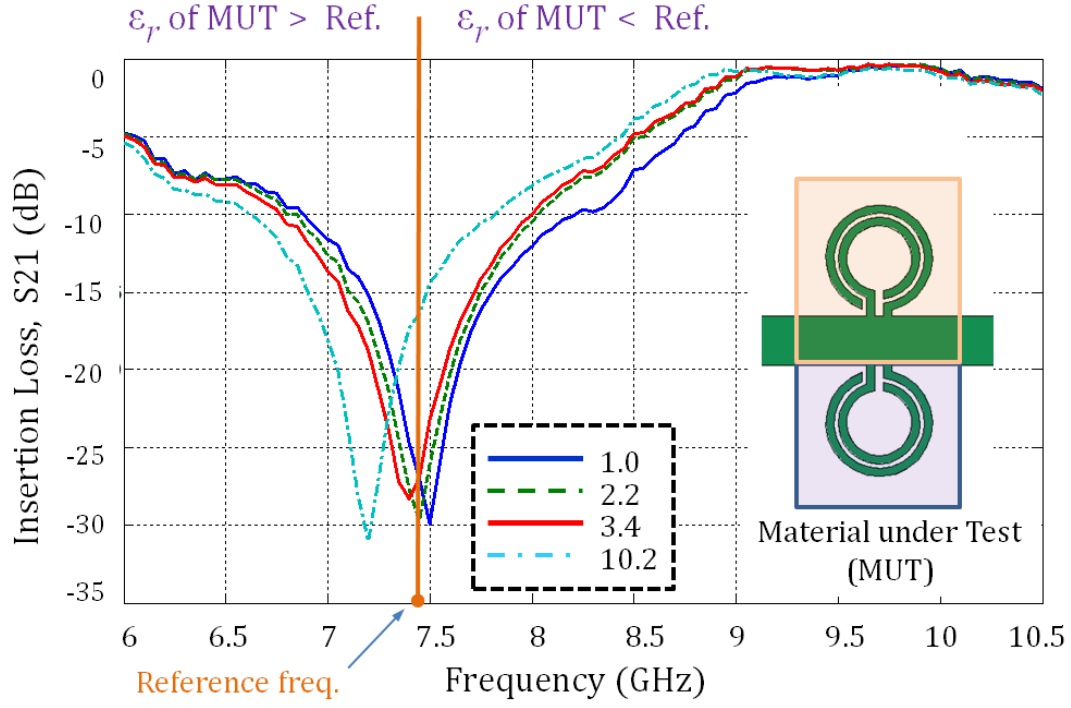


(a)

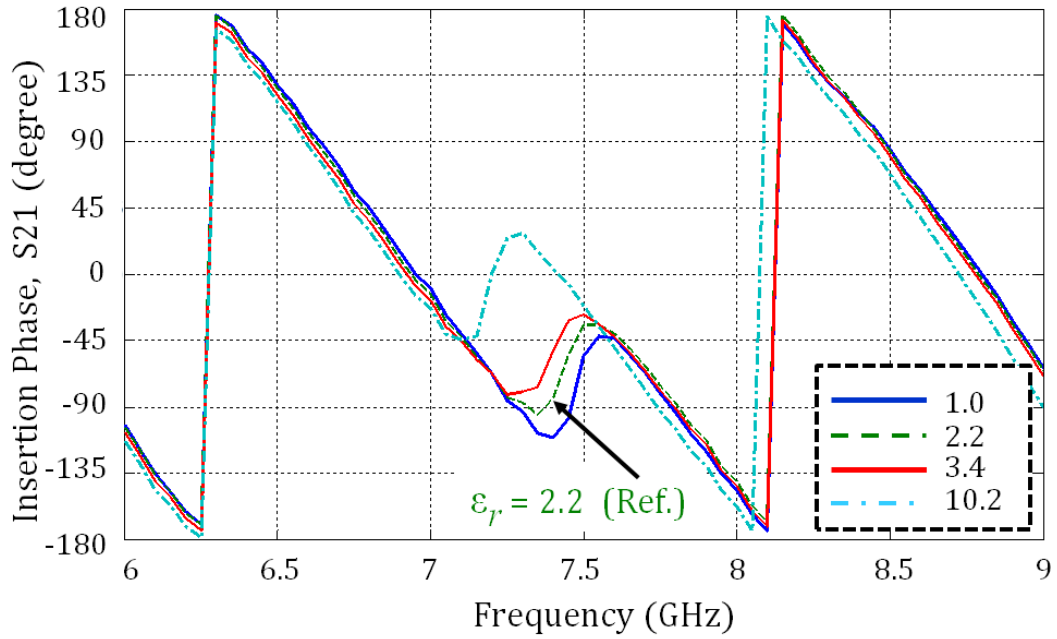


(b)

Figure 7-9. (a) The measured insertion loss (S_{21} , dB) and (b) the measured insertion phase (degree) of the mSRRs sensing probe loaded with different dielectric constant samples.



(a)



(b)

Figure 7-10. (a) The measured insertion loss (S_{21} , dB) and (b) the measured insertion phase (degree) of the mSRRs sensing probe loaded with different dielectric constant samples (one-side is loaded by reference dielectric material).

Figure 7-10 shows the measured results of insertion loss (S_{21} , dB) and insertion phase (degree) for different dielectric loadings. Other than the magnitude of S_{21} , the phase can also be exploited in characterizing the samples. Figure 7-10(b) shows the measured phase for different sample loadings. The correlation between the shift in resonance frequency and dielectric constant using RT5880 as reference is plotted in Figure 7-11. This approach allows a simple approach to compare two samples using a single probe. If the dielectric constant of the sample is higher than the reference, frequency shifts to higher values. On the other hand, the shift is to lower frequency if the sample has a lower dielectric constant than the reference sample.

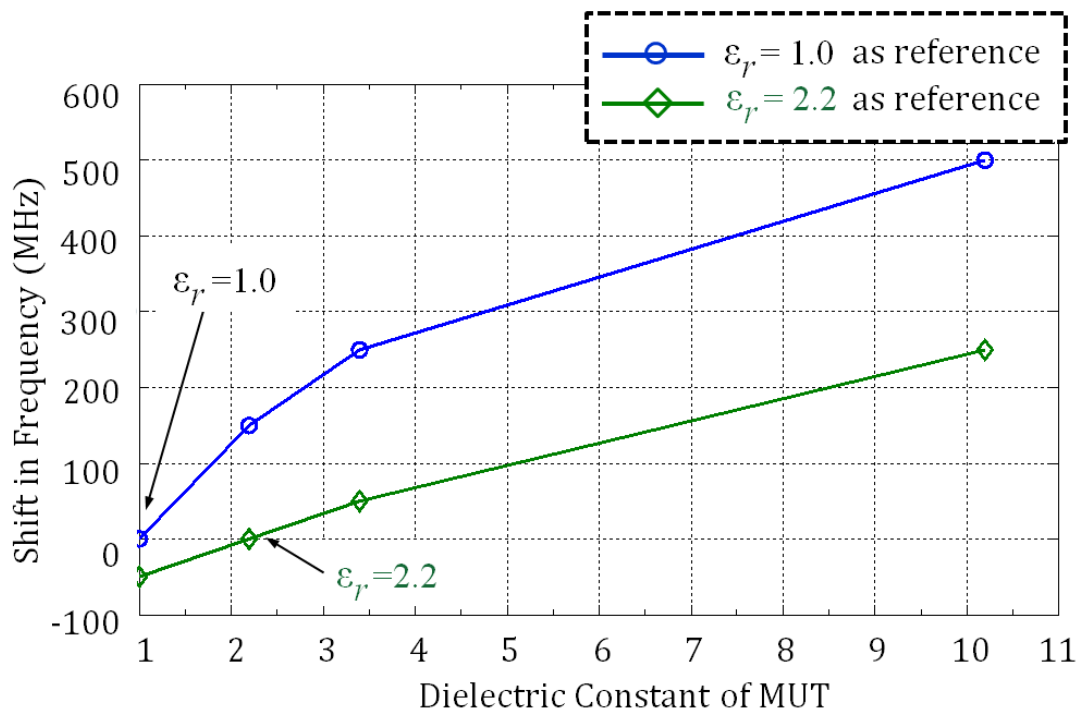


Figure 7-11. Shift in resonance frequency as a function of dielectric loading relative to two different reference samples.

7.3.2 Experiments on Reflective Split Ring Resonators

This structure is a band-stop structure, thus it allows in the integration of multiple unit cells on the same microstrip transmission line. Two rSRR unit cells were designed and incorporated on a single microstrip line, having center frequencies of 7 and 9 GHz. For the 7 GHz resonator structure, the dimensions are as follows: ring width $c = 0.2$ mm, the gap between the rings $d = 0.2$ mm, average radius between rings $r_{av} = 0.98$ mm, the gap between each resonator and the microstrip line $g = 0.1$ mm, and split-gap of each ring $e = 0.2$ mm. It is important to note that the effective dimension of such a rSRR-geometry corresponds to approximately $\lambda/16$ of free space wavelength.

Figure 7-12 illustrates the fabricated array of the microwave sensing probe based rSRRs with a zoom-in picture of two rSRRs unit cells that were incorporated an array. The bigger unit cells have resonance frequency at 7 GHz and the smaller ones have resonance frequency at 9 GHz. Figure 7-13 shows the measured and simulated insertion loss (S_{21} , dB) of rSRRs inspired the array of microwave sensing probe. Measured and simulation results match very closely. Measured resonance frequencies of the fabricated structure were 8.81 GHz and 7.05 GHz as compared to 8.83 GHz and 7.03GHz for the simulation results.

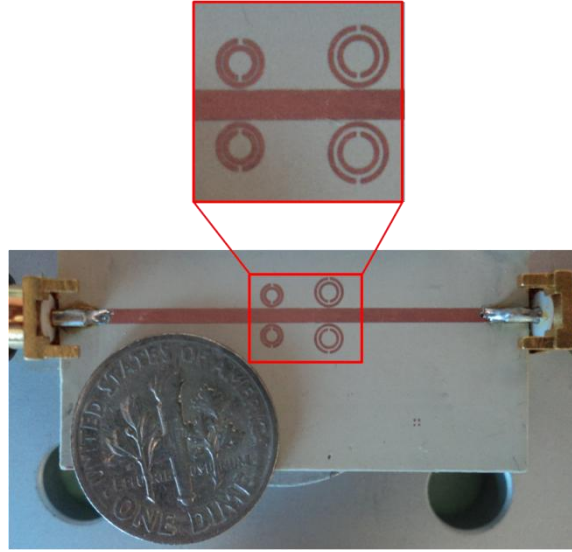


Figure 7-12. Photograph of a fabricated microwave sensing probe based rSRRs, (inset) a blow-out of the figure showing arrayed rSRR structure.

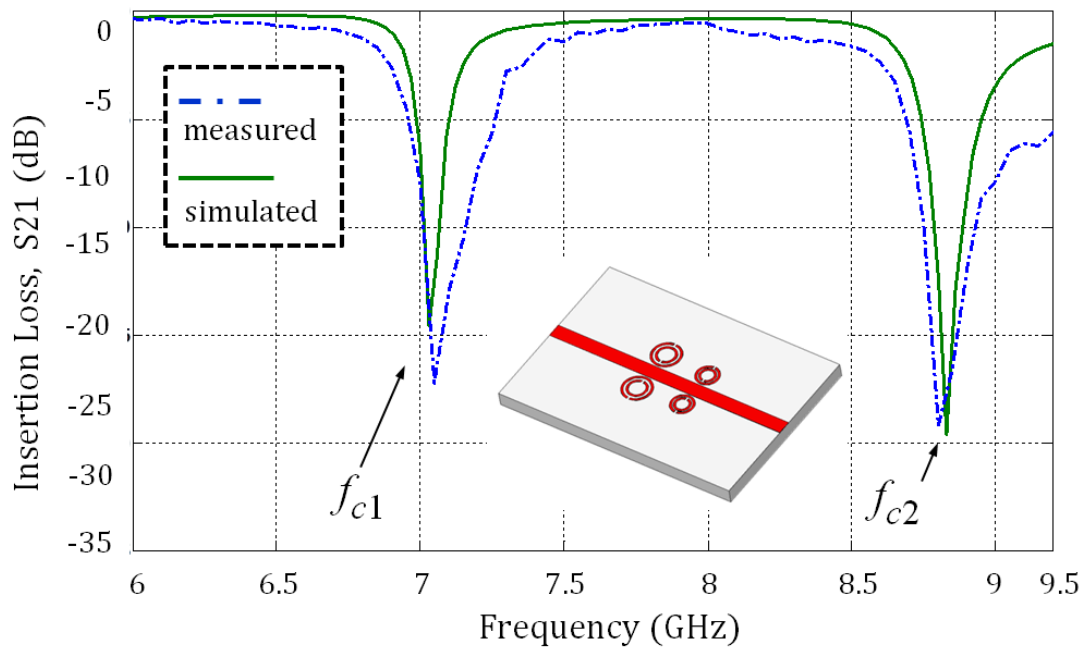


Figure 7-13. Measured and simulated insertion loss (S21, dB) of an array of microwave sensing probe utilizing rSRRs, (inset) the structure model of the sensing probe.

To characterizing these structures for sensing applications, the resonators were loaded with dielectric samples. Figure 7-14 shows the measured results of insertion loss (S_{21} , dB) after loading one side of the 7GHz resonator using RO3010 ($\epsilon_r = 10.2$). As a result, there are 2 resonance frequencies that originate from each unit cell, 5.95 GHz and 7.1 GHz. Since rSRRs are weakly coupled to each other, one side maintains its original frequency and the loaded sided resonates at a lower frequency. A delta shift in resonance frequency is dictated by the dielectric properties of the sample. The second unit cell (9 GHz cell) still maintains its original frequency as seen in Figure 7-14. This clearly shows that such a structure can be utilized in designing a probe that allows interrogation of multiple samples and also allows in building structures for reference frequency measurements.

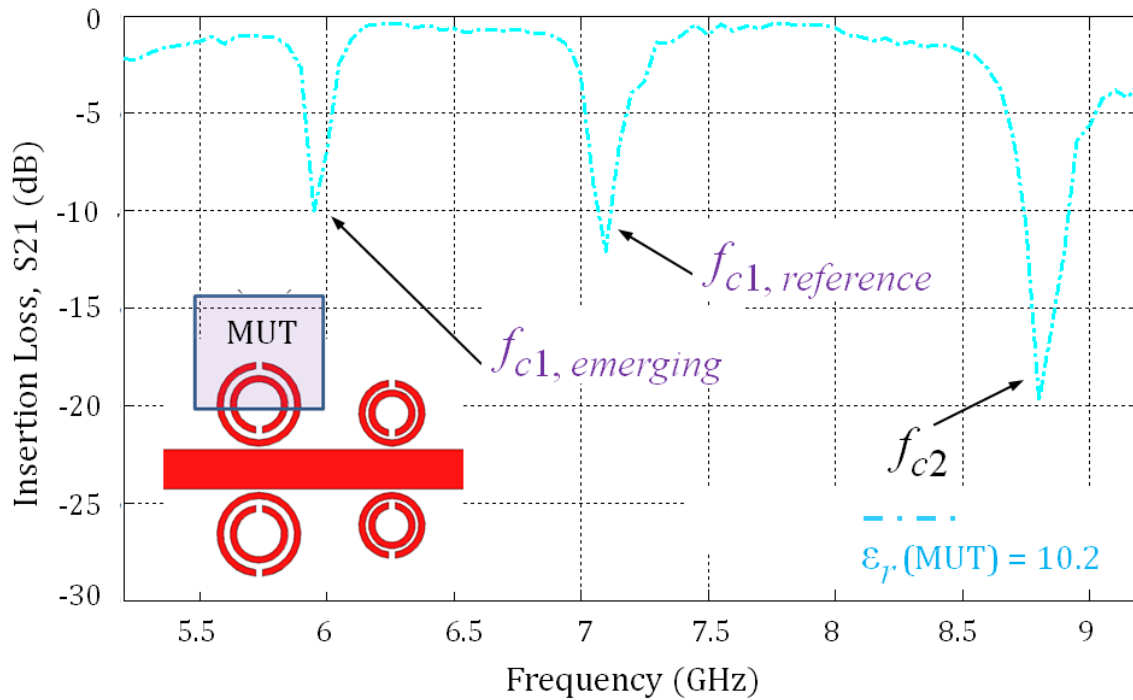


Figure 7-14. Measured insertion loss (S_{21} , dB) of an array of rSRRs microwave sensing probe loaded with different dielectric samples; MUT is in half side of probing region array with only on single side of the unit cell.

In the next experiment, different samples were introduced on one side of the unit cells, see inset of Figure 7-15. Upon loading both of the resonators, four resonance frequencies are attained. Table 1 summarizes the shifts in resonance frequencies resulting from the change in the capacitances due to the introduction of dielectric samples. These frequency shifts are plotted in Figure 7-16(a). It can be noticed from these results that the bigger structure (lower frequency structure) provides higher sensitivity than the smaller structure (higher frequency structure) for samples having higher dielectric constant values. However, the smaller rSRRs structure provides higher sensitivity in case of MUT having low dielectric constant values. In both of these cases, the reference frequency is maintained close to constant. The delta shifts in each frequency are plotted in Figure 7-16(b).

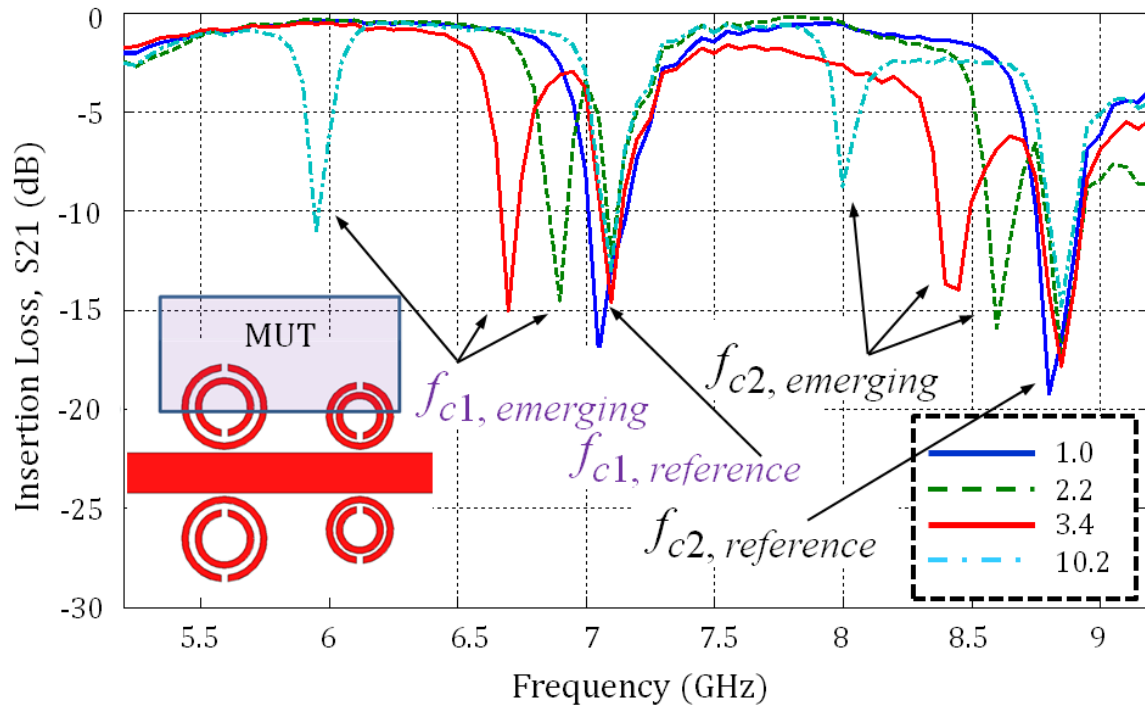
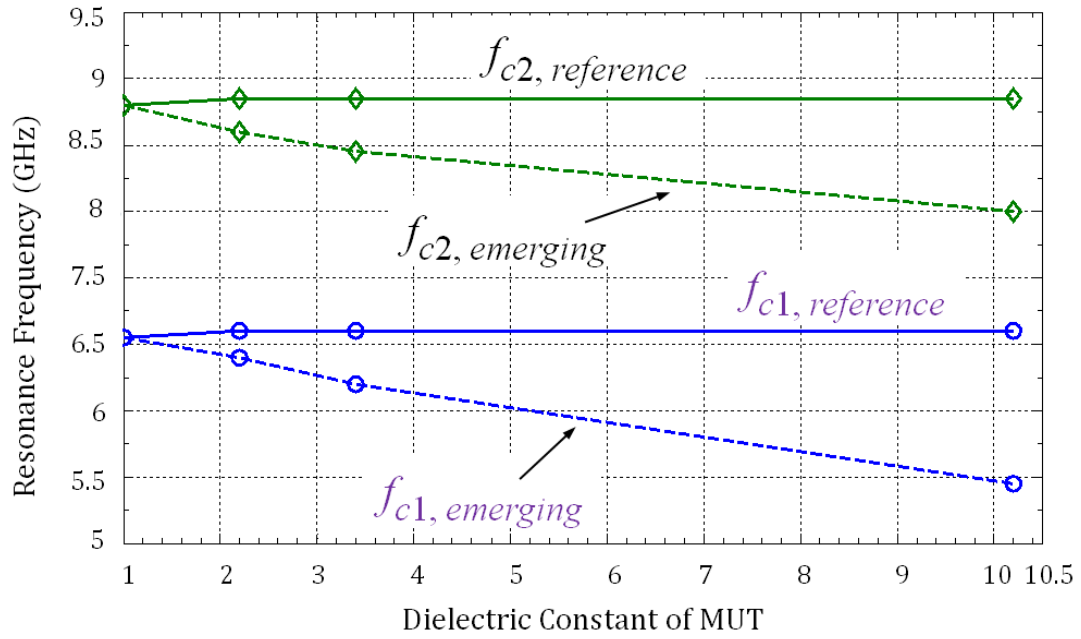
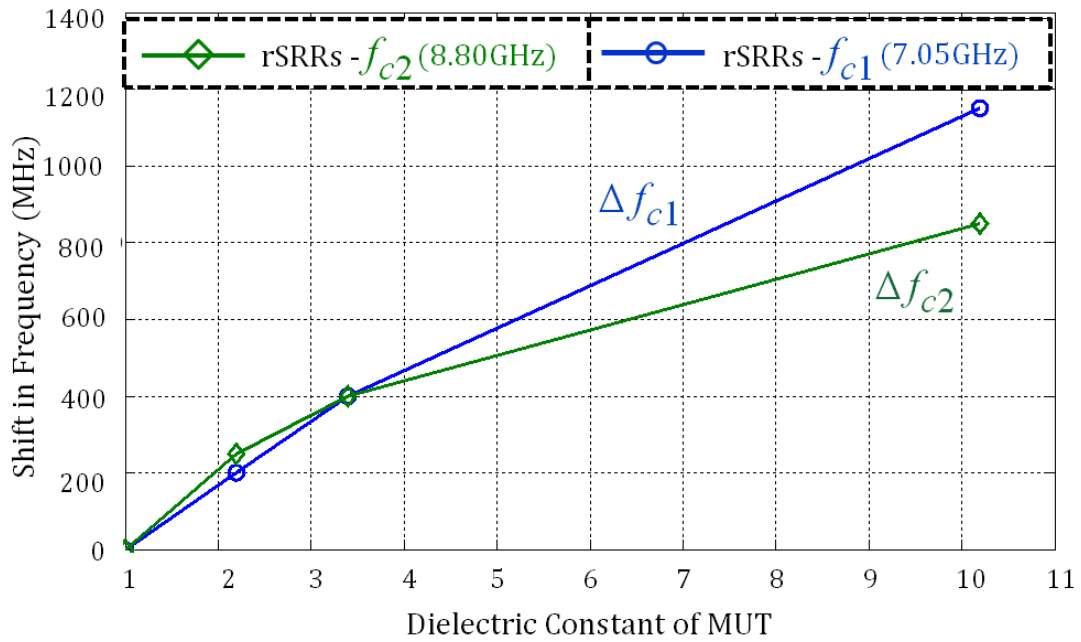


Figure 7-15. Measured insertion loss (S_{21} , dB) of an array of rSRRs microwave sensing probe loaded with different dielectric samples; MUT is in all of probing region array with only on single side of the unit cell.



(a)



(b)

Figure 7-16. The correlation between the measured frequency and dielectric constant of MUT in probing regions, (a) resonance frequency, (b) difference in each resonance frequency of the array of microwave sensing probe.

Table 7-1. Delta resonant frequency shift from dielectric loading in the probing regions.

MUT	f_{c1} (GHz)	f_{c2} (GHz)
Air	7.05	8.80
RT5880 ($\epsilon_r = 2.2$)	6.90 / 7.10	8.60 / 8.85
RO4003 ($\epsilon_r = 3.4$)	6.70 / 7.10	8.45 / 8.85
RO3010 ($\epsilon_r = 10.2$)	5.95 / 7.10	8.00 / 8.85

Notes: f_{C1} and f_{C2} are the peak resonance frequency of such an array of microwave sensing probe based rSRRs.

7.4 Probing and Dielectric Imaging by Edge Coupling Array

An array of miniaturized microwave sensing probe based rSRRs can be utilized for field imaging of dielectric sample as depicted in Figure 7-17. The elements are incorporated on a single microstrip lines in series. Each of the unit cells is designed to have a unique resonant frequency. Through edge coupling, as shown in figure, and restring over a sample, the surface image of the sample material can be constructed by observing the resonance frequency for each of the unit SRR structure. As an example, a defect present in the sample will provide a resonant frequency shift in the unit cell relative to its reference when it passes above the defect. This resonant frequency shift can be observed and used in reconstruction of surface image of a sample showing varying dielectric properties across its surface. This can also be used for sensing and will also prove useful in imaging electronics circuits buried within thin dielectric layers.

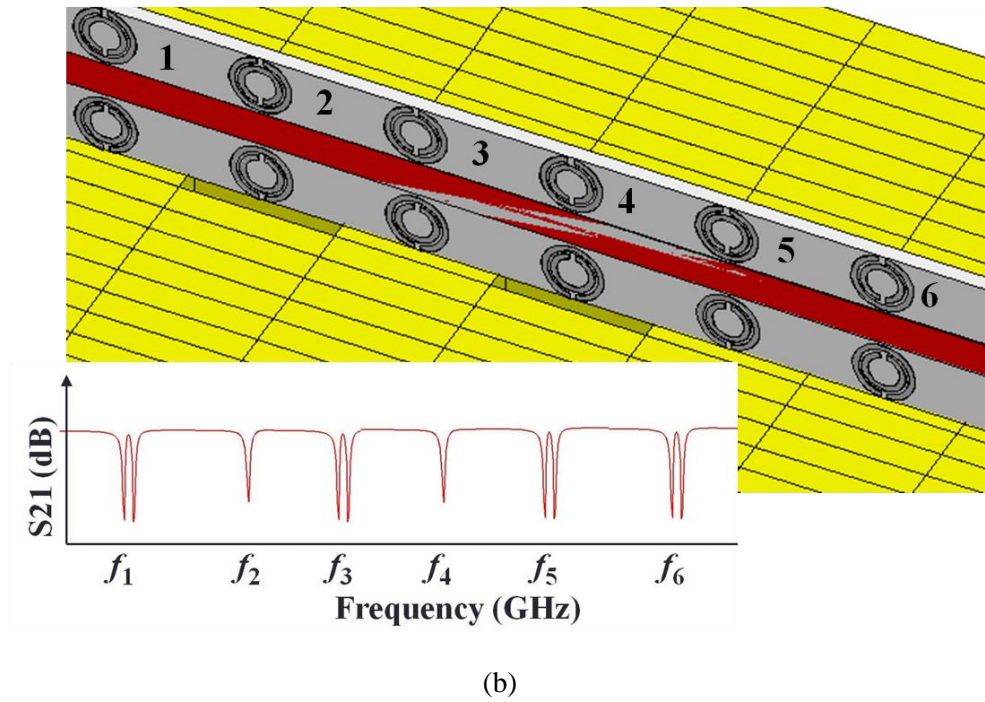
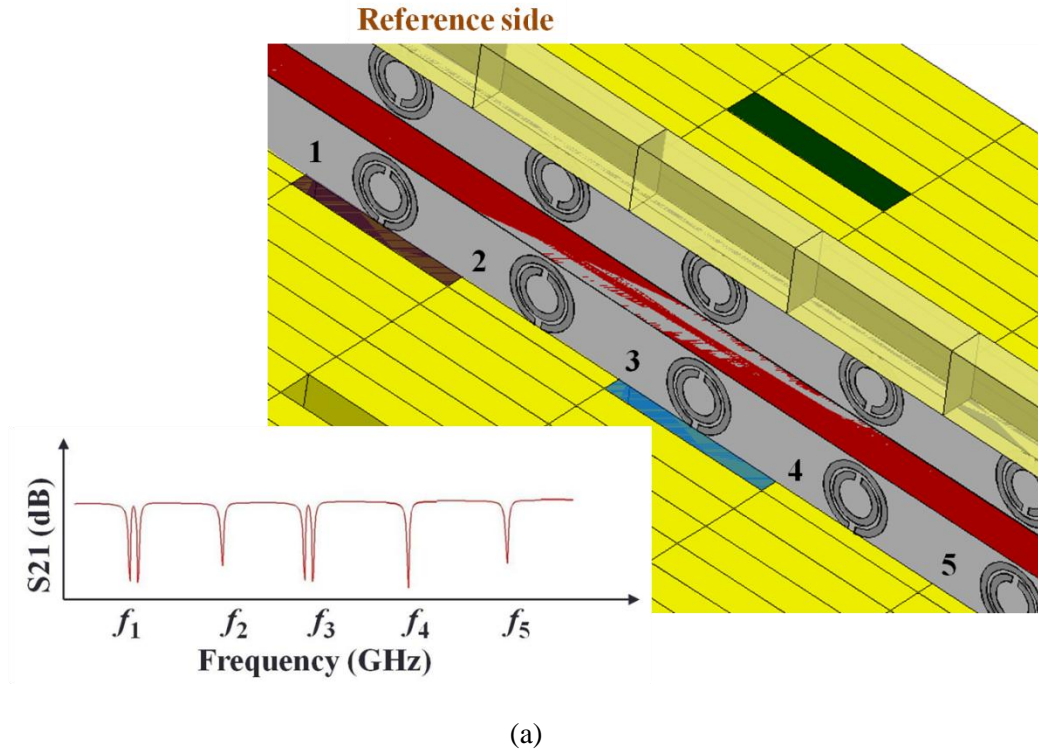


Figure 7-17. A proposed approach to image the surface of a plane structure using a linear array of band stop resonator structure for imaging applications, (a) using a material sample as reference, (b) using air as reference.

7.4.1 Realization of Edge-Coupling Under Dielectric Loading

For realization on non-destructive evaluation, two reflective split ring resonators as the previous design are incorporated on a T-line again. Since it is redesigned for using edge coupling, the T-line is blended in order to have a same level at the edge of each resonator. Figure 7-18 shows the layout of the actual circuit to be fabricated. The effective dimension of each SRR geometry is approximately $\lambda/16$ in size in free space wavelength as the previous design. In this design, two resonators are incorporated on a blended T-line having two different resonant frequencies (f_{c1} and f_{c2}). For each of the resonator design, a probe resonator and a reference resonator is included in the design. The bottom structures probe the sample and the top structures are free to resonate without any loading from the sample. The top structures act as reference points. It is worth noting that the design allows for cascading of multiple resonators on a single transmission line and thus allows measurement in parallel using a single network analyzer (or a RF source and a detector). Here only two resonators are cascaded to show proof of principle; however, more resonators can easily be incorporated.

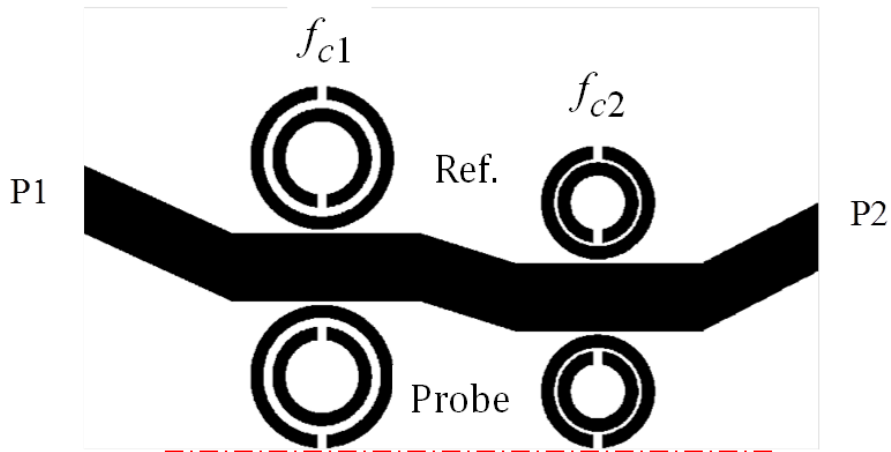


Figure 7-18. Layout of the edge-coupling probe design (resonance frequencies for each resonator, f_{c1} 7 GHz and f_{c2} 9 GHz).

As shown in Figure 7-18, probe side of the circuit is cut close to the edge of the rings and this side is used in probing a sample under test. Under loading condition, a dielectric substrate having different dielectric properties is brought in contact to the bottom rings. The resonance frequency of the bottom rings shift to higher frequency as the dielectric constant of the sample under test becomes less than the dielectric constant of the circuit. For an example, a dielectric constant of a sample is 10.2 leading to the resonance frequency of the bottom and top resonators are at the same frequencies (f_{c1} and f_{c2}). Figure 7-19 shows the measured insertion loss, S_{21} (dB) of such a design under loading condition. Alternatively, the resonance frequency can be measured from phase plots of S_{21} signal as illustrated in Figure 7-20.

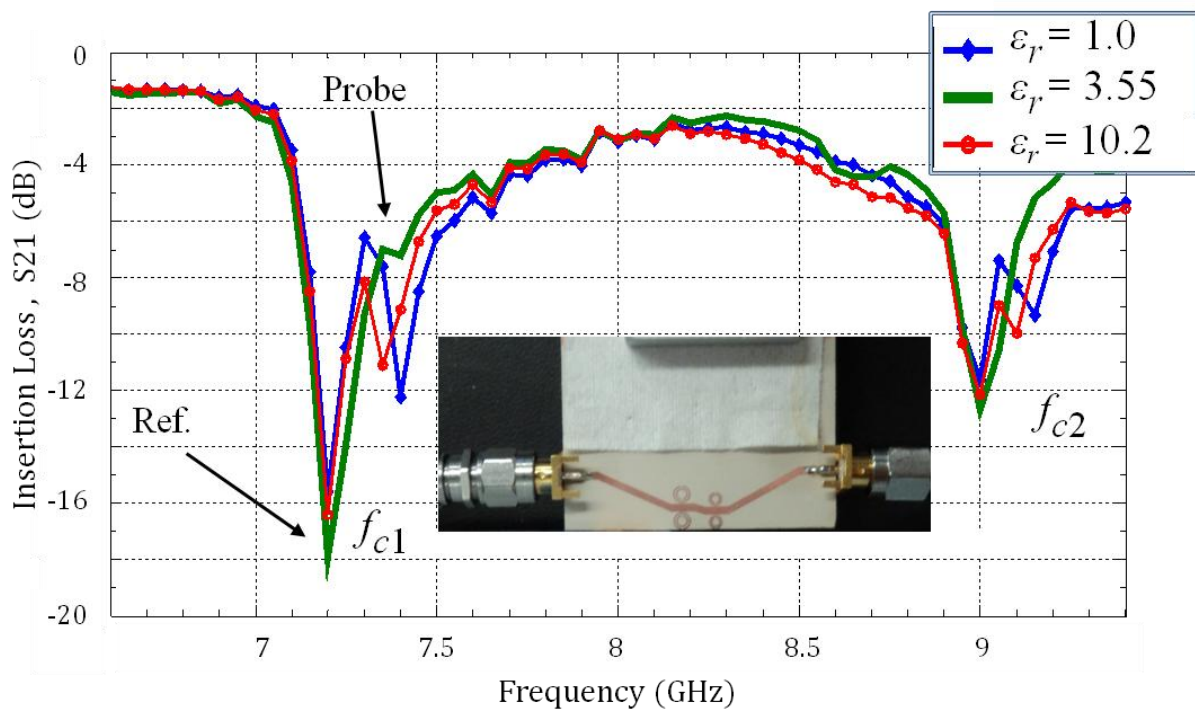


Figure 7-19. Measured S_{21} of the edge-coupling dual ring design loaded transmission line with different dielectric materials. Inset is the fabricated circuit in the experiment.

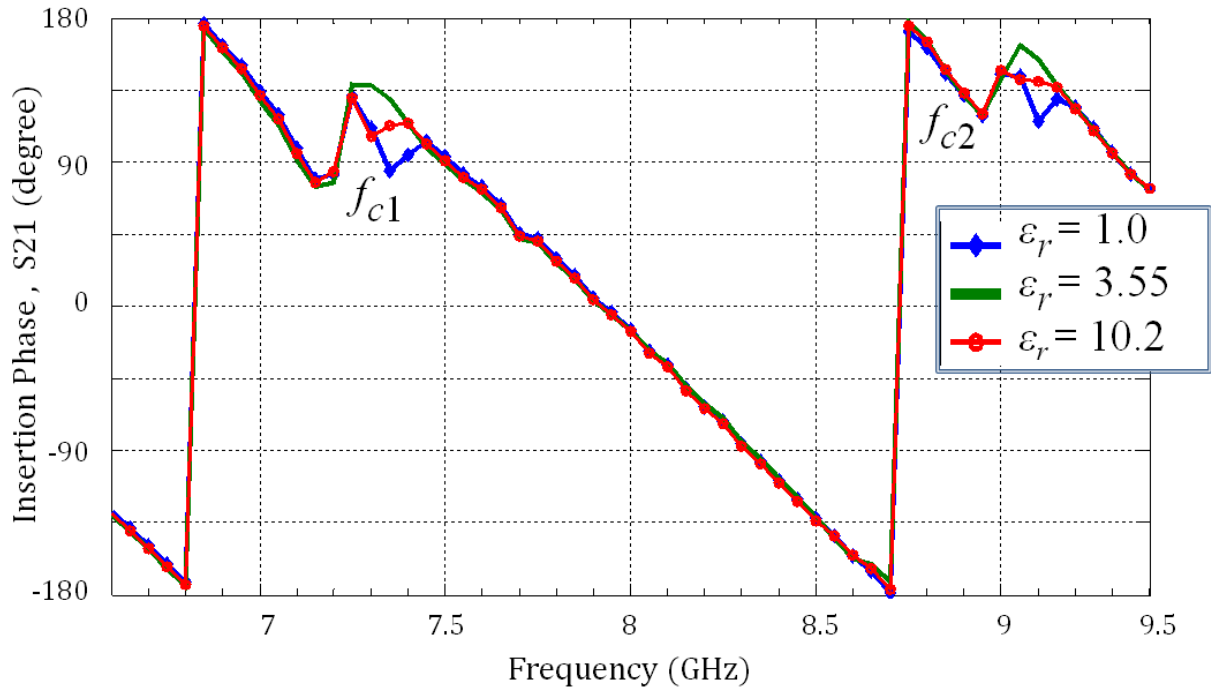


Figure 7-20. Measured insertion phase, S21(degree) of the edge-coupling dual ring design loaded transmission line with different dielectric materials.

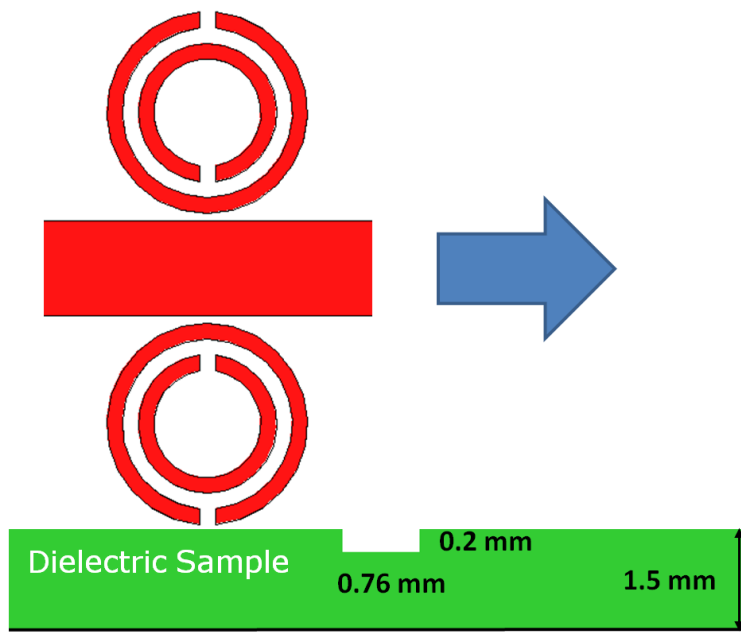
7.4.2 Realization of Non-Destructive Evaluation

There is significant need for Non-Destructive Evaluation (NDE) of structures and devices made from dielectrics. A dielectric sample may contain multiple types of defects such as air pockets, embedded structures, surface defects and film delamination to name a few. It is desirable to develop a sensor that allows in measuring such defects. Measurement of defects that are sub-wavelength in size will allow higher resolution detection. One of the design approaches to enhance sub-wavelength wave focusing and localization is through the use of metamaterials.

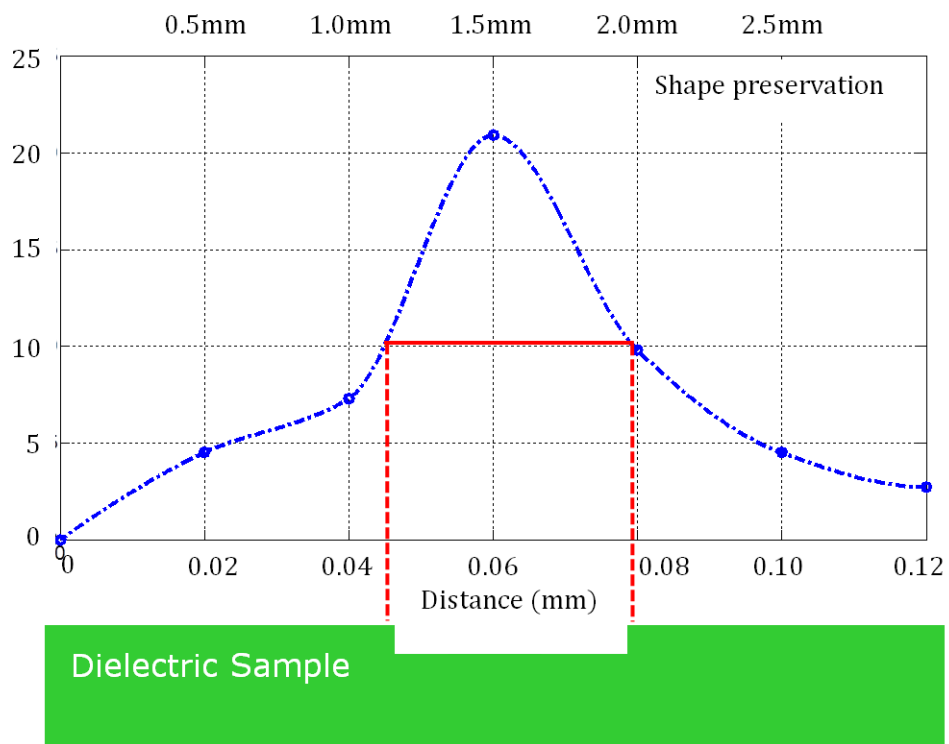
To realize such a defect for NDE, a notch was fabricated in a dielectric sample and the probe scans the sample approximately less than 1 mm above the surface. Delta insertion phase shift is observed when the probe scans the sample. Figure 7-21 shows the resolution measurement setup and measured results on such a dielectric sample. A half power resolution is approximately 1.75

mm. The measured frequency is 7.1 GHz which translates into a wavelength of 39 mm in free space. This measurement shows that sub-wavelength size defects can easily be measured using the proposed approach.

Figure 7-22 shows the scan of a smart card (made from plastic) that incorporates a buried antenna and a silicon chip. Typically the antenna element is printed using conductive silver paste. Left Inset of Figure 7-22 shows measurement setup. The metamaterial probe was used to interrogate a line section of the smart card. In the Figure, a relative shift in phase of the resonant frequency is plotted as a function of spatial position on the smart card. Middle inset in the Figure 7-22 shows the THz image of the smart card which shows the presence of loop antenna and a Si chip [80]. The probe was used to scan over a section of the antenna and the Si chip (shown with red line in the THz image picture). From the scanning, it is worth noting that the resonance frequency is significantly perturbed by the presence of dielectric or metal elements within the plastic card. The thickness of the card is 0.76 mm and the probe scans the card at an approximate distance of less than 1mm from the surface. In the future a complete image of the buried objects will be carried out. This figure clearly demonstrates that such a metamaterial probe can be utilized in imaging buried objects within a dielectric substrate. High resolution into subwavelength range can be achieved using this approach.



(a)



(b)

Figure 7-21. Realization on a defect dielectric material, (a) resolution measurement setup, (b) measured resolution characteristics.

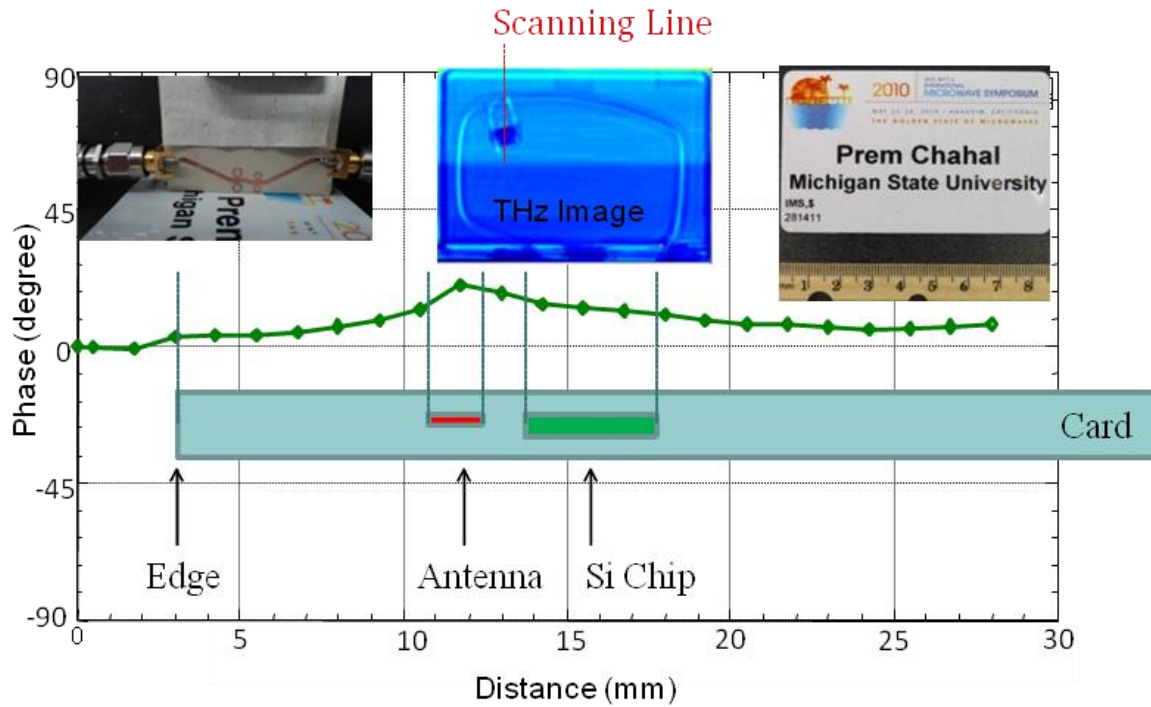


Figure 7-22. Scanned smart card using the proposed probe. Shown on the top are optical photographs and THz image in the transmission mode. Measured relative insertion phase changes correlate well with THz image.

7.5 Conclusion

In this chapter, novel types of sensing probe are introduced that utilizes metamaterial unit cells coupled to microstrip lines. Using this approach, multiple ring structures can be incorporated onto a single microstrip line to achieve parallelism for high throughput sensing. One design utilizes the band-stop properties and the other design exploits the band-pass properties. Both sides of the transmission lines are loaded with resonators. One side allows probing of samples and the other side provides reference region. Therefore, such an approach allows in the design of a built in calibration structure which relaxes stringent calibration that are required in conventional capacitive probe designs. The probe allows high sensitivity interrogation of dielectric samples and allows in the examination of defects buried within the

structure. The proposed MTM probes are low-cost, compact in size, simple to implement in NDE and sensing applications through surface imaging as well.

CHAPTER 8

METAMATERIAL-INSPIRED RECONFIGURABLE ANTENNA

Metamaterials (MTMs) based antenna designs has gained significant attention to realize length independent antennas because of the unique electromagnetic properties that can be achieved through this approach [58-59]. In particular, small loop and small dipole antennas loaded with left-handed LC-structures have been reported that leads to both miniaturization and performance enhancement [58-59]. Moreover, the unconventional characteristics of the MTM unit cell, such as the split ring resonator (SRR) producing negative permeability (MNG) [5], allows higher degree of design freedom to achieve desired resonant frequency using limited physical dimensions [59]. In general, such metamaterial-loaded or metamaterial-inspired antennas allow miniaturization of classical antennas. To achieve added functionality, the ability to reconfigure the operating frequency of such antennas is desirable. The proposed antenna design allows integration of tunable elements as an integral part of the antenna structure to meet this need.

This chapter demonstrates an antenna design that integrates directly the unit cell of previous work [34-35] as an integral part of a monopole antenna structure. This leads to significant reduction in antenna size and allows for seamless integration of a tuning element, such as a varactor diode, as integral part of the antenna element. Reconfigurability, miniaturization, and one-side fabrication are the key desirable aspects of this design. Full-wave electromagnetic simulation tool, Ansoft HFSS[®], is employed in the design and optimization of the proposed antenna design. Details of design and simulation are presented.

8.1 Antenna Description

The structure of the proposed antenna is shown in Figure 8-1. It mainly consists of an mSRR in addition to a folded monopole antenna. A conventional substrate, RO4003 with a dielectric constant (ϵ_r) of 3.55 is used in the antenna design. A 50- Ω coplanar waveguide (CPW) having a 0.7 mm wide signal line and 0.15 mm wide gaps is used to feed the antenna element. The thickness of the metal conductor and the substrate are 0.017 mm and 1.52 mm, respectively. The physical dimensions of this structure are as follows: $l_1 = 20$ mm, $l_2 = 9$ mm, $l_3 = 5$ mm, $l_4 = 3.35$ mm, $w_1 = 25$ mm, $w_2 = 3.5$ mm, $w_{g1} = 10.6$ mm, $w_{g2} = 13.4$ mm, $r_{ext} = 3$ mm, $d = 0.15$ mm, $w = 0.30$ mm, $s_1 = 0.5$ mm and $s_2 = 0.3$ mm.

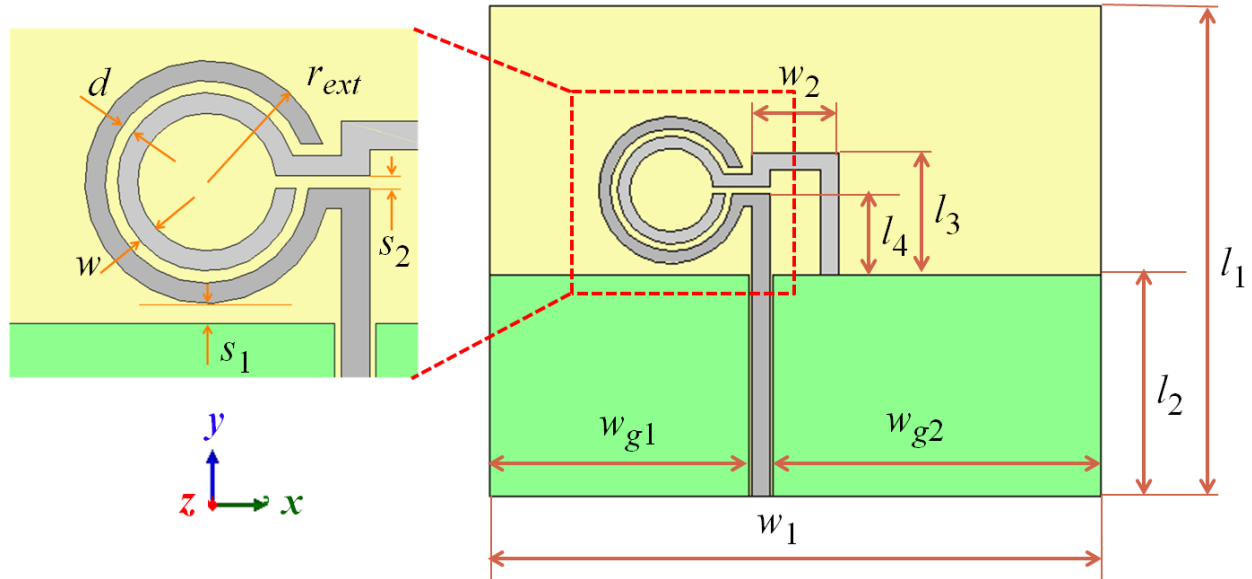


Figure 8-1. Configuration of the mSRR inspired compact antenna structure.

Generally, a conventional monopole antenna is a quarter wavelength length at the operating frequency. By incorporating the mSRR structure in a folded monopole antenna layout, the resonant characteristics of the antenna can be improved at a specific frequency. For relative comparison, a conventional folded monopole antenna (U-folded), a ring-folded monopole

antenna (R-folded) and the mSRR loaded monopole antenna are designed and simulated for a substrate that has the same board size and material properties. Simulation results for these three structures are shown in Figure 8-2. The antenna resonance frequencies are 5.42 GHz, 3.44GHz and 3.44 GHz, respectively. The modified split ring resonator is optimized to resonate at the same resonant frequency of the ring-folded monopole antenna. Reflection coefficient (S11) of the mSRR loaded monopole antenna has improved characteristics. The proposed antenna provides 37% reduction in the operating frequency over that of the U-folded monopole antenna for designs utilizing a same size board. Further improvements can be made by optimizing the location of the mSRR structure within the folded monopole antenna structure and by incorporating a solid ground plane on the flip side of the antenna pattern.

Table 8-1 summarizes miniaturization techniques of antennas that are related with this study. Only the use of metamaterial approach is considered and discussed. Normally, MTM-inspired antenna designs can be utilized for miniaturization into 2 fold: MTM loading antenna structure and MTM being a part of antenna structure. Besides compact in size, the designed antenna can be efficiently matched in impedance without additional circuit. For MTM loading antenna type, the finite ground plane plays a key role for the antenna performance. The finite ground plane is exploited to achieve spherical shell of epsilon negative (ENG), Mu-negative (MNG) or double-negative (DNG) material structures. The lower designed frequency, the larger finite ground plane [84]. However, the MTM being a part of antenna structure exploits grounding from the feed line to form the composite right/left handed (CRLH) equivalent circuit to achieve the LH phenomenon.

Table 8-1. Summary and comparison of MTM-inspired antenna structure for miniaturization

MTM-inspired antenna structure	Ref.	Extra-Finite Ground Plane	Antenna Dimension (mm x mm)	Resonant Frequency (f_c)	Metal patterning
(a) MTM loading antenna 	[81]	Required	22.4 × 21.5	960 MHz (Fixed)	Double side
	[82]	Required	36.8 × 17.0	2 GHz (Fixed)	Double side
	[83]	Required	30.0 × 30.0	910 MHz (Fixed)	Double side
	[84]	Required	22.0 × 10.0	1580 MHz (Fixed)	Double side
(b) MTM being antenna part 	[85]*	No need	70.0 × 20.0	2.1 GHz (Fixed)	Single side
	In this study	No need	25.0 × 20.0	3.4 GHz (Tunable)	Single side

* Note: The antenna has polarization diversity function (z-polarization and x-polarization).

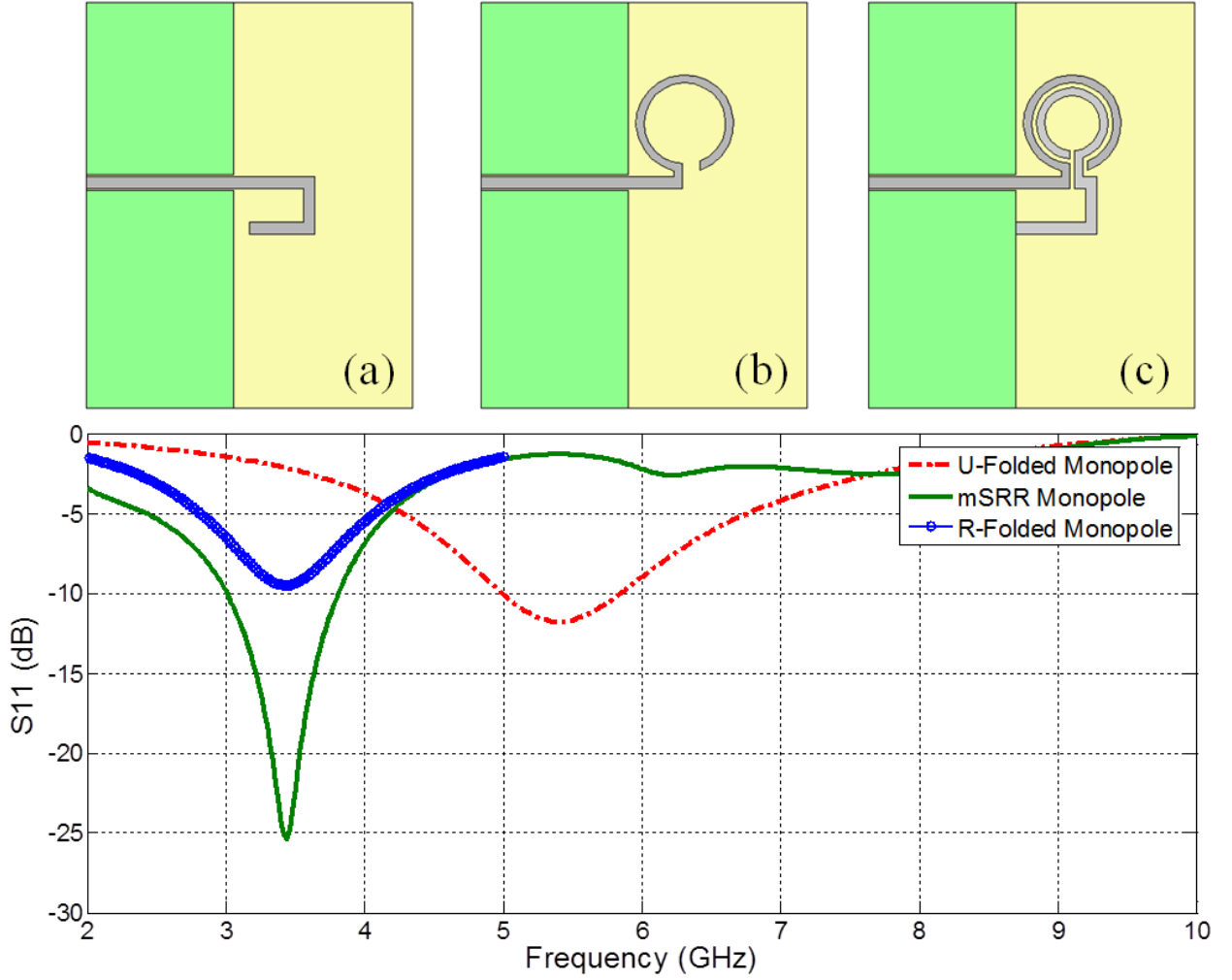


Figure 8-2. Physical layout and simulated reflection coefficients of monopole antennas: (a) U-folded type, (b) R-folded type, (c) mSRR type.

8.2 Validation of Reconfigurable Antenna Model

The design of proposed mSRR loaded monopole antenna is further refined to exploit unconventional electromagnetic properties of metamaterials. A ground plane is added on the back side of the substrate. Here the mSRR structure becomes a metamaterial-like unit cell characterized by having negative permeability. As a result, the resonant frequency of the system shifts to lower frequency while maintaining same physical layout. This effect leads to achieving

a significant size reduction in the antenna. However, the radiation pattern of the new proposed antenna changes due to the solid ground plane leading to higher gain.

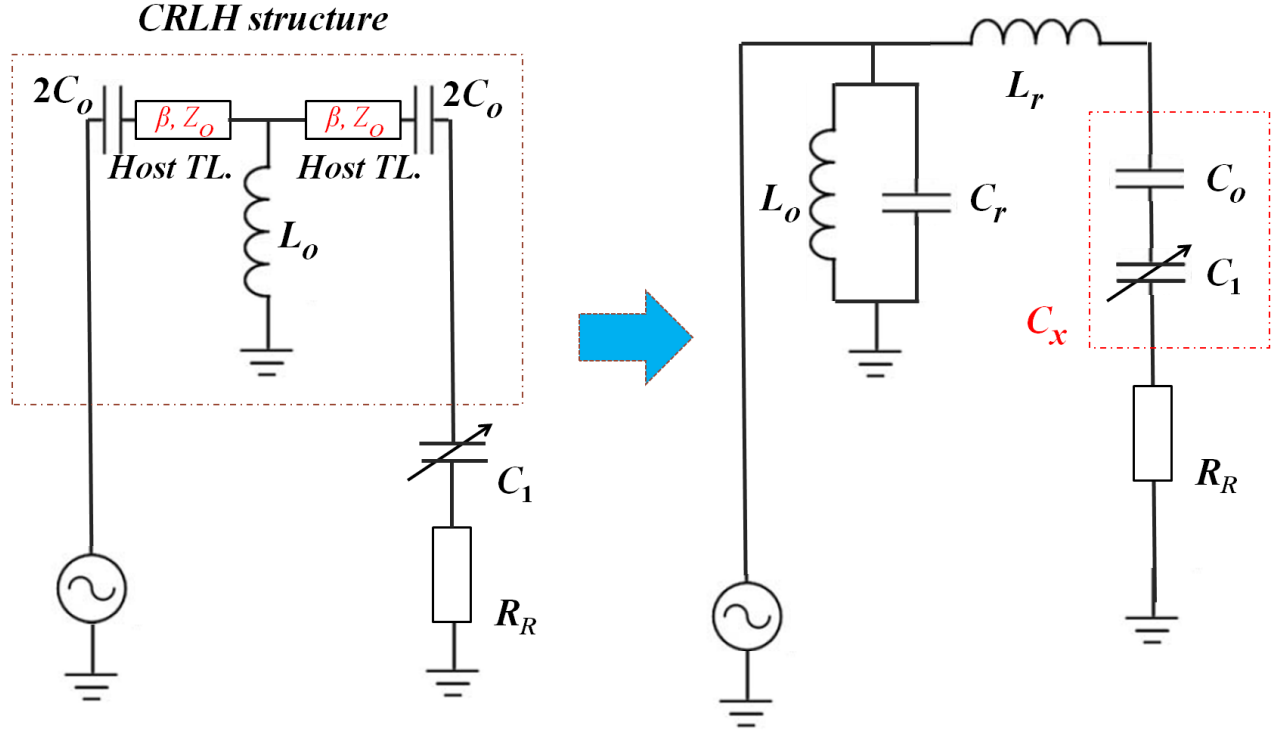


Figure 8-3. Equivalent circuit model of the proposed reconfigurable mSRR inspired microstrip antenna.

$$f_{resonance} = \frac{1}{2\pi\sqrt{LC}} \quad (8-1)$$

$$C \approx C_x = \frac{C_o \cdot C_1}{C_o + C_1} \quad (8-2)$$

$$L \approx L_x \quad (8-3)$$

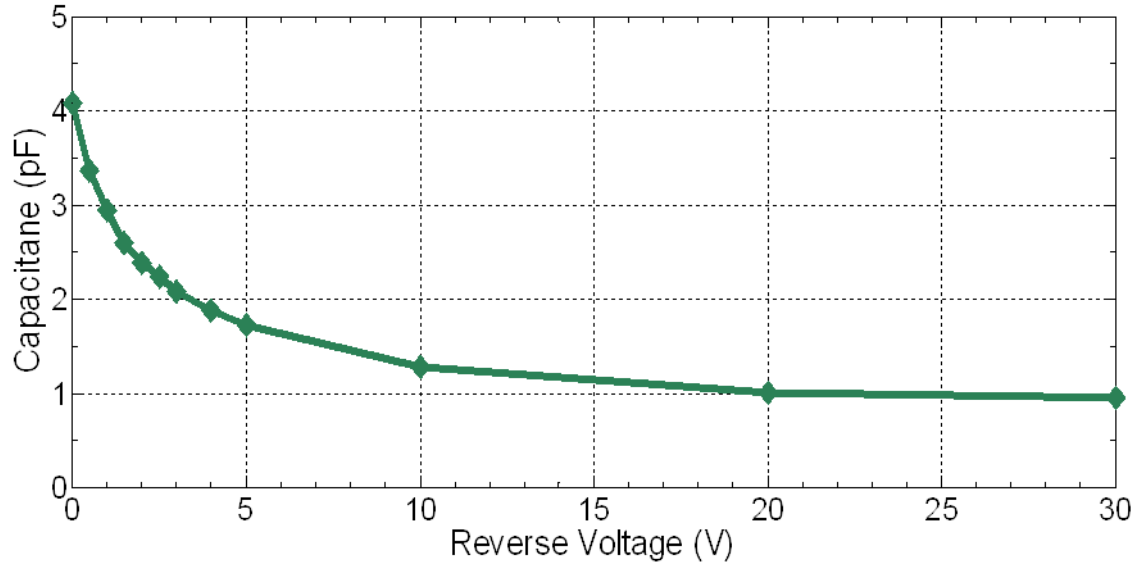


Figure 8-4. The relationship between capacitance and bias voltage from a candidate varactor diode (SMV1408-079LF) [42].

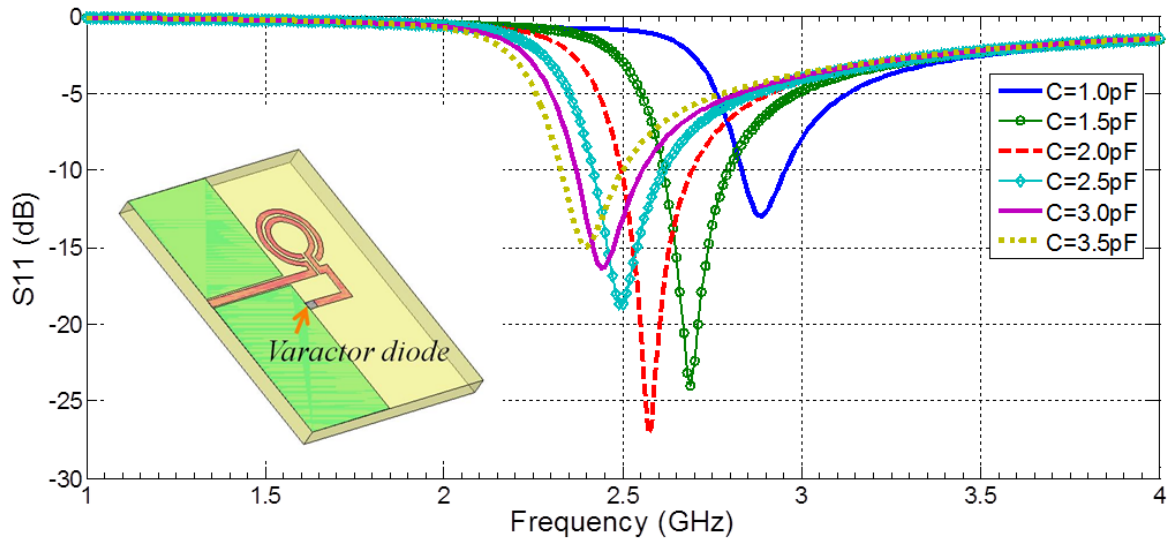
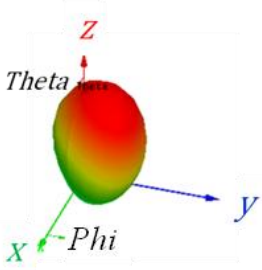
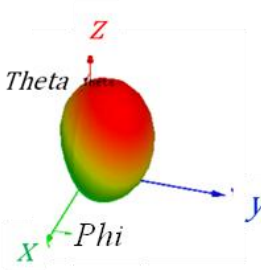
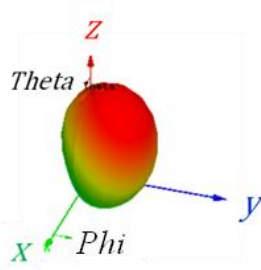


Figure 8-5. Simulated reflection coefficients of the reconfigurable mSRR inspired microstrip antenna. Inset shows the structure of the mSRR integrated with a varactor diode (with a ground plane at the back side).

In order to incorporate a tuning element in the proposed antenna structure, a 1mm-long gap is added at the end tip of the folded dipole. A varactor diode is placed across the gap in order to drive capacitive load with the structure, see inset of Figure 8-3. The effective capacitance of the varactor diode can be tuned by changing the DC bias. The mSRR-inspired reconfigurable microstrip antenna and a plot of the S11 as a function of frequency are shown in Figure 8-3. It can be seen that a 480MHz tuning range can be achieved as the capacitance varied from 1pF to 3.5pF. A candidate varactor diode for this design is the SMV1408 from Skyworks®. Table 8-1 shows the radiation patterns of the designed antenna for three capacitance values. The radiation pattern remains the same while the resonant frequency can be tuned. The antenna with MNG loading provides a 30% reduction in the operating frequency over previous design of Figure 8-2(c).

Table 8-2 The Resonant Frequency and Radiation Pattern of the Reconfigurable Antenna.

C (pF)	1.0pF	2.0pF	3.5pF
Resonant Frequency (B.W. -10dB)	2.89GHz (120MHz)	2.58GHz (190MHz)	2.41GHz (170MHz)
Radiation Pattern at Resonant Frequency			

Simulated results by Ansoft HFSS.

8.3 Experimental Results

The proposed reconfigurable antenna was fabricated using microstrip technology on a *Rogers* RO4003 substrate having $\epsilon_r = 3.55$ and dielectric height $h = 1.52$ mm. This circuit is simple to fabricate since it is a planar structure requiring one-side metal patterning. Measurements of scattering parameters were carried out using a PNA network analyzer. Figure 8-6 shows a fabricated reconfigurable antenna. A varactor diode, SMV 1408-079LF, is surface mounted onto the structure. As seen in the picture, Cu-tape on the edges was used to connect the front ground plane to the ground plane on the back side of the board. This helps suppress any unwanted modes that may arise when the ground planes are not properly connected. The measurement setup for this experiment is also shown in Figure 8-7. The measured return loss S_{11} (dB) of the proposed reconfigurable antenna is shown in Figure 8-8. Comparing between the simulated and measured results, the results match very closely. However, a slight difference can be attributed to parasitics and packaging associated with the varactor diode which is not included in the simulations.

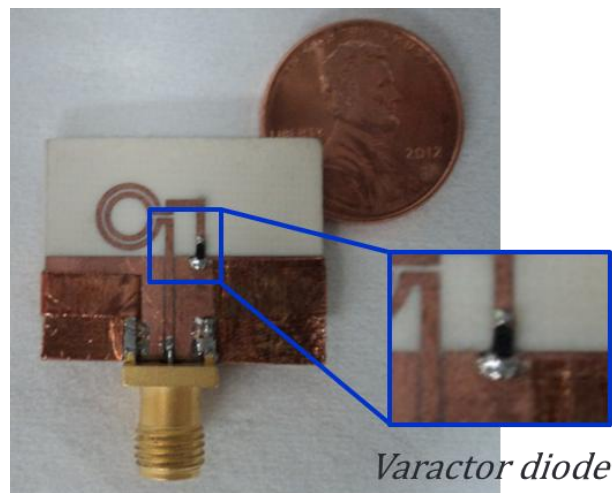


Figure 8-6. Photograph of the fabricated novel reconfigurable antenna (integrated with a varactor diode and a solid ground plane at the back side).

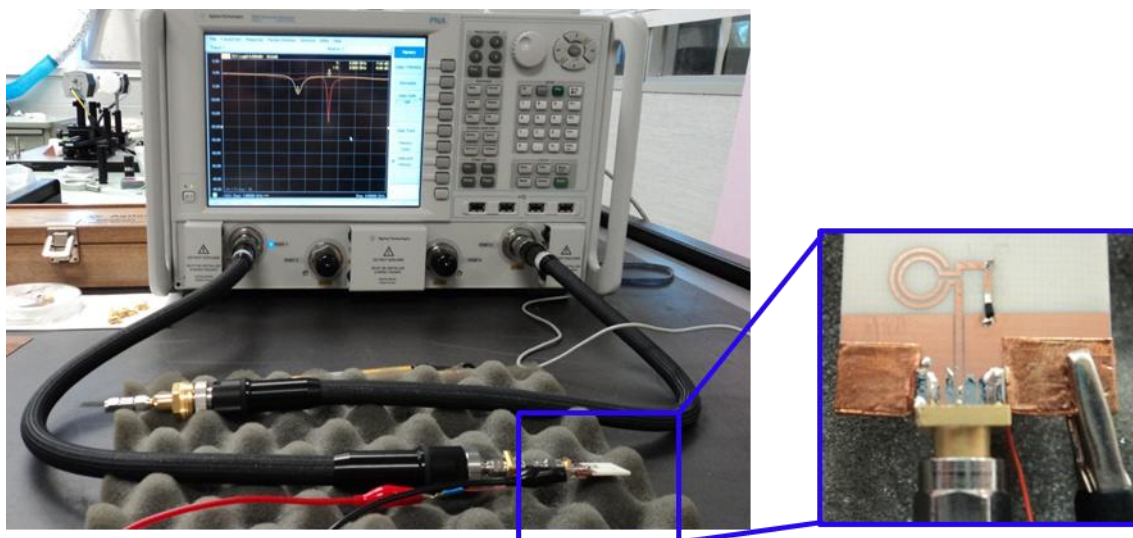


Figure 8-7. Measurement setup for the experiment with zoom-in picture of the proposed antenna.

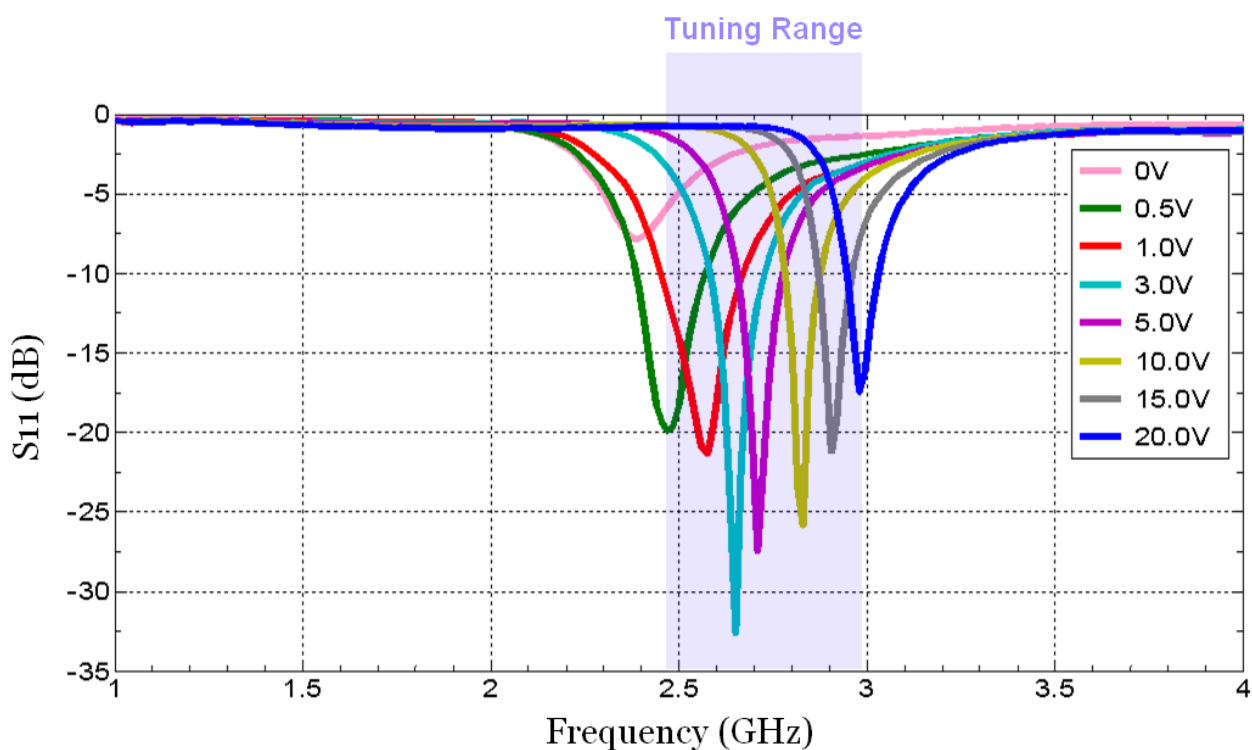


Figure 8-8. Measured return loss, $S_{11}(\text{dB})$ of the proposed reconfigurable antenna with various reverse bias voltages.

As expected, the resonance frequency can be tuned by electronically varying the capacitance through dc biasing. The experiment was carried out and approximately 500 MHz tuning range can be achieved as reverse voltage is varied from 0.5 V to 20 V. According to the datasheet of SMV1408-079LF from Skywork® [42], the relationship between the capacitance and dc reverse related with the resonance frequency of the proposed antenna is expressed in Figure 8-9.

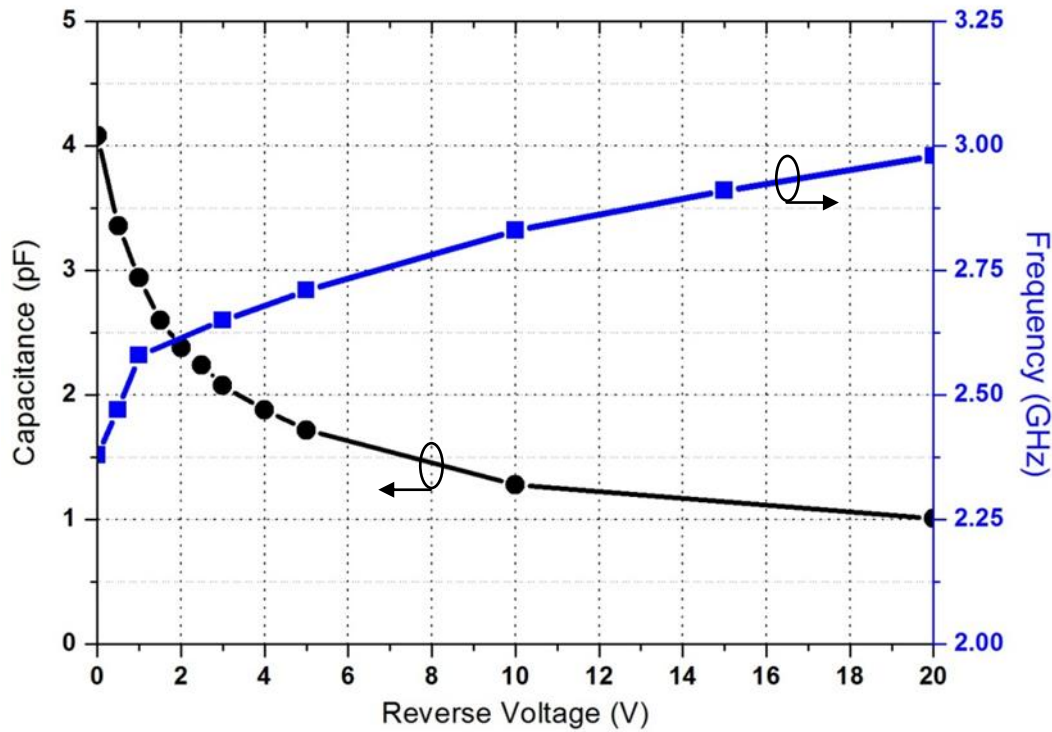


Figure 8-9. The correlation between reverse bias voltage versus capacitance and operating frequency of the proposed antenna.

In addition, the 3-D radiation pattern of the proposed antenna is measured using Satimo Passive Measurement 1.16 system as shown in Figure 8-10. The measured 3-D radiation pattern is expressed in Figure 8-11. It is important to note that the coordinates in measurement setup is different from the simulation. Therefore, it can be compared from each other that (x, y, z) of measurement represents (z, y, x) in simulation.

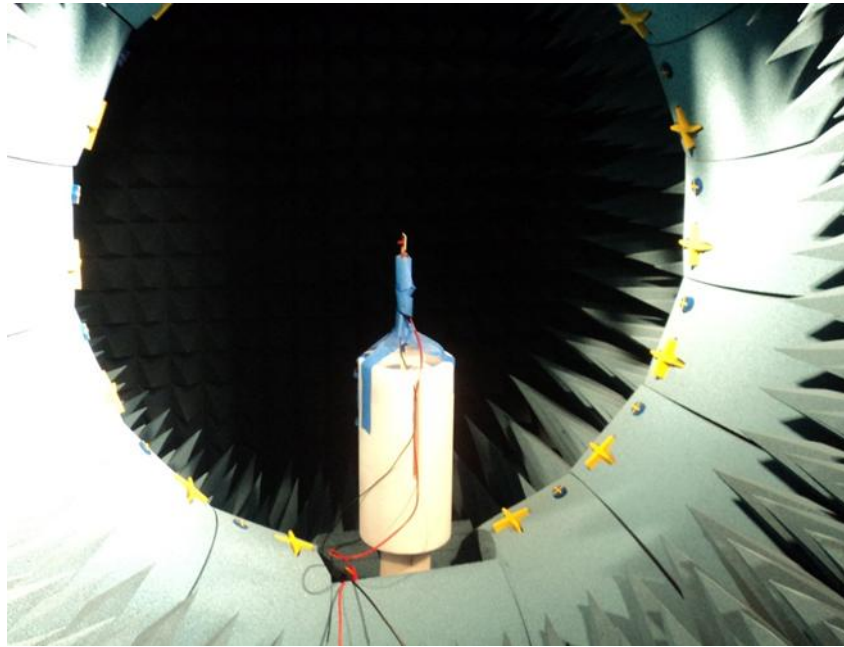


Figure 8-10. Antenna measurement setup for observation of radiation pattern by Satimo Passive Measurement 1.16.

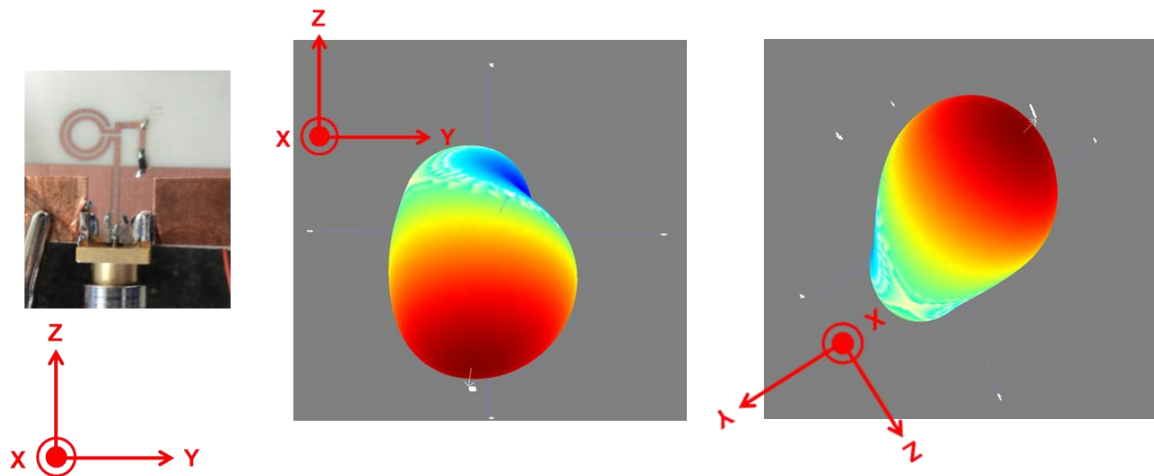


Figure 8-11. Measured 3-D radiation pattern of the proposed antenna by Satimo Passive Measurement 1.16.

8.4 Conclusion

A mSRR loaded compact antenna has been proposed and demonstrated through simulations and experiments. By incorporating a ground plane, to achieve negative permeability, a significant reduction in operating frequency is achieved. The mSRR-inspired reconfigurable antenna exhibits resonance characteristics independent of the radiator length and is electrically small. The structure is simple to fabricate as it requires only single side metal patterning, and it is compatible with MMIC integration. The proposed antenna design allows tuning of center frequency using a single varactor diode element while maintaining a similar radiation pattern over the frequency tuning range of approximately 500 MHz.

CHAPTER 9

CONCLUSIONS AND FUTURE WORK

9.1 Conclusions

In this dissertation, a novel MTM unit cell for microwave circuits and applications in the *X*-band has been presented and validated. Seamless integration with active device and many hot spots from electromagnetic fields play a key role in geometry of unit cell for reconfigurability. The metamaterial allows integration of active elements that allows active tuning of the resonance frequency of the unit cell. This allows in the design of tunable or adaptable microwave circuits that are difficult to design using conventional approaches. In contrast, the metamaterial unit cells allows in the design of sensor where the material under test is used to load the unit cell and this leads to changes in the scattering parameter of the unit cells. This allows in the adoption of metamaterial cells for chemical and biological sensor designs.

Based on the novel MTM unit cell, a power splitter with new functionality is presented in Chapter 3 to validate the practical uses in the *X*-band to design miniaturized microwave circuits. By integrating with active devices such as varactor diodes, the dispersive relationship of the unit cell can be electronically reconfigured through dc voltage tuning. Besides miniaturization, the proposed circuit can exhibit new functionalities such as equal and unequal power transferred conditions. Such conditions can be achieved comfortably by equal and unequal dc bias voltage to each varactor diode.

In Chapter 4, a new type of the reconfigurable *X*-band phase shifter is designed and demonstrated. In the proposed design, 2 MTM unit cells are cascaded and also integrate a varactor diode within one unit cell. Consequently, such an *X*-band phase shifter circuit can be

reconfigured and it exhibits linear phase responses over the desired frequency range. The proposed design offers significant advantages over conventional phase shifters as it provides stronger linearity in phase over a wide frequency range.

In Chapter 5, the double spiral unit cell design is utilized in demonstrating microwave MTM-inspired microfluidics sensors. The measured and simulated results show high sensitivity. Both dielectric constant and loss tangent of sample affect the resonance frequency. This structure allows in the characterization of dielectric samples. Both dielectric constant and loss-tangent can be determined accurately. Also this design requires very small volume (nano- to pico-liter) samples.

A compact volatile molecular sensor is introduced and validated in Chapter 6. The sensor is based on a planar MTM-inspired OmSRR structure. It provides very high sensitivity utilizing the vaporized molecular density in nano-mole per cubic-millimeter. The proposed sensor can also be highly selective by exploiting the Q-factor and the resonance frequency of the return loss (S_{11}). Besides high sensitivity and selectivity, the proposed volatile molecular sensor is compact in size, low-cost and easy to integrate for lab-on-chip applications.

In Chapter 7, microstrip transmission lines based MTM-structures (sub-wavelength sized resonators) are designed and implemented for near-field sensing of dielectric materials. Both band-pass and band-stop characteristics are designed for resonators coupling the microstrip line in the X-band region. Since the resonator unit cells are designed by loading at each side of the transmission line, one side allows probing of samples and the other side offers the reference resonance frequency. Since incorporating a built in reference resonators, such sensor designs provide improvement in signal noise ratio (S/N) and simplification of sensor calibration. It is

clearly confirmed from the results that the probes offer high sensitivity and have high potential for non-destructive evaluation of samples through near-field imaging.

The mSRR-inspired compact reconfigurable antenna is proposed and demonstrated in Chapter 8. Resonant frequency can be tuned by loading with a capacitive element (a varactor diode). The proposed design allows seamless integration of the varactor diode in the antenna structure. That means the resonance characteristics of such an antenna is independent of its radiator length. The circuit is low-cost, compact in size and simple to fabricate.

In summary, the theoretical and design methodologies of 1-D CRLH transmission line utilizing MTM unit cells are presented in a systematic way. The novel unit cells are proposed and designed for various microwave circuit applications and sensors. These lead to miniaturized circuits, simple to fabricate and low-cost. Several prototypes fabricated by a simple photolithographic process with one-side patterning are presented and demonstrated with a good agreement between simulation and measured data.

9.2 Future Work on MTM Microstrip T-Line based Microwave Circuits and Sensors

Future work could include further explorations in the development of microwave sensors from bio-molecular level to DNA level. It will be desirable to exploit dispersion diagram of MTM-inspired microwave sensors as a DNA of each dielectric material under test. Moreover metamaterials could be exploited to improve performances of microwave circuits in many possible areas such as phase shifters, power splitters, power amplifiers, oscillators, etc. Another extension of the existing work is to develop such an OmSRR for much more compact designs for higher operating frequencies. Some of these ideas are discussed below.

9.2.1 Fully Hybrid Split Ring Resonator and Higher Bit Phase Shifter

The MTM unit cell proposed in this dissertation can be further miniaturized for the design of the microwave circuits. The unit cell of this thesis is largely a distributed element. This unit cell can be miniaturized by incorporating lumped elements (inductors and capacitors).

As an example, in the unit cell discussed in this dissertation, a via can be introduced at the ends of the ring structure. By incorporating such a via, the inductance in the unit cell is increased and thus decreasing the resonance frequency. The via diameter is controlled to achieve desired inductance value. This modified structure is termed fully hybrid split ring resonator (FhSRR). It is worth noting that the novel circuit design can be miniaturized approximately from its original design which is no via (hybrid split ring resonator or hSRR) at $\lambda/12$ of free space to the novel design (FhSRR) at $\lambda/27$. An FhSRR-inspired reconfigurable X-band phase shifter circuit, Figure 9-1, is designed and simulated using Ansoft HFSS®. This example phase shifter design using such a novel unit cell shows wider bandwidth and is significantly miniaturized. Figures 9-2 and 9-3 show the simulated insertion loss (S21) and return loss (S11) of such a FhSRR-inspired reconfigurable X-band phase shifter. On average, 45-degree of phase tuning can be achieved over a wide range when the capacitances are altered from 0.06 pF to 0.15 pF as shown in Figure 9-4. Similarly, more cells can be further cascaded to increase phase tuning range.

Instead of controlling the capacitance in a digital fashion (high or low), it can be controlled in analog fashion to achieve a phase shifter with higher bits. The capacitance loading the unit cells should be controlled independently.

Example presented here demonstrates that the proposed circuit can be significantly improved in size and performance. A detailed analysis of field distribution should be carried out to achieve circuit with low loss characteristics and also an approach to fabricate vias having tight control.

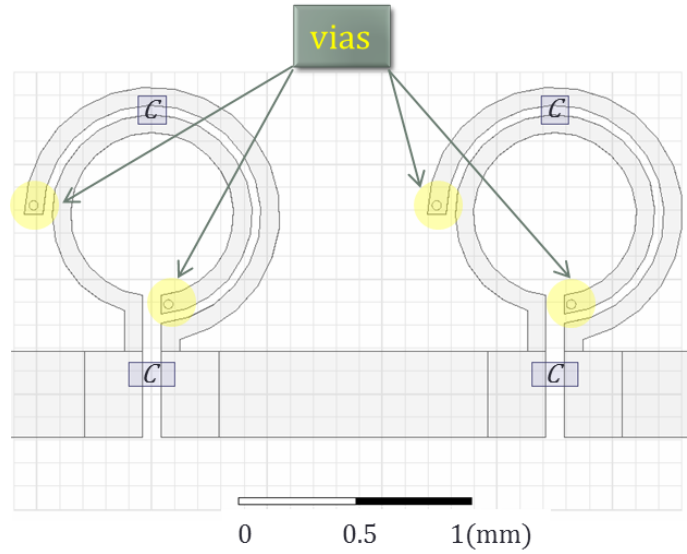


Figure 9-1. A novel reconfigurable X-band phase shifter design using fully hybrid split ring resonators (FhSRRs).

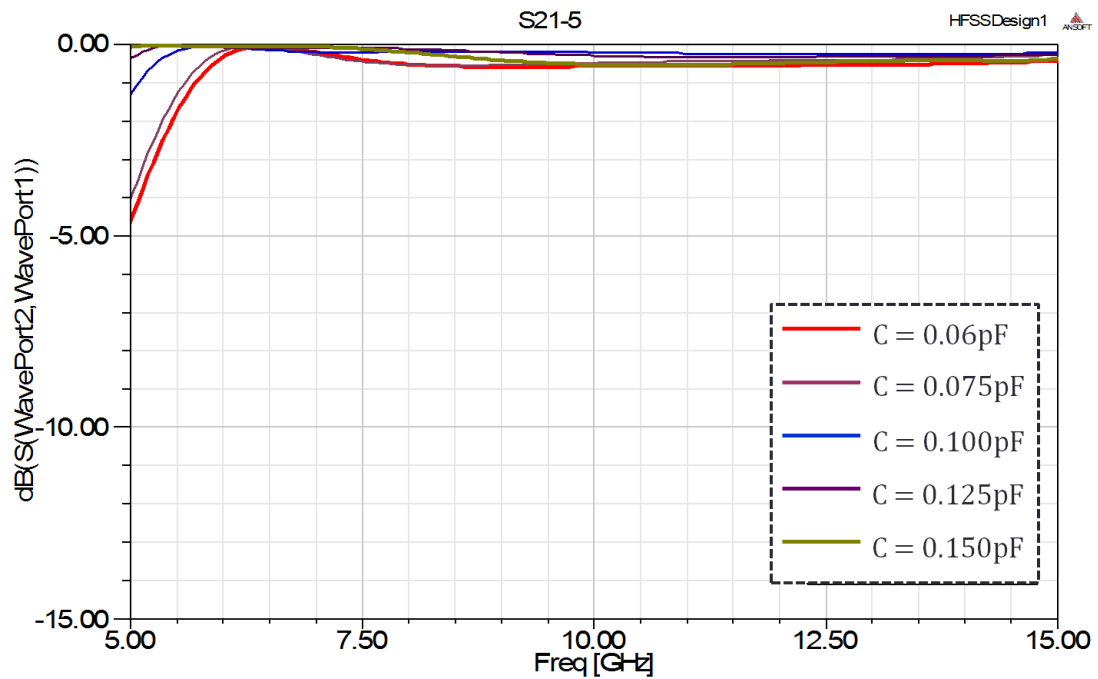


Figure 9-2. Simulated insertion loss, S21 (dB) with various capacitances of the FhSRR-inspired reconfigurable X-band phase shifter circuit.

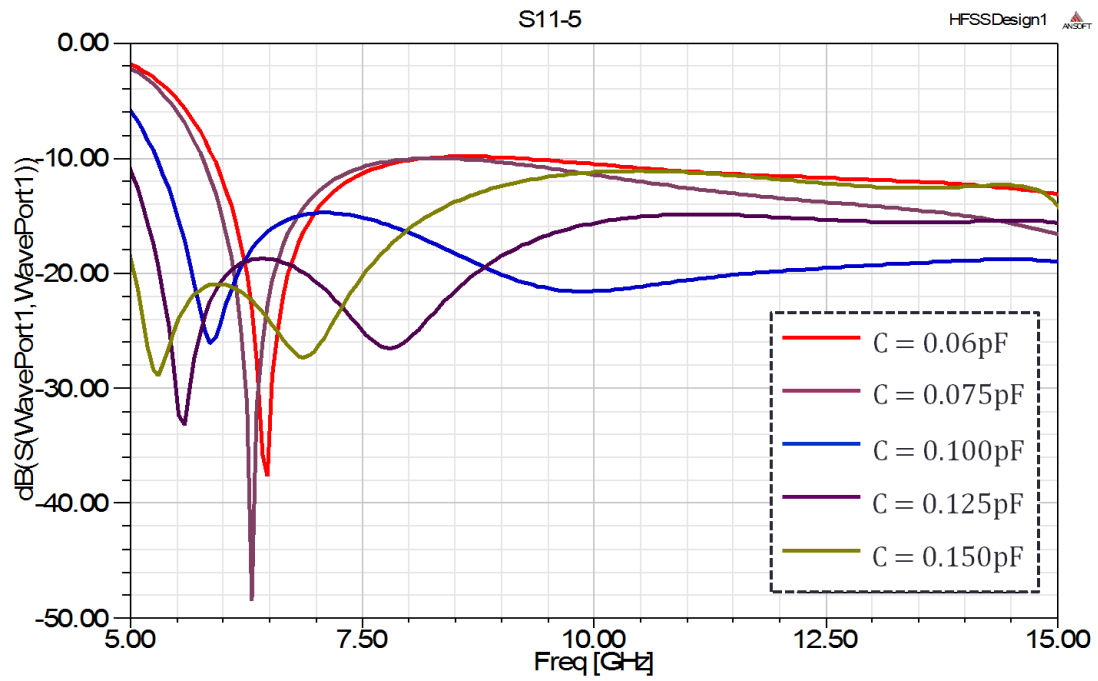


Figure 9-3. Simulated return loss, S_{11} (dB) with various capacitances of the FhSRR-inspired reconfigurable X-band phase shifter circuit.

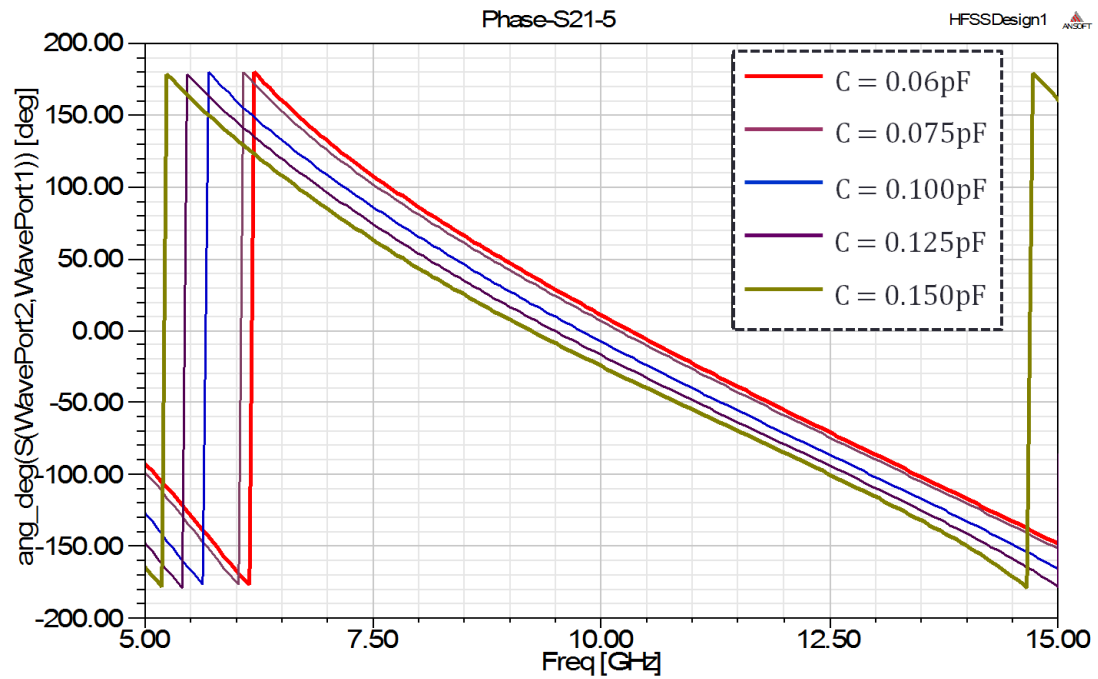


Figure 9-4. Simulated insertion phase responses (degree) with various capacitances of the FhSRR-inspired reconfigurable X-band phase shifter circuit.

9.2.2 Novel Chemical and Biological Sensors based MTM Resonator

There are various improvements that can be carried out in the design of novel chemical and biological sensors utilizing the designs presented in this thesis. Two example improvements are discussed here.

9.2.1.1 Use of Antibodies to Achieve Specificity

In the case of biosensors based on MTM resonators in the microwave domain, it is possible for direct molecule detection down to the DNA level. To improve sensitivity and selectivity characteristics of unit cells, the structure surface can be coated with gold (Au) and some types of acid linked specific biotin in order to immobilize a desired protein, such as single-stranded DNA-binding streptavidin. Au can be used to coat the surface of the unit cells because of its good chemical inertness.

Sensors for parallel interrogation of samples should be designed for high throughput analysis. This can be achieved by coupling multiple resonators to the transmission line forming an array of bandstop circuits. This is on similar lines as the NDE probe built using ring resonators. Each of the resonators is to be designed for specific frequency and Q-factor. Each resonator can be sensitized with binding agent for specificity. This approach will allow in the interrogation of multiple samples simultaneously.

9.2.2.2 Incorporation of Nano-particles with High Surface Area

In order to achieve larger surface area near the probe region (region with high field strength), carbon nanotubes (CNTs) (or graphenes) can be integrated within a unit cell structure to provide further selectivity and sensitivity for gas detection as depicted in Figure 9-5. It is well known that conductive properties of CNTs change upon exposure to different types (e.g., Methane) and concentration of gases. This change modifies the effective equivalent model of the metamaterial

unit cell. Consequently, it leads to changes in resonance frequency and Q-factor of the circuit. This leads to a new type of sensor that is expected to have higher both sensitivity and selectivity as compared to existing gas sensors.

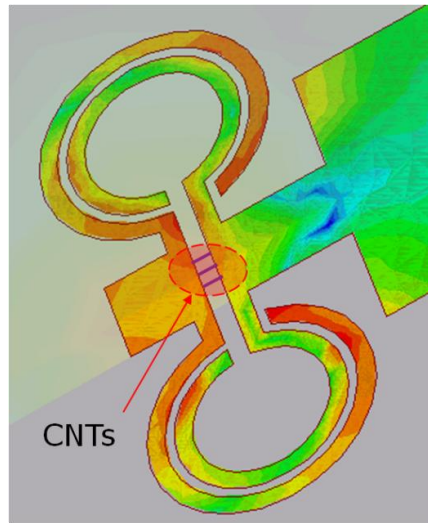


Figure 9-5. Proposed idea for the volatile molecular sensor integrated with CNTs in order to improve the sensor performance.

Furthermore, the nonlinear dynamical effect under particular conditions can be considered with particular interest for developing novel MTM-inspired microwave sensors. Scattering responses is a function of the RF power level. Non-linear effects in the sample medium can be exploited in characterizing different types of materials. Electric field interacts with the sensor circuit hence inducing perturbation in the polarization of samples under test. Dependence of polarization as a function of field strength can be utilized to explore specificity. MTM-based sensors can be designed to provide tailored field distribution for sensing applications.

9.2.3 Metamaterial Antennas Based Phased Arrays

It is very difficult, if not impossible, to achieve beam steering at a fixed frequency using a single antenna element (discounting traveling wave antennas that are multi-wavelength long). The same footprint of a conventional antenna element can be utilized in beam steering by using an array of metamaterial antennas that can be independently controlled using varactor diodes. The antenna demonstrated in this thesis can be arranged in an array format to achieve beam steering and also design high gain antennas. Such an antenna array will find application in communication in smart antenna designs for next generation of communication systems (e.g., cell phones) and wireless sensors arrays.

9.2.4 Use of Metamaterial Structures for MMIC Designs

To reduce overall cost of monolithic microwave circuits (MMICs), it will be desirable to reduce the size of passive components present on the semiconductor chip. As an example, a high power amplifier consists of multiple power dividers or couplers. These power dividers can be miniaturized using metamaterial structure demonstrated under this thesis work. This would lead to decrease in chip size and thus reduced overall materials cost.

Metamaterial structures can be implemented in the design of multichip modules where by coupling between the chips can be attained by using metamaterial structures. This approach will help avoid use of wire bonds and ribbon bonds. This will allow in removing large pads from MMIC necessary for wire or ribbon bonding. Furthermore, metamaterial structures can be implemented in the design of ground plane to achieve desired impedance. This will allow in the design of novel integrated circuits and help reduce cross-talk.

APPENDICES

Appendix A

Equivalent Circuit for the 1-D CRLH Transmission Line

A.1 Analysis of Incremental Circuit using Telegrapher's Equations

A.1.1 Propagation Constant

$$\gamma = \alpha + j\beta = js(\omega) \sqrt{\left(\frac{\omega}{\omega'_R}\right)^2 + \left(\frac{\omega'_L}{\omega}\right)^2 - \kappa\omega'_L{}^2} \quad (\text{A-1})$$

Therefore,

$$\beta = s(\omega) \sqrt{\left(\frac{\omega}{\omega'_R}\right)^2 + \left(\frac{\omega'_L}{\omega}\right)^2 - \kappa\omega'_L{}^2} \quad (\text{A-2})$$

In balanced condition, $\omega_{se} = \omega_{sh} = \omega_o$, and

In the sense that $\omega < \omega_o$ leads to $s(\omega) = -1$ and $\omega > \omega_o$ leads to $s(\omega) = +1$, therefore

$$\beta = s(\omega) \left| \frac{\omega}{\omega'_R} - \frac{\omega'_L}{\omega} \right| = \left(\frac{\omega}{\omega'_R} - \frac{\omega'_L}{\omega} \right)$$

A.1.2 Phase Velocity

$$v_p = \frac{\omega}{\beta} = s(\omega) \frac{\omega}{\sqrt{\left(\frac{\omega}{\omega'_R}\right)^2 + \left(\frac{\omega'_L}{\omega}\right)^2 - \kappa\omega'_L{}^2}} \quad (\text{A-3})$$

Thus,

$$\begin{aligned}
\frac{v_p}{\omega'_R} &= s(\omega) \cdot \frac{\omega}{\omega'_R} \cdot \frac{1}{\sqrt{\left(\frac{\omega}{\omega'_R}\right)^2 + \left(\frac{\omega'_L}{\omega}\right)^2 - \kappa \omega'_L{}^2}} \\
&= s(\omega) \cdot \frac{1}{\sqrt{1 + \left(\frac{\omega'_R \cdot \omega'_L}{\omega^2}\right)^2 - \kappa \left(\frac{\omega'_R \cdot \omega'_L}{\omega}\right)^2}} \\
&= s(\omega) \cdot \frac{1}{\sqrt{1 + \left(\frac{\omega_o}{\omega}\right)^4 - \kappa \cdot \frac{\omega_o^4}{\omega^2}}}
\end{aligned}$$

In balanced condition, $\omega_{se} = \omega_{sh} = \omega_o$

$$\begin{aligned}
\frac{v_p}{\omega'_R} &= s(\omega) \cdot \frac{1}{\sqrt{1 + \left(\frac{\omega_o}{\omega}\right)^4 - 2 \cdot \left(\frac{\omega_o}{\omega}\right)^2}} \\
&= s(\omega) \cdot \frac{1}{\left|1 - \left(\frac{\omega_o}{\omega}\right)^2\right|} \\
&= s(\omega) \cdot \frac{\omega^2}{|\omega^2 - \omega_o^2|}
\end{aligned}$$

In the sense that $\omega < \omega_o$ leads to $s(\omega) = -1$ and $\omega > \omega_o$ leads to $s(\omega) = +1$, thus

$$\frac{v_p}{\omega'_R} = \frac{\omega^2}{\omega^2 - \omega_o^2} = \frac{\omega^2}{\omega^2 - (\omega'_R \cdot \omega'_L)} \quad (\text{A-4})$$

A.1.3 Group Velocity

$$v_g = \left(\frac{d\beta}{d\omega} \right)^{-1} = \frac{\sqrt{\left(\frac{\omega}{\omega'_R} \right)^2 + \left(\frac{\omega'_L}{\omega} \right)^2 - \kappa \omega'^2_L}}{\left| \left(\omega / \omega'^2_R \right) - \left(\omega'^2_L / \omega^3 \right) \right|} \quad (\text{A-5})$$

Thus,

$$\begin{aligned} \frac{v_g}{\omega'_R} &= \frac{1}{\omega'_R} \cdot \frac{\omega}{\omega'_R} \cdot \frac{\sqrt{1 + \frac{\omega_o^4}{\omega^4} - \kappa \cdot \frac{\omega_o^4}{\omega^2}}}{\left| \left(\omega / \omega'^2_R \right) - \left(\omega'^2_L / \omega^3 \right) \right|} \\ &= \frac{\sqrt{1 + \frac{\omega_o^4}{\omega^4} - \kappa \cdot \frac{\omega_o^4}{\omega^2}}}{\left| 1 - \left(\omega'^2_R \cdot \omega'^2_L / \omega^4 \right) \right|} \end{aligned}$$

In balanced condition, $\omega_{se} = \omega_{sh} = \omega_o$

$$\frac{v_g}{\omega'_R} = \frac{\omega^2 - \omega_o^2}{\omega^2} \cdot \frac{\omega^4}{\left| \omega^4 - (\omega'_R \cdot \omega'_L)^2 \right|}$$

Therefore,

$$\frac{v_g}{\omega'_R} = \frac{\omega^2}{\omega^2 + \omega_o^2} = \frac{\omega^2}{\omega^2 + (\omega'_R \cdot \omega'_L)} \quad (\text{A-6})$$

A.1.4 Derivative of Group Velocity on Balanced Mode

$$\frac{dv_g}{d\omega} = \frac{d}{d\omega} \left(\frac{\omega'_R \cdot \omega^2}{\omega^2 + (\omega'_R \cdot \omega'_L)} \right)$$

Therefore,

$$\frac{dv_g}{d\omega} = \frac{2\omega \cdot \omega_o^2 \cdot \omega'_R}{(\omega^2 + \omega_o^2)^2} \quad (\text{A-7})$$

A.2 Analysis of the proposed MTM unit cell model using *ABCD* Matrix-Periodic Approach

According to equation (2-36), *ABCD*-matrix will be repeated here again

$$\begin{bmatrix} A & B \\ C & D \end{bmatrix} = \begin{bmatrix} 1 & \frac{Z}{2} \\ 0 & 1 \end{bmatrix} \begin{bmatrix} 1 & 0 \\ Y & 1 \end{bmatrix} \begin{bmatrix} 1 & \frac{Z}{2} \\ 0 & 1 \end{bmatrix} = \begin{bmatrix} 1 + \left(\frac{Z \cdot Y}{2}\right) & Z + \left(\frac{Z^2 \cdot Y}{4}\right) \\ Y & 1 + \left(\frac{Z \cdot Y}{2}\right) \end{bmatrix} \quad (\text{A-8})$$

Therefore, it corresponds to non-attenuation, for lossless condition, leading to propagating wave on the periodic structure as bandpass characteristic.

$$\cosh(\gamma d) \approx \cos(\beta_{BL} \cdot d) = 1 + \left(\frac{Z \cdot Y}{2}\right)$$

Since $\sin^2 \theta = (1 - \cos 2\theta)/2$, therefore

$$\sin^2 \left(\frac{\beta_{BL} \cdot d}{2} \right) = -\frac{1}{4} Z \cdot Y$$

Referring to the MTM unit cell model, *ABCD*-matrix of Figure 2-19 is repeated here again.

$$\begin{aligned}
\begin{bmatrix} A & B \\ C & D \end{bmatrix} &= \begin{bmatrix} 1 & \frac{Z}{2} \\ 0 & 1 \end{bmatrix} \begin{bmatrix} \cos\left(\frac{\theta}{2}\right) & jZ_o \sin(\theta/2) \\ jY_o \sin(\theta/2) & \cos\left(\frac{\theta}{2}\right) \end{bmatrix} \begin{bmatrix} 1 & 0 \\ Y & 1 \end{bmatrix} \\
&\quad \begin{bmatrix} \cos\left(\frac{\theta}{2}\right) & jZ_o \sin(\theta/2) \\ jY_o \sin(\theta/2) & \cos\left(\frac{\theta}{2}\right) \end{bmatrix} \begin{bmatrix} 1 & \frac{Z}{2} \\ 0 & 1 \end{bmatrix}
\end{aligned} \tag{A-9}$$

Therefore, it corresponds to non-attenuation, for lossless condition, leading to propagating wave on the periodic structure as bandpass characteristic.

$$\begin{aligned}
\cosh(\gamma d) &\approx \cos(\beta_{BL} \cdot d) = \left(1 + \frac{ZY}{4}\right) \cos\theta + \frac{j}{2}(ZY_o + YZ_o) \sin\theta + \frac{ZY}{4} \\
&= \cos\theta + \frac{ZY}{4}(\cos\theta + 1) + \frac{j}{2}\left(\frac{Z}{Z_o} + \frac{Y}{Y_o}\right) \sin\theta \\
&= \cos\theta + \frac{ZY}{2} \cos^2\left(\frac{\theta}{2}\right) + \frac{j}{2}\left(\frac{Z}{Z_o} + \frac{Y}{Y_o}\right) \sin\theta
\end{aligned}$$

Since $\sin^2\theta = (1 - \cos 2\theta)/2$, thus

$$1 - 2 \sin^2\left(\frac{\beta_{BL} \cdot d}{2}\right) = \cos\theta - \frac{1}{2\omega^2 L_o C_o} \cos^2\left(\frac{\theta}{2}\right) + \left(\frac{1}{2\omega C_o Z_o} + \frac{Z_o}{2\omega L_o}\right) \sin\theta$$

$$\begin{aligned}
\sin^2\left(\frac{\beta_{BL} \cdot d}{2}\right) &= \sin^2\left(\frac{\theta}{2}\right) + \frac{1}{4\omega^2 L_o C_o} \cos^2\left(\frac{\theta}{2}\right) - \left(\frac{1}{2\omega C_o Z_o} + \frac{Z_o}{2\omega L_o}\right) \sin\frac{\theta}{2} \cos\frac{\theta}{2} \\
&= \left(\sin\left(\frac{\theta}{2}\right) - \frac{\cos\left(\frac{\theta}{2}\right)}{2\omega C_o Z_o}\right) \left(\sin\left(\frac{\theta}{2}\right) - \frac{\cos\left(\frac{\theta}{2}\right) Z_o}{2\omega L_o}\right)
\end{aligned}$$

As Taylor series approximations, if θ is small then,

$$\sin\theta \approx \theta$$

$$\cos\theta \approx 1 - \frac{\theta^2}{2}$$

Therefore,

$$\begin{aligned} \left(\frac{\beta_{BL} \cdot d}{2}\right)^2 &= \left(\frac{\beta_{TL} \cdot d}{2} - \frac{1}{2\omega C_o Z_o}\right) \left(\frac{\beta_{TL} \cdot d}{2} - \frac{Z_o}{2\omega L_o}\right) \\ \beta_{BL}^2 &= \left(\beta_{TL} - \frac{1}{\omega C_o Z_o \cdot d}\right) \left(\beta_{TL} - \frac{Z_o}{2\omega L_o \cdot d}\right) \\ &= \left(\omega L - \frac{1}{\omega C_o d}\right) \left(\omega C - \frac{1}{\omega L_o d}\right) \\ \beta_{BL} &= \pm \omega \sqrt{\left(L - \frac{1}{\omega^2 C_o d}\right) \left(C - \frac{1}{\omega^2 L_o d}\right)} \end{aligned} \quad (\text{A-10})$$

When it complies with matching condition between host T-line (distributed) and LH contributions (lumped) and also in the sense that RH band (positive phase shift) and LH-band (negative phase shift) therefore,

$$\beta_{eff} = \beta_{BL} = \omega\sqrt{LC} + \frac{-1}{\omega\sqrt{L_o C_o} \cdot d} \quad (\text{A-11})$$

$$|\phi_o| = \beta_{eff} \cdot d = \phi_{TL} + \frac{-1}{\omega\sqrt{L_o C_o}} \quad (\text{A-12})$$

Appendix B

Microfabrication Process

B.1 Copper-Wet Etchant

Process Flow:

prepare a substrate, clean the substrate, spin on photoresist, soft bake, expose, hard bake, develop, submerge sample in copper etchant, rinse, dry and wash of all photoresist.

Process Steps:

- 1) Cut the substrate board as the designed size.
- 2) Laminate one side of the substrate with 3M protective tapes since the circuit design requires one-side metal patterning with solid ground plane.
- 3) Spray rinse the substrate in acetone for 20 seconds.
- 4) Spray rinse the substrate in methanol for 20 seconds.
- 5) Spray rinse the substrate in deionized water (DI-water) for > 1 minute.
- 6) Blow dry the substrate carefully with nitrogen gas (N₂).
- 7) Bake the substrate at 95°C for 1 minute on the hot plate (this step will help drive off some of the surface moisture leading to be helpful in promote photoresist adhesion to wafer).
- 8) Spin positive photoresist (PR) on the substrate:
 - Using a dropper to drop SI813 (PR-solution) cover the entire substrate.
 - Spin the substrate for 30 seconds at 4000 rpm.
- 9) Soft bake the substrate at 90°C for 1 minute 30 seconds on the hot plate.

- 10) Inspect the photoresist. If the quality of the film is not satisfied, then please return to step-1.
- 11) Use the MJB 3 Mask Aligner to expose the photoresist (exposed rate at 275 W in 1 minute 6 seconds).
- 12) Hard bake for 1 minute 30 seconds at 110°C.
- 13) Dissolve the exposed area of the positive photoresist in developer MF-319 to generate a pattern in the photoresist:
 - Immerse the substrate in the developer agitating continuously for 50 seconds
 - Spray rinse the substrate in DI-water 1 minute.
 - Blow dry carefully with N₂.
- 14) Prepare the copper etch solution.
 - Sodium persulfate: DI-water (250grams per liter of DI water)
- 15) Heat up the copper etchant on the hot plate at 90°C (maintain the etchant temperature at 45°C).
- 16) Immerse the substrate in the copper etchant for 5-10 minutes until the pattern of the circuit is complete.
- 17) Rinse the sample for 1 minute and blow the sample dry with N₂.
- 18) Inspect the sample under microscope to check the circuit pattern. If some copper has not been fully removed, return to step-15 again.
- 19) Spray rinse the substrate in acetone in order to remove the photoresist on the wafer.
- 20) Rinse the substrate with methanol
- 21) Rinse the substrate with DI-water for 1 minutes, and then blow dry with N₂

B.2 Mask Layout

Generally, an isotropic etch produces round sidewalls that can make the dimension of the circuit is smaller than the desired circuit pattern as shown in Figure B-1. Therefore, a mask layout should be compensated in order to achieve the right pattern after wet etching process. The compensated size is introduced which is added with an equal size of copper thickness. Since the copper thickness of the *Rogers* substrate is approximately 17 μm , in this study, the dimension of the mask is added with 15-20 μm in each side for compensating the isotropic etch as illustrated in Figure B-2.

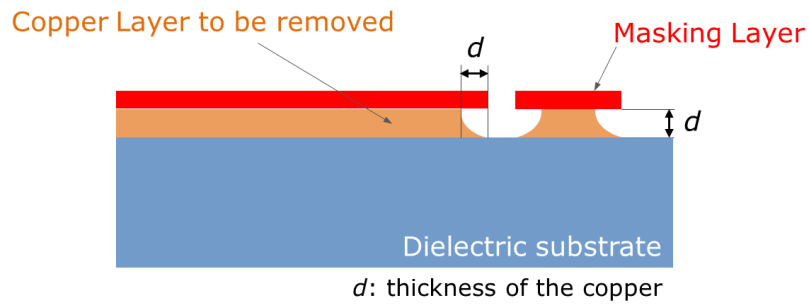


Figure B-1. An isotropic wet etch on a substrate creating round side walls.

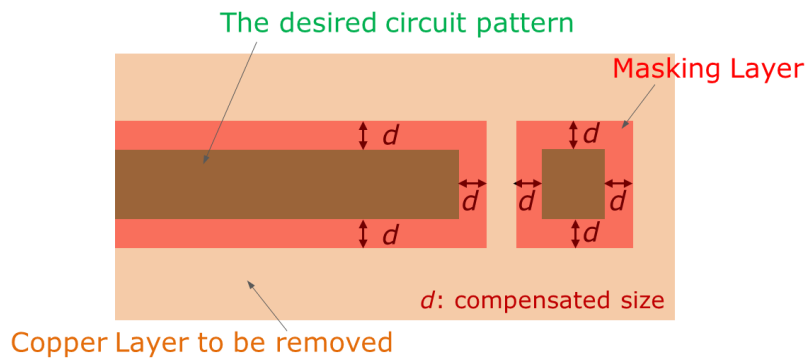


Figure B-2. The example of a mask that its dimension is compensated to achieve the right dimension from the isotropic etch.

Appendix C

Basic Calculation Based on the Ideal Gas Law

According to Table 6-1 in Chapter 6, the calculation process can be determined as below:

C.1 The amount of molecules in one droplet (0.05 cc)

Acetone: $\text{Mass} = 0.05\text{mL} \times 0.791\text{g/mL} = 39.55 \times 10^{-3}\text{g}.$

$$\text{Molecules} = 39.55 \times 10^{-3}\text{g} / 58.081\text{g/mol} = 6.860946 \times 10^{-4} \text{ mol.}$$

Methanol: $\text{Mass} = 0.05\text{mL} \times 0.7918\text{g/mL} = 39.59 \times 10^{-3}\text{g}.$

$$\text{Molecules} = 39.59 \times 10^{-3}\text{g} / 32.04\text{g/mol} = 12.35643 \times 10^{-4} \text{ mol.}$$

C.2 Maximum number of molecules of vaporized liquid in an enclosed bell jar (250 mL).

According to each specific vapor pressure and the ideal gas law [52], the maximum densities of vaporized molecules at 30°C can be determined by

Acetone:

$$n_{\text{acetone}}^{30} = \frac{\left(\frac{180}{760}\right) \times (250 \times 10^{-3})}{(0.0821) \times (273 + 20)} = 37.68647 \times 10^{-4} \text{ mol.}$$

Methanol:

$$n_{\text{methanol}}^{30} = \frac{\left(\frac{157}{760}\right) \times (250 \times 10^{-3})}{(0.0821) \times (273 + 20)} = 20.76062 \times 10^{-4} \text{ mol.}$$

C.3 Maximum droplets of vaporized liquid in an enclosed bell jar (250 mL).

Acetone: Maximum droplets = $\left(37.68647 \times 10^{-4}\right) / \left(6.80946 \times 10^{-4}\right) = 5.534$

Methanol: Maximum droplets = $\left(20.76062 \times 10^{-4}\right) / \left(12.35643 \times 10^{-4}\right) = 1.680$

C.4 Vaporized liquid density in the enclosed bell jar (250 mL).

Acetone (1 droplet):

$$d_{acetone}^1 = \frac{6.80946 \times 10^{-4}}{250} \text{ mol/mL} = 2.724 \text{ nano-mol/mm}^3$$

Methanol (1 droplet):

$$d_{methanol}^1 = \frac{12.35643 \times 10^{-4}}{250} \text{ mol/mL} = 4.943 \text{ nano-mol/mm}^3$$

BIBLIOGRAPHY

BIBLIOGRAPHY

- [1] V. G. Veselago, "The electrodynamics of substances with simultaneously negative values of ϵ and μ ," *Soviet Physics Uspekhi*, Vol. 10, pp. 509-514, January-February 1968. (Russian version in 1967).
- [2] J. B. Pendry, A. J. Holden, W. J. Stewart, and I. Youngs, "Extremely low frequency plasmons in metallic mesostructures," *Phys. Rev. Lett.*, 76:4773, 1996.
- [3] J. B. Pendry, A. J. Holden, D. J. Robbins, and W. J. Stewart, "Magnetism from conductors and enhanced nonlinear phenomena," *IEEE Trans. Microwave Theory Tech.*, 47:2075, 1999.
- [4] J.-S. G. Hong, M. J. Lancaster. *Microstrip Filters for RF/Microwave Applications*, Wiley-Interscience, 2001.
- [5] C. Caloz and T. Itoh. *Electromagnetic Metamaterials: Transmission Line Theory and Microwave Applications*, Wiley-IEEE Press, 2006.
- [6] D. R. Smith, W. J. Padilla, D. C. Vier, S. C. Nemat-Nasser, and S. Schultz. "Composite medium with simultaneously negative permeability and permittivity," *Phys. Rev. Lett.*, vol. 84, no. 18, pp. 4184–4187, May 2000.
- [7] S. Ramo, J. R. Whinnery and T. Van Duzer. *Fields and Waves in Communication Electronics*, 3rd ed., John Wiley & Sons, 1994.
- [8] S. Lim, C. Caloz, and T. Itoh, "Metamaterial-based electronically controlled transmission line structure as a novel leaky-wave antenna with tunable radiation angle and beamwidth," *IEEE Trans. Microwave Theory Tech.*, vol. 52, no. 12, pp. 2678-2690, Dec. 2004.
- [9] J. Martel, R. Marqués, F. Falcone, J. D. Baena, F. Medina, F. Martín, and M. Sorolla, "A new LC series element for compact bandpass filter design", *IEEE Microw. Wireless Compon. Lett.*, vol. 14, no. 5, pp. 210-212, May 2004.
- [10] F. Martín, J. Bonache, F. Falcone, M. Sorolla, and R. Marqués, "Split ring resonator-based left-handed coplanar waveguide", *Appl. Phys. Lett.*, vol. 83, pp. 4652-4654, Dec. 2003.
- [11] M. Gil, J. Bonache, I. Gil, J. García-García, and F. Martín, "On the transmission line properties of left-handed microstrip line implemented by complementary split rings resonators", *Int. J. Num. Model.*, vol. 19, pp. 87-103, Mar./Apr. 2006.
- [12] M. Gil, J. Bonache, I. Gil, J. García-García, and F. Martín, "Miniaturization of planar microwave circuits by using resonant-type left handed transmission lines", *IEEE Trans. Antennas Propagat.*, vol. 1, pp. 73-79, Mar. 2007.

- [13] J. D. Baena, J. Bonache, F. Martín, R. Marqués, F. Falcone, T. Lopetegui, M. A. G. Laso, J. García, I. Gil, and M. Sorolla, "Equivalent circuit models for split ring resonators and complementary split rings resonators coupled to planar transmission lines," *IEEE Trans. Microw. Theory Tech.*, vol. 53, no. 4, pp. 1451–1461, Apr. 2005.
- [14] F. Martín, F. Falcone, J. Bonache, T. Lopetegui, R. Marqués, and M. Sorolla, "Miniaturized CPW stop band filters based on multiple tuned split ring resonators," *IEEE Microw. Wireless Compon. Lett.*, vol. 13, no. 12, pp. 511–513, Dec. 2003.
- [15] F. Falcone, T. Lopetegui, J. D. Baena, R. Marqués, F. Martín, and M. Sorolla, "Effective negative-" stop-band microstrip lines based on complementary split ring resonators," *IEEE Microw. Wireless Compon. Lett.*, vol. 14, no. 6, pp. 280–282, Jun. 2004.
- [16] G. V. Eleftheriades, A. K. Iyer, and P.C. Kremer, "Planar negative refractive index media using periodically L-C loaded transmission line," *IEEE Trans. Microw. Theory Tech.*, vol. 50, no. 12, pp. 2702–2712, Dec. 2002.
- [17] R. E. Collin, *Foundations for Microwave Engineering*, 2nd ed., New York, NY: McGraw-Hill, 1992.
- [18] G. Matthaei, L. Young, and E. M. T. Jones, *Microwave Filters, Impedance-Matching Networks, and Coupling Structures*. Norwood, MA: Artech House, 1980.
- [19] C. Caloz, A. Sanada and T. Itoh, "Microwave application of transmission-line based negative refractive index structures", *IEEE Asia-Pacific Microw. Conf. (APMC 2003)*, Seoul, Korea, Nov. 2003.
- [20] M. A. Antoniades, G. V. Eleftheriades, "Compact linear lead/lag metamaterial phase shifters for broadband applications", *IEEE Antenna and Wireless Propag. Lett.*, vol. 2, no. 1, pp. 103–106, 2003.
- [21] F. Falcone, T. Lopetegui, J. D. Baena, R. Marqués, F. Martín, and M. Sorolla, "Effective negative-mu stop-band microstrip lines based on complementary split ring resonators," *IEEE Microw. Wireless Compon. Lett.*, vol. 14, no. 6, pp. 280–282, Jun. 2004.
- [22] J. Garcia-Garcia, F. Martín, F. Falcone, J. Bonache, J. D. Baena, I. Gil, E. Amat, T. Lopetegui, M. A. G. Laso, J. A. M. Iturmendi, M. Sorolla, and R. Marqués, "Microwave filters with improved stopband based on sub-wavelength resonators," *IEEE Trans. Microw. Theory Tech.*, vol. 53, no. 6, pp. 1997–2006, Jun. 2005.
- [23] J. Garcia-Garcia, F. Martín, F. Falcone, J. Bonache, J. D. Baena, I. Gil, E. Amat, T. Lopetegui, M. A. G. Laso, J. A. M. Iturmendi, M. Sorolla, and R. Marqués, "Microwave filters with improved stopband based on sub-wavelength resonators," *IEEE Trans. Microw. Theory Tech.*, vol. 53, no. 6, pp. 1997–2006, Jun. 2005.

- [24] J. Naqui, A. Fernandez-Prieto, M. Duran-Sindreu, J. Selga, F. Medina, F. Mesa, and F. Martín, "Split rings-based differential transmission lines with common-mode suppression," *IEEE MTTs Int. Microw. Symp.*, Baltimore, MD, pp. 1-4, June 2011.
- [25] C. Caloz, H. Okabe, T. Iwai, and T. Itoh. "Transmission line approach of left-handed (LH) materials," *USNC/URSI National Radio Science Meeting*, San Antonio, TX, vol. 1, p. 39, June 2002.
- [26] C. Caloz and T. Itoh, "Transmission line approach of left-handed (LH) materials and microstrip implementation of an artificial LH transmission line," *IEEE Trans. Antennas Propag.*, vol. 52, no. 5, pp. 1159–1166, May 2004.
- [27] C. Caloz and T. Itoh, "A novel mixed conventional microstrip and composite right/left-handed backward-wave directional coupler with broadband and tight coupling characteristics," *IEEE Microwave Wireless Compon. Lett.*, vol. 14, pp. 31–33, Jan. 2004.
- [28] A. Sanada, C. Caloz, and T. Itoh, "Zeroth order resonance in composite right/left-handed transmission line resonators," in *Proc. Asia-Pacific Microw. Conf.*, Seoul, Korea, 2003, vol. 3, pp. 1588–1592.
- [29] I. Lin, C. Caloz, and T. Itoh, "A branch-line coupler with two arbitrary operating frequencies using left-handed transmission lines," in *IEEE-MTT Int. Symp. Dig.*, Philadelphia, PA, 2003, vol. 1, pp. 325–327.
- [30] E. Saenz, A. Cantora, I. Ederra, R. Gonzalo, and P. de Maagt, "A metamaterial T-junction power divider," *IEEE Microw. Wireless Compon. Lett.*, vol. 17, no. 3, pp. 172–174, Mar. 2007.
- [31] Y. Guo, G. Goussetis, A. P. Feresidis, and J. C. Vardaxoglou, "Efficient modeling of novel uniplanar left-handed metamaterials", *IEEE Trans. Microwave Theory Tech.*, vol. 53, pp. 1462–1468, Apr. 2005.
- [32] T. Kokkinos, A. P. Feresidis, and J. C. Vardaxoglou, "Analysis and application of metamaterial spiral-based transmission line", *IEEE IWAT '07 International Workshop on* (2007), pp. 233-236, Mar. 2007.
- [33] N. Wiwatcharagoses, K. Y. Park, J. A. Hejase, L. Williamson, and P. Chahal, "Microwave Artificially Structure Periodic Media Microfluidic Sensors", in *IEEE 61th Electronic Components and Technology Conf. Proc.*, Orlando, FL, 2011, pp. 1889-1893.
- [34] N. Wiwatcharagoses, K. Y. Park, and P. Chahal, "A New Metamaterial Unit Cell for Compact Microstrip Designs", in *IEEE 61th Electronic Components and Technology Conf. Proc.*, Orlando, FL, 2011, pp. 169-172.
- [35] N. Wiwatcharagoses, and P. Chahal, "A Novel Reconfigurable Metamaterial Unit Cell based Composite Right/Left Handed Microstrip Design", *IEEE AP-S/URSI Int. Symp Dig.*, Spokane, WA, 2011, pp. 2954-2957.

- [36] G. V. Eleftheriades, "Analysis of bandwidth and loss in negative-refractive-index transmission-line (NRI-TL) media using coupled resonators," *IEEE Microw. Wireless Compon. Lett.*, vol. 17, no. 6, pp. 412–414, Jun. 2007.
- [37] R. Islam and G. V. Eleftheriades, "Elliptic-type bandpass filter and bandstop notch filter inspired by metamaterial NRI-TL topology," *Electronics Letters*, vol. 44, no. 25, pp. 1470–1472, Dec. 2008.
- [38] M. Studniberg and G. V. Eleftheriades, "Physical implementation of a generalized NRI-TL medium for quad-band applications," in *Proc. 37th Eur. Microw. Conf. (EuMC 2007)*, Munich, Germany, pp. 408–411, Oct. 2007.
- [39] G. V. Eleftheriades, "A generalized negative-refractive-index transmission-line (NRI-TL) metamaterial for dual-band and quad-band applications," *IEEE Microw. Wireless Compon. Lett.*, vol. 17, no. 6, pp. 415–417, Jun. 2007.
- [40] D.M. Pozar, *Microwave Engineering*, 3rd ed., Hoboken, NJ: John Wiley & Sons, 2005.
- [41] Skywork®, "SMV2019-SMV2023 Series: Plastic Package Abrupt Junction Tuning Varactors," datasheet, June 14, 2012.
- [42] Skywork®, "SMV1405-SMV1430 Series: Plastic Package Abrupt Junction Tuning Varactors," datasheet, May 25, 2011.
- [43] H. Lee, and J. Yook, "Biosensing using split-ring resonators at microwave regime", *Applied Physics Letters*, 92, pp. 254103-1 – 3, 2008.
- [44] S. Mashimo, and T. Umehara, "Structure of water and primary alcohol studied by microwave dielectric analyses", *J. Chem. Phys.*, vol. 95, pp.6257-6260, Nov. 1991.
- [45] J. Barthel, K. Bachhuber, R. Buchner, and H. Hetzenauer, "Dielectric spectra of some common solvents in the microwave region water and lower alcohols", *Chem. Phys. Lett.*, vol. 165, pp.369-373, Jan. 1990.
- [46] C. Oliver Kappe, and A. Stadler, *Microwave in Organic and Medicinal Chemistry*, Wiley-VCH (Weinheim, 2005), pp. 13.
- [47] C. Chunrong, and P. Wang, "A radio frequency device for measurement of minute dielectric property changes in microfluidic channels", *Appl. Phys. Lett.*, vol. 94, 023901, Jan. 2009.
- [48] P. Alivisatos, "The use of nanocrystals in biological detection", *Nature Biotechnology*, vol. 22, pp. 47-52, Jan 2004.
- [49] N. Wiwatcharagoses, K. Y. Park, and P. Chahal, "Metamaterial transmission line based reconfigurable X-band phase shifter design", in *IEEE 62nd Electronic Components and Technology Conf. Proc.*, San Diego, CA, 2012, pp. 2018-2024.

- [50] J. B. Pendry, “Metamaterials in the sunshine”, *Nature Materials*, vol. 5, pp. 599-600, Aug. 2006.
- [51] J. A. Dean, *Lange’s Handbook of Chemistry*: sec.5 physical properties, 14th-ed. McGraw-Hill, Inc., 1994.
- [52] M. S. Silberberg, *Chemistry: The Molecular Nature of Matter and Change*: chapter 12, 4th-ed., McGraw-Hill Science.
- [53] M. D. Belrhiti, S. Bri, A. Nakheli, M. Haddad, A. Mamouni, “Dielectric constant determination of liquid using rectangular waveguide structure combined with EM simulation”, *J. Mater. Environ.*, pp. 575-584, Sci 3 (3) (2012).
- [54] G.V. Eleftheriades and K.G. Balmain, *Negative-Refraction Metamaterials: Fundamental Principles and Applications*. Hoboken, NJ: John Wiley & Sons, 2005.
- [55] N. Engheta and R.W. Ziolkowski, *Metamaterials: Physics and Engineering Explorations*. Hoboken, NJ: John Wiley & Sons, 2006.
- [56] R. A. Shelby, D. R. Smith, and S. Schultz, “Experimental verification of a negative index of refraction,” *Sci. Mag.*, vol. 292, no. 5514, pp. 77–79, Apr. 2001.
- [57] H. J. Lee, H. S. Lee, K. H. Yoo, and J. G. Yook, “DNA sensing using split-ring resonator alone at microwave regime”, *Journal of Applied Physics*, vol. 108, pp. 014908-1-6, 2010.
- [58] K.-L. Wong, *Antennas for Wireless Communications*. Wiley-Interscience, Hoboken, NJ, 2003.
- [59] N. Engheta and R. W. Ziolkowski (eds.), *Electromagnetic Metamaterials: Physics and Engineering Explorations*. Wiley and IEEE Press, 2006.
- [60] C. A. Balanis, Ed., *Modern Antenna Handbook*. Hoboken, NJ: John Wiley & Sons, 2008.
- [61] C. A. Balanis, *Antenna Theory: Analysis and Design*, 3rd Edition, Hoboken, NJ: John Wiley & Sons, 2005.
- [62] D.H. Staelin, A.W. Morgenthaler, and J.A. Kong, *Electromagnetic Waves*. Englewood Cliffs, NJ: Prentice Hall, 1994.
- [63] N. Wiwatcharagoses, K. Y. Park, and P. Chahal, “A New Metamaterial Unit Cell for Compact Microstrip Designs”, in *IEEE 61th Electronic Components and Technology Conf. Proc.*, Orlando, FL, 2011, pp. 169-172.
- [64] NBS, Tables of dielectric dispersion data for pure liquids and dilute solutions, National Bureau of Standards Circular 589, U.S. Dept. of Commerce, Washington, DC.

- [65] R. Marqués, J. D. Baena, J. Martel, F. Medina, F. Falcone, M. Sorolla, and F. Martín, "Novel small resonant electromagnetic particles for metamaterial and filter design," in *Proc. Int. Electromagnetics in Advanced Applications Conf.*, Sep. 2003, pp. 439–443.
- [66] J. Bonache, I. Gil, J. García-García, and F. Martín, "Novel microstrip bandpass filters based on complementary split-ring resonators," *IEEE Trans. Microw. Theory Tech.*, vol. 54, no. 1, pp. 265–271, Jan. 2006.
- [67] I. Gil, J. García-García, J. Bonache, F. Martín, M. Sorolla, and R. Marqués, "Varactor-loaded split rings resonators for tunable notch filters at microwave frequencies," *Electron. Lett.*, vol. 40, pp. 1347–1348, Oct. 2004.
- [68] H. Kim, A. Kozyrev, A. Karbassi, and D.W. van der Weide, "Linear tunable phase shifter using a left-handed transmission line," *IEEE Microw. Wireless Compon. Lett.*, vol. 15, no. 5, pp. 366–368, May 2005.
- [69] D. Kuylensstierna, A. Vorobiev, P. Linner, and S. Gevorgian, "Composite right/left handed transmission line phase shifter using ferroelectric varactors," *IEEE Microw. Wireless Compon. Lett.*, vol. 16, no. 4, pp. 167–169, Apr. 2006.
- [70] A. D. Acher, C. T. Rodenbeck, and K. Chang, "Compact gap coupled resonator using negative refractive index microstrip line," *Electronics Letters*, vol. 40, no. 2, pp. 126–127, Jan. 2004.
- [71] C. A. Allen, K. M. K. H. Leong, and T. Itoh, "Design of microstrip resonators using balanced and unbalanced composite right/left-handed transmission lines," *IEEE Trans. Microw. Theory Tech.*, vol. 54, no. 7, pp. 3104–3112, Jul. 2006.
- [72] M. Studniberg and G. V. Eleftheriades, "Physical implementation of a generalized NRI-TL medium for quad-band applications," in *Proc. 37th Eur. Microw. Conf. (EuMC 2007)*, Munich, Germany, Oct. 2007, pp. 408–411.
- [73] R. Islam and G. V. Eleftheriades, "Elliptic-type bandpass filter and bandstop notch filter inspired by metamaterial NRI-TL topology," *Electronics Letters*, vol. 44, no. 25, pp. 1470–1472, Dec. 2008.
- [74] C.-H. Tseng and T. Itoh, "Dual-band bandpass and bandstop filters using composite right/left-handed metamaterial transmission lines," in *Proc. IEEE Int. Microw. Symp.*, San Francisco, CA, Jun. 2006, pp. 931–934.
- [75] M. A. Antoniadis and G. V. Eleftheriades, "A broadband Wilkinson balun using microstrip metamaterial lines," *IEEE Antennas Wireless Propag. Lett.*, vol. 4, no. 1, pp. 209–212, 2005.
- [76] A. Grbic and G. V. Eleftheriades, "A backward-wave antenna based on negative refractive index L-C networks," in *Proc. IEEE Int. Symp. Antennas and Propag.*, San Antonio, TX, Jun. 2002, pp. 340–343.

- [77] A. Grbic and G. V. Eleftheriades, “Experimental verification of backward-wave radiation from a negative refractive index metamaterial,” *Journal of Applied Physics*, vol. 92, no. 10, pp. 5930–5935, Nov. 2002.
- [78] P. P. Wang, M. A. Antoniades, and G. V. Eleftheriades, “An investigation of printed Franklin antennas at X-band using artificial (metamaterial) phase-shifting lines,” *IEEE Trans. Antennas Propag.*, vol. 56, no. 10, pp. 3118–3128, Oct. 2008.
- [79] W. J. R. Hoefer, “The transmission-line matrix method—theory and applications,” *IEEE Trans. Microw. Theory Tech.*, vol. 33, no. 10, pp. 882–893, Oct. 1985.
- [80] J. A. Hejase, *Terahertz time domain method for material characterization of layered dielectric media*, Dissertation, Michigan State University, East Lansing, MI, 2012.
- [81] R. O. Ouedraogo, E. J. Rothwell, A. R. Diaz, S. Y. Chen, A. Temme, and K. Fuchi, “In situ optimization of metamaterial-inspired loop antennas,” *IEEE Antennas Wireless Propag. Lett.*, vol. 9, pp. 75–78, 2010.
- [82] Y. J. Kim, J. K. Kim, J. H. Kim, H. Y. Kim, and H. M. Lee, “Negative permeability metamaterial structure based electrically small loop antenna,” in *Proc. of the 10th Int. Conf. on Adv. Commu. Tech. (ICACT’08)*, Gangwon-Do, Korea, Feb. 2008, pp. 769–773.
- [83] S. Y. Chen, R. Ouedraogo, E. J. Rothwell, A. Temme, and A. R. Diaz, “MNG-metamaterial-based efficient small loop antenna,” in *Proc. Int. Symp. Antennas Propag. URSI Radio Sci. Meeting*, Charleston, SC, Jun. 2009, pp. 1–4.
- [84] A. Erentok and R. W. Ziolkowski, “Metamaterial-inspired efficient electrically-small antennas,” *IEEE Trans. Antennas Propag.*, vol. 56, no. 3, pp. 691–707, Mar. 2008.
- [85] S. H. Kim and J. H. Jang, “Folded monopole LC-loaded antenna and its polarization reconfigurability,” *Microw. Opt. Technol. Lett.*, vol. 53, no. 6, pp. 1197–1201, Jun. 2011.